الجمهورية الجزائرية الديمقراطية الشعبية

République Algérienne Démocratique et Populaire
Ministère de L'Enseignement Supérieur et de la Recherche Scientifique



UNIVERSITÉ SETIF1-Ferhat ABBAS

FACULTÉ DE TECHNOLOGIE

THÈSE

Présentée au Département de Génie des Procédés

Pour l'obtention du diplôme de

DOCTORAT

Domaine : Sciences et Technologie

Filière : Génie des Procédés **Option : Génie chimique**

Par

BENDRIHEM Aymene SALAH

THÈME

Synthèse et caractérisation des matériaux à structure lamellaire et de charbon actif issu de la biomasse. Investigation expérimentale et théorique.

Soutenue le 30/05/2026 devant le Jury :

BENCHIKH Lahcen	**Professeur**	**Univ. Sétif1-Ferhat ABBAS**	**Président**
BOUTAHALA Mokhtar	**Professeur**	**Univ. Sétif1-Ferhat ABBAS**	**Directeur de thèse**
TIAR Chafia	**MCA**	**Univ. Sétif1-Ferhat ABBAS**	**Co-Directrice de thèse**
Chafai Nadjib	**Professeur**	**Univ. Sétif1-Ferhat ABBAS**	**Examinateur**
FADEL Ammar	**Professeur**	**Univ. Biskra-Med khaider**	**Examinateur**
KAABACH Khatima	**Professeure**	**Ecole National Polytechnique de Constantine**	**Examinatrice**
GUELLEUL Messaoud	**Professeur**	**Univ. Sétif1-Ferhat ABBAS**	**Invité**

الجمهورية الجزائرية الديمقراطية الشعبية

DEMOCRATIC AND POPULAR REPUBLIC OF ALGERIA
MINISTRY OF HIGHER EDUCATION AND SCIENTIFIC RESEARCH



Setif 1 University-Ferhat ABBAS

FACULTY OF TECHNOLOGY

Thesis submitted to the Process Engineering Department for a Doctorate Degree

Domain : Science and Technology

Section : Process Engineering **Option : Chemical Engineering**

BY

BENDRIHEM Aymene Salah

TITLE OF THE THESIS

Synthesis and Characterization of Lamellar-Structured Materials and Biomass-Derived Activated Carbon: Experimental and Theoretical Investigation

Defended on 30/05/ 2026 in front of the Jury:

BENCHIKH Lahcen	**Professor**	**SETIF1 University-Ferhat ABBAS**	**Chairman**
BOUTAHALA Mokhtar	**Professor**	**SETIF1 University-Ferhat ABBAS**	**Supervisor**
TIAR Chafia	**MCA**	**SETIF1 University-Ferhat ABBAS**	**Co-Supervisor**
CHAFAI Nadjib	**Professor**	**SETIF1 University-Ferhat ABBAS**	**Examinator**
FADEL Ammar	**Professor**	**BISKRA University- Mohammed khaider**	**Examinator**
KAABACH Khatima	**Professor**	**National Polytechnic school of Constantine-ENPC**	**Examinator**
GUELLAL Messaoud	**Professor**	**SETIF1 University-Ferhat ABBAS**	**Guest**

Acknowledgments

First and foremost, I express my deepest gratitude to Allah for His guidance and blessings throughout this journey, and for granting me the health, perseverance, courage, and strength required to successfully complete this work.

I would like to convey my sincere and profound appreciation to my advisors and mentors, ***Pr. Boutahala Mokhtar*** *and* ***Dr. Tiar Chafia****, for their invaluable guidance, constant encouragement, and unwavering support. Their expertise, patience, and dedication were fundamental in guiding me through the complexities of my research and in enabling me to reach this important academic achievement.*

I am also sincerely thankful to ***Dr. Merir Roufaida****, whose continuous support, kindness, and availability were a great source of comfort and motivation. Her presence throughout this journey went far beyond academic assistance, and I am truly grateful for her sisterly support.*

My special appreciation goes to ***Dr. Bounoukta Charf Eddin****, with whom I had the privilege of collaborating. His insightful observations, thoughtful advice, and extensive expertise contributed significantly to the depth and quality of this research.*

I would also like to sincerely thank my colleagues for their cooperation, support, and assistance, which made the research process considerably smoother and more manageable.

My sincere appreciation is extended to the director of our laboratory, ***Pr. Guelel Messouad****, for his continuous support and guidance during this journey.*

I am deeply grateful to the members of my dissertation committee: ***Mr. President Benchick Lahcen****, and the examining members* ***Pr. Fadel Ammar****,* ***Pr. Chafai Nadjib****, and* ***Pr. Kaabach Khatima****, for their time, insightful evaluations, constructive remarks, and valuable recommendations, all of which have greatly enhanced the quality and rigor of this work.*

I am especially indebted to my family, whose love, patience, and encouragement have been my greatest source of strength. To my parents, I offer my deepest thanks for your sacrifices, your unwavering support, and your constant faith in me.

Finally, I extend my sincere gratitude to all those who contributed to this research, whether directly or indirectly. This work would not have been possible without their support and generosity.

Dedication

To my dear parents,

You have given me the most precious gifts of all, love, education, and a strong sense of responsibility. You believed in me even in moments when I doubted myself. Your patience, sacrifices, and unwavering dedication have been my guiding compass throughout this journey. This work stands as the fruit of your encouragement and your silent, heartfelt prayers.

*To my brother and sisters **Nedjm Eddin, Nour, Aridj, and Khadidja**,*

For your love, constant encouragement, and solidarity during the moments when I needed it most. Your reassuring words and comforting presence have been an invaluable source of strength and support.

To my friends and colleagues,

For your understanding, shared experiences, and continuous encouragement. Your friendship has been a true breath of fresh air throughout these demanding years of hard work.

*To my dear **Oumnia**,*

For your endless patience and unwavering support. You have been my refuge in difficult times and my greatest source of motivation when my energy faltered. For all that you are and all that you have given, I dedicate this thesis to you.

To all those who, whether near or far, have contributed in any way to the completion of this work,

I express my deepest gratitude and humbly dedicate this achievement to you.

Contents

Acknowledgment

List of figures

List of tables

List of abbreviations

General introduction ……..……1

Chapter I: Literature Review

1. Introduction ……4

2. Dyes ……4

2.1.Classification of dyes ……..5

2.1.1. Natural dye ……...……5

2.1.2. Synthetic dyes ……...6

2.1.3. Chemical classification of dyes ……8

3. Ecotoxicological impacts of synthetic dyes ……9

4. Processes for the remediation of dye-contaminated effluent ……10

5. Adsorption ……11

5.1. Chemisorption ……11

5.2. Physisorption ……...12

6. Clay minerals ……12

7. Structure of clay minerals ……13

7.1.Tetrahedral sheet ……...13

7.2.Octahedral sheet ……...14

8. Classification of clay minerals ……15

8.1.The kaolinite …….15

8.1.1. Halloysite ……15

8.2.Smectite ……16

8.3.Chlorite ……..17

9. Characteristics properties of clays ……18

10. Organophilic clays ……19

11. Double layered hydroxides ……..21

12. Alginate ……22

13. Polyaniline ……23

Chapter II: Experimental Protocols and Analytical Techniques

1. Introduction ……..26

2. Product and materials used ……...26

3. Synthesis and characterization ……..26

3.1.Preparation of HAL, PANI, HAL/PANI, SAg, HAL/SAg, HAL/PANI/Sag, BC500, BC500/SA, K10, and K10/CTAB …….27

3.2.Characterization of materials ……34

4. Analysis of errors ……..36

5. Density functional theory (DFT) ……...37

6. Molecular dynamics simulation (MDS) ……38

7. Artificial intelligence (AI) techniques ……..39

8. Experimental Design in Adsorption processes …..…… ……..40

9. Methylene blue as a model for cationic dye adsorption ……41

10. Methyl orange as a model for anionic dye adsorption ……..42

11. Theoretical models ……...43

11.1. Kinetic models ……43

11.2. Isotherm models …… ..45

12. Influencing Factors in Adsorption Processes ……47

13. Adsorption thermodynamics ……47

Chapter III: Removal of methylene bleu using raw Algerian halloysite

1. Introduction ……..49

2. Experimental design ……49

3. Adsorption Study ……51

4. Structural and simulation details ……52

4.1. Quantum chemical calculations ……52

4.2. Molecular Dynamic simulations (MDs) ……53

5. Results and discussion ……..54

5.1.Characterization ……54

5.2. Model validation ……59

5.3. Effect of process variable and interactions on the system performance ……61

5.4. Optimization ……...64

5.5.Kinetic study ……65

5.6. Isotherm study ……67

5.7. Statistical physics ……69

5.8. Quantum chemical calculations ……...71

5.9.MD simulations ……74

5.10. Proposal of an adsorption mechanism …… ……76

5.11. Adsorbent efficiency ……...……...77

Chapter IV: Insights into the adsorption mechanism of Methyl Orange using Halloysite/Polyaniline composite

1. Introduction ……..78

2. Choice of adsorbent ……..78

3. Results and discussion …….81

3.1.Materials characterizations ……..81

3.2.Macroscopic analysis of MO adsorption behavior on HNT-PANI……93

3.3.Theoretical studies of MO adsorption by HNT-PANI …… 101

3.4. Adsorption conditions optimization ……..…… ……... 104

3.5. Adsorption mechanism …… .107

Chapter V: The removal of anionic and cationic dyes using novel adsorbent

1. Introduction ……108

2. Design of experiments ……108

3. ANN-GWO & ANN-GA hybrid algorithms ……..111

4. Results and discussion ……114

4.1.Choice of adsorbent ……..114

4.2. Characterization ……...115

4.3. Box Behnken design ……122

4.4. System performance as a function of process variables ……125

4.5. Interaction effects on response and process optimization ……128

4.6. ANN Model ……..130

4.7. Optimization ……132

4.8. Kinetic study ……133

4.9. Isotherm modeling ……135

4.10. Thermodynamic study ……...138

4.11. Adsorption mechanism …… ..140

Chapter VI: Biomass application for the removal of cationic dye

1. Introduction ……140

2. Adsorbent choice ……140

3. Characterization ……..141

3.1.FTIR analysis ……142

3.2.ATG/DTA analysis ……..145

3.3. DRX spectrum analysis ……148

4. Effects of process parameters ……..150

5. Design of Experiments ……151

5.1.Interactions effect ……..……..153

5.2. Optimization study ……153

6. Kinetic study ……..154

7. Adsorption isotherms ……..156

8. Thermodynamic study ……158

9. Desorption and regeneration studies …….……159

10. Adsorption mechanism ……..160

Chapter VII: Organophilic montmorillonite application for water treatment

1. Introduction

2. Characterization ……162

2.1.FTIR analysis ……..162

2.2.X-ray diffraction analysis ……163

2.3.ATG analysis ……164

2.4. Iso-electric point (pHpzc) ……165

3. Kinetic study ……..166

4. Isotherm study ……169

5. Adsorption mechanism ……..170

Chapter VIII: Application of layered double hydroxides (LDHs) for the removal of anionic dyes

1. Introduction …….…….…..172

2. Adsorption screening……..173

General conclusion and perspective ……163

Scientific list

Abstract

List of figures

Figure of chapter I

Figure I. 1: Classification scheme of synthetic dyes based on their chemical composition and functional characteristics. **6**

Figure I. 2: The environmental consequences of dye pollution. **9**

Figure I. 3: Treatment technologies approaches for treating dye-contaminated effluents..... **10**

Figure I. 4: Graphical representation of adsorption pathways. **12**

Figure I. 5: Tetrahedral and octahedral sheets structure. **14**

Figure I. 6: Kaolinite structure. **15**

Figure I. 7: Halloysite structure. **16**

Figure I. 8: Montmorillonite structure. **17**

Figure I. 9: Chlorite structure..... **17**

Figure I. 10: Organophilic clay treatment. **21**

Figure I. 11: Schematic illustration of LDH structure and chemical component. **22**

Figure I. 12: Chemical structure of alginate. **23**

Figure I. 13: Mechanism of interaction between alginate and $Ca2^{+}$. **23**

Figure I. 14: Chemical structures of different forms of polyaniline. **24**

Figure of Chapter II

Figure II. 1: Schematic presentation of the preparation procedure of HAL/PANI. **28**

Figure II. 2: Schematic presentation of the preparation procedure of HNTs/PANI/SA beads. **30**

Figure II. 3: Schematic presentation of the preparation procedure of BC500/Sag bead. **32**

Figure II. 4: Schematic presentation of the organophilic preparation of MTM-K10-CTAB. **33**

Figure II. 5: Schematic presentation of Co-precipitation method for MgAl-CO3, MgAl-SO4 and MgAl-PO4 LDHs. **34**

Figure II. 6: Schematic Representation of Neural Network with single hidden layer. **40**

Figure II. 7: the structure of the MB dye molecule. **42**

Figure II. 8: the structure of the MO dye molecule. **43**

Figure II. 9: Key parameters affecting adsorption. **47**

Figure of Chapter III

Figure III. 1: A schematic representation of the crystalline structure of HNT, the Side and Top view. **54**

Figure III. 2: TEM images of halloysite at 200 nm magnitude. **55**

Figure III. 3: XRD pattern of HNTs. **56**

Figure III. 4: FTIR spectrum of HNTs. **57**

Figure III. 5: TGA /DTA curves of of HNTs. **58**

Figure III. 6: N2 adsorption/ desorption isotherms of HNTs. **59**

Figure III. 7: (a) Normal probability plot of residuals for Halloysite adsorption capacity, (b) plot of the relationship between the predicted and actual values of HNTs adsorption capacity. **61**

Figure III. 8: PHpzc of HNTs. **63**

Figure III. 9: Contour and 3D surface plots for the interactive effects of (a, c), initial pH and adsorbent dosage (b, d), initial dye concentration and adsorbent dosage on the HNTs adsorption capacity. **64**

Figure III. 10: Optimized values for the process parameters. **65**

Figure III. 11: Nonlinear PFO, PSO and IPD kinetics models fits for MB adsorption on HNTs (C0=10, 30 and 100mg/l). **67**

Figure III. 12: Langmuir, Freundlich, Sips, Temkin and Statistical physics non- linear fits to the experimental data of MB adsorption by HNTs at 298 K (pH=10, m=10mg, V=30ml). **70**

Figure III. 13: (a) optimized molecular structure, (b) total electron density surfaces mapped with electrostatic potential (MEP), (d) Lowest Unoccupied Molecular Orbital (LUMO), and (c) Highest Occupied Molecular Orbital (HOMO) of the molecule (MB), calculated conside. **... 72**

Figure III. 14: Side view of the atomic structure of kaolinite crystal. Hydrogen is white, oxygen is red, aluminum is purple, and silicon is yellow. **..... 74**

Figure III. 15: Side view of the most equilibrium configuration of MB adsorption onto HNTs surface. **..... 75**

Figure III. 16: Illustration of the possible interaction between HNTs and MB dye.**..... 76**

Figure of Chapter IV

Figure IV. 1: Effect of adsorbent on MO adsorption capacity. **..... 79**

Figure IV. 2: a) XRD patterns of the studied samples, b) JPCDS files for the detected phases of the studies materials**. 82**

Figure IV. 3: SEM images for a) HNT, b) PANI and c) HNT-PANI.**..... 86**

Figure IV. 4: BET and BJH plots for HNTs, PANI, HNT-PANI**. 87**

Figure IV. 5: FTIR spectrums of the studied materials**. 90**

Figure IV. 6: ATG/DTA plots for HNTs, PANI and HNTs/PANI**. 92**

Figure IV. 7: pH_{pzc} for HNT, PANI and HNT-PANI. **..... 93**

Figure IV. 8: Effect of contact time on MO quantity adsorbed at various initial concentrations. a)PFO, PSO, and Elovich nonlinear kinetic fits; b) IPD plots showing adsorption steps.**..... 94**

Figure IV. 9: Equilibrium isotherms modelling of MO by HNT-PANI at different temperature **..... 97**

Figure IV. 10: plot of Ln(k) = f(1/T). **..... 101**

Figure IV. 11: Electro density distributions in optimized molecular geometries of MO. **... 102**

Figure IV. 12: Optimized equilibrium configurations of MO on the investigated surfaces from DFT calculations **103**

Figure IV. 13: Influence of the operator conditions parameters on the adsorption of MO by HNT-PANI a) effect of HNT-PANI dosage on the MO adsorbed quantity and removal efficiency, b) Effect of pH_{sol} on the adsorbed quantity. **104**

Figure IV. 12: Illustration of the possible interaction between HNTs/PANI composite and MO..**107**

Figure of Chapter V

Figure V. 1: Schematic diagram of the ANN model. **113**

Figure V. 2: Different materials adsorption capacities for MB and MO. **114**

Figure V. 3: SEM images of a). HNT, b). HNT-PANI, c). HNT-SA, d) HNT-PANI-SA beads, e) HNT-PANI-SA surface before adsorption and f) HNT-PANI-SA surface after adsorption **116**

Figure V. 4: FTIR spectrum for HNT-PANI-SA, SA, HNT-PANI, HNT-SA, PANI and HNT. **118**

Figure V. 5: XRD patterns for HNTs/PANI/SA, HNTs/SA, SA, HNTs/PANI, PANI and HNTs. **119**

Figure V. 6: TGA /DTA curves of a) HNTs, b) PANI, c) HNTs/PANI, d) HNTs/SA and e) HNTs/PANI/SA. **121**

Figure V. 7: N_2 adsorption-desorption isotherms for HNTs, PANI, HNTs/PANI and HNTs/PANI/SA. **122**

Figure V. 8: (a) Normal probability plot of residuals for MB% (b) plot of the relationship between the predicted and actual values of MB%. **124**

Figure V. 9: pHpzc of HNTs/PANI/SA composite..... **126**

Figure V. 10: pH effect on the removal of MB. **126**

Figure V. 11: pH effect on the removal of MB. **127**

Figure V. 12: Contour and 3D surface plots for the interactive effects of (a, c), initial pH and adsorbent dosage (b, d), initial dye concentration and adsorbent dosage on the MB%. **130**

Figure V. 13: The correlation values of the datasets in the ANN model. **132**

Figure V. 14: Nonlinear PFO, PSO and IPD kinetics models fits for MB adsorption on HNTs/PANI/SA composite (C0=100, 200 and 300mg/l). **135**

Figure V. 15: Langmuir, Freundlich, and D-R non- linear fits to the experimental data of MB adsorption by HNTs/PANI/SA composite at different temperatures (pH=9, m=30mg, V=30ml). **137**

Figure V. 16: Proposed mechanism for the adsorption of MB on the surface of HNTs-PANI/SA……**139**

Figure of Chapter VI

Figure VI. 1: Adsorption capacities of different biochars at different pyrolysis temperatures. **140**

Figure VI. 2: SEM micrographs of (a) raw biomass, (b) biochar, and (c) alginate–biochar composite. **142**

Figure VI. 3: FTIR spectrum of Biomass, BC500, BC500H and BC500-SA. **142**

Figure VI. 4: ATG/DTA plots of Biomass, BC500, and BC500-SA. **145**

Figure VI. 5: XRD patterns of raw biomass. **148**

Figure VI. 6: Effect of pH. **149**

Figure VI. 7: the masse effect on the adsorption of MB on BC500, BC500H and BC500-SA. **150**

Figure VI. 8: (a) Normal probability plot of residuals for BC500-SA adsorption capacity, (b) plot of the relationship between the predicted and actual values of BC500-SA adsorption capacity. **152**

Figure VI. 9: (a), Contour and (b) 3D surface plots for the interactive effects of adsorbent dosage and initial dye concentration BC500-SA adsorption capacity. **153**

Figure VI. 10: Optimized values for the process parameters. **154**

Figure VI. 11: Nonlinear PFO, PSO and IPD kinetics models fits for MB adsorption on BC500-SA (C0=50, 100, 200 and 300mg/L). **155**

Figure VI. 12: Langmuir and Freundlich non- linear fits to the experimental data of MB adsorption by BC500-SA at 298 K. **157**

Figure VI. 13: Langmuir non- linear fits to the experimental data of MB adsorption by BC500-SA at different temperatures. **159**

Figure VI. 14: Regeneration cycles of MB adsorption by BC500-SA beads. **160**

Figure VI. 15: Proposed mechanism of adsorption of MB by BC500-SA beads. **161**

Figure of Chapter VII

Figure VII. 1: FTIR spectrum of MTM-K10 and MTM-K10-CTAB. **163**

Figure VII. 2: X-ray diffraction patterns of MTM-K10 and MTM-K10-CTAB. **163**

Figure VII. 3: ATG curve plots for MTM-K10 and MTM-K10-CTAB. **165**

Figure VII. 4: pHpzc points for MTM-K10 and MTM-K10-CTAB. **166**

Figure VII. 5: Nonlinear PFO, PSO and IPD kinetics models fits for MO adsorption on MTM-K10-CTAB (C0=50 and 100mg/L). **168**

Figure VII. 6: Langmuir and Freundlich non linear fits for a). MTM-K10-CTAB/MO and b). MTM-K10/MB at pH=6, v=30ml, m=30mg and T=25°C. **170**

Figure VII. 7: Proposed mechanism for the adsorption of MO on the surface of MTM-K10-CTAB. **171**

Figure VIII.1: Adsorption capacity of Mg_2Al_1LDH-based adsorbent..... **174**

Figure VIII.2: Langumir, Frendlich, Temkin and sips non-linear fits to the experimental data of MO adsorption by **Mg_2Al_1LDH-based adsorbent**……..…….176

List of Tables

Table I. 1: overview of textile dye categories based on the nature of their chromophoric groups**.** **7**

Table I. 2: CEC of some clay minerals**.** **18**

Table III. 1: Experimental range and levels of independent process variables. **50**

Table III. 2: BBD design matrix with experimental values. **51**

Table III. 3: XRF analysis of raw and purified HNTs. **54**

Table III. 4: ANOVA results for the adsorption capacity of HAL. **59**

Table III. 5: PFO and PSO models parameters for MB adsorption on HNTs at different concentrations (10, 30 and 100mg/l). **66**

Table III. 6: Parameters of the langumir, Freundlich, Sips, and Temkin isotherms and statistical physics models for MB adsorption on HNTs at 298K. **70**

Table III. 7: Quantum Chemical Parameters of MB as Computed at the B3LYP/6-311+G(d,p) Level of Theory in Aqueous Solution. **73**

Table III. 8: Calculated energies for the adsorption of the BM molecule on the HNT surface. **75**

Table III. 9: Adsorption capacities for MB by different clay adsorbents……**77**

Table IV. 1: Kinetic model parameters for MO adsorption by different adsorbents. **80**

Table IV. 2: Calculated XRD parameters for the studied samples. **83**

Table IV. 3: Kinetic models parameters for MO adsorption on HNT-PANI at different concentrations **95**

Table IV. 4: Conventional isotherm parameters for MO adsorption on HNT-PANI. **99**

Table IV. 5: Thermodynamic parameters for the of MO on HNT-PANI. **100**

Table IV. 6: Obtained adsorption energies and MO/surface distances distances from DFT calculatios. **104**

Table IV. 7: Comparative overview of modified clay-based adsorbents reported in the literature in the literature for MO removal. **106**

Table V. 1: Experimental range and levels of independent process variables. **109**

Table V. 2: BBD design matrix with experimental values. **110**

Table V. 3: The elemental analysis, and textural properties of HNTs, PANI, HNTs/PANI and HNTs/PANI/SA. **122**

Table V. 4: ANOVA results for MB removal efficiency. **124**

Table V. 5: Optimal process conditions following RSM-BBD, ANN-GWO and ANN-GA. **133**

Table V. 6: PFO, PSO and IPD nonlinear fits parameters for MB adsorption on HNTs/PANI/SA at different concentrations (100, 200 and 300mg/l). **134**

Table V. 7: Parameters of the Langumir, Freundlich and D-R isotherms models for MB adsorption on HNTs/PANI/SA at different temperature. **137**

Table V. 8: Thermodynamic properties of MB adsorption on HNTs/PANI/SA **138**

Table VI. 1: ANOVA results for the adsorption capacity of MB. **152**

Table VI. 2: PFO, PSO and IPD models parameters for MB adsorption on BC500-SA at different concentrations (50, 100, 200 and 300mg/L) **155**

Table VI. 3: Parameters of the Langumir and Freundlich models for MB adsorption on BC500-SA at 298K. **157**

Table VI. 4: Langmuir parameters at different temperature. **158**

Table VI. 5: thermodynamic properties of MB adsorption on BC500-SA. **159**

Table VII. 1: PFO, PSO and IPD models parameters for MO adsorption on MTM-K10-CTAB at different concentrations (50 and 100 mg/L). **168**

Table VII. 2: Langmuir and Freundlich parameters values for different adsorption systems…. **169**

Table VII. 1: parameters of the Langmuir, Frendlich, Temkin and Sips isotherms models for MO adsorption on Mg_2Al_1LDH-CO3,Mg_2Al_1LDH-SO_4 and Mg_2Al_1LDH-PO_4 at 20°C **..... 177**

Nomenclature

HNT Halloysite nanotubes

PANI Polyaniline

SA Sodium alginate

MTM Montmorillonite

LDH Double layered hydroxides

DOE Design of experiments

RSM Response of surface methodology

BBD Box Behnken design

ANN Artificial neural network

GA Genetic algorithm

GWO Grey wolf optimization algorithm

MB methylene blue

MO methyl orange

C the intercept of Intraparticle diffusion function

C_o initial concentration of MB ($mg \cdot L^{-1}$)

Ce final concentration of MB in the solution

C_t: concentration of MB at time t ($mg \cdot L^{-1}$)

G Gibbs free enthalpy ($J \cdot mol^{-1}$)

k_1 equilibrium rate constant of PFO equation ($L \cdot min^{-1}$)

k_2 equilibrium rate constant of PSO equation ($L \cdot min^{-1}$)

K_F Freundlich constant ($g \cdot L \cdot mg$)

K_{id} the rate constant of intraparticle diffusion($mg \cdot g\text{-}1 \cdot min^{-0.5}$)

K_L Langmuir constant ($L \cdot mg^{-1}$)

K_s Sips constant ($L \cdot mg^{-1}$)

M mass of the mixture (g)

ns the exponent of the Sips model

nf Freundlich constant

PFO pseudo-first-order,

PSO pseudo-second-order

PNO pseudo-nth-order

qe amount of dye adsorbed at equilibrium ($mg \bullet g^{-1}$)

qt quantity adsorbed at time t ($mg \bullet g^{-1}$)

R the correlation coefficient

RMSE Root Mean Squared Error

ΔS Entropy ($J \bullet mol \bullet K^{-1}$)

ΔH Enthalpy (kJ/mol)

T temperature (°C or °K)

GENERAL INTRODUCTION

General introduction

Serving as an essential natural resource for planetary life support, water dominates 71% of Earth's surface, yet the fraction available as freshwater is limited to just 2.5% [1]. In light of the limited availability of natural resources, their sustainable management has become essential. However, aquatic systems continue to be adversely affected by pollution arising from both natural sources such as surface runoff, volcanic emissions, atmospheric deposition, and geomorphological processes and anthropogenic activities, including industrial effluents, agricultural and medical wastes, sewage discharges, and municipal wastewater [2]. Among these, industrial effluents pose a particularly significant global threat, with synthetic dyes being among the most hazardous pollutants released into aquatic systems [3]. Dyes are synthetic organic molecules that exhibit solubility in aqueous or organic media, in contrast to pigments, which remain insoluble and persist as dispersed solid particles [4]. Structurally, dyes are complex unsaturated organic frameworks that absorb portions of visible light, thereby generating color [5].

At the international scale, the use of more than 100,000 commercial dyes has been reported, resulting in an estimated discharge of approximately 280,000 tonnes per year into wastewater generated by dyeing and printing processes [6]. The inadequate fixation of numerous dye types results in nearly 80% of dye containing wastewater being released without treatment, thereby exerting harmful impacts on humans and surrounding ecosystems [7].

The removal of synthetic dyes from wastewater is critical due to their ecological and health risks. They reduce light penetration, disrupt aquatic ecosystems, and introduce toxic compounds that bioaccumulate [8]. Exposure can cause irritation, allergic reactions, and long-term mutagenic or carcinogenic effects, with azo dyes posing particular carcinogenic hazards [9].

A wide range of remediation technologies has been developed for the treatment of dye-contaminated effluents, including physical methods (such as flotation [10] and reverse osmosis [11]), chemical approaches (such as coagulation–flocculation [12] and electrochemical oxidation [13]), and biological processes (including microbial degradation and photodegradation [14]). Among these techniques, adsorption is widely recognized as the most versatile and effective method [8]. Although each treatment method offers specific benefits, adsorption is particularly advantageous due to its operational simplicity, high efficiency in continuous-flow systems, cost-effectiveness, environmental compatibility, sludge-free operation, non-destructive nature, biocompatibility, and ease of implementation [15], [16].

An extensive spectrum of adsorptive media has been examined, encompassing alginate-derived biopolymers, high surface area activated carbons, thermochemically produced biochars, layered double hydroxides and clay minerals [17], [18], [19].

Within this framework, the primary objective of the present study is to valorize locally available products through the development of innovative, low-cost adsorbent materials that meet key performance and sustainability criteria. These include the use of abundant and readily accessible raw materials, the production of non-toxic and environmentally benign adsorbents, the implementation of reproducible and well-controlled synthesis procedures, cost-effective fabrication, high adsorption efficiency for wastewater decolorization, and the ability to be easily regenerated after use.

The present investigation aims at the synthesis of different materials engineered into fine powdered and beads adsorptive materials whose physicochemical characteristics and adsorption efficiencies will be systematically examined. The comprehensive results obtained in this research will be consolidated and presented in the form of scientific manuscripts, organized within the seven subsequent chapters of this PhD thesis.

Chapter I, presents a comprehensive literature review contextualizing the research problem. It covers the classification, physicochemical properties, and environmental impacts of dyes, followed by a critical evaluation of wastewater decolorization methods with emphasis on adsorption. Low-cost adsorbents, including natural, industrial, and agricultural residues, are discussed alongside comparative data on their adsorption performance. Composite materials designed to overcome the limitations of conventional powders are also introduced.

Chapter II, presents the experimental methods applied and chemicals in use.

Chapters III, IV, and V provide a detailed and systematic investigation into the application of halloysite and its composite materials for the removal of both anionic and cationic dyes.

Chapter VI, presents an experimental study focused on the synthesis of various biochars and evaluates their effectiveness in the treatment of dye-contaminated effluents.

Chapter VII, discusses the organophilization of montmorillonite, emphasizing its role in enhancing the adsorption capacity of this clay mineral.

Chapter VIII, aims to deliver a preliminary assessment of the influence of interlayer anions on the adsorption behavior of layered double hydroxides (LDHs), with particular emphasis on the removal of Methyl Orange from aqueous solutions.

Reference of general introduction

[1] X. Wang, J. Jiang, et W. Gao, « Reviewing textile wastewater produced by industries: characteristics, environmental impacts, and treatment strategies », *Water Science and Technology*, vol. 85, nº 7, p. 2076-2096, 2022.

[2] UNESCO, *The United Nations world water development report 2018: nature-based solutions for water*. UN, 2019.

[3] D. Ş. Arslan, H. Ertap, Z. M. Şenol, N. El Messaoudi, et V. Mehmeti, « Preparation of polyacrylamide titanium dioxide hybrid nanocomposite by direct polymerization and its applicability in removing crystal violet from aqueous solution », *Journal of Polymers and the Environment*, vol. 32, nº 2, p. 573-587, 2024.

[4] R. Rehman *et al.*, « Recent Literature Review of Significance of Polypyrrole and Its Biocomposites in Adsorption of Dyes from Aqueous Solution », *Adsorption Science & Technology*, vol. 2022, p. 7047832, janv. 2022, doi: 10.1155/2022/7047832.

[5] M. C. Mounia, B. S. EDDINE, R. DJAMEL, et B. ALI, « ANALYSE, SYNTHESE ET ETUDE SOLVATOCHROMIQUE DE COMPOSES TINCTORIAUX ».

[6] Kusumlata, B. Ambade, A. Kumar, et S. Gautam, « Sustainable solutions: reviewing the future of textile dye contaminant removal with emerging biological treatments », *Limnological Review*, vol. 24, nº 2, p. 126-149, 2024.

[7] D. Yaseen et M. Scholz, « Textile dye wastewater characteristics and constituents of synthetic effluents: a critical review », *International journal of environmental science and technology*, vol. 16, nº 2, p. 1193-1226, 2019.

[8] R. Agarwala et L. Mulky, « Adsorption of Dyes from Wastewater: A Comprehensive Review », *ChemBioEng Reviews*, vol. 10, nº 3, p. 326-335, 2023, doi: 10.1002/cben.202200011.

[9] A. P. Periyasamy et A. Negi, « Alkoxide-based solvent dyeing: a feasible strategy for pollution minimization and sustainable approach for the reactive dyeing of cellulosic materials », *Cellulose*, vol. 31, n° 12, p. 7765-7791, 2024.

[10] J. A. Gobai, I. M. Joni, C. Panatarani, et F. Faizal, « A critical review of nanobubble flotation for seawater treatment process », *Water*, vol. 17, n° 7, p. 1054, 2025.

[11] Y. Liang, « Solar-powered forward osmosis as a sustainable water treatment solution: A review », *Journal of Environmental Chemical Engineering*, p. 116332, 2025.

[12] M. S. Lucas, A. R. Teixeira, N. Jorge, et J. A. Peres, « Industrial wastewater treatment by coagulation–flocculation and advanced oxidation processes: A review », *Water*, vol. 17, n° 13, p. 1934, 2025.

[13] R. S. Dhamorikar, V. G. Lade, P. V. Kewalramani, et A. B. Bindwal, « Review on integrated advanced oxidation processes for water and wastewater treatment », *Journal of Industrial and Engineering Chemistry*, vol. 138, p. 104-122, oct. 2024, doi: 10.1016/j.jiec.2024.04.037.

[14] K. Madi *et al.*, « Green Fabrication of ZnO Nanoparticles and ZnO/rGO Nanocomposites from Algerian Date Syrup Extract: Synthesis, Characterization, and Augmented Photocatalytic Efficiency in Methylene Blue Degradation », *Catalysts*, vol. 14, n° 1, p. 62, 2024.

[15] O. R. Benkouachi *et al.*, « Advanced green peel utilization for efficient methylene blue removal: Integrated analysis and predictive modeling », *Journal of Molecular Liquids*, p. 125951, 2024.

[16] S. Bakhtiari, M. Salari, M. Shahrashoub, A. Zeidabadinejad, G. Sharma, et M. Sillanpää, « A comprehensive review on green and eco-friendly nano-adsorbents for the removal of heavy metal ions: synthesis, adsorption mechanisms, and applications », *Current Pollution Reports*, vol. 10, n° 1, p. 1-39, 2024.

[17] T. G. Ambaye, « Mechanisms and adsorption capacities of biochar for the removal of organic and inorganic pollutants from industrial wastewater », *International Journal of Environmental Science and Technology*, 2021.

[18] A. S. Bendrihem *et al.*, « Experimental and theoretical studies of the interaction of cationic dye in halloysite nanotubes », *Reaction Kinetics, Mechanisms and Catalysis*, p. 1-29, 2025.

[19] H. Chaima *et al.*, « Adsorptive removal of cationic dye from aqueous solutions using activated carbon prepared from Crataegus monogyna/sodium alginate/polyaniline composite beads: Experimental study and molecular dynamic simulation », *Journal of Molecular Liquids*, vol. 408, p. 125372, 2024.



CHAPTER I



1. Introduction

Aquatic pollution has emerged as one of the most urgent environmental issues globally, necessitating immediate intervention. The provision of safe and clean water is becoming increasingly challenging as freshwater resources continue to decline. A major contributor to this problem is the discharge of industrial effluents that are either untreated or inadequately treated. These effluents typically contain a complex mixture of pollutants, including synthetic dyes, pesticides, heavy metals, pharmaceutical residues, and various chemical byproducts from industrial activities.

2. Dyes

Dyes are synthetic organic molecules that exhibit solubility in aqueous or organic media, in contrast to pigments, which remain insoluble and persist as dispersed solid particles. Structurally, dyes are complex unsaturated organic frameworks that absorb portions of visible light, thereby generating color [1]. A dye is distinguished by the presence of chromophoric groups, which absorb specific wavelengths within the visible spectrum (380–750 nm). The perceived color corresponds to the wavelengths that are not absorbed but instead reflected, transmitted, or diffused [2]. The light-absorbing properties of dyes arise mainly from extended systems of conjugated double bonds, which facilitate electronic transitions. For this reason, many dyes incorporate aromatic amine functionalities within their molecular structure. The dye's chemical constitution directly governs the degree and nature of coloration, since selective absorption by chromophores determines the complementary color observed. In essence, a dye is a compound that interacts with visible radiation by absorbing defined wavelengths while reflecting the remainder, thus imparting characteristic coloration. Dyes are extensively employed in various industrial and domestic applications, including the coloration of paper, leather, and textiles [3]. In textile processing, it is estimated that up to 50% of the applied dyes do not bind to the fibers and are discharged into wastewater, where they persist as organic

pollutants. Structurally, dyes are organic molecules composed of three essential components: the chromophore, the auxochrome, and the molecular matrix. The chromophore constitutes the principal functional unit responsible for light absorption [4]. Chromophores (e.g., $–NO_2$, –N═N–, –C═O, –C═S, –C═C–) absorb electromagnetic radiation, while auxochromes (–COOH, $–SO_3H$, –OH, $–NH_2$) enhance solubility, modify absorption, and promote dye fixation. The chemically stable framework of textile dyes, particularly carboxyl, amino, and azo groups, renders them resistant to degradation and difficult to remove from wastewater [5].

2.1.Classification of dyes

2.1.1. Natural dye

For millennia, dyeing practices have relied on colorants extracted from botanical and zoological sources [6], typically processed through rudimentary operations such as mechanical grinding or thermal treatment. Historically, these dyes are principally categorized into **mordant dyes** and **vat dyes**, based on their chemical behavior and application pathways [7].

- **Mordant dyes** comprise water-insoluble chromophoric compounds that form coordinate complexes with metal ions pre-adsorbed onto the fiber. The interaction between the dye's functional groups and the metal ions yields a stable metal ligand complex, significantly enhancing dye-fiber affinity, fixation, and overall fastness properties.
- **Vat dyes** are inherently water-insoluble chromogens characterized by the presence of two or more carbonyl (ketone) functionalities. Their application requires a reductive alkaline bath that transforms the dye into its leuco-soluble enolate form. This reduced species exhibits high substantivity toward cellulosic substrates, particularly upon substitution at the enolate centers, after which oxidative reconstitution regenerates the insoluble, colored form within the fiber matrix.

2.1.2. Synthetic dyes

Synthetic dyes, derived from organic or inorganic chemical compounds, are systematically classified based on their molecular architecture and physicochemical properties. This classification framework, widely used in the textile sector, is presented in Figure I.1.[1]

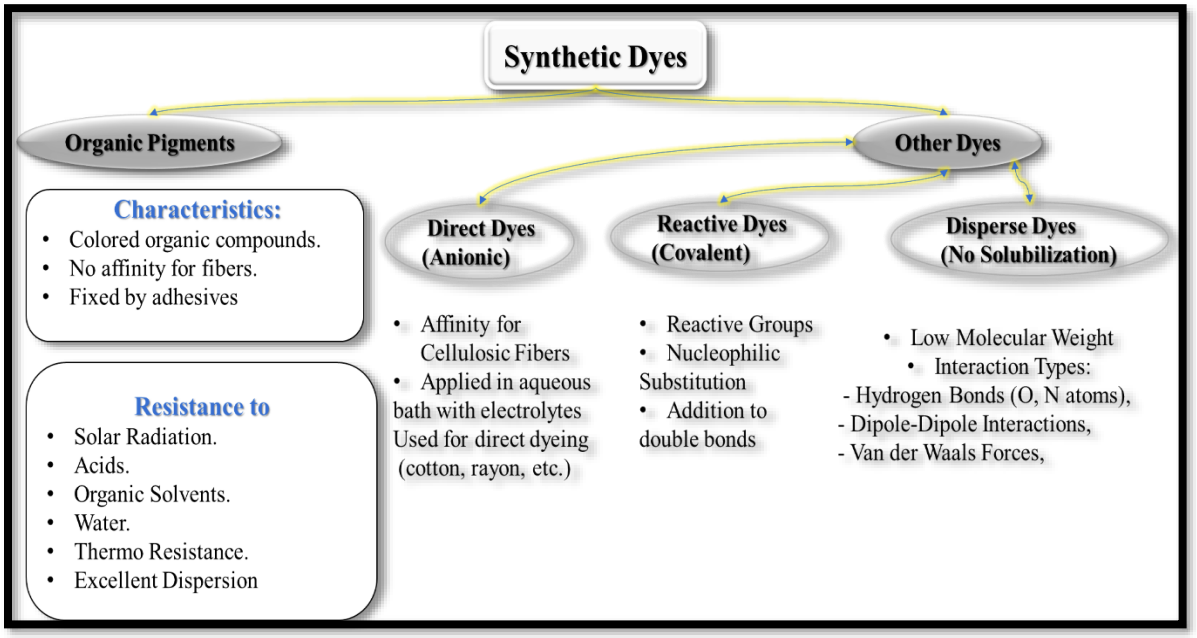
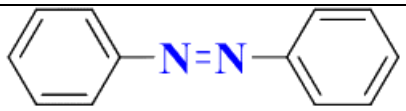
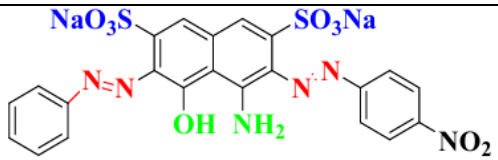
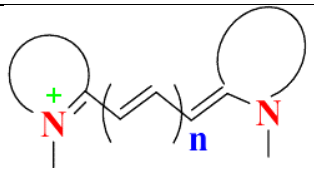
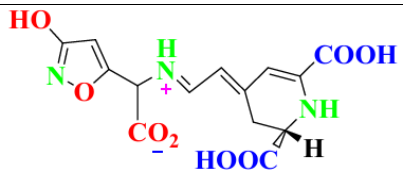
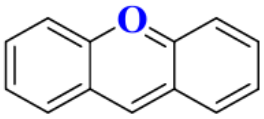
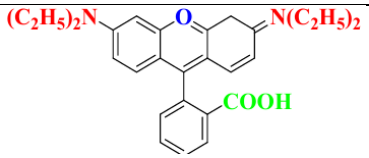
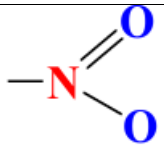
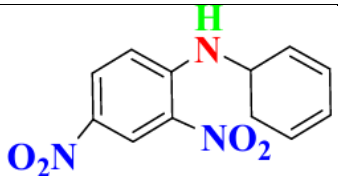
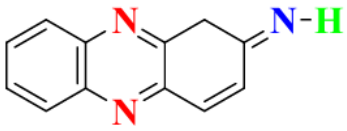
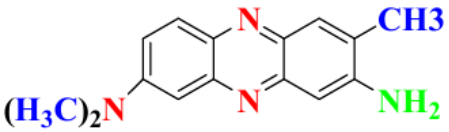
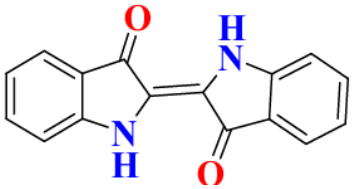
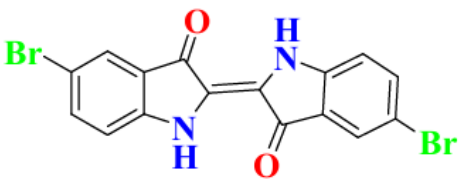
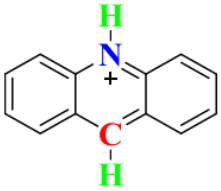
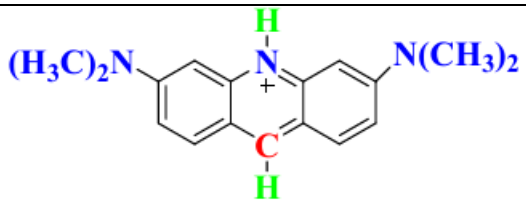


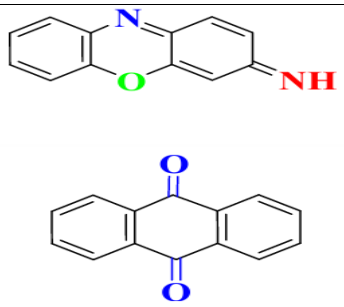
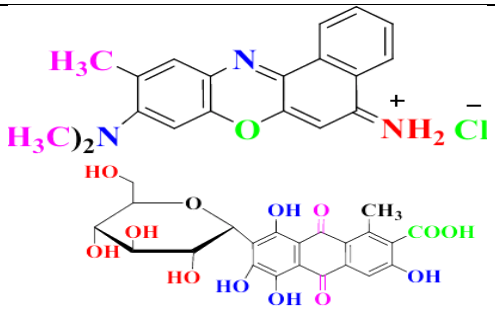
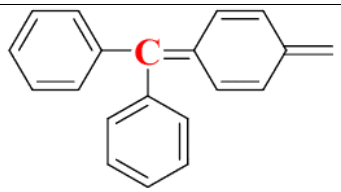
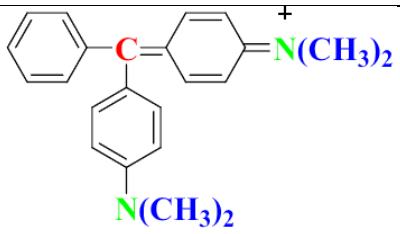
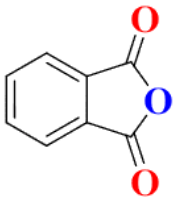
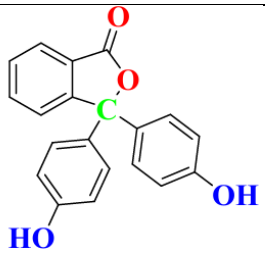
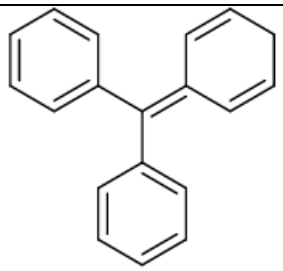
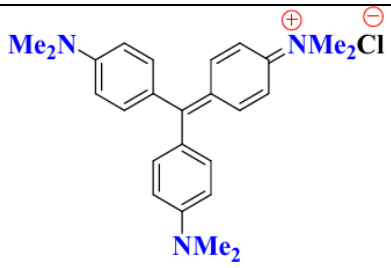
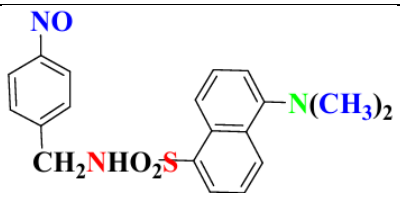
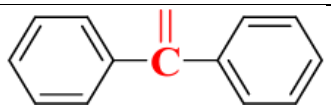
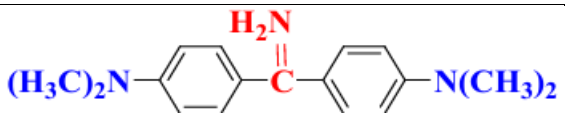
Figure I. 1: *Classification scheme of synthetic dyes based on their chemical composition and functional characteristics.*

2.1.3. Chemical classification of dyes

Textile dyes are commonly classified either by their chemical structure encompassing groups such as azo, nitro, indigo, anthraquinone, phthalein, triphenylmethyl, and nitrated dyes or by their intended industrial applications [1]. **Table I.1** provides an overview of textile dye categories based on the nature of their chromophoric groups, which define the fundamental light absorbing units responsible for coloration [1], [8], [9].

Table I. 1: *overview of textile dye categories based on the nature of their chromophoric groups.*

Class of dye	Chromophore	Example
Azo		
Cyanine		
Xanthene		
Nitro		
Quinione-imine		
Indigoid		
Acridine		

Oxazsine **anthraquinone**		
Triarylmethane		
Phthalein		
Triphenylmethane **dye**		
Nitroso		
Diarylmethane		

3. Ecotoxicological impacts of synthetic dyes

Dyes are composed of aromatic molecular structures derived from hydrocarbons such as benzene, toluene, naphthalene, anthracene, and xylene [10]. Their origin may be natural sourced

from plants, insects, animals, or minerals or synthetic, produced through various chemical processes [11]. Synthetic dyes, in particular, are widely utilized across numerous industrial applications. However, their extensive use and subsequent release into the environment often together with other hazardous organic and inorganic contaminants represent a major ecological concern. Dyes are commonly classified according to their chemical structure, physicochemical behaviour, origin, application, and the toxicity of the effluents in which they occur. Industrial discharges frequently contain toxic and carcinogenic compounds that pose significant risks to both human health and aquatic ecosystems [12]. The environmental consequences of this pollution are illustrated in Figure I.2. [13]

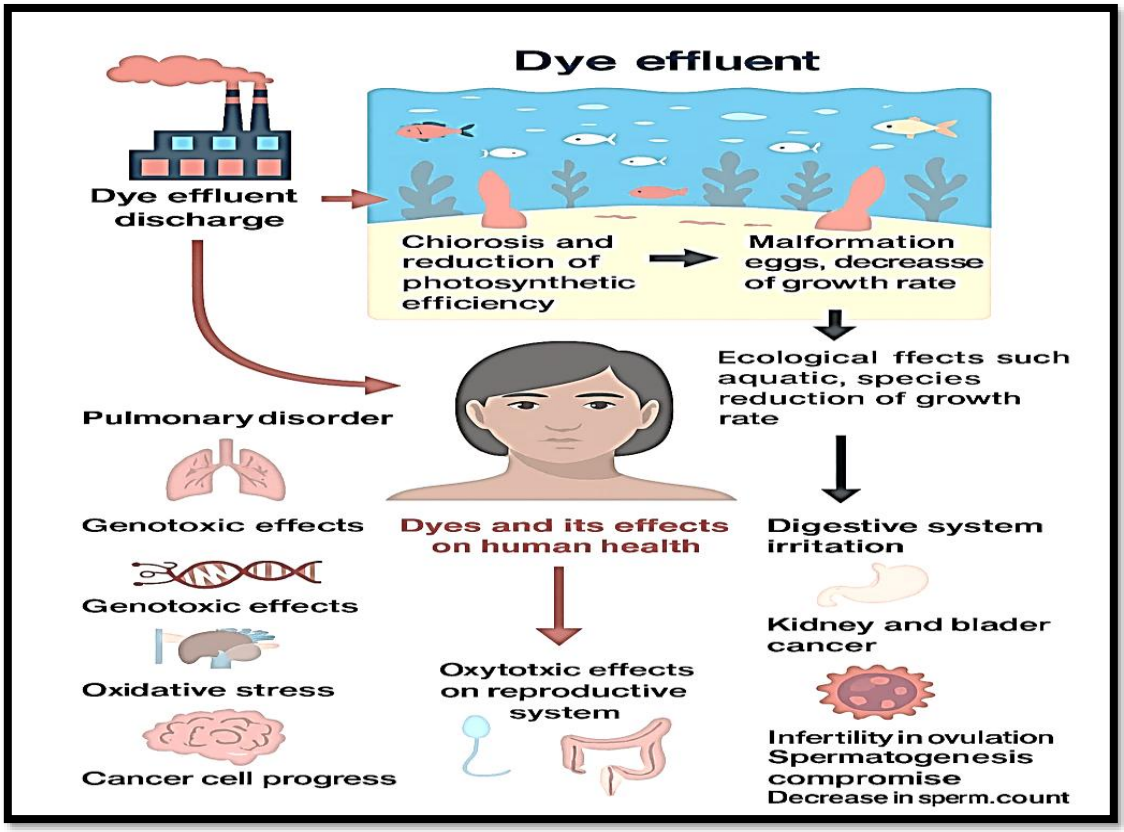


Figure I. 2: *The environmental consequences of dye pollution.*

4. Processes for the remediation of dye-contaminated effluent

A diverse range of technologies is available for treating dye-contaminated effluents. Despite the use of methods such as coagulation flocculation [14], chemical oxidation [15], adsorption [16], electrochemical processes [17], and aerobic or anaerobic biodegradation [18], each technique exhibits inherent operational constraints [19]. These dye removal strategies are broadly classified into three main categories: physical, chemical, and biological treatments, each characterized by specific advantages and drawbacks [20]. Figure I.3 presents a comparative assessment of the key strengths and limitations of these treatment approaches [21].

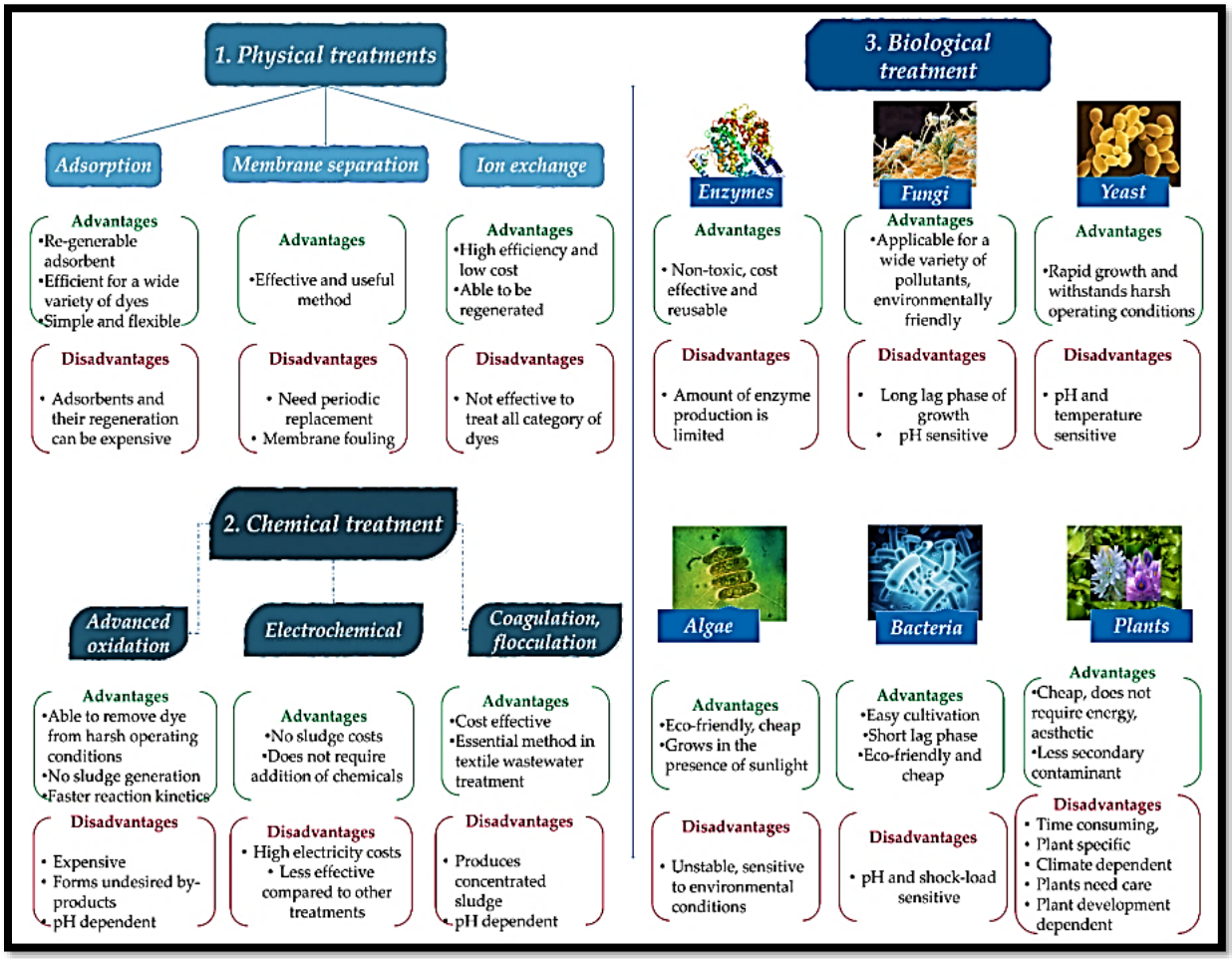


Figure I. 3: *Treatment technologies approaches for treating dye-contaminated effluents.*

5. Adsorption

Sorption is defined as the overall process through which synthetic compounds associate with solid phases [22]. The primary difference between adsorption and absorption is structural: adsorption involves the attachment of molecules onto a two-dimensional surface, whereas absorption involves their penetration and distribution within a three-dimensional matrix [23]. According to the nature and strength of the intermolecular forces involved, adsorption can be broadly categorized as physisorption or chemisorption [24]. A variety of intermolecular interactions can govern adsorption, including electrostatic forces, π–π stacking, hydrogen bonding, surface complexation, and cation-bridging phenomena. The dominant mechanism is determined by the physicochemical nature of the pollutant or dye and the functional groups present on the adsorbent surface. Frequently, adsorption does not proceed through a single mechanism; instead, several mechanisms act concurrently to enhance retention [25].

5.1. Chemisorption

Chemisorption takes place when the adsorbate forms covalent bonds with the surface of the adsorbent through electron sharing or electron transfer processes. Although chemisorption generally occurs less frequently than physisorption, the interaction energies involved are significantly higher [26]. This type of sorption is governed by specific chemical forces operating between the solute molecules and the active sites on the adsorbent surface. Consequently, the enthalpy of adsorption (ΔH_{ads}) associated with chemisorption typically reaches values tens to hundreds of kJ / mol, clearly exceeding those observed in physisorption. Chemisorption is most prominent at ambient temperatures, while its reversal generally requires a substantial increase in temperature due to the strong and specific nature of the formed chemical bonds. [27]

5.2. Physisorption

Physisorption arises from weak intermolecular forces between the adsorbate and adsorbent, including dipole-dipole interactions and van der Waals forces. Because these interactions are weak, the adsorption heat is low, and the process is generally rapid and reversible [28]. Physical adsorption occurs when the attractive forces between solute molecules and the solid surface exceed the intermolecular interactions among solute species in the fluid phase. It is an exothermic process that does not require activation energy, and therefore proceeds quickly. At equilibrium pressure, the amount adsorbed decreases with increasing temperature. Additionally, the medium pH can influence physisorption efficiency. [29]

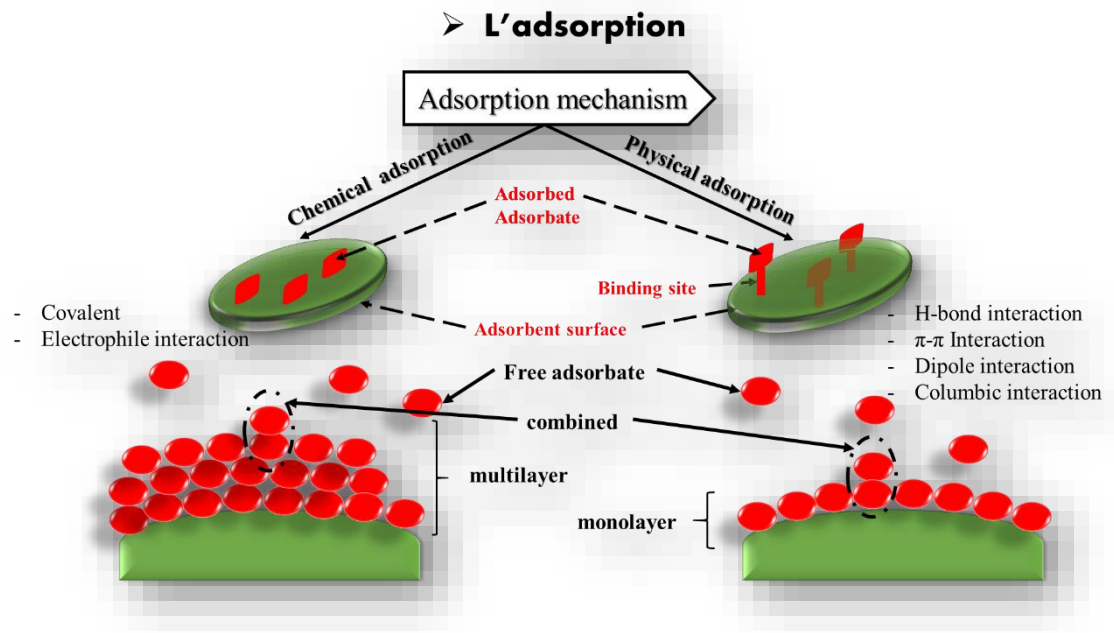


***Figure I. 4**: Graphical representation of adsorption pathways.*

6. Clay minerals

Clays and clay minerals are low-cost, non-toxic, and naturally abundant materials that have been widely employed in water treatment and remediation processes [30]. Clays such as bentonite and kaolin are hydrous aluminosilicate materials composed of various clay minerals, along with crystalline phases of other components including quartz and metal oxides [31]. Clay

minerals such as montmorillonite and kaolinite belong to the broad family of phyllosilicates, which encompasses both planar hydrous and non-planar hydrous structures [32]. Their characteristic two dimensional (2D) layered architecture, combined with distinctive physicochemical properties particularly swelling behavior and ion-exchange capability facilitates the adsorption of a wide range of organic and inorganic contaminants from water [33]. In certain clays, notably bentonite, the interlayer space can expand and accommodate pollutant molecules, a phenomenon referred to as swelling capacity. The adsorption efficiency of clays and clay minerals is governed by several key factors, including surface charge, specific surface area, and swelling characteristics. Moreover, these materials exhibit a cation exchange capacity (CEC), defined as the amount of exchangeable positive ions per unit mass of dry clay mineral.

7. Structure of clay minerals

Clay particles consist of a stack of a variable number of elementary layers. Each layer is defined by the arrangement of a constant sequence of tetrahedral and octahedral sheets. The interlayer region may be empty, but it can also host anhydrous or hydrated cations originating from alkali or alkaline-earth elements. These cations can readily migrate out of the interlayer space and be substituted by others [34].

7.1.Tetrahedral sheet

This layer is composed of a sequence of tetrahedra whose vertices are occupied by oxygen atoms and whose centers contain a silicon atom; in some cases, the central position may also be occupied by a trivalent aluminum atom (Al^{3+}) (shown in the Figure I.5).

7.2.Octahedral sheet

It is composed of a series of octahedra whose vertices are occupied by oxygen atoms and hydroxyl groups, thereby forming a compact hexagonal structure. The central positions may be filled by various atoms with a valence of three (Al, Fe) or two (Fe, Mg) (shown in Figure I.5).

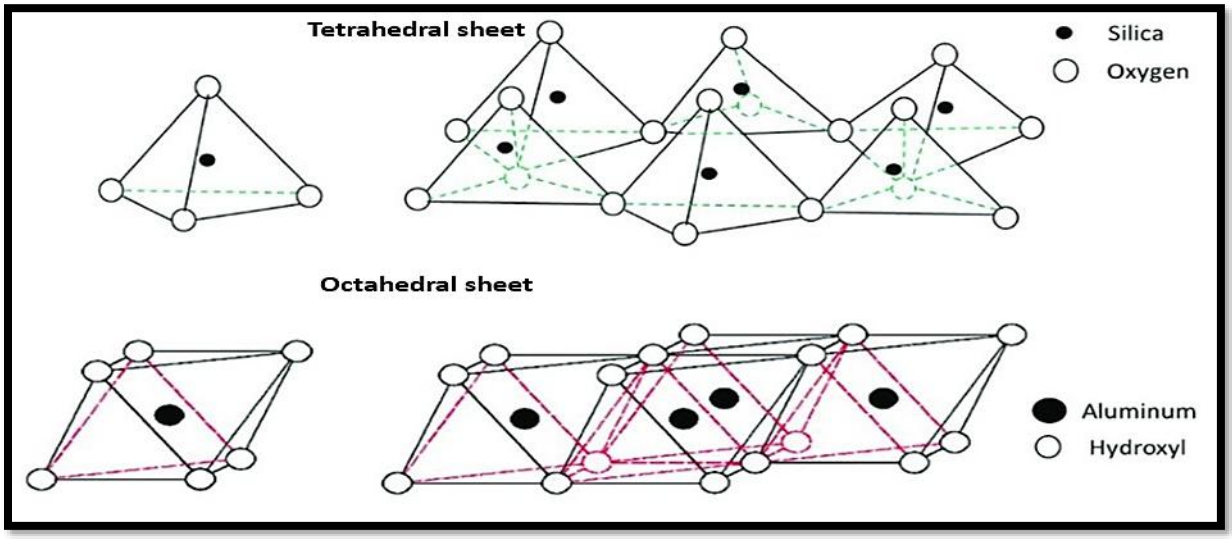


Figure I. 5: *Tetrahedral and octahedral sheets structure.*

8. Classification of clay minerals

Several classifications of clays exist. The most common is based on the thickness of the layer, which allows distinguishing three main families:

8.1.**The kaolinite:**

The layer is composed of one tetrahedral sheet and one octahedral sheet (T/O or 1:1). The representative mineral of this group is kaolinite (shown in Figure I.6) [35]. In the octahedral sheet, two out of three octahedral sites are occupied by Al^{3+} cations, while the tetrahedral sheet is generally free of isomorphic substitution. As a result, the layer is electrically neutral, and its cation-exchange capacity (CEC) is very low, ranging from 0.03 to 0.15 meq/g. [36]

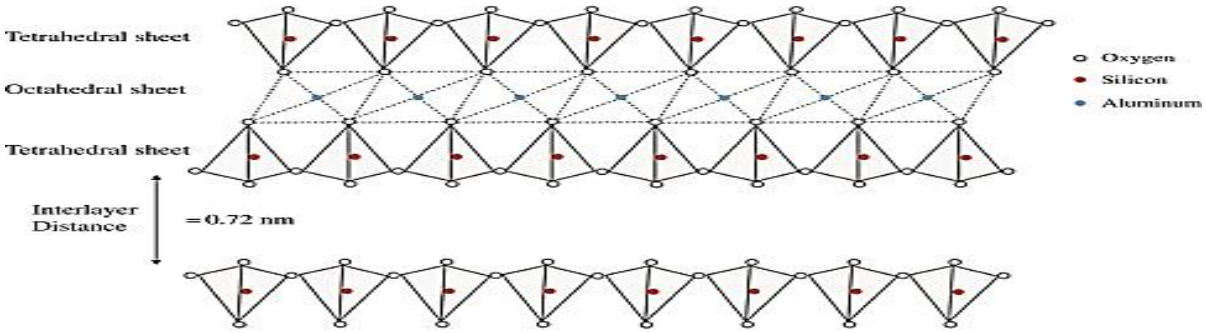


Figure I. 6: *Kaolinite structure [35].*

8.1.1. Halloysite:

Halloysite (HAL) is a clay mineral closely related to kaolinite in both physical and chemical properties [37]. It is distinguished by a hollow nanotubular morphology formed from rolled kaolinite layers. The nanotubes typically exhibit an outer diameter of 50–200 nm, an inner diameter of 5–30 nm, and lengths ranging from 0.5 to 25 µm. Structurally, HAL consists of multiple concentric layers of aluminosilicate sheets [38].

HAL occurs mainly in two forms: a hydrated form, with a basal spacing of approximately 1.0 nm and the formula $Al_2Si_2O_5(OH)_4 \cdot nH_2O$, and a dehydrated form, with a basal spacing near 0.7 nm and the formula $Al_2Si_2O_5(OH)_4$, which is identical to kaolinite [39]. The outer surface of HAL nanotubes is predominantly composed of negatively charged SiO_2, while the inner surface is rich in positively charged Al_2O (**Figure I.7**) [40]. In addition, HAL nanotubes are characterized by high specific surface area, thermal stability, low cost, and significant adsorption capacity for micropollutants, especially dyes. These properties make HAL nanotubes highly effective as supports for the adsorption of various micropollutants [41].

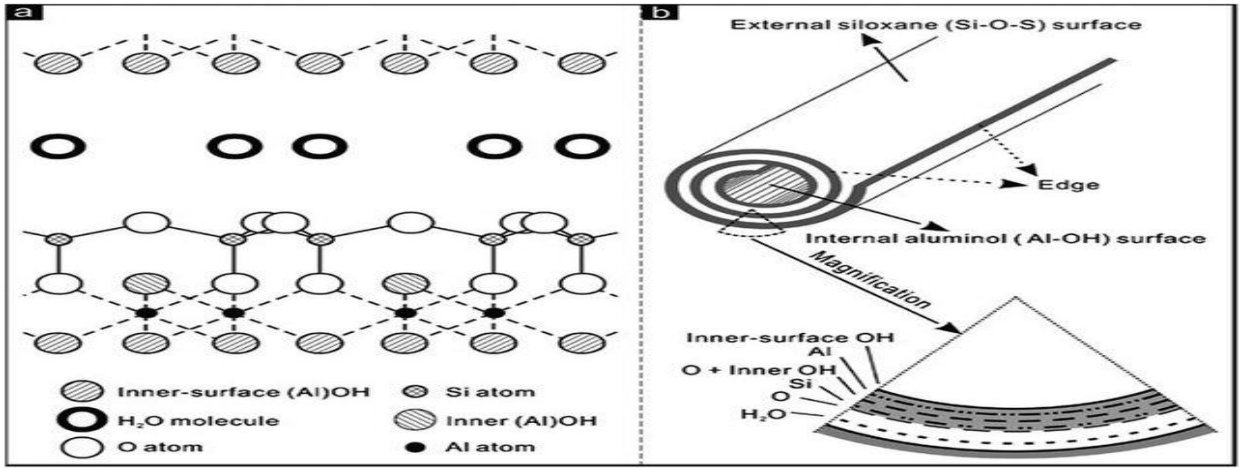


Figure I. 7: *Halloysite structure [40].*

8.2.Smectite:

The layer is composed of two tetrahedral sheets and one octahedral sheet (T–O–T or 2:1) (Figure I.7). The spacing between two adjacent layers can range from 10 to 17.5 Å. This series includes the smectite and mica families. Two types of these materials can be distinguished: dioctahedral and trioctahedral varieties [41].

8.2.1. Montmorillonite

The elementary layer of montmorillonite consists of an octahedral sheet in between two tetrahedral sheets (T–O–T). The Si^{4+} ions occupy the centers of tetrahedra whose vertices are formed by oxygen atoms. The Al^{3+} ions are located at the centers of octahedra whose vertices are composed of oxygen atoms and two hydroxyl ions. The elementary layers are of the 2:1 type and are separated by water molecules and exchangeable cations. [42]

The general formula for the half-unit cell is: $\mathbf{Si_4O_{10}(Al_{(2-x)}R_x)(OH)_2.CE_x.nH_2O}$ where **CE** denotes the exchangeable cations and **R** represents magnesium. numerous chemical variants exist in which **R** is substituted by different divalent cations. [35]

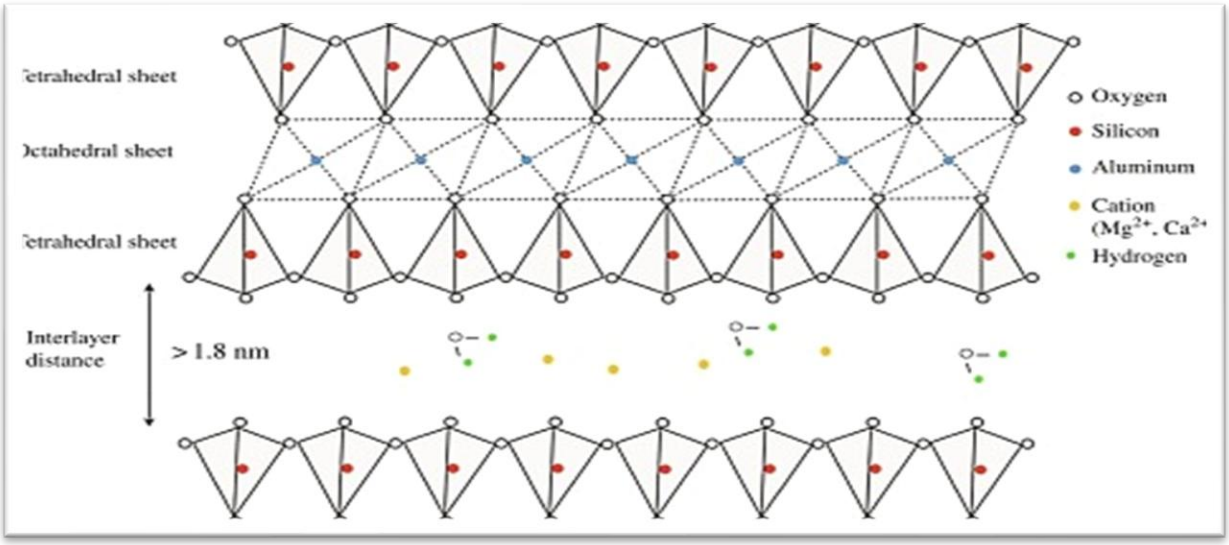


Figure I. 8: *Montmorillonite structure [35].*

8.3.Chlorite

In addition to the structural composition of the 2:1-layer series, this group contains an extra brucite-type octahedral sheet inserted into the interlayer space. This results in the presence of a fourth octahedral sheet, typically composed of aluminum, magnesium, or iron. The spacing between two consecutive layers is 14 Å. [43]

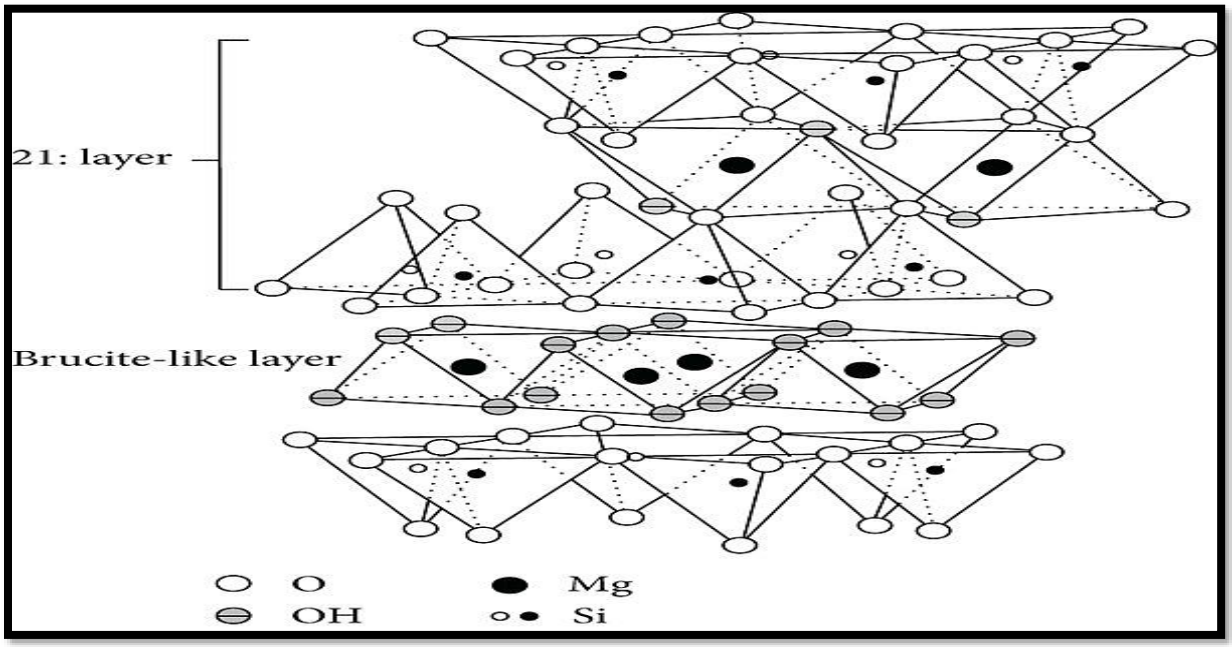


Figure I. 9: *Chlorite structure [43].*

9. Characteristics properties of clays

9.1.The cationic exchange capacity

The cation-exchange capacity (CEC) is defined as the quantity of monovalent cations required to replace the compensating cations to neutralize the electric charge of 100 g of dry clay (Table I.2). It depends on the radius of the hydrated cations, their charge, and their atomic mass. The CEC is generally expressed in milliequivalents per 100 grams (m_{eq}/100 g) [32].

Table I. 2: *CEC of some clay minerals.*

Clay	Cation exchange capacity (m_{eq}/100 g)
Kaolinite	3-15
Chlorites	30-60
Smectites	80-120

In clays, two principal factors give rise to ion-exchange capacity: one is internal, and the other is external.

9.1.1. The presence of isomorphic substitutions (internal CEC)

The most common substitution is that of Al^{3+} by Mg^{2+} within the octahedral sheet, which constitutes the principal exchange mechanism in montmorillonite. In this clay, the distance between the negative sites located in the octahedral sheet and the exchangeable cation positioned at the layer surface is such that the attractive forces remain weak. Substitutions of Si by Al within the tetrahedral sheet can also occur. [44]

9.1.2. Edge-related phenomena (external CEC)

At the edges of a layer, the valences of silicon and oxygen in the tetrahedral sheet, and those of aluminum and oxygen in the octahedral sheet, are not fully saturated. To compensate for these unsatisfied valences, water molecules undergo hydrolysis, leading to the formation of silanol

(Si–OH) or aluminol (Al–OH) groups [32]. Depending on the pH, these groups may capture or release protons. These protons can then be exchanged with other cations. Consequently, both the magnitude and the nature of the edge charges are directly governed by the pH [33].

9.2.Specific surface area

The properties of clays are primarily governed by their surface characteristics. The total surface area includes the external surface, located between clay particles, and the internal surface, corresponding to the interlayer space [45].

9.3.The swelling propriety

Swelling involves the separation of layers up to an equilibrium interlayer distance under a given pressure [46]. The swelling properties of montmorillonites arise from the hydrophilic nature of their surfaces, due to the presence of hydratable cations within the interlayer galleries. However, this condition alone is not sufficient, as the swelling behavior is also governed by the type and quantity of inorganic cations present in the galleries. Not all phyllosilicates exhibit this swelling capability [47]. Generally, the smaller and less charged the compensating cations, the greater the clay's swelling potential. These easily hydratable ions, through their interaction with water molecules, reduce the attractive forces between layers. The swelling decreases in the following order according to the type of compensating cation: $Li^+ > Na^+ > Ca^{2+} > Fe^{2+} > K^+$ [48].

10. Organophilic clays

Natural clay minerals are generally hydrophilic and organophobic, meaning they have an affinity for water but repel organic substances. The purpose of organophilic modification is to reverse this behavior, rendering the clay hydrophobic and organophilic, thereby increasing its affinity for organic compounds [49].

This transformation is achieved through cation exchange Figure I.10: the compensating inorganic cations, typically alkali ions such as Na^+, Li^+, or K^+, present in the clay's interlayer

space, are replaced by organic cations bearing alkyl chains, known as surfactants. The most commonly used surfactants are alkylammonium ions [50].

During this exchange, the polar head of the surfactant replaces the inorganic cation, while the hydrophobic carbon chain of the surfactant inserts into the interlayer space. This carbonaceous structure imparts an increased affinity of the clay for organic molecules, rendering it organophilic. Moreover, these organic cations, being much larger than the original alkali cations, increase the spacing between clay layers, expanding the interlayer region and reducing the electrostatic attraction between the layers [51].

This treatment renders the clay organophilic, thereby enhancing its affinity for the adsorption of organic molecules. It also leads to an increase in the interlayer spacing, that is, the distance between the elementary layers. However, this spacing depends on the conformation adopted by the alkyl chain of the surfactant, which may be horizontal, vertical, or inclined. [50]

Two main parameters influence this organization: [52]

- The cation-exchange capacity (CEC) of the montmorillonite, which is approximately 120 meq/100 g and determines the density of cations on the surfaces of the layers.
- The length of the alkyl chain in the surfactant in this case Cetyl-Trimethyl-Ammonium Bromide (CTAB, or C16) with chemical formula $C_{19}H_{42}BrN$ which directly affects the interlayer spacing.

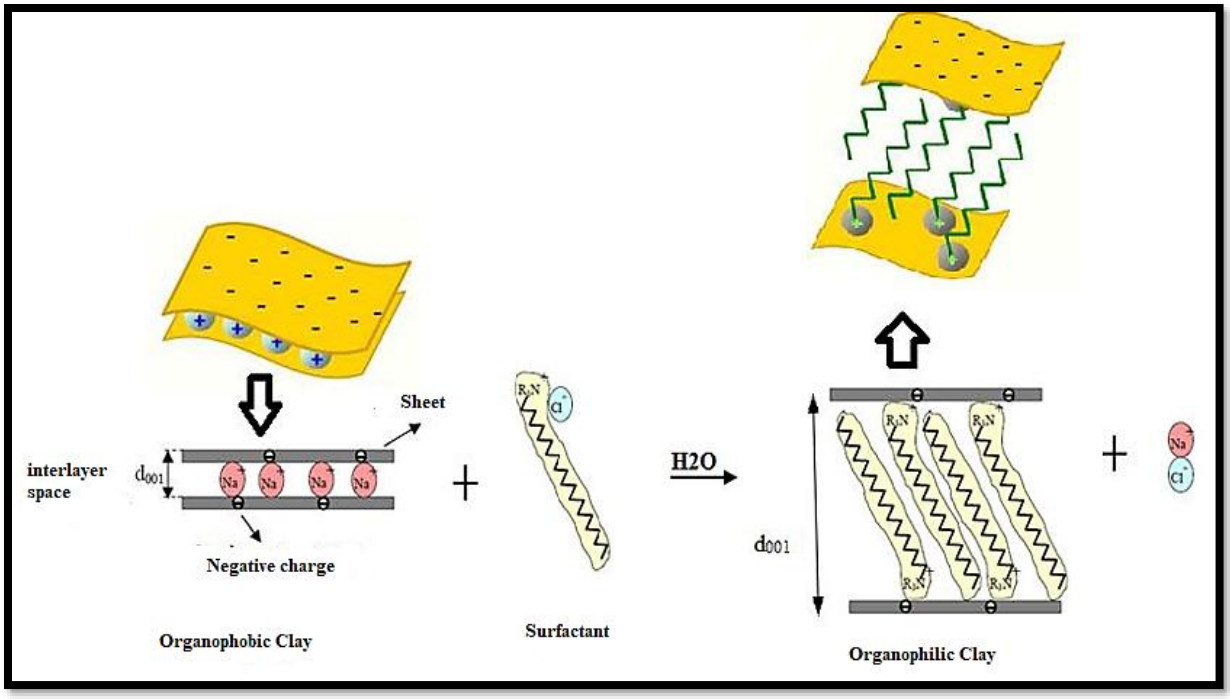


Figure I. 10: *Organophilic clay treatment [52].*

11. Double layered hydroxides

The interest in Layered Double Hydroxides lies in their two-dimensional structure and their anion-exchange capability, which provide access to a wide verity of intercalation compounds. This versatility can be achieved either through modification of the chemical composition of the hydroxide layers or via chemical and/or structural alteration of the interlayer domain [53].

These compounds, referred to as LDHs (Layered Double Hydroxides), are structurally related to natural hydrotalcite, $Mg_6Al_2\ (OH)_{16}(CO_3)\cdot 4H_2O$, in which a fraction of divalent magnesium cations is substituted by trivalent aluminum cations. Their general chemical formula can be expressed as $[\ M^{2+}{}_{1-x}\ M_x{}^{3+}(OH)_2]\ [\ A^{m-}{}_{x/m}\ .nH_2O]$ where M^{2+} and M^{3+} denote divalent and trivalent metal cations, respectively, and A^{m-} represents the interlayer anions [54].

Structurally, LDHs consist of stacked brucite-like layers, $(M^{2+}, M^{3+})\ (OH)_2$ built from edge-sharing $(M^{2+}, M^{3+})\ (OH)_6$ octahedra. The partial substitution of divalent M^{2+} cations by trivalent M^{3+} cations generates an excess positive charge within the layers, which is compensated by the

intercalation of anionic species in the interlayer galleries, accompanied by water molecules [55].

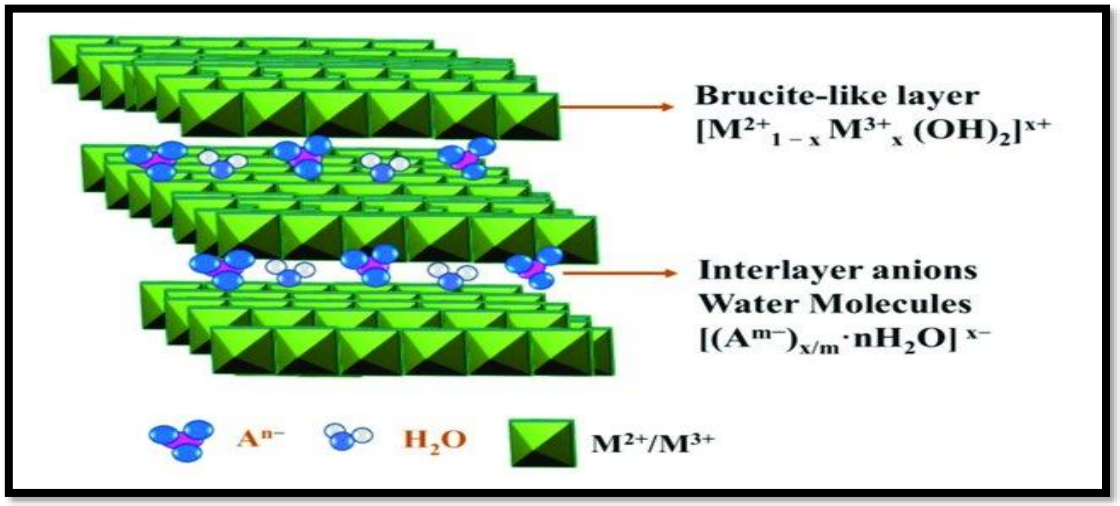


Figure I. 11: *Schematic illustration of LDH structure and chemical component [55].*

12. Alginate

Alginate is a naturally abundant polysaccharide derived mainly from brown algae (e.g., Laminaria hyperborea, Macrocystis pyrifera, Ascophyllum nodosum) and, to a lesser extent, from bacteria such as Azotobacter and Pseudomonas [56]. Commercial production typically relies on algal extraction due to the high cost of microbial synthesis. Structurally, alginate consists of β-D-mannuronic (M) and α-L-guluronic (G) acids linked by 1→4 bonds, forming M-, G-, and MG-blocks (**Figure I.12**) [57]. M-rich polymers yield elastic gels, while G-rich chains form stiffer, brittle structures. Sodium alginate (SAg) exhibits strong gelation capacity in the presence of divalent ions, especially Ca^{2+} (Figure I.12) [58]. Upon Ca^{2+} addition, Na^{+} is replaced, producing calcium alginate (CaAg) through ionic crosslinking. The polymer's carbonyl, hydroxyl, and carboxyl groups enable cation binding via ion exchange, enhancing its adsorption performance. Owing to its biocompatibility, non-toxicity, and crosslinking ability, alginate is widely used for encapsulation and is an excellent material for preparing porous beads for wastewater treatment applications [59].

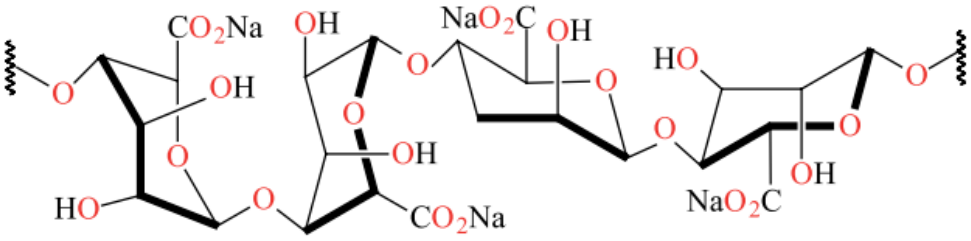


Figure I. 12: *Chemical structure of alginate.*

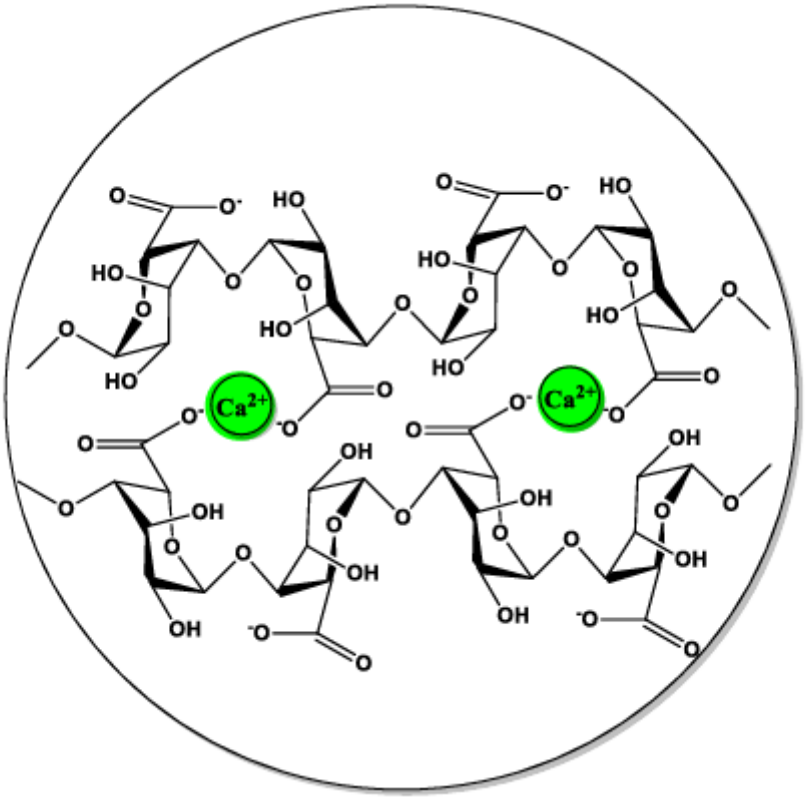


Figure I. 13: *Mechanism of interaction between alginate and Ca2⁺.*

13. Polyaniline

polyaniline (PANI) is regarded as one of the most effective conductive polymers, largely due to the presence of –NH– groups within its structure [60]. It is widely employed in applications such as batteries, electronic components, solar cells, sensors, electromagnetic shielding materials, and anticorrosion coatings. This polymer has attracted extensive research interest because of its straightforward synthesis, ease of doping, favorable physicochemical properties, mechanical flexibility, environmental stability, and the availability of its monomer [61].

Moreover, polyaniline has been extensively explored in the design of adsorbent materials through chemical modification and composite formation [61]. Its suitability as an adsorbent in wastewater treatment arises from the active amine and imine functional groups, which enable interactions with a wide range of contaminants present in polluted water as well as The charge transfer induced by doping enables PANI to interact with ionic species through electrostatic interactions [60].

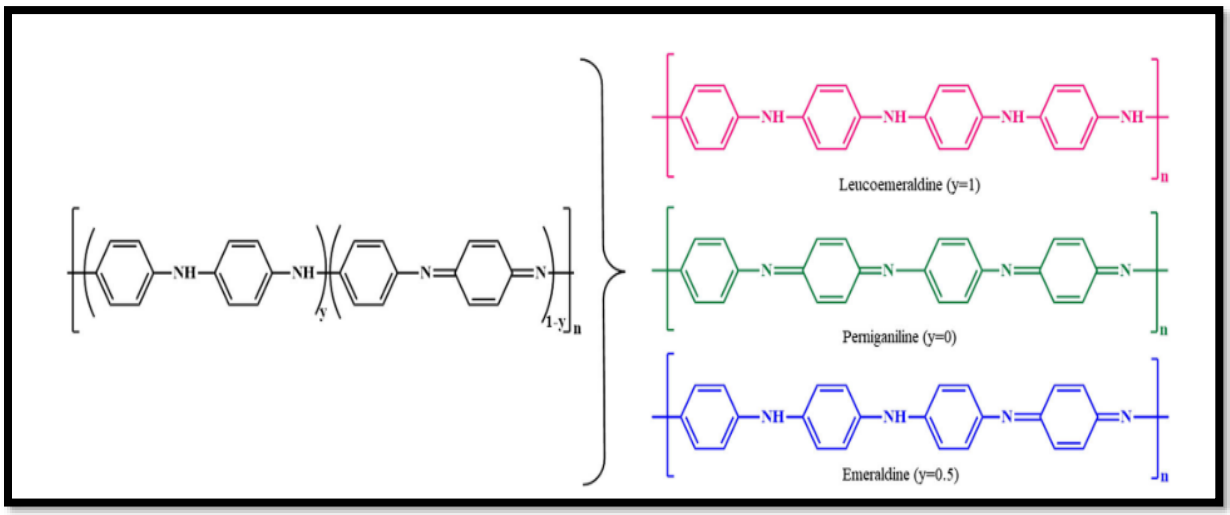


Figure I. 14: *Chemical structures of different forms of polyaniline.*

PANI consists of monomeric units composed of reduced (y) and oxidized (1–y) segments. Its structure is represented by the formula shown in **Figure I.14** [62], which results directly from the oxidation of aniline monomers under specific conditions. PANI can be synthesized either chemically or electrochemically [63]. In chemical synthesis, the most common approach is oxidative chemical polymerization. This process can be carried out in aqueous or organic media using inorganic oxidants. Various oxidizing agents such as ammonium persulfate $(NH_4)_2S_2O_8$, hydrogen peroxide (H_2O_2), or ferric chloride ($FeCl_3$), are typically employed.

PANI also exhibits three distinct oxidation states, each associated with a characteristic color. Each oxidation level *y* corresponds to a specific form of polyaniline, possessing its own physical

and chemical properties. These forms are known as leucoemeraldine (y = 1; fully reduced state), emeraldine (y = 0.5; partially oxidized state), and pernigraniline (y = 0; fully oxidized state).

Emeraldine is the most stable form of PANI, containing an equal number of oxidized and reduced units, Pernigraniline and emeraldine can exist either in their salt form or in their base form, the various forms of polyaniline are illustrated in **Figure I.13**.

Reference of chapter I:

[1] E. O. Alegbe et T. O. Uthman, « A review of history, properties, classification, applications and challenges of natural and synthetic dyes », *Heliyon*, vol. 10, nº 13, 2024.

[2] M. L. Firmansyah, M. Ashraf, et N. Ullah, « A critical review on the removal of anionic dyes by cross-linked resin: Recent progress, challenges and future perspective », *Sep. Purif. Technol.*, vol. 360, p. 131111, 2025.

[3] M. Liaqat, R. R. M. Khan, T. Iqbal, et X.-Z. Fu, « Introduction to Dyes », 2025.

[4] E. El-Sayed, E. Abd El-Aziz, H. Othman, et A. G. Hassabo, « Azo dyes: Synthesis, classification and utilisation in textile industry », *Egypt. J. Chem.*, vol. 67, nº 13, p. 87-97, 2024.

[5] M. T. Yagub, T. K. Sen, S. Afroze, et H. M. Ang, « Dye and its removal from aqueous solution by adsorption: a review », *Adv. Colloid Interface Sci.*, vol. 209, p. 172-184, 2014.

[6] M. Shahid et F. Mohammad, « Recent advancements in natural dye applications: a review », *J. Clean. Prod.*, vol. 53, p. 310-331, 2013.

[7] J. M. Jabar, « Classification of natural dyes for sustainable exploitation », in *Natural Dyes and Sustainability*, Springer, 2024, p. 153-191.

[8] S. El Harfi et A. El Harfi, « Classifications, properties and applications of textile dyes: A review », *Appl. J. Environ. Eng. Sci.*, vol. 3, nº 3, p. 00000J-Envir, 2017.

[9] K. F. Kayani, S. J. Mohammed, M. S. Mustafa, et S. B. Aziz, « Dyes and their toxicity: removal from wastewater using carbon dots/metal oxides as hybrid materials: a review », *Mater. Adv.*, vol. 6, nº 16, p. 5391-5409, 2025, doi: 10.1039/D5MA00572H.

[10] K. F. Kayani, D. Sh. Hamad, N. N. Mohammad, S. J. Mohammed, H. R. Ahmed, et M. A. Salih, « Uses, toxicity, and removal of fuchsin dye from wastewater using low-cost adsorbents », *Desalination Water Treat.*, vol. 323, p. 101395, juill. 2025, doi: 10.1016/j.dwt.2025.101395.

[11] A. Negi, « Environmental impact of textile materials: challenges in fiber–dye chemistry and implication of microbial biodegradation », *Polymers*, vol. 17, n° 7, p. 871, 2025.

[12] M. Kumar, V. P. Singh, S. B. Bhat, et R. Kumar, « Environmental risks of textile dyes and photocatalytic materials for sustainable treatment: current status and future directions », *Discov. Environ.*, vol. 3, n° 1, p. 1-36, 2025.

[13] U. Kumari, « Textile dyes and their impact on the natural environment », in *Dye Pollution from Textile Industry: Challenges and Opportunities for Sustainable Development*, Springer, 2024, p. 17-30.

[14] W. Y. A. Abdiy et A. J. A. Shammary, « Removal of Turbidity and Congo Red Dye from Aqueous Solution by Coagulation-Flocculation Process », *Tikrit J. Eng. Sci.*, vol. 32, n° 2, p. 1-9, 2025.

[15] S. Ziembowicz et M. Kida, « The Optimization of Advanced Oxidation Processes for the Degradation of Industrial Pollutants », *Sustainability*, vol. 17, n° 5, p. 1908, 2025.

[16] O. R. Benkouachi *et al.*, « Advanced green peel utilization for efficient methylene blue removal: Integrated analysis and predictive modeling », *J. Mol. Liq.*, p. 125951, 2024.

[17] M. U. Farooq *et al.*, « Performance of indirect electrochemical processes using transition metal oxide electrodes for the abatement of food dye in aqueous solution », *Water Pract. Technol.*, vol. 20, n° 4, p. 786-799, 2025.

[18] J. Sun, M. Yuan, H. Zhou, Z. Chen, Y. Wang, et H. Cheng, « Enhanced printing and dyeing wastewater treatment using anaerobic-aerobic systems with bioaugmentation », *J. Hazard. Mater.*, vol. 486, p. 136982, 2025.

[19] K. Abhisek, S. S. Vhatkar, H. T. Mathew, P. Singh, et R. Oraon, « A critical review on the challenges and techno-economic assessment of dyes removal technologies from waste water », *Discov. Chem.*, vol. 2, n° 1, p. 41, mars 2025, doi: 10.1007/s44371-025-00111-4.

[20] S. Dutta, B. Gupta, S. K. Srivastava, et A. K. Gupta, « Recent advances on the removal of dyes from wastewater using various adsorbents: A critical review », *Mater. Adv.*, vol. 2, n° 14, p. 4497-4531, 2021.

[21] M. Rahman et Z. Tabassum, « Biotechnological approach to treat textile dyeing effluents: a critical review analysing the practical applications », *Text Leather Rev*, vol. 7, p. 124-152, 2024.

[22] R. Agarwala et L. Mulky, « Adsorption of Dyes from Wastewater: A Comprehensive Review », *ChemBioEng Rev.*, vol. 10, n° 3, p. 326-335, 2023, doi: 10.1002/cben.202200011.

[23] S. E. Pour, A. H. Mamaghani, et Z. Hashisho, « Modeling of adsorption process on monolith adsorbents: A mini-review », *Sep. Purif. Technol.*, vol. 354, p. 128846, 2025.

[24] A. Guediri *et al.*, « The Enhanced Adsorption Capacity of Ziziphus jujuba Stones Modified with Ortho-Phosphoric Acid for Organic Dye Removal: A Gaussian Process Regression Approach », *Water*, vol. 16, n° 9, Art. n° 9, janv. 2024, doi: 10.3390/w16091208.

[25] R. Yousef, H. Qiblawey, et M. H. El-Naas, « Adsorption as a process for produced water treatment: A review », *Processes*, vol. 8, n° 12, p. 1657, 2020.

[26] S. Mohamed Nasser, M. Abbas, et M. Trari, « Understanding the rate-limiting step adsorption kinetics onto biomaterials for mechanism adsorption control », *Prog. React. Kinet. Mech.*, vol. 49, p. 14686783241226858, 2024.

[27] S. Karimi, M. T. Yaraki, et R. R. Karri, « A comprehensive review of the adsorption mechanisms and factors influencing the adsorption process from the perspective of bioethanol dehydration », *Renew. Sustain. Energy Rev.*, vol. 107, p. 535-553, 2019.

[28] A. H. Berger et A. S. Bhown, « Comparing physisorption and chemisorption solid sorbents for use separating CO2 from flue gas using temperature swing adsorption », *Energy Procedia*, vol. 4, p. 562-567, 2011.

[29] M. A. Alsharif, « Understanding Adsorption: Theories, Techniques, and Applications », in *Adsorption-Fundamental Mechanisms and Applications*, IntechOpen, 2025.

[30] S. Gu, X. Kang, L. Wang, E. Lichtfouse, et C. Wang, « Clay mineral adsorbents for heavy metal removal from wastewater: a review », *Environ. Chem. Lett.*, vol. 17, n° 2, p. 629-654, 2019.

[31] A. A. Adeyemo, I. O. Adeoye, et O. S. Bello, « Adsorption of dyes using different types of clay: a review », *Appl. Water Sci.*, vol. 7, n° 2, p. 543-568, 2017.

[32] A. Alshameri *et al.*, *A review of the role of natural clay minerals as effective adsorbents and an alternative source of minerals*. IntechOpen, 2019.

[33] R. M. Tuzingila, L. Kong, et R. Koy Kasongo, « A review on experimental techniques and their applications in the effects of mineral content on geomechanical properties of reservoir shale rock », *Rock Mech. Bull.*, vol. 3, p. 100110, 2024.

[34] R. Huang *et al.*, « Review on the effect of isomorphic replacement on the structure and application performance of typical clay minerals », *Prog. Nat. Sci. Mater. Int.*, vol. 34, n° 2, p. 251-262, 2024.

[35] A. Hamza, I. A. Hussein, et M. Mahmoud, « Introduction to reservoir fluids and rock properties », in *Developments in petroleum science*, vol. 78, Elsevier, 2023, p. 1-19.

[36] H. Cheng, Y. Zhou, P. Xu, M. Zhang, et L. Sun, « Kaolinite-based form-stable phase change materials for thermal energy storage », *J. Energy Storage*, vol. 87, p. 111349, 2024.

[37] L. Fu, D. Fan, J. Zhang, P. Ouyang, J. Fan, et H. Yang, « Microstructure and properties of halloysite nanotubes and modification methods: a comprehensive review », *Appl. Clay Sci.*, vol. 253, p. 107348, 2024.

[38] M. Fahimizadeh *et al.*, « Halloysite clay nanotubes: Innovative applications by smart systems », *Appl. Clay Sci.*, vol. 251, p. 107319, 2024.

[39] O. Mazloumi, F. Z. Biabanpour, et S. Nojavan, « Halloysite-Based Sorbents: Synthesis, Characterization, and Applications in Sample Preparation », *TrAC Trends Anal. Chem.*, p. 118241, 2025.

[40] B. H. Bac et N. T. Dung, « Finding nanotubular halloysite at Lang Dong kaolin deposit, Phu Tho province », *Vietnam J. Earth Sci.*, vol. 37, nº 4, p. 299-306, 2015.

[41] H. S. Aljibori, A. Al-Amiery, et W. N. R. W. Isahak, « Unveiling the Potential of Halloysite Nanotubes: Insights into Their Synthesis, Properties, and Applications in Nanocomposites », *Starch-Stärke*, vol. 77, nº 3, p. 2400080, 2025.

[42] W. Wang *et al.*, « Functionality developments in montmorillonite nanosheet: Properties, preparation, and applications », *Chem. Eng. J.*, vol. 499, p. 156186, 2024.

[43] M. Yang, M. Ye, H. Han, G. Ren, L. Han, et Z. Zhang, « Near-Infrared Spectroscopic Study of Chlorite Minerals », *J. Spectrosc.*, vol. 2018, nº 1, p. 6958260, 2018.

[44] A. Kausar *et al.*, « Preparation and characterization of chitosan/clay composite for direct Rose FRN dye removal from aqueous media: comparison of linear and non-linear regression methods », *J. Mater. Res. Technol.*, vol. 8, nº 1, p. 1161-1174, 2019.

[45] B. Gyawali, R. Haghnazar, P. Akula, K. Alba, et V. Nasir, « A review on 3D printing with clay and sawdust/natural fibers: Printability, rheology, properties, and applications », *Results Eng.*, vol. 24, p. 103024, 2024.

[46] F. T. Madsen et M. Müller-Vonmoos, « The swelling behaviour of clays », *Appl. Clay Sci.*, vol. 4, nº 2, p. 143-156, 1989.

[47] M. D. Foster, « The relation between composition and swelling in clays », présenté à Clays and Clay Minerals (National Conference on Clays and Clay Minerals), Cambridge University Press & Assessment, 1954, p. 205-220.

[48] E. J. Hensen et B. Smit, « Why clays swell », *J. Phys. Chem. B*, vol. 106, n° 49, p. 12664-12667, 2002.

[49] F. Qadir et I. Hafeez, « Effect of impregnated organophilic (hydrophobic) nano clay on asphalt binder properties and performance », *Constr. Build. Mater.*, vol. 419, p. 135577, 2024.

[50] N. A. Burger, B. Loppinet, A. Clarke, et G. Petekidis, « Tuning the mechanical properties of organophilic clay dispersions: Particle composition and preshear history effects », *J. Rheol.*, vol. 68, n° 5, p. 695-707, 2024.

[51] L. Perelomov *et al.*, « Organoclays based on bentonite and various types of surfactants as heavy metal remediants », *Sustainability*, vol. 16, n° 11, p. 4804, 2024.

[52] A. Mokhtar *et al.*, « Polymer/Clay Nanocomposites as Advanced Adsorbents for Textile Wastewater Treatment », *Minerals*, vol. 14, n° 12, p. 1216, 2024.

[53] X. Zhao, Y. Zheng, Q. Zhu, M. Cheng, Y. Zhang, et Z. Zhou, « Removal of chloride ions from aqueous phase as layered double hydroxides via uptake strategies: A critical review », *Desalination*, vol. 595, p. 118317, févr. 2025, doi: 10.1016/j.desal.2024.118317.

[54] A. K Satheesan *et al.*, « Current progress in layered double hydroxide-based electrocatalysts for urea oxidation: insights into strategies and mechanisms », mars 2025, doi: 10.1039/D4CC05405A.

[55] X. Zhang *et al.*, « Active Corrosion Protection of Mg–Al Layered Double Hydroxide for Magnesium Alloys: A Short Review », *Coatings*, vol. 11, n° 11, oct. 2021, doi: 10.3390/coatings11111316.

[56] N. Qosim, Y. Dai, G. R. Williams, et M. Edirisinghe, « Structure, properties, forming, and applications of alginate fibers: A review », *Int. Mater. Rev.*, vol. 69, n° 5-6, p. 309-333, 2024.

[57] H. Wang, L. Yang, et Y. Yang, « A review of sodium alginate-based hydrogels: Structure, mechanisms, applications, and perspectives », *Int. J. Biol. Macromol.*, vol. 292, p. 139151, 2025.

[58] B. Kumar, N. Singh, et P. Kumar, « A review on sources, modification techniques, properties and potential applications of alginate-based modified polymers », *Eur. Polym. J.*, vol. 213, p. 113078, 2024.

[59] J. Lai, A. K. Azad, W. M. A. W. Sulaiman, V. Kumarasamy, V. Subramaniyan, et S. A. Alshehade, « Alginate-based encapsulation fabrication technique for drug delivery: an updated review of particle type, formulation technique, pharmaceutical ingredient, and targeted delivery system », *Pharmaceutics*, vol. 16, n° 3, p. 370, 2024.

[60] P. K. Mishra, H. K. Sharma, R. Gupta, M. Manglik, et R. Brajpuriya, « A critical review on recent progress on nanostructured polyaniline (PANI) based sensors for various toxic gases: Challenges, applications, and future prospects », *Microchem. J.*, vol. 208, p. 112369, 2025.

[61] N. Sharma, A. Singh, N. Kumar, A. Tiwari, M. Lal, et S. Arya, « A review on polyaniline and its composites: from synthesis to properties and progressive applications », *J. Mater. Sci.*, vol. 59, n° 15, p. 6206-6244, 2024.

[62] M. Beygisangchin, S. K. Kamarudin, et S. A. Rashid, « Synthesis, properties, and applications of polyaniline–graphene quantum dot nanocomposites: comprehensive review », *J. Environ. Chem. Eng.*, vol. 12, n° 5, p. 113460, 2024.

[63] P. Kaushik, R. Bharti, R. Sharma, M. Verma, R. T. Olsson, et A. Pandey, « Progress in synthesis and applications of Polyaniline-Coated Nanocomposites: A comprehensive review », *Eur. Polym. J.*, vol. 221, p. 113574, 2024.

CHAPTER II

1. Introduction

This chapter provides a comprehensive description of the methodologies applied in this work, beginning with the synthesis of the adsorbent materials and the analytical techniques used for their physicochemical characterization. It further details the experimental protocols implemented to evaluate adsorption performance under a range of operational parameters. The chapter also presents the computational framework employed, including quantum chemical analyses based on Density Functional Theory (DFT) and Molecular Dynamics (MD) simulations. Finally, it introduces the optimization procedures developed using hybrid algorithms, alongside the Design of Experiments methodology adopted to structure, refine, and enhance the overall experimental strategy.

2. Product and materials used

The raw Halloysite was directly collected from a mine of Djebbel Debbagh (Guelma) from the east region of Algeria, grinded, sieved and dried at 100˚C for 24h.

Sodium alginate (Sag), Calcium chloride ($CaCl_2$), Ammonium persulfate (APS, (NH4)2S2O8), Methyl orange (MO, $C_{14}H_{14}N_3SO_3Na$), Methylene bleu (MB, $C_{16}H_{14}N\,SCl{\cdot}3H_2O$), and Aniline ($C_6H_7N$) were purchased by Sigma-Aldrich Chemicals, Germany.

Sodium hydroxide (NaOH), Ethanol (C_2H_5OH 96%), Hydrochloric acid (HCl 36%), Phosphoric acid (H_3PO_4 98%) and Sodium chloride (NaCl) were obtained from Scharlau.

3. Synthesis and characterization

3.1. Preparation of HAL, PANI, HAL/PANI, SA, HAL/SA, HAL/PANI/SA, BC500, BC500/SA, K10, and K10/CTAB

3.1.1. HAL purification

To purify the raw halloysite, 20 g of the sample were dispersed in 1 L of distilled water and stirred for 24 hours, then centrifuged at 5000 rpm for 5 minutes. The resulting precipitate was washed with 2 L of a 0.1 M HCl solution under vigorous stirring at room temperature for 4 hours in order to remove carbonates. The precipitate was then repeatedly washed with distilled water and centrifuged at least five times until the supernatant became neutral [1].

To eliminate organic matter, the solid residue was added to a hydrogen peroxide solution (10% v/v) and stirred overnight at room temperature. The residual hydrogen peroxide was decomposed by heating the mixture at 70 °C for 30 minutes. The precipitate was then washed with hot water, dried at 60 °C for 24 hours, and stored in sealed containers. The purified sample was designated as HAL. Finally, the sample was analyzed by X-ray fluorescence (XRF).

3.1.2. PANI preparation

A 50 mL HCl/aniline solution was prepared by mixing 48.15 mL of hydrochloric acid with 1.85 mL of aniline, followed by magnetic stirring until complete dissolution of the aniline. Separately, 2 g of ammonium persulfate (APS) was dissolved in 100 mL of distilled water. The APS solution was then added dropwise to the aniline mixture under continuous stirring at room temperature. During the reaction, the solution color changed from transparent to a dark green, indicating the formation of polyaniline. After complete addition of APS, stirring was maintained for an additional 2 h.

The resulting polyaniline was subsequently washed with ethanol to remove excess coloration, followed by repeated rinsing with distilled water to eliminate residual hydrochloric acid. The product was finally recovered by precipitation in distilled water and dried in an oven at 32 °C.

3.1.3. HAL/PANI preparation

A precursor solution was prepared by mixing 48 mL of hydrochloric acid (HCl) with 2 mL of aniline monomer (50 mL total volume) in a glass reaction vessel. The mixture was homogenized

using magnetic stirring (500 rpm) at ambient temperature (25±2°C) until complete dissolution of the aniline was achieved. Subsequently, 2 g of purified halloysite nanotubes (HNTs) were dispersed into the acidic aniline solution under continuous agitation.

Concurrently, an initiator solution was prepared by dissolving 2 g of ammonium persulfate (APS) in 100 mL of deionized water. This oxidizing solution was introduced to the aniline/HNT mixture via controlled dropwise addition while maintaining constant stirring (500 rpm) at room temperature.

The polymerization reaction was monitored through visual colorimetric changes, with the system transitioning from a colorless solution to a characteristic dark green emulsion, confirming the successful formation of polyaniline (PANI) on the halloysite substrate. The observed coloration corresponds to the emeraldine salt form of PANI, indicating protonation of the polymer backbone in the acidic medium [2].

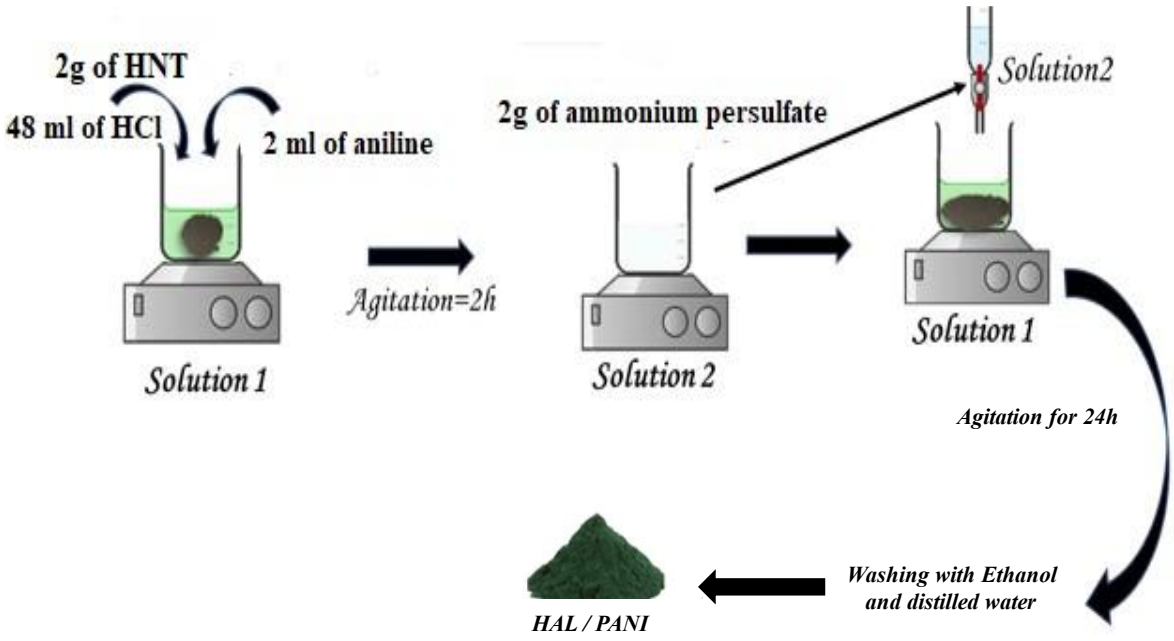


Figure II. 1: *Schematic presentation of the preparation procedure of HAL/PANI.*

3.1.4. HAL//SA beads preparation

A solution was prepared by dissolving 2 g of sodium alginate (SA) in 100 mL of distilled water under continuous stirring. Subsequently, 2 g of Halloysite (HAL) were added to the alginate solution and stirred thoroughly until a homogeneous suspension was obtained. The beads formation was achieved by dropwise addition of the mixture, using a fine syringe, into an 8% calcium chloride ($CaCl_2$) solution. The resulting beads were maintained under continuous stirring for 24 h to ensure complete gelation.

After gelation, the beads were carefully washed with distilled water and allowed to air-dry for 24 h. The dried beads were then stored in a dry container.

3.1.5. HAL/PANI/SA beads preparation

Two grams of sodium alginate (SA) were dissolved in 100 mL of distilled water under constant agitation. Subsequently, 2 grams of HNTs/PANI were added to the mixture and stirred rigorously until a homogeneous suspension was obtained [3].

The SA-HNTs/PANI suspension was extruded through a gauge syringe needle into a gelation bath containing 8% (w/v) calcium chloride ($CaCl_2$) solution. The extrusion rate was maintained at 5 mL/min with a working distance of 10 cm between the needle tip and the crosslinking solution surface to ensure spherical bead formation. The system was maintained under gentle agitation (200 rpm) for 24 hours at ambient temperature to facilitate complete ionotropic gelation.

The crosslinked composite beads were then rinsed thoroughly with distilled water to remove residual $CaCl_2$, air-dried for 24 hours at 30°C in a controlled environment and stored in amber glass vials at 25°C until further use.

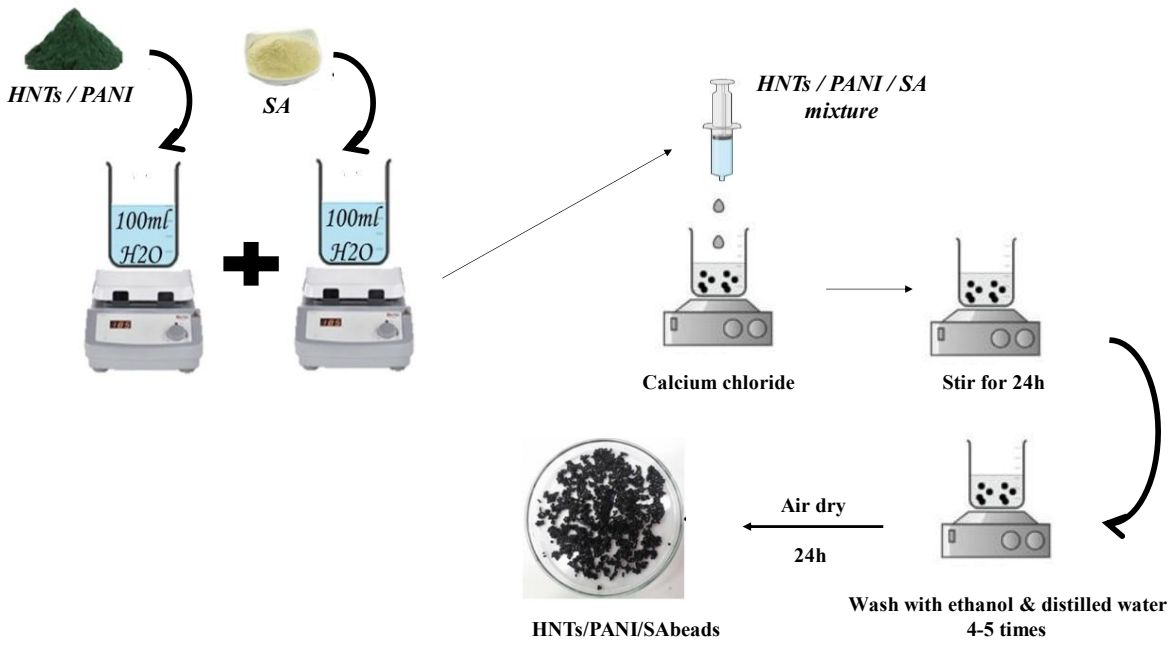


Figure II. 2: *Schematic presentation of the preparation procedure of HNTs/PANI/SA beads.*

3.1.6. Biomass preparation:

The biomass used in this study consists of a mixture derived from pomegranate, mandarin, and walnut peels. The peels were collected, homogenized, dried, and ground, with respective mass ratios of 50:50:50.

3.1.7. Biochar preparation:

Biochar is a carbonaceous material produced through the pyrolysis of biomass. In this study, 25 g of biomass were placed in a calcination furnace, with the heating rate set at 10 °C/min. The temperature range extended from ambient temperature to the desired pyrolysis temperature, maintained for two hours. The pyrolysis temperatures employed were 300, 500, and 700 °C. The resulting biochars were designated as BC300, BC500, and BC700, respectively. Since BC500 exhibited the highest adsorption capacity among the prepared samples, only BC500 was selected for further investigation in this study.

- **Chemical activation:**

Several activating agents can be used for chemical activation, including acids, bases, and salts. Among the acids, phosphoric acid (H_3PO_4) has been widely employed for the activation of various biomasses. In this method, 10 g of BC500 were mixed with 20 g of a 40 wt.% H_3PO_4 solution under continuous stirring for 24 hours at room temperature. The resulting material was then repeatedly washed with distilled water until the pH of the washing water reached neutrality. Finally, the material was dried at 110 °C for 24 hours. The obtained material is designated as BC500H.

3.1.8. Preparation of BC500-SA beads

Two grams of sodium alginate were dissolved in 100 mL of distilled water under continuous stirring. Subsequently, 2 grams of the previously prepared BC500 were added to the alginate solution and stirred until a homogeneous mixture was obtained. This mixture was then used to form BC500 beads encapsulated within the alginate matrix. The beads were produced by dropwise addition of the mixture into an 8% calcium chloride solution. The calcium chloride solution was prepared by dissolving 4 grams of $CaCl_2$ in 200 mL of distilled water and stirred for 24 hours to ensure complete gelation of the beads. The formed beads were then thoroughly washed with distilled water and air-dried for 24 hours before being stored in a dry container. The preparation process of the beads is illustrated in the schematic diagram below.

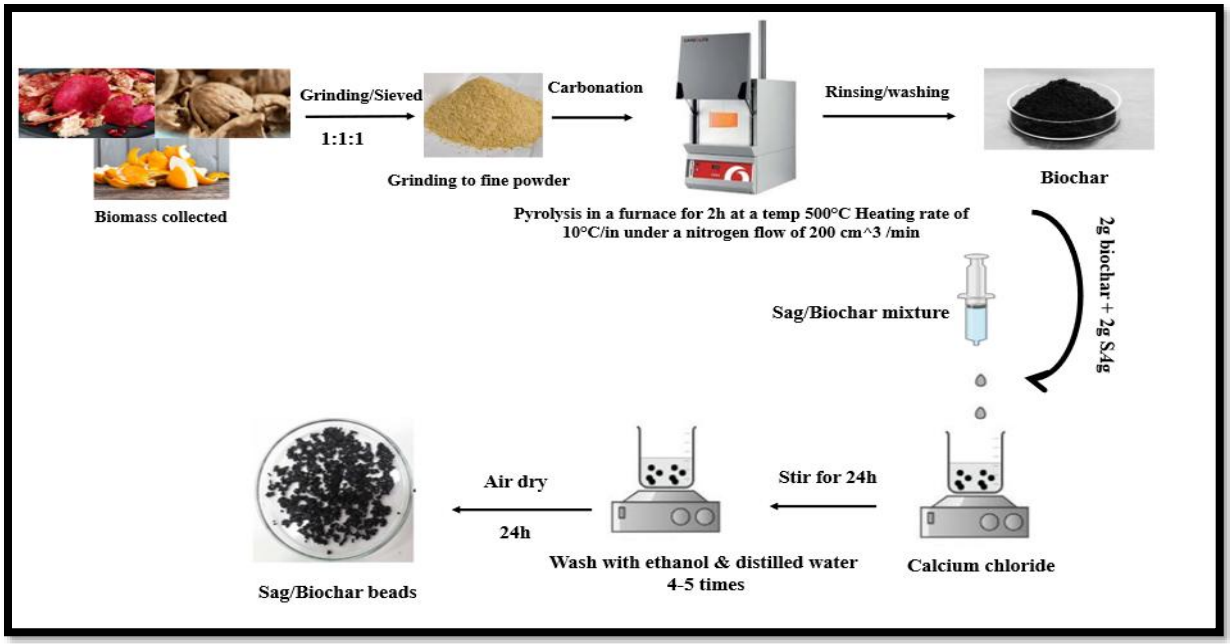


Figure II. 3: *Schematic presentation of the preparation procedure of BC500/Sag bead.*

3.1.9. Preparation of MTM-K10-CTAB

Commercial montmorillonite MTM-K10 was purchased from Sigma-Aldrich. CTAB was first dissolved in a hot acidic solution at 80 °C, after which the commercial montmorillonite was added and the mixture was maintained under stirring for 3 h to allow the cation-exchange process to occur. After the reaction was completed, the resulting solid was thoroughly washed until complete removal of bromide ions, then dried and ground to obtain CTAB-modified MTM-K10.

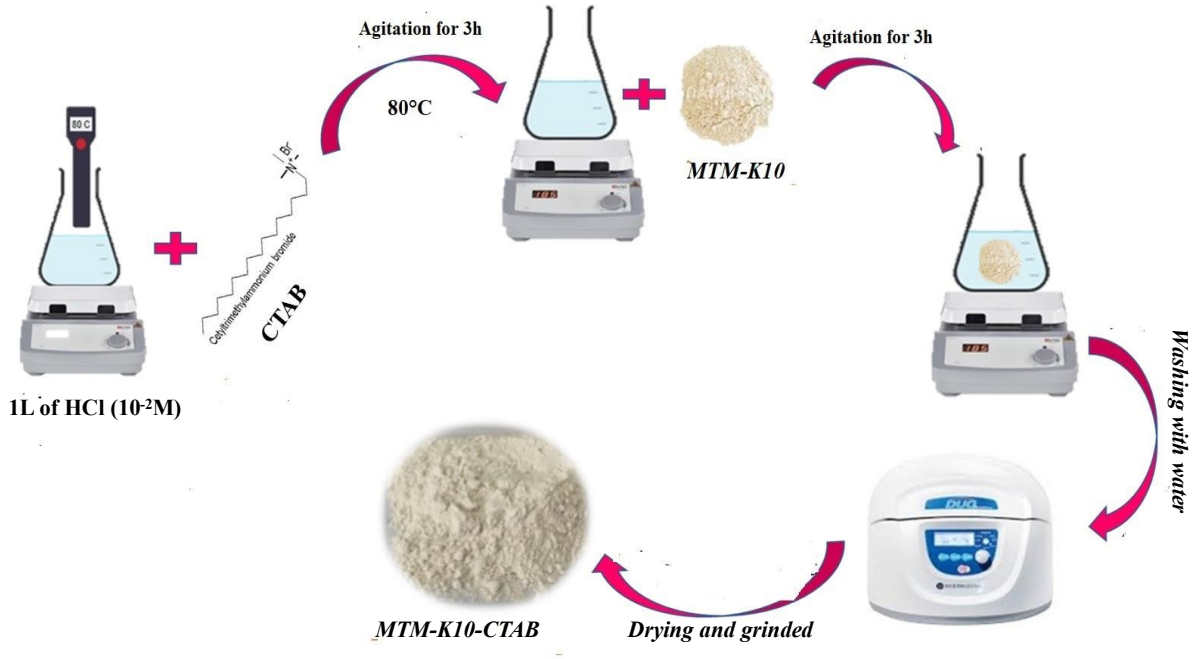


Figure II. 4: *Schematic presentation of the organophilic preparation of MTM-K10-CTAB.*

3.1.10. **Preparation of MgAl-CO3, MgAl-SO4 and MgAl-PO4 LDHs**

To enable a comparative investigation, three hydrotalcite-type materials MgAl-CO_3, MgAl-PO_4, and MgAl-SO_4 were synthesized using a co-precipitation approach. The preparation procedure involved the simultaneous dropwise addition of two separate solutions into an initially empty reactor (**Figure II.5**). One solution consisted of precursor metal chloride salts, while the second comprised an alkaline mixture containing sodium hydroxide (NaOH), sodium carbonate (Na_2CO_3), monobasic sodium phosphate (NaH_2PO_4), and sodium sulfate (Na_2SO_4). Vigorous stirring was applied from the onset of the process, and the pH of the resulting medium was consistently maintained at 10 throughout the addition by means of a 1 M NaOH solution. This control ensured a homogeneous and well-regulated precipitation process.

Following complete addition, the obtained suspension was continuously stirred for 1 hour at ambient temperature to promote adequate aging and the development of the lamellar structure. Subsequently, the mixture was subjected to thermal treatment at 70 °C for 18 hours in order to enhance the crystallinity of the layered double hydroxides (LDHs).

The resulting suspension was then filtered and thoroughly washed with distilled water until the filtrate reached neutral pH (pH = 7). Finally, the recovered solid was dried at 70 °C for 24 hours, yielding the MgAl-CO_3, MgAl-SO_4, and MgAl-PO_4 materials.

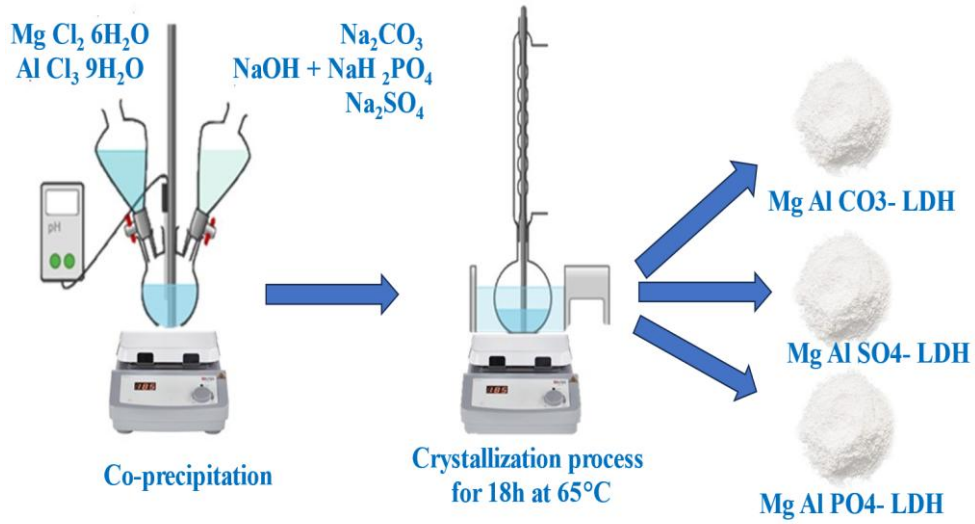


Figure II. 5: *Schematic presentation of Co-precipitation method for MgAl-CO3, MgAl-SO4 and MgAl-PO4 LDHs.*

3.2.Characterization of materials

The crystalline structure and phase composition of different materials and composites were analyzed using a Bruker D8 Advance diffractometer with Cu Kα radiation (λ = 1.5406 Å), operated at 40 kV and 15 mA. Diffraction patterns were recorded from 5° to 80° (2θ) with a step size of 0.02° and a scan rate of 2°(2θ) min^{-1}.

Phase identification was performed using the JCPDS database, and quantitative analysis was carried out by Rietveld refinement in HighScore software. Peak widths and shapes were analyzed to separate contributions. The refinement quality was judged based on R-factors (Rwp, Rp) and the goodness-of-fit (χ^2), ensuring consistency between observed and calculated patterns.

Key XRD parameters were determined as follows. The basal spacing (d-spacing), representing the distance between adjacent crystallographic planes, was calculated using Bragg's law: $\boldsymbol{n\lambda = 2\ sin\ \theta}$

where λ is the X-ray wavelength and θ is the Bragg angle.

The crystallite size (d), representing the coherent domain size along a specific crystallographic direction, was estimated using the Scherrer equation: $\boldsymbol{d = K\lambda/\beta\ cos\ \theta}$

where K is the shape factor (typically ~0.9), β is the full width at half maximum (FWHM) of the diffraction peak in radians, and θ is the Bragg angle. From the crystallite size, the number of coherently stacked layers along the c-axis can be inferred, providing insight into the structural ordering and stacking coherence of the nanotube walls.

The morphology and surface features of the samples were examined using scanning electron microscopy (SEM). Imaging was performed on a Thermo Fisher Scientific Quattro S field-emission microscope under optimal resolution conditions.

Nitrogen physisorption measurements were carried out using a Micromeritics ASAP 2020 surface area and porosity analyzer to evaluate the textural properties of the samples. Prior to analysis, all samples were degassed under vacuum at 120°C for 4 h to remove adsorbed moisture and impurities. Adsorption–desorption isotherms were recorded at liquid nitrogen temperature (77 K) over a relative pressure (P/P_0) range of 0.01–1.0. The Brunauer–Emmett–Teller (BET) method was used to determine the specific surface area, while the Barrett–Joyner–Halenda (BJH) model was applied to analyze the pore size distribution and total pore volume.

$$\frac{P/P0}{V(1-\frac{P}{P0})} = \frac{c-1}{Vm*c}\frac{P}{P0} + \frac{1}{Vm*c} \qquad \text{(1)}$$

Where P is the equilibrium pressure, P_0 is the saturation pressure,Vm is the adsorbed gas volume, Vm is the monolayer adsorbed gas volume, and c is the BET constant related to adsorption energy.

Thermogravimetric analysis (TGA) was carried out on a Mettler Toledo TGA/DSC 3+ system under a nitrogen atmosphere (25 cm^3/min sample purge, 10 cm^3/min balance purge). Samples (5 - 18mg) were heated to 820 °C at 10 °C/min.

Fourier transform infrared (FTIR) spectroscopy was employed to identify chemical functional groups and assess polymer–nanotube interactions. Spectra were recorded using a Shimadzu IR Affinity-1S spectrometer over the range 4000–500 cm^{-1} with a resolution of 2 cm^{-1} and 64 scans per sample.

The point of zero charge (pH_pzc) of the samples was determined using the pH drift method[4]. Solutions with initial pH values ranging from 2 to 12 were prepared, and a known amount of the sample was added. After 48 h of equilibration, the final pH was measured. The pH_pzc corresponds to the pH at which the initial and final values are equal, indicating a neutral net surface charge.

4. Analysis of errors

The parameters for the isotherm and kinetic models were determined through nonlinear regression analysis using OriginPro 2018 software. The most suitable model was selected based on the highest coefficient of determination (R^2) and the lowest Akaike Information Criterion (AIC), ensuring optimal alignment with the experimental data [4]. Both models are represented mathematically as:

$$R^2 = 1 - \frac{\sum_{N=1}^{N} (q_{e,t.\exp.N} - q_{e,t.cal.N})^2}{\sum_{N=1}^{N} (q_{e,t.\exp.N} - \overline{q_{e,t.\exp.N}})^2} \quad \text{..... (2)}$$

$$AIC = N \times Ln\left(\frac{SSE}{N}\right) + 2K \quad \text{..... (3)}$$

Where SSE represents the error sum of squires $= \sum (q_e - q_e^{cal})^2$

5. Density functional theory (DFT)

In the context of investigating the adsorption of organic dyes onto natural and composite materials, quantum chemical calculations represent an essential tool for elucidating, at the atomic scale, the fundamental mechanisms governing adsorbent–adsorbate interactions [5]. By relying on the approximate resolution of the Schrödinger equation, these methods provide detailed insights into the intrinsic electronic properties of dye molecules such as Methylene Blue and methyl orange, as well as the functional groups that constitute these materials. Density Functional Theory (DFT), particularly hybrid and dispersion-corrected functionals (e.g., B3LYP-D3, PBE0-D3), is especially suitable for modeling the non-covalent interactions (hydrogen bonding, van der Waals forces, π–π stacking, and electrostatic attraction) that play a dominant role in the immobilization of dye molecules on adsorbents surfaces [6]. DFT calculations allow the optimization of molecular geometries and the determination of key electronic descriptors such as HOMO–LUMO energy levels, electronic density distributions, electrostatic potential maps (MEP), and local reactivity indices derived from Fukui functions, thereby identifying the active sites responsible for dye uptake [7], [8]. The adsorption energy calculated as the difference between the energy of the adsorbent–dye complex and the sum of the isolated components provides a quantitative measure of adsorption strength and clarifies whether the interaction is predominantly physisorption or chemisorption, explaining their capacity to interact with aromatic dye structures through electrostatic attraction, π–π stacking, and hydrogen bonding. Overall, quantum chemical calculations offer a powerful predictive framework that links the electronic structure of different materials to their adsorption

performance, thereby rationalizing experimentally observed trends in the removal of organic dyes from aqueous effluents.

The following formulas [7], [8], [9], [10] are employed to determine potential (μ), electronegativity (χ), global hardness (η), global softness (S), global electrophilicity index (ω), softness (σ), and the maximum amount of electronic charge (ΔN_{max}).

$$\mu = E_{HOMO} + E_{LUMO} \quad \text{(4)}$$

$$\chi = -\mu \quad \text{(5)}$$

$$\eta = \frac{E_{LIMO} - E_{HOMO}}{2} \quad \text{(6)}$$

$$\omega = \frac{\chi^2}{2\eta} \quad \text{(7)}$$

$$\Delta E_{b-d} = \frac{-\eta}{4} \quad (8)$$

6. Molecular dynamics simulation (MDS)

Molecular Dynamics Simulation (MDS) represents an indispensable computational approach for probing the dynamic behavior, structural evolution, and physicochemical interactions governing the adsorption of organic dyes onto different adsorbents at the atomic scale [11]. By integrating Newton's equations of motion, MDS generates time-dependent trajectories that capture the continuous movement of atoms under the influence of interatomic forces described by empirical or quantum-derived force fields [12]. These force fields incorporate both bonded interactions, such as bond stretching, angle bending, and dihedral torsions, and non-bonded contributions, including van der Waals dispersion and Coulombic electrostatic forces, enabling the realistic modeling of complex supramolecular systems involving clay based materials and aromatic dye molecules like Methylene blue and methyl orange. Through simulations conducted under various statistical ensembles (NVT, NPT, or NVE), MDS facilitates the

characterization of thermodynamic stability, adsorption conformations, mass transport, and diffusion kinetics of dye molecules within the heterogeneous microenvironment of clay surfaces [13].

The objective of this computational work is to identify low-energy adsorption sites and explore the species' preferred adsorption on the surface of clays. Based on an initial evaluation of the possible interaction energy of the adsorbate–substrate system, the adsorption research of the molecules, or molecules set, is conducted. Typically, the calculation of this energy involves adding together the following three factors: [14]

- The equilibrium surface and the total interaction energy (E_{Tot}) between the molecule and the surface.
- The surface's total internal energy, marked $E_{Tot\ (surface)}$, in the absence of the molecule and after any potential relaxation.
- Without the surface, the molecule's total energy relaxes, as shown by $E_{Tot\ (molecule)}$. Accordingly, the surface molecule system's adsorption energy has the following form:

$$\boldsymbol{E_{ads} = E_{Tot\ (molecule/surface)} - \left(E_{Tot\ (surface)} + E_{Tot\ (molecule)}\right)} \ldots\ldots\ldots\ldots\ldots\ldots\ldots\ldots\ldots\ldots (\mathbf{9})$$

7. Artificial intelligence (AI) techniques

Adsorption processes play a crucial role in various industrial applications, including wastewater treatment, gas purification, and material separation. However, the efficient optimization of adsorption systems requires a comprehensive understanding of kinetic, isothermal, thermodynamic, and overall performance parameters. Conventional approaches often struggle to address the complexity and nonlinearity of adsorption phenomena, resulting in suboptimal process performance [15]. In this context, Artificial intelligence (AI) techniques currently represent powerful tools for improving the efficiency and optimization of wastewater treatment processes contaminated with dyes. Advanced models such as Artificial Neural

Networks (ANNs), Convolutional Neural Networks (CNNs), and Support Vector Machines (SVMs) are increasingly used to predict adsorption performance, optimize operating parameters, and model the complex interactions between pollutants and adsorbent materials[16]. These intelligent approaches enable a better analysis of nonlinear relationships within treatment systems while reducing experimental time and operational costs. Furthermore, hybrid techniques combining adsorption with other processes, such as biodegradation or membrane separation, have demonstrated superior performance for dye removal compared with conventional methods. The integration of AI with these hybrid systems therefore provides improved process control, enhanced treatment efficiency, and a more sustainable approach for the remediation of industrial effluents containing dyes[17].

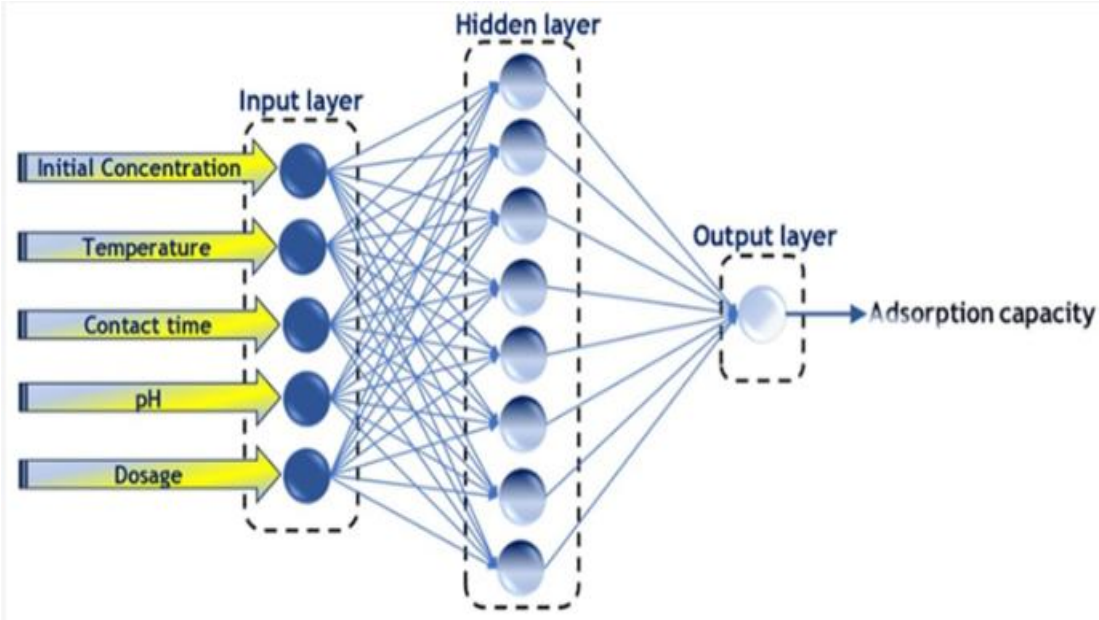


Figure II. 6: *Schematic Representation of Neural Network with single hidden layer.*

8. Experimental Design in Adsorption Processes

Experimental Design in Adsorption Processes refers to the systematic planning and organization of experiments to evaluate and optimize the factors affecting adsorption performance. In adsorption studies, experimental design techniques are used to investigate the influence of operational parameters such as pH, adsorbent dosage, initial pollutant

concentration, contact time, and temperature on the removal efficiency of contaminants. Unlike the traditional one-factor-at-a-time approach, Design of Experiments (DOE) enables simultaneous analysis of multiple variables and their interactions, reducing the number of experiments, experimental cost, and time consumption while improving the reliability of the results. Statistical methods such as Full Factorial Design, Central Composite Design (CCD), and Box–Behnken Design (BBD), often combined with Response Surface Methodology (RSM), are widely employed to model adsorption behavior and determine optimal operating conditions. These approaches provide a deeper understanding of adsorption mechanisms and contribute to the development of efficient and sustainable wastewater treatment systems [18].

9. Methylene blue as a model for cationic dye adsorption

Methylene Blue (MB) is an aromatic, heterocyclic basic dye with a molecular weight of 319.85 $g \cdot mol^{-1}$ [19]. It is a well-known cationic thiazine dye with the molecular formula $C_{16}H_{18}N_3ClS$ and exhibits a maximum absorption wavelength (λmax) at 663 nm [20]. Classified as a polymethine dye, it contains an amino auxochrome group and carries a positive charge. According to the International Union of Pure and Applied Chemistry (IUPAC), its chemical name is *3,7-bis(dimethylamino)phenothiazine chloride)* [21]. The structure of MB is presented in the **Fig. II.7** [22]**.** Methylene Blue (MB) is widely employed as a model compound in adsorption research due to its well-defined molecular structure, strong cationic nature, and high solubility in water, which facilitates accurate experimental measurements [23]. Its intense blue color and high molar absorptivity allow precise quantification using UV–Vis spectrophotometry, making it suitable for monitoring adsorption kinetics and equilibrium behavior. Additionally, MB is commonly found in textile, paper, and plastic industry effluents, representing a major class of persistent organic pollutants in aquatic environments. For these reasons, MB serves as an ideal representative cationic dye for evaluating the adsorption capacity, mechanisms, and efficiency of various adsorbent materials [24].



Figure II. 7: *the structure of the MB dye molecule.*

10. Methyl orange as a model for anionic dye adsorption

Methyl orange (MO) is a monoazo dye classified as an anionic chromophore, bearing the IUPAC designation *Sodium 4-[(4-dimethylamino)phenyldiazenyl]benzenesulfonate*), The structure of MO is presented in **Fig. II.8** [25]**.** It possesses the molecular formula $C_{14}H_{14}N_3NaO_3S$ and a molecular weight of 327.34 $g \cdot mol^{-1}$ [26]. Due to its extensive utilization as a pH indicator and as a coloring agent in textile, paint, and chemical manufacturing processes, MO is frequently detected in industrial wastewater streams. Structurally, MO contains an azo (–N=N–) linkage and a sulfonate group that confers strong anionic character and enhances its solubility and persistence in aqueous matrices [27]. Its release into the aquatic environment is of significant concern, as it can induce dermatological and ocular irritation and exhibits potential ecotoxicity. Furthermore, the chemical stability and resistance of MO to biological and photolytic degradation make its removal from wastewater particularly challenging, thereby necessitating advanced treatment approaches, such as adsorption, for efficient decolorization and pollutant mitigation [28].

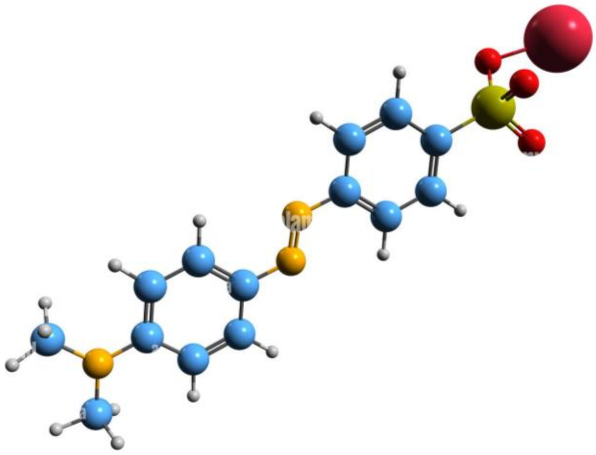


Figure II. 8: *the structure of the MO dye molecule.*

11. Theoretical models

11.1. Kinetic models

Kinetic evaluation of adsorption, expressed through the determination of intrinsic rate constants, is fundamental for elucidating mass-transfer limitations and refining the overall adsorption mechanism. The adsorption rate constitutes a critical design parameter, as it directly dictates adsorbent performance, governs interfacial transport phenomena, and ultimately influences material selection based on kinetic competency rather than capacity alone [29].

The experimental data were analyzed using non-linear forms of the pseudo-first-order (PFO), pseudo-second-order (PSO) and intra particle diffusion (IPD) kinetic models. The applicability of each model was evaluated based on correlation coefficients (R^2) and agreement between calculated and experimental equilibrium adsorption capacities [30].

Equilibrium was assumed once no further change in solute concentration was detected. The instantaneous adsorption uptake was computed according to Equation (II.10), enabling precise quantification of time-dependent solute adsorbent interactions [20].

$$q_e = \frac{(C_0 - C_t)\,V}{m} \quad \ldots \ldots \ldots (10)$$

11.1.1. Pseudo first order

The pseudo-first-order kinetic model assumes that the adsorption rate depends on the number of unoccupied sites in the liquid–solid system [31]. In this model, adsorption is considered a reversible process and is time-limited due to the formation of bonds between active sites and the solute [32]. It follows the equation (II.11) [33]:

$$qt = qe \times (1 - e^{-k_1 \times t}) \quad \ldots\ldots (11)$$

Where $\mathbf{k_1}$ represents the first-order adsorption rate constant, $\mathbf{q_t}$ is the amount of adsorbate taken up at time ***t*** (mg/g), and $\mathbf{q_e}$ denotes the adsorption capacity at equilibrium (mg/g).

11.1.2. Pseudo second order

This model assumes that the adsorption capacity is proportional to the number of active sites occupied by the adsorbed molecules [33]. It further suggests heterogeneity of the adsorption sites, the absence of interactions between adsorbate molecules, and a constant adsorption energy [34]. The model is expressed by the following equation II.12 [35]:

$$qt = \frac{k_2 \times q_e^2 \times t}{1 + k_2 \times q_e \times t} \quad \ldots\ldots (12)$$

In this model, $\mathbf{k_2}$ denotes the second-order rate constant, $\mathbf{q_t}$ the adsorbed quantity at time *t*, and $\mathbf{q_e}$ the adsorbed amount at equilibrium.

11.1.3. Intraparticle models

The intraparticle diffusion model is employed to characterize sorption diffusion kinetics, using the equations shown below [36]:

$$\boldsymbol{q_t = Kt^{1/2} + c} \quad \ldots\ldots \textbf{(13)}$$

where $\mathbf{q_t}$ (mg/g) is the adsorption capacity at time **t** (min), **k** (mg/g·min$^{1/2}$), and **c** is a constant (mg/g).

11.2. Isotherm models

11.2.1. Langmuir isotherm

The Langmuir isotherm is one of the most frequently applied models for interpreting physisorption equilibrium data [37]. It assumes that adsorption occurs on a homogeneous surface with energetically identical sites, each capable of binding only one adsorbate molecule, leading to monolayer coverage. The model further presumes the absence of interactions between adsorbed species and no lateral mobility on the surface [38]. It is given by the equation II.14:

$$q_e = \frac{q_m K C_e}{1 + K C_e} \quad \textbf{.....(14)}$$

where q_e (mg·g^{-1}) represents the amount of adsorbate retained per unit mass of adsorbent at equilibrium, C_e (mg·L^{-1}) is the equilibrium concentration of the adsorbate remaining in solution, K_L (L·g^{-1}) denotes the Langmuir equilibrium constant, and q_m is the theoretical maximum monolayer adsorption capacity.

11.2.2. Freundlich isotherm

The Freundlich isotherm, proposed in 1906, is among the first models developed to interpret sorption data. It is commonly applied to describe adsorption occurring on heterogeneous surfaces and to represent non-ideal and multilayer adsorption mechanisms. The corresponding mathematical formulation is provided in Eq. (II.15). [39]

$$q_e = kFC_e^{\frac{1}{n}} \quad \text{.....(15)}$$

In the Freundlich model, $\mathbf{K_F}$ represents the adsorption capacity, and 1/n represents the adsorption intensity,

Values of **1/n** characterize: favorable adsorption: <1 for normal, =1 for linear, and >1 for unfavorable adsorption. Both $\mathbf{K_F}$ and **n** vary with temperature, reflecting changes in adsorption affinity and surface saturation [40].

11.2.3. Temkin model

The Temkin isotherm incorporates the effect of adsorbate–adsorbate interactions throughout the adsorption process [38]. It assumes that the heat of adsorption (H_{ads}) decreases linearly with increasing surface coverage due to these interactions [41]. This model therefore provides a more realistic description for systems in which adsorbate interactions cannot be neglected. The formal mathematical expression of the Temkin isotherm is given in Eq. (II.16): [42]

$$q_e = \frac{RT}{b_{TM}} \ln K_{TM} \, C_e \quad \ldots (16)$$

In this model, ***b*** represents the Temkin isotherm constant (mg L^{-1}), ***A*** denotes the Temkin equilibrium binding constant, and ***B*** corresponds to the parameter associated with the heat of adsorption (J mol^{-1}).

11.2.4. Dubinin-raduchkevich (D-R) model

The Dubinin-Radushkevich (D-R) isotherm is used to describe adsorption on heterogeneous surfaces characterized by a Gaussian energy distribution [43]. Based on Polanyi's adsorption potential theory, it provides a more general framework than the Langmuir model and does not assume a constant sorption energy or a uniform surface. The D-R equation, which is suitable for systems dominated by pore-filling mechanisms, is given in Eq. (II.17): [38]

$$\boldsymbol{ln(q_m) = q_s - K\varepsilon^2} \quad \ldots (17)$$

where **ε** represents the Polanyi adsorption potential and **K** is the Dubinin–Radushkevich constant.

12. Influencing Factors in Adsorption Processes

Adsorption is the accumulation of liquid-phase molecules (**adsorbate**) on a solid surface (**adsorbent**), driven by intermolecular forces. The process typically occurs in three stages: diffusion to the surface, migration into pores, and monolayer formation at active sites. Its efficiency in aqueous systems is governed by competitive solute interactions, adsorption kinetics, and thermodynamic equilibrium [37]. Key parameters affecting adsorption include particle size, adsorbent dosage, pH, temperature, and initial solute concentration [44].

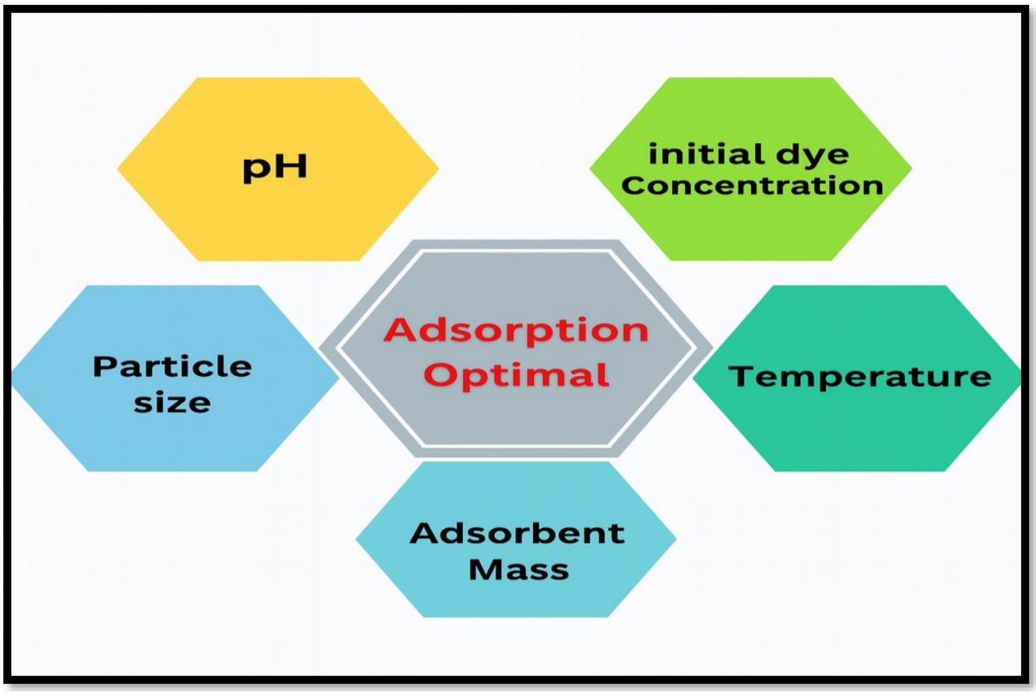


Figure II. 9: *Key parameters affecting adsorption.*

13. Adsorption thermodynamics

The thermodynamic characteristics, namely the standard Gibbs free energy (ΔG°), enthalpy change (ΔH°), and entropy change (ΔS°), were determined based on the following equations II.18: [45]

$$\begin{cases} \Delta G^\circ = -RT\ln(K_L) \\ \ln(K_L) = (\Delta S^\circ/R) - (\Delta H^\circ/RT) \end{cases} \quad \dots (18)$$

Where **R** is the gas constant (8.3145 J/mol/K), **T** is the temperature in Kelvin, and $\mathbf{K}_L$ is the thermodynamic distribution coefficient, as in the equation: $\boldsymbol{K_L = {q_e}/{C_e}}$

Reference of chapter II

[1] A. S. Bendrihem *et al.*, « Experimental and theoretical studies of the interaction of cationic dye in halloysite nanotubes », *React. Kinet. Mech. Catal.*, août 2025, doi: 10.1007/s11144-025-02933-w.

[2] B. Faouzia *et al.*, « Sustainable biomass-derived activated biochar/polyaniline/alginate composite beads for enhanced methylene blue adsorption: Experimental and theoretical investigations », *Int. J. Biol. Macromol.*, vol. 305, p. 141338, 2025.

[3] H. Chaima *et al.*, « Adsorptive removal of cationic dye from aqueous solutions using activated carbon prepared from *Crataegus monogyna*/sodium alginate/polyaniline composite beads: Experimental study and molecular dynamic simulation », *J. Mol. Liq.*, vol. 408, p. 125372, août 2024, doi: 10.1016/j.molliq.2024.125372.

[4] M. Radjai *et al.*, « Adsorptive removal of cationic and anionic dyes on a novel mesoporous adsorbent prepared from diatomite and anionic cellulose nanofibrils: Experimental and theoretical investigations », *J. Mol. Liq.*, vol. 361, p. 119670, sept. 2022, doi: 10.1016/j.molliq.2022.119670.

[5] P. I. Ravikovitch et A. V. Neimark, « Density Functional Theory Model of Adsorption Deformation », *Langmuir*, vol. 22, n° 26, p. 10864-10868, déc. 2006, doi: 10.1021/la061092u.

[6] J. P. Olivier, « Modeling physical adsorption on porous and nonporous solids using density functional theory », *J. Porous Mater.*, vol. 2, n° 1, p. 9-17, juill. 1995, doi: 10.1007/BF00486565.

[7] J. Attarki *et al.*, « Adsorption mechanism investigation of methylthioninium chloride dye onto some metal phosphates using Monte Carlo dynamic simulations and DFT calculations », *Inorg. Chem. Commun.*, vol. 149, p. 110436, mars 2023, doi: 10.1016/j.inoche.2023.110436.

[8] H. A. Hussein et G. F. Fadhil, « Theoretical investigation of para amino-dichloro chalcone isomers. Part II: a DFT structure–stability study of the FMO and NLO properties », *ACS Omega*, vol. 8, nº 5, p. 4937-4953, 2023.

[9] S.-A. Naicker et M. Moodley, « A computational study of the adsorption of corrosive sulphur on Ag surfaces », *J. Mater. Sci.*, vol. 56, nº 23, p. 13386-13399, août 2021, doi: 10.1007/s10853-021-06120-9.

[10] H. R. Belhouchet, T. Abbaz, A. Bendjedou, A. Gouasmia, et D. Villemin, « A computational study of the inclusion of β-cyclodextrin and nicotinic acid: DFT, DFT-D, NPA, NBO, QTAIM, and NCI-RDG studies », *J. Mol. Model.*, vol. 28, nº 11, p. 348, 2022.

[11] Z. Ma et P. G. Ranjith, « Review of application of molecular dynamics simulations in geological sequestration of carbon dioxide », *Fuel*, vol. 255, p. 115644, nov. 2019, doi: 10.1016/j.fuel.2019.115644.

[12] H. Yi, X. Zhang, Y. Zhao, L. Liu, et S. Song, « Molecular dynamics simulations of hydration shell on montmorillonite (001) in water », *Surf. Interface Anal.*, vol. 48, nº 9, p. 976-980, 2016, doi: 10.1002/sia.6000.

[13] Abraham Vidal-Limon, « Integration of Molecular Docking Analysis and Molecular Dynamics Simulations for Studying Food Proteins and Bioactive Peptides | Journal of Agricultural and Food Chemistry ». Consulté le: 24 décembre 2025. [En ligne]. Disponible sur: https://pubs.acs.org/doi/full/10.1021/acs.jafc.1c06110

[14] M. Khnifira *et al.*, « Combined DFT and MD simulation approach for the study of SO2 and CO2 adsorption on graphite (111) surface in aqueous medium », *Curr. Res. Green Sustain. Chem.*, vol. 4, p. 100085, 2021, doi: 10.1016/j.crgsc.2021.100085.

[15] M. Gheibi, S. R. Masoomi, M. U. Magala, A. M. Fathollahi-Fard, A. Ghazikhani, et K. Behzadian, « The Application of Artificial Intelligence (AI) in Adsorption Process of

Heavy Metals: A Systematic Review », *Environ. Ind. Lett.*, vol. 2, nº 2, p. 57-78, oct. 2024, doi: 10.15157/eil.2024.2.2.57-78.

[16] H. Patel, R. Patel, A. R. N. Aina, et B. Pal, « Current reviews of various AI techniques used for dye adsorption », *IET Conf. Proc.*, vol. 2025, nº 7, p. 968-975, sept. 2025, doi: 10.1049/icp.2025.1453.

[17] M. Gheibi, S. Masoomi, M. Uzairu Magala, A. Fathollahi-Fard, A. Ghazikhani, et K. Behzadian, « The Application of Artificial Intelligence (AI) in Adsorption Process of Heavy Metals: A Systematic Review », vol. 2, p. 57-78, nov. 2024, doi: 10.15157/eil.2024.2.2.57-80.

[18] Q. Ibrahim, L. Creedon, et S. Gharbia, « A Literature Review of Modelling and Experimental Studies of Water Treatment by Adsorption Processes on Nanomaterials », *Membranes*, vol. 12, nº 4, p. 360, avr. 2022, doi: 10.3390/membranes12040360.

[19] O. R. Benkouachi *et al.*, « Innovative Valorization of Agricultural Waste for Enhanced Adsorption Efficiency of Organic Pollutants: Leveraging Density Functional Theory, Molecular Dynamics Simulations, and Advanced Artificial Intelligence Techniques (Ann_Fdb-Lfd, Svm_Fdb-Lfd, Gpr_Fdb-Lfd, and Knn_Fdb-Lfd) », *Mol. Dyn. Simul. Adv. Artif. Intell. Tech. AnnFdb-Lfd SvmFdb-Lfd GprFdb-Lfd KnnFdb-Lfd*, Consulté le: 15 octobre 2024. [En ligne]. Disponible sur: https://papers.ssrn.com/sol3/papers.cfm?abstract_id=4869666

[20] O. R. Benkouachi *et al.*, « Advanced green peel utilization for efficient methylene blue removal: Integrated analysis and predictive modeling », *J. Mol. Liq.*, p. 125951, 2024.

[21] M. Mohammed, A. Shitu, et A. Ibrahim, « Removal of methylene blue using low cost adsorbent: a review », *Res J Chem Sci ISSN*, vol. 2231, p. 606X, 2014.

[22] P. O. Oladoye, T. O. Ajiboye, E. O. Omotola, et O. J. Oyewola, « Methylene blue dye: Toxicity and potential elimination technology from wastewater », *Results Eng.*, vol. 16, p. 100678, déc. 2022, doi: 10.1016/j.rineng.2022.100678.

[23] S. Shakoor et A. Nasar, « Adsorptive treatment of hazardous methylene blue dye from artificially contaminated water using *cucumis sativus* peel waste as a low-cost adsorbent », *Groundw. Sustain. Dev.*, vol. 5, p. 152-159, sept. 2017, doi: 10.1016/j.gsd.2017.06.005.

[24] Maryam Khodaie et al, « Removal of Methylene Blue from Wastewater by Adsorption onto ZnCl2 Activated Corn Husk Carbon Equilibrium Studies - Khodaie - 2013 - Journal of Chemistry - Wiley Online Library ». Consulté le: 24 décembre 2025. [En ligne]. Disponible sur: https://onlinelibrary.wiley.com/doi/10.1155/2013/383985

[25] S. S. Shah, T. Sharma, B. A. Dar, et R. K. Bamezai, « Adsorptive removal of methyl orange dye from aqueous solution using populous leaves: Insights from kinetics, thermodynamics and computational studies », *Environ. Chem. Ecotoxicol.*, vol. 3, p. 172-181, 2021, doi: 10.1016/j.enceco.2021.05.002.

[26] K. O. Iwuozor, J. O. Ighalo, E. C. Emenike, L. A. Ogunfowora, et C. A. Igwegbe, « Adsorption of methyl orange: A review on adsorbent performance », *Curr. Res. Green Sustain. Chem.*, vol. 4, p. 100179, 2021.

[27] M. F. Hanafi et N. Sapawe, « A review on the water problem associate with organic pollutants derived from phenol, methyl orange, and remazol brilliant blue dyes », *Mater. Today Proc.*, vol. 31, p. A141-A150, 2020.

[28] S. S. Emmanuel, A. A. Adesibikan, E. A. Opatola, et C. O. Olawoyin, « A pragmatic review on photocatalytic degradation of methyl orange dye pollutant using greenly biofunctionalized nanometallic materials: A focus on aquatic body », *Appl. Organomet. Chem.*, vol. 37, n° 7, p. e7108, 2023.

[29] A. K. Khanzada *et al.*, « Hydrochar as a bio-based adsorbent for heavy metals removal: A review of production processes, adsorption mechanisms, kinetic models, regeneration and reusability », *Sci. Total Environ.*, vol. 945, p. 173972, 2024.

[30] J. Wang et X. Guo, « Adsorption kinetic models: Physical meanings, applications, and solving methods », *J. Hazard. Mater.*, vol. 390, p. 122156, 2020.

[31] E. D. Revellame, D. L. Fortela, W. Sharp, R. Hernandez, et M. E. Zappi, « Adsorption kinetic modeling using pseudo-first order and pseudo-second order rate laws: A review », *Clean. Eng. Technol.*, vol. 1, p. 100032, 2020.

[32] M. Musah, Y. Azeh, J. Mathew, M. Umar, Z. Abdulhamid, et A. Muhammad, « Adsorption Kinetics and Isotherm Models: A Review », *Caliphate J. Sci. Technol.*, vol. 4, n° 1, p. 20-26, févr. 2022, doi: 10.4314/cajost.v4i1.3.

[33] H. Moussout, H. Ahlafi, M. Aazza, et H. Maghat, « Critical of linear and nonlinear equations of pseudo-first order and pseudo-second order kinetic models », *Karbala Int. J. Mod. Sci.*, vol. 4, n° 2, p. 244-254, 2018.

[34] E. Allahkarami, E. Allahkarami, A. Azadmehr, et M. E. Shahrabadi, « Kinetics and statistical physics modeling of heavy metal ions adsorption onto functionalized pyrite composite: Experimental and modeling », *Results Chem.*, p. 102536, 2025.

[35] F.-C. Wu, R.-L. Tseng, S.-C. Huang, et R.-S. Juang, « Characteristics of pseudo-second-order kinetic model for liquid-phase adsorption: A mini-review », *Chem. Eng. J.*, vol. 151, n° 1-3, p. 1-9, 2009.

[36] F.-C. Wu, R.-L. Tseng, et R.-S. Juang, « Initial behavior of intraparticle diffusion model used in the description of adsorption kinetics », *Chem. Eng. J.*, vol. 153, n° 1-3, p. 1-8, 2009.

[37] J. Zhang *et al.*, « Water absorption behavior of starch: A review of its determination methods, influencing factors, directional modification, and food applications », *Trends Food Sci. Technol.*, vol. 144, p. 104321, 2024.

[38] M. Kanagalakshmi, S. G. Devi, P. Ananthi, et A. Pius, « Adsorption isotherms and kinetic models », in *Carbon Nanomaterials and their Composites as Adsorbents*, Springer, 2024, p. 135-154.

[39] H. R. Ahmed, K. F. Kayani, A. M. Ealias, et K. H. H. Aziz, « A Comprehensive Review of Forty Adsorption Isotherm Models: An In-depth Analysis of Ten Statistical Error Measures », *Water. Air. Soil Pollut.*, vol. 236, n° 6, p. 346, 2025.

[40] S. S. Imam et M. F. Hamza, « Adsorptive removal of neutral red dye from aquatic environments: a review of adsorbent materials, kinetics, isotherms, thermodynamics and future prospects », *Environ. Technol. Rev.*, vol. 14, n° 1, p. 69-93, 2025.

[41] A. Mudhoo, « Unveiling new Insights: Revised Temkin adsorption isotherm parameters from fresh Curve fits in adsorption studies », *Chem. Eng. Sci.*, vol. 311, p. 121585, 2025.

[42] I. Mechnou, S. Meskini, E. Elqars, A.-I. Chham, et M. Hlaibi, « Classical and advanced isotherms to model the adsorption of drugs, dyes and metals on activated carbonaceous materials: a review », *Environ. Chem. Lett.*, vol. 22, n° 5, p. 2375-2404, 2024.

[43] A. A. Marhoon, S. A. Hasbullah, N. Asikin-Mijan, et W. N. A. W. Mokhtar, « Adsorption of metal porphyrins using chitosan/zeolite-X composite as an efficient demetallization agent for crude oil: Isotherm, kinetic, and thermodynamic studies », *Int. J. Biol. Macromol.*, vol. 274, p. 133358, 2024.

[44] S. Bakhtiari, M. Salari, M. Shahrashoub, A. Zeidabadinejad, G. Sharma, et M. Sillanpää, « A comprehensive review on green and eco-friendly nano-adsorbents for the removal of heavy metal ions: synthesis, adsorption mechanisms, and applications », *Curr. Pollut. Rep.*, vol. 10, n° 1, p. 1-39, 2024.

[45] C. R. Girish, « Determination of thermodynamic parameters in adsorption studies: a review », *Chem. Pap.*, vol. 79, n° 9, p. 5687-5706, 2025.

CHAPTER III

1. Introduction

This chapter investigates the adsorption-based removal of the cationic dye methylene blue (MB) dissolved in water using halloysite nanotubes (HAL) of Algerian origin, by combining experimental and theoretical approaches. The material was characterized using FTIR, XRD, XRF, TEM, TGA/DTA, and BET techniques. Response Surface Methodology (RSM), based on a Box-Behnken design (BBD), was employed to identify pH, adsorbent dosage, and initial MB concentration as key influencing factors. A statistical physics-based modelling approach, combined with DFT/MD simulations, helped to elucidate the interaction mechanism between MB and HAL.

2. Experimental design

The adsorption study was carried out using Box Behnken Design (BBD) with 3 factors: pH, initial concentration C and adsorbent dose W. The chosen values of the previous parameters were based on preliminary study that was carried out by changing one factor at a time.

The range and values of independent factors are shown in **table III.1**. The statistical software Design Expert 13.0 (Stat-Ease, Minneapolis, USA), was used to analyze the obtained data.

The adsorption capacity q(mg/g) was chosen as response (Y) in the experimental study and was calculated as below:

$$q = \frac{(C_0 - C_{t,e})V}{W} \quad \text{..... (III.1)}$$

Where $\mathbf{C_0}$ and $\mathbf{C_{t,e}}$ are the concentrations of MB at time 0, at time t and at equilibrium (mg/L), respectively and **V** represents the volume of solution (L)

Table III. 1: Experimental range and levels of independent process variables.

Independent variable	Range and level		
	-1	0	+1
PH	6	8	10
W (mg)	10	30	50
C0 (mg/l)	20	60	100

The study was carried out with 17 experiments with five replicates at center points.

The minimum number of experimental runs (N) required for robust design development is determined by [1]:

$$N = 2K(K-1) + C_0 \quad \text{(III.2)}$$

Where k is the factor number and C_0 is the replicate number of the central point

For statistical calculations, the variables X_i are coded as xi according to the following relationship:

$$X_i = ((X_i - X_0)/\delta X \quad \text{(III.3)}$$

where xi dimensionless coded value of the variable X_i, X_0 is the value of the Xi at the center point, and δX is the step change

The experimental data derived from the BBD were fitted to a second-order polynomial regression model to predict optimal process conditions [2]. The generalized response surface model can be expressed as:

$$Y = \beta_0 + \sum \beta i\, Xi + \sum \beta ii\, Xi^2 + \sum \beta ij\, Xi\, Xj \quad \text{(III.4)}$$

where Y indicates the predicted response associated with each factor level; Xi and Xj represent the coded values of the independent variables; β_0 refers to intercept; βi, βii and βij denotes regression coefficient. The results of the experimental design are mentioned in **table III.2**. the factors values are showed in uncoded unit.

Table III. 2: BBD design matrix with experimental values.

Run	pH	W(mg)	C(mg/l)	Q(mg/g)
1	10	30	100	50.08
2	6	30	100	27.05
3	8	50	20	9.73
4	10	50	60	26.25
5	8	50	100	29.18
6	10	30	20	43.03
7	6	30	20	16.49
8	8	30	60	30.29
9	8	30	60	29.33
10	6	10	60	38.79
11	8	30	60	31.82
12	8	30	60	30.84
13	8	10	20	41.15
14	8	30	60	30.29
15	6	50	60	26.18
16	10	10	60	66.56
17	8	10	100	58.58

3. Adsorption Study

Batch adsorption experiments were performed in 100 mL Erlenmeyer flasks containing 50 mL of aqueous MB solution. The initial pH of each solution was precisely adjusted to predetermined values using 0.1 M NaOH and HCl solutions. A predetermined mass of adsorbent was introduced into each flask, which were then agitated at 120 rpm in a temperature-controlled orbital shaker (25±1°C) for specified time intervals.

Following the adsorption period, the residual MB concentration in solution was quantified using UV-Vis spectrophotometry (Shimadzu UV-1700 PharmaSpec) by measuring absorbance at the characteristic λmax of 664 nm.

4. Structural and simulation details

4.1. Quantum chemical calculations

The quantum chemical calculations based on density functional theory implemented in Gaussian-09 package [3] were performed using the Becke-3-Lee-Yang-Par (B3LYP) functional and 6-311+G (d,p) level approach [4]. All parameters were selected to achieve a stable structure with the lowest energy. The quantum chemical calculations were performed to compute the optimized molecular structure, the Mapping Electrostatic Potential, and the Frontier molecular orbitals (FMOs) that include the highest occupied (E_{HOMO}) and lowest unoccupied molecular orbitals.

From FMOs' energies, some Global Quantum Chemical Descriptors (GQCD) were calculated according to the formulas (5 to 11) including: the energy gap (ΔE), chemical potential (μ), global hardness (η), global softness (σ), absolute electronegativity (χ), electrophilicity index (ω), and electronic energy (ΔE_{b-d}) [5], [6].

$$\Delta E_{Gap} = E_{LUMO} - E_{HOMO} \quad \text{(III.5)}$$

$$\mu = \frac{(E_{LUMO} + E_{HOMO})}{2} \quad \text{(III.6)}$$

$$\eta = \frac{(E_{LUMO} - E_{HOMO})}{2} \quad \text{(III.7)}$$

$$\sigma = \frac{1}{\eta} \quad \text{(III.8)}$$

$$\chi = \frac{-(E_{HOMO} + E_{LUMO})}{2} \quad \text{(III.9)}$$

$$\omega = \frac{x^2}{2\eta} \quad \text{(III.10)}$$

$$\Delta E_{b-d} = \frac{-\eta}{4} \quad \text{(III.11)}$$

4.2. Molecular Dynamic simulations (MDs)

Molecular Dynamic simulations (MDs) based on Monte Carlo theory were performed using the Adsorption Locator modulus integrated in Materials Studio 2017 package [7]. It aims to optimize the most equilibrium configuration of MB onto HAL surface, as well as to compute the adsorption energy.

In this work, we employed an atomistic model representing an isolated kaolinite layer with complete basal surface terminations. The model explicitly incorporates both crystallographic planes characteristic of kaolinite's 1:1 layer structure: the tetrahedral surface, terminated by basal oxygen atoms and the octahedral (surface, terminated by hydroxyl groups. This approach preserves the fundamental structural polarity of kaolinite while enabling detailed investigation of surface-specific interactions [8]. A cleaved surface of HNTs in the direction (0 0 -1) having the dimensions: a = 10.36 Å, b = 8.98 Å, $\alpha = 87.2^{o}$, $\beta = 105.3^{o}$, $\gamma = 90.0^{o}$, with an interlamellar spacing d = 7.03 Å. To adsorb MB molecule a vacuum slab was made up of six atomic layers, HO-Al-O-Si-O (**Fig. III.1**). The calculations were supported by classical force fields to evaluate the adsorption energetics and configurations. The parameters for the simulations were carefully selected to ensure accurate modeling of the adsorption processes, including the adsorption modulus to characterize the mechanical response of the system [9], [10], [11].

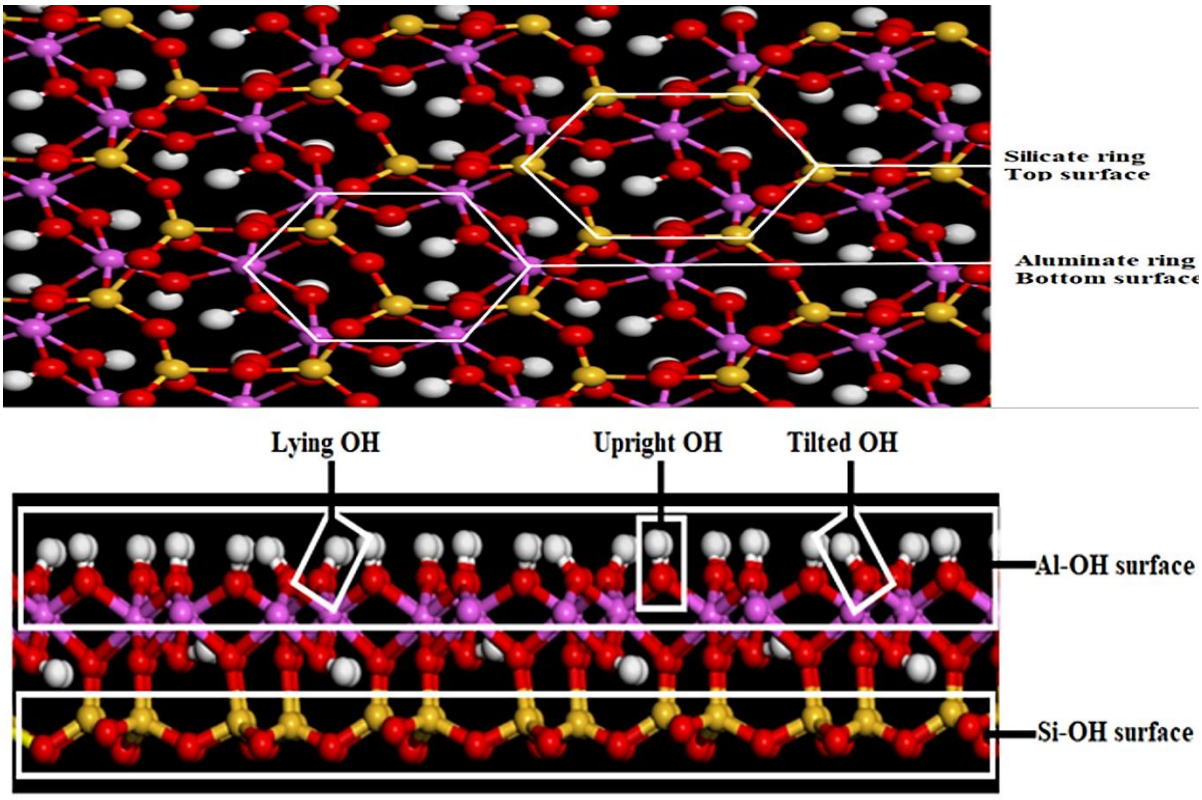


Figure III. 1: A schematic representation of the crystalline structure of HNT, the Side and Top view.

5. Results and discussion

5.1. Characterization

The chemical compositions of raw halloysite and after purification (HNTs) are presented in **Table 3**. The purification process resulted in an increase in SiO_2 content and a reduction in Al_2O_3 content. Consequently, the SiO_2/Al_2O_3 ratio slightly increased from 1.20 to 1.29. The reduction in alumina content in HNTs is attributed to the leaching of aluminum ions from the octahedral layers, induced by acid hydrolysis during purification [12]. This dealumination process is also accompanied by a decrease in impurities such as CaO, Fe_2O_3, K_2O, and MnO_2.

Table III. 3: XRF analysis of raw and purified HNTs.

	SiO2	Al2O3	CaO	Fe2O3	K2O	MgO	MnO	Na2O	SiO2/Al2O	Others
Raw HNTs	49.8	41.4	0.713	0.593	0.586	0.0995	2.35	0.21	1.20	Traces
Purified HNTs	52.4	40.7	0.174	0.521	0.482	0.105	2.09	0.27	1.29	Traces

Transmission electron microscopy (TEM) analysis (**Fig. 2**) reveals the tubular morphology of HNTs, clearly showing their hollow structure and internal architecture. As illustrated in Figure 2, the HNTs exhibit elongated, cylindrical shapes with open channels clearly visible at their ends. These observations are consistent with previously reported data on the morphology of HNTs [12]. The analyzed nanotubes show a length distribution ranging from 40 to 1300 nm, which falls within the typical range for natural halloysite (20–2000 nm) [12], [13]. Moreover, based on Gaussian distribution analysis, the external and internal diameters of the halloysite were estimated to be 35 ± 13 nm and 8 ± 3 nm, respectively.

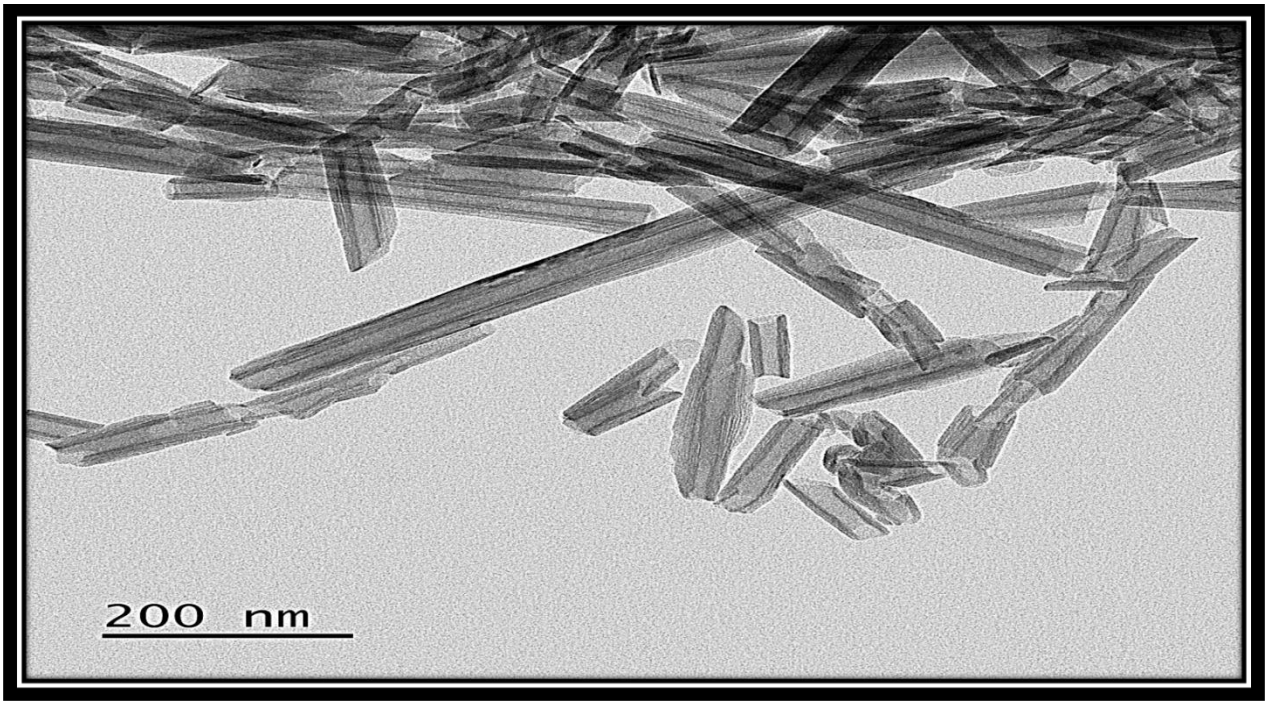


Figure III. 2: TEM images of halloysite at 200 nm magnitude.

The X-ray diffraction (XRD) pattern of HNTs is shown in **Fig. 3(a)** According to this diffractogram, the HNTs pattern exhibits characteristic diffraction peaks at 2θ angles of 12.25°, 20.24°, 24.97°, 35.27°, 36.19°, 55.31°, and 62.59°, corresponding to the Miller indices of the crystal planes: (001), (020), (002), (003), (200), (211), and (−3 1 1), respectively [3]. Crystalline phases of quartz, carbonate, alumina, and cristobalite are also observed in the HNTs sample, but only in trace amounts. The interplanar spacings d (001) = 0.723 nm and d (020) = 0.440 nm

are characteristic of the dehydrated phase of HNTs ($Al_2Si_2O_5$), which has a tubular morphology [14], [15].

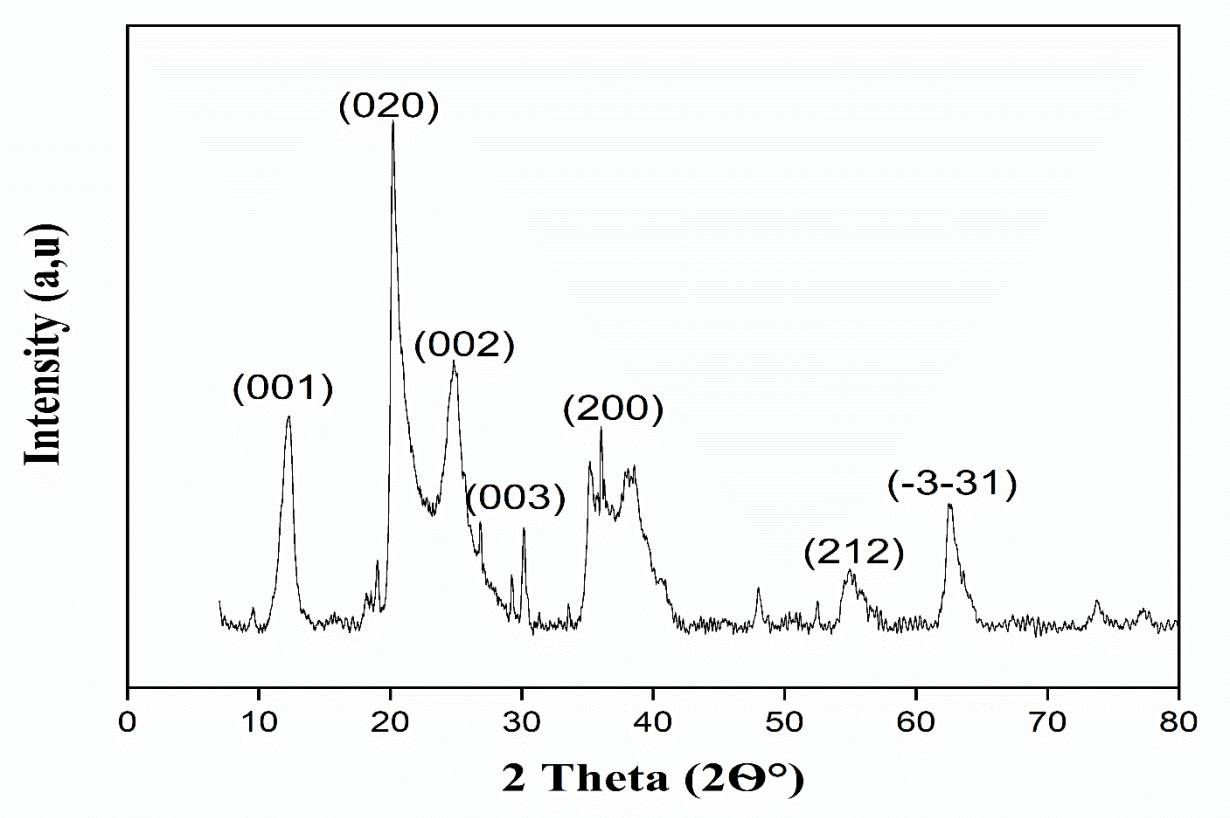


Figure III. 3: XRD pattern of HNTs.

FTIR (Fourier Transform Infrared) spectroscopy is a highly effective technique used for identifying and quantifying the functional groups (chemical bonds) present in a material. As shown and in **Fig. III.4** HNTs exhibit two primary peaks at 3697 and 3626 cm^{-1} representing the stretching vibrations of Al-OH in the lumen and the curled layer [16], respectively. The in-plane Si-O-Si bond typically appears around 1030 cm^{-1} [17], while Si-O and Al-O bonds are observed predominantly near 500 cm^{-1}[18] The stretching vibration at 3460 cm^{-1} is attributed to water located between the HNT layers. The band at 1640 cm^{-1} is associated with bending vibrations of adsorbed water [12].

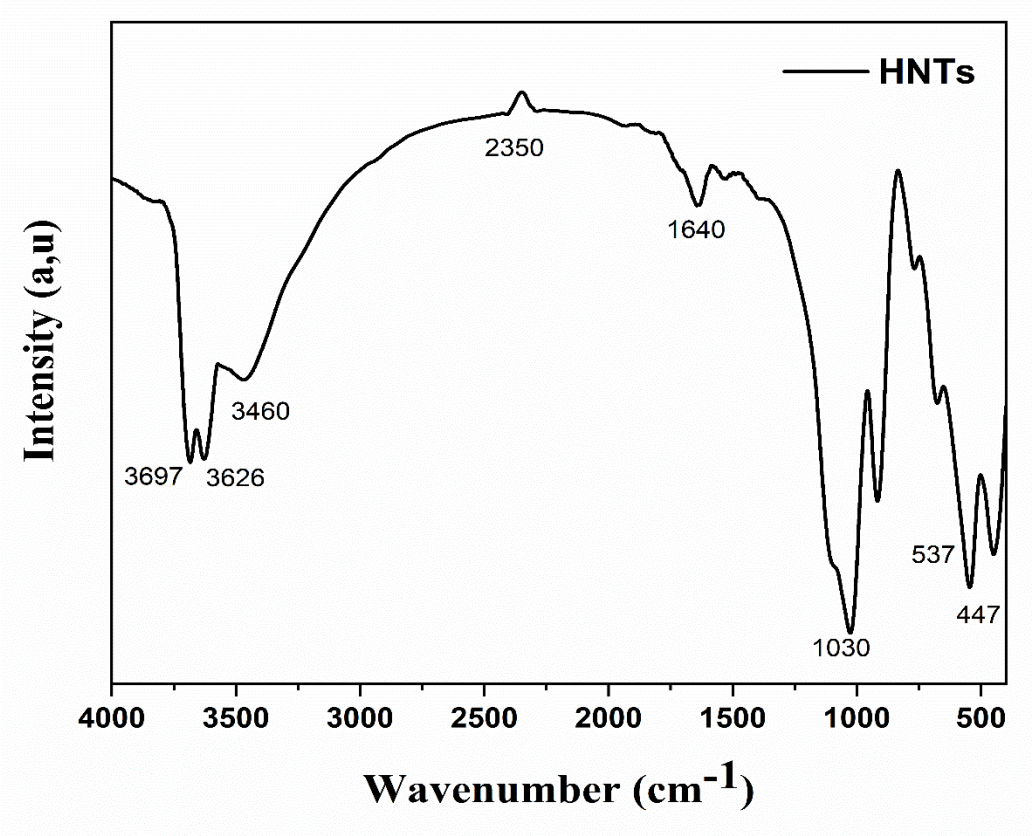


Figure III. 4: FTIR spectrum of HNTs.

The TGA analysis for HNTs in **Fig. III.5** showed two significant mass losses clearly observed. The first loss from ambient temperature to 200°C represents the departure of open water and weakly bound to compensatory cations, this loss represents 8% [18], [19]. The second loss from 200°C to 600°C represents water strongly linked to the structure (OH), this loss represents 13%. The differential thermal analysis, illustrated in the figure, highlights three distinct peaks: (i) an endothermic peak around 100°C, associated with the removal of hydration water, (ii) a second endothermic peak around 500°C corresponding to the structural water, OH [20]. (iii) a final exothermic peak near 800°C, attributed to the recrystallization of halloysite.

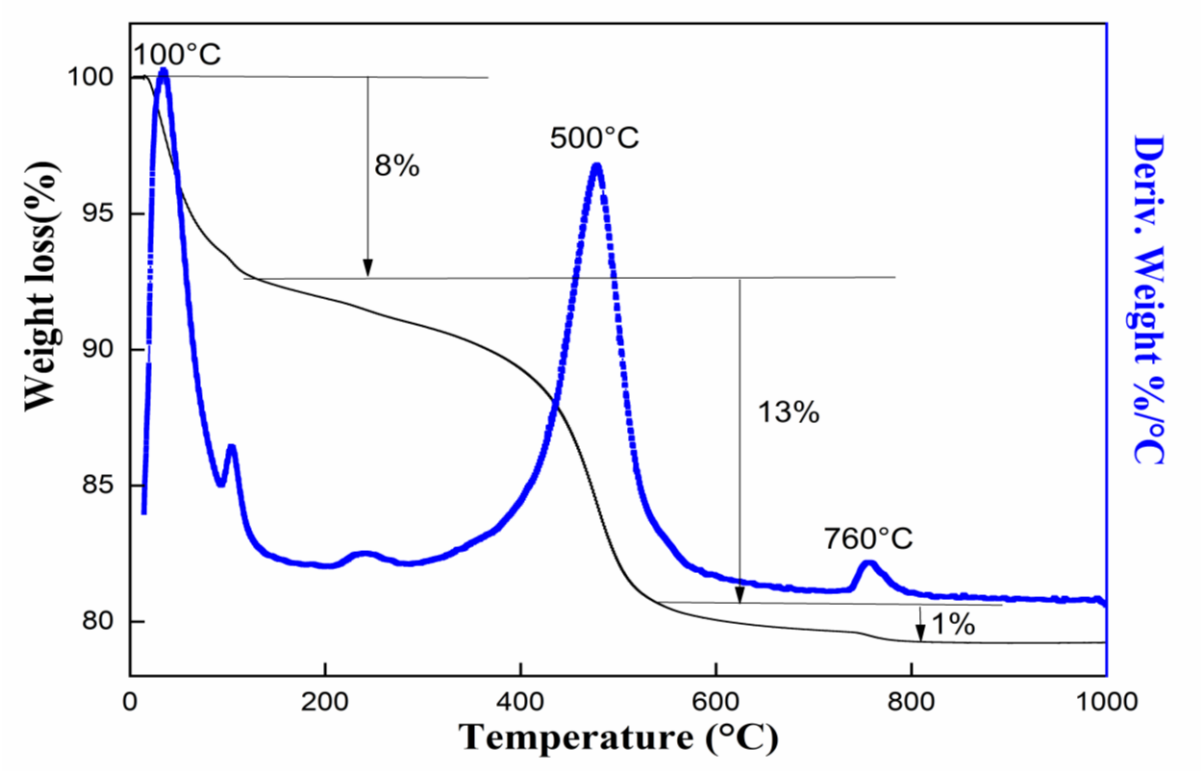


Figure III. 5: TGA /DTA curves of of HNTs.

Fig. III.6 presents the N_2 adsorption-desorption isotherm of Algerian halloysite, displaying characteristic type IV behavior (IUPAC classification) that confirms its mesoporous structure [20]. Quantitative analysis reveals the following textural properties: Specific surface area (BET) of 185.4 m^2/g, a total pore volume of 0.21 cm^3/g and average pore diameter of 11.5 nm. These parameters, falling within the IUPAC-defined mesoporous range (2-50 nm) [12] combined with the substantial surface area, demonstrate the material's strong potential as an effective adsorbent.

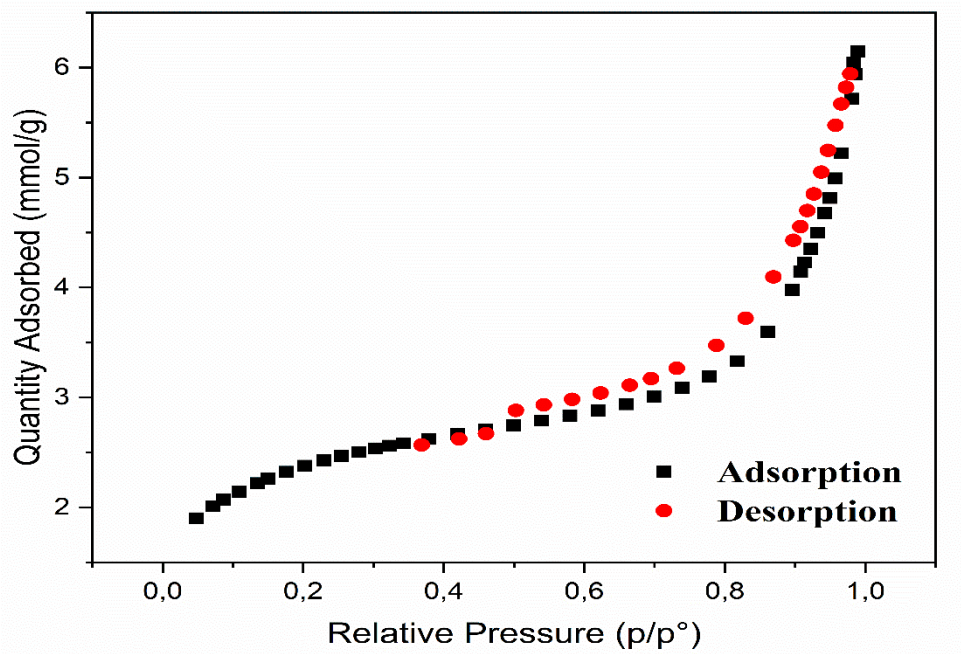


Figure III. 6: N2 adsorption/ desorption isotherms of HNTs.

5.2. Model validation

The BBD methodology was employed to plan 17 experimental runs, as detailed in **Table III.2**. Three key independent variables were investigated: Initial solution pH (Factor A), Adsorbent dosage (Factor B) and Initial solution concentration (Factor C). The BBD approach enabled systematic evaluation of both individual and interactive effects of these parameters on the adsorption capacity of HNTs (response variable) [21]. A second-order polynomial model was implemented to mathematically describe the relationship between the response and independent variables. The model's statistical significance was rigorously evaluated through analysis of variance (ANOVA) [22], with complete results presented in **Table III.4**.

Table III. 4: ANOVA results for the adsorption capacity of HAL.

Source	Sum of squares	df	Mean square	F-value	p-value
Model	3181.30	6	530.22	32.36	<0.0001
A-pH	749.18	1	749.18	45.72	<0.0001
B-W	1792.26	1	1792.26	109.39	<0.0001
C-C	293.98	1	293.98	17.94	0.0017
AB	191.73	1	191.73	11.70	0.0065
BC	16.07	1	16.07	0.9806	0.3454
B^2	138.09	1	138.09	8.43	0.0157
Residual	163.84	10	16.38		

Statistical analysis revealed model terms with probability values (Prob) below 0.0500 were considered statistically significant under the experimental conditions [23]. For the adsorption capacity (q), the significant terms were identified as main effects: A (pH), B (adsorbent dose), C (concentration), interaction effects: AB, BC and the quadratic effect B^2.

The remaining non-significant terms were excluded to enhance model robustness. The reduced quadratic model expressed in coded factors is presented below:

$$q = +32.10+9.68*A-14.97*B+6.06*C-6.92*AB+2.00*BC+5.71*B^2 \quad (12)$$

The sign convention in the regression model provides critical mechanistic insights: positive coefficients indicate synergistic interactions between factors, whereas negative coefficients denote antagonistic effects [24]. The statistical significance of these coefficients was rigorously evaluated using: Fisher's F-test to assess overall model significance and to compares model variance with residual variance, and Student's t-test to evaluates individual coefficient significance: Smaller p-values (< 0.05) confirm statistical relevance [25]. The combined interpretation of these tests follows established statistical principles where coefficient importance increases with higher absolute t-statistic magnitudes and lower corresponding p-values ($p < 0.05$ being statistically significant) [26]**.**

The p-value of 0.0001 ($p < 0.05$) for the regression model equation implies that the second-order polynomial modes fitted to the experimental results well [26]. In addition, a high R^2 -value is desirable and ensures a satisfactory adjustment of the model to the experimental data [23]. In present study, the R^2 values of 95.10% for adsorption capacity was adequately high and confirm the accuracy of the models [20]. Moreover, The Predicted R^2 of 76.58% is in reasonable agreement with the Adjusted R^2 of 92.16%.

The validity of the BBD model was additionally confirmed through graphical analysis, which involved evaluating the residual distribution patterns and assessing the correlation between experimentally observed values and model-predicted adsorption capacities for MB [2]. **Fig.7(a)**

presents the normal probability plot of residuals for the BBD model. The observed linear alignment of data points along the theoretical distribution line indicates that the residuals follow an ideal normal distribution and exhibit independence, thereby validating the model's assumptions [27]. The correlation between experimental measurements and model-predicted values for HNTs adsorption capacity is illustrated in **Fig. 7(b)**. The close alignment of data points along the 45° reference line demonstrates strong concordance between experimental observations and theoretical predictions, thereby validating the model's accuracy in simulating the adsorption process [28].

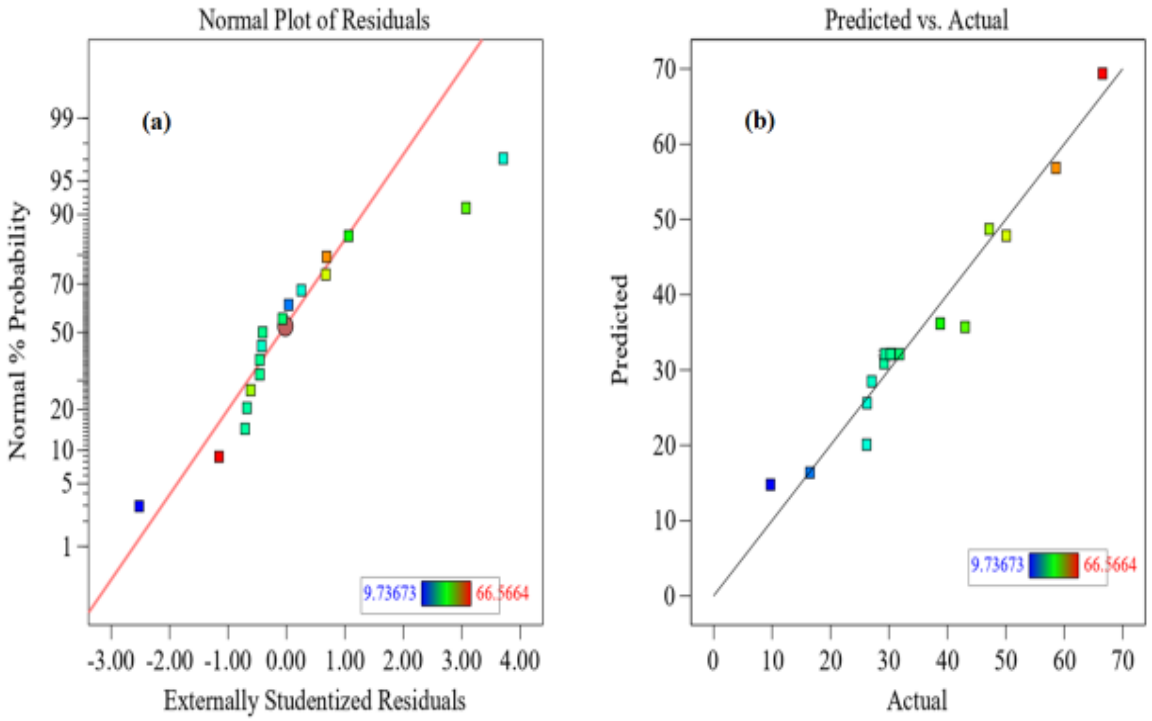


Figure III. 7: (a) Normal probability plot of residuals for Halloysite adsorption capacity, (b) plot of the relationship between the predicted and actual values of HNTs adsorption capacity.

5.3. Effect of process variables and interactions on the system performance

The adsorbent dosage (W) (**Fig. 8**) had the greatest effect on the chosen response, and we could easily observe that the adsorption capacity decreased from 73.43mg/g to 33.66mg/g by increasing the HNTs dosage. This could be justified by the existence of a relatively low concentration gradient between the bulk solution and the adsorbent surface after 24 h [29], which restricts the driving force for additional MB adsorption. In addition, the amount of

adsorbent used has the potential to influence the surface charge. Moreover, in the case of HNTs, which has a high concentration of nano clay, which makes it more likely to adsorb MB molecules, its surface area is large and has many vacant sites for adsorption [30]. Additionally, because of its negative charge, it has a greater propensity to attract cationic MB molecules (electrostatic attraction) [31].

The initial MB concentration (Factor C) exhibited a significant impact on adsorption performance, as evidenced in **Fig. 8**. This parameter plays a critical role in overcoming the mass transfer resistance between aqueous and solid phases. The adsorption capacity showed a positive correlation with increasing initial concentration, demonstrating enhanced uptake at higher MB concentrations [30], this increase was significant, and once the sites for adsorption are full, the response increases at a slow rate until it reaches the equilibrium [32].

The pH-dependent adsorption behavior of MB onto halloysite nanotubes (HNTs) is illustrated in **Fig. 8**, showing enhanced removal efficiency with increasing pH, this trend stems from the surface charge characteristics of Algerian HNTs, which exhibit a negative charge across a broad pH range (7.04-12), as evidenced in **Fig. 9**. The surface chemistry of HNTs plays a pivotal role, with the outer surface resembling SiO_2 (silica) and the inner lumen resembling Al_2O_3 (alumina) [33]. As pH increases, deprotonation of surface hydroxyl groups intensifies the negative charge on the HNT surface, thereby strengthening the electrostatic attraction between the negatively charged adsorption sites and positively charged MB cations (MB) [34]. This not only boosts adsorption capacity but also accelerates the kinetics, leading to faster attainment of equilibrium at higher pH conditions. The dual nature of HNTs surface chemistry, combining silica-like and alumina-like properties, contributes to their pH-responsive adsorption behavior, making them particularly effective for cationic dye removal under alkaline conditions [35].

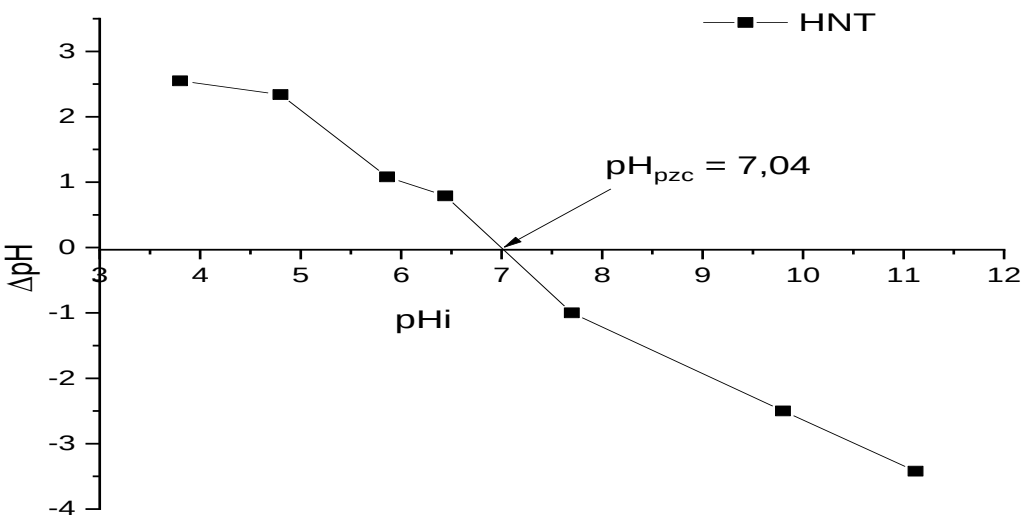


Figure III. 8: PHpzc of HNTs.

The three-dimensional response surfaces and corresponding contour plots (**Fig. 10**) graphically elucidate the optimal operational zones for maximal MB removal efficiency by HNTs. These surfaces were generated through regression modeling of the interactive effects between three critical parameters: (1) solution pH, (2) adsorbent dosage, and (3) initial MB concentration. The analysis reveals two statistically significant interaction terms: pH- adsorbent dosage (AB) and adsorbent dosage- initial concentration (BC). **Fig. 10** shows that reducing the adsorbent dose and increasing the solution pH improved the adsorption capacity of MB dye.

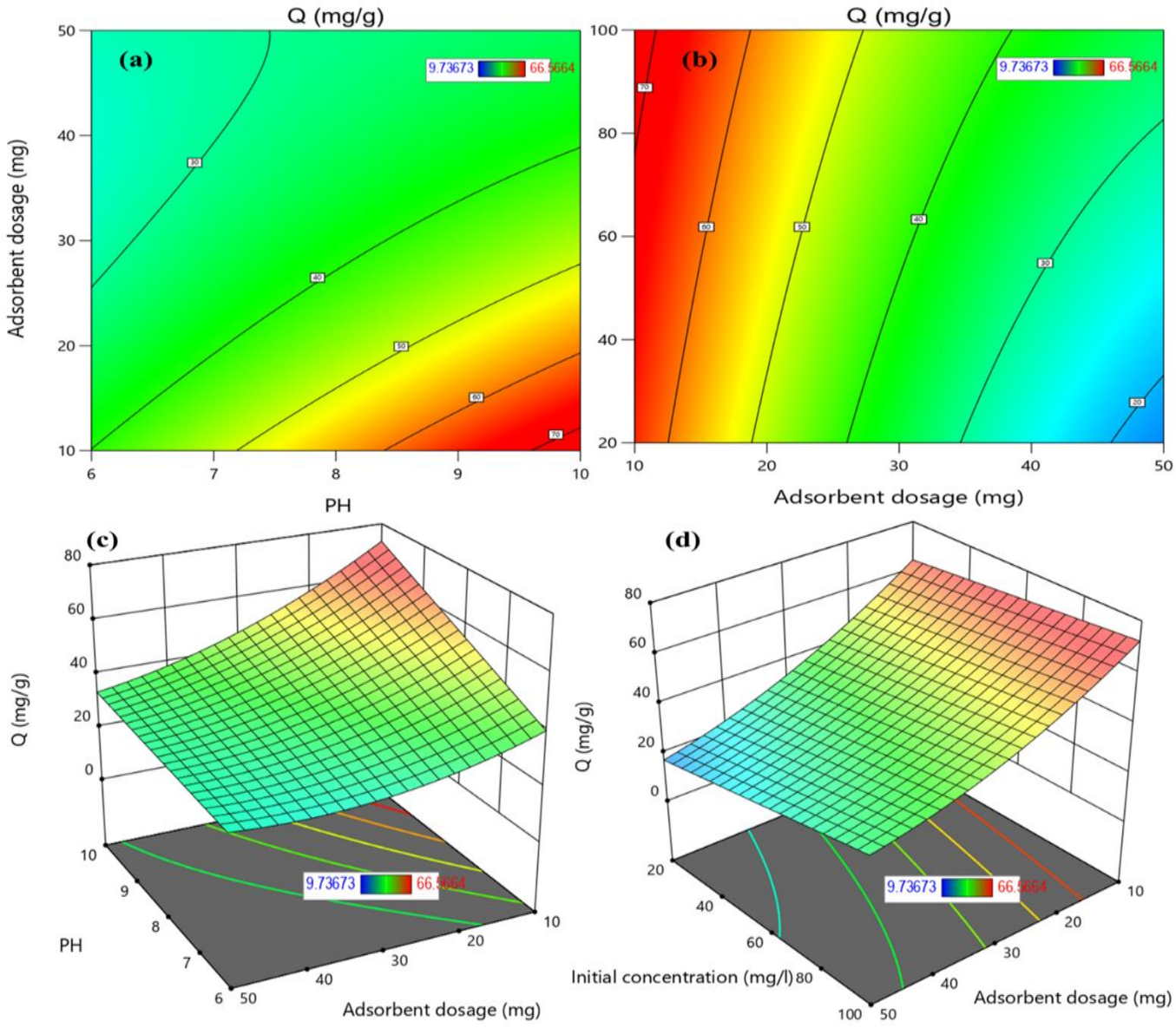


Figure III. 9: Contour and 3D surface plots for the interactive effects of (a, c), initial pH and adsorbent dosage (b, d), initial dye concentration and adsorbent dosage on the HNTs adsorption capacity.

5.4. Optimization

To determine the best conditions that would maximize the percentage of MB adsorption, the Design of Expert program utilized the numerical analysis method. The process optimization involved setting "in range" levels for adsorption variables and "maximize" for the response, which is the adsorption capacity. The program generated multiple solutions, and the solution with the highest desirability function was chosen as the optimized points that favor maximum

response [36]. The optimal values discovered by the program were as follows: 80 mg/L of Co, 9.96 of initial pH, and 10 mg of adsorbent dosage (**Fig. III.10)**. These conditions resulted in a maximum MB adsorption capacity of 71.01mg/g, Verification tests were conducted using the obtained optimum points to confirm the adequacy of the model. The results showed that the predicted value was very close to the experimental value in addition a desirability rate of 100% was reached. Therefore, RSM-BBD can be successfully employed to simulate MB adsorption onto HNTs.

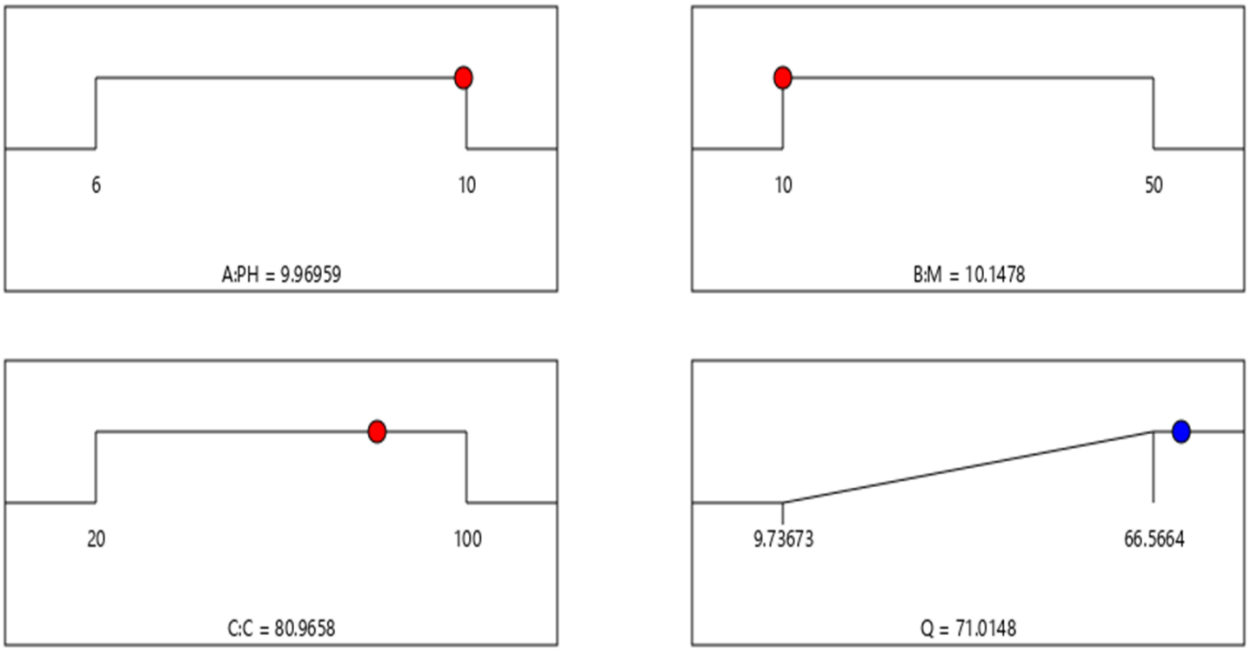


Figure III. 10: Optimized values for the process parameters.

5.5.Kinetic study

To elucidate the adsorption mechanism, the experimental data were analyzed using non-linear forms of the pseudo-first-order (PFO), pseudo-second-order (PSO) and intra particle diffusion (IPD) kinetic models. The applicability of each model was evaluated based on correlation coefficients (R^2) and agreement between calculated and experimental equilibrium adsorption capacities. For this study a volume of 50 ml of MB solution was used at a pH= 10 with concentrations: 10, 30, 100 mg/L. Agitation speed was kept constant at 120 rpm. The results of

this study are showed in **Fig. 12**, The non-linear forms of PFO, PSO and IPD models are given by the equations 13, 14 and 15 respectively [37].

$$qt = qe \times (1 - e^{-k_1 \times t}) \quad \text{.....(III.13)}$$

$$qt = \frac{k_2 \times q_e^2 \times t}{1 + k_2 \times q_e \times t} \quad \text{.....(III.14)}$$

$$qt = ki \times \sqrt{t} \quad \text{.....(III.15)}$$

Where q_e and q_t represents the amount of MB adsorbed by HNTs at equilibrium and at a time t, respectively. k_1 PFO rate constant (1/min), k_2 PSO rate constant (g/mg.min). ki is the intraparticle diffusion rate constant, which is related to the effective diffusivity of the solute inside the adsorbent pores (mg g^{-1} $min^{-1/2}$) and C (mg/g) is a constant that relies on the boundary layer effect and t is the time parameter (min) [38]. The kinetic parameters are mentioned in **table III. 5.** Accordingly, it was found that the PSO model is best suited for the adsorption of MB by HNTs when it comes of correlation coefficient R^2, which indicates the chemisorption nature of MB on HNTs surface [39]. Furthermore, the nonlinear nature of the curves, which do not intersect the origin across the entire concentration range, implies that intraparticle diffusion is not the dominant mechanism governing the adsorption kinetics [29], [40] Instead, the process is likely controlled by alternative rate-limiting steps.

Table III. 5: PFO and PSO models parameters for MB adsorption on HNTs at different concentrations (10, 30 and 100mg/l).

Concentration	q_{exp}	PFO			PSO			IPD		
mg/l	mg/g	q_{cal} mg/g	K_1 1/h	R^2	q_{cal} mg/g	K_2 g/mgh	R^2	K_{IPD}	C	R^2
10	21.41	22.15±0.6	0.055±0	0.963	26.49±1.8	0.002±7.7	0.928	2.14±0.32	2.79±2.3	0.777
30	41.24	39.37±0.9	0.078±0	0.960	44.54±0.7	0.002±2.3	0.991	3.51±0.38	9.15±2.7	0.872
100	84.22	86.89±2.24	0.039±0	0.981	106.76±4.7	0.0003±7.6	0.977	8.41±0.70	6.99±5.0	0.922

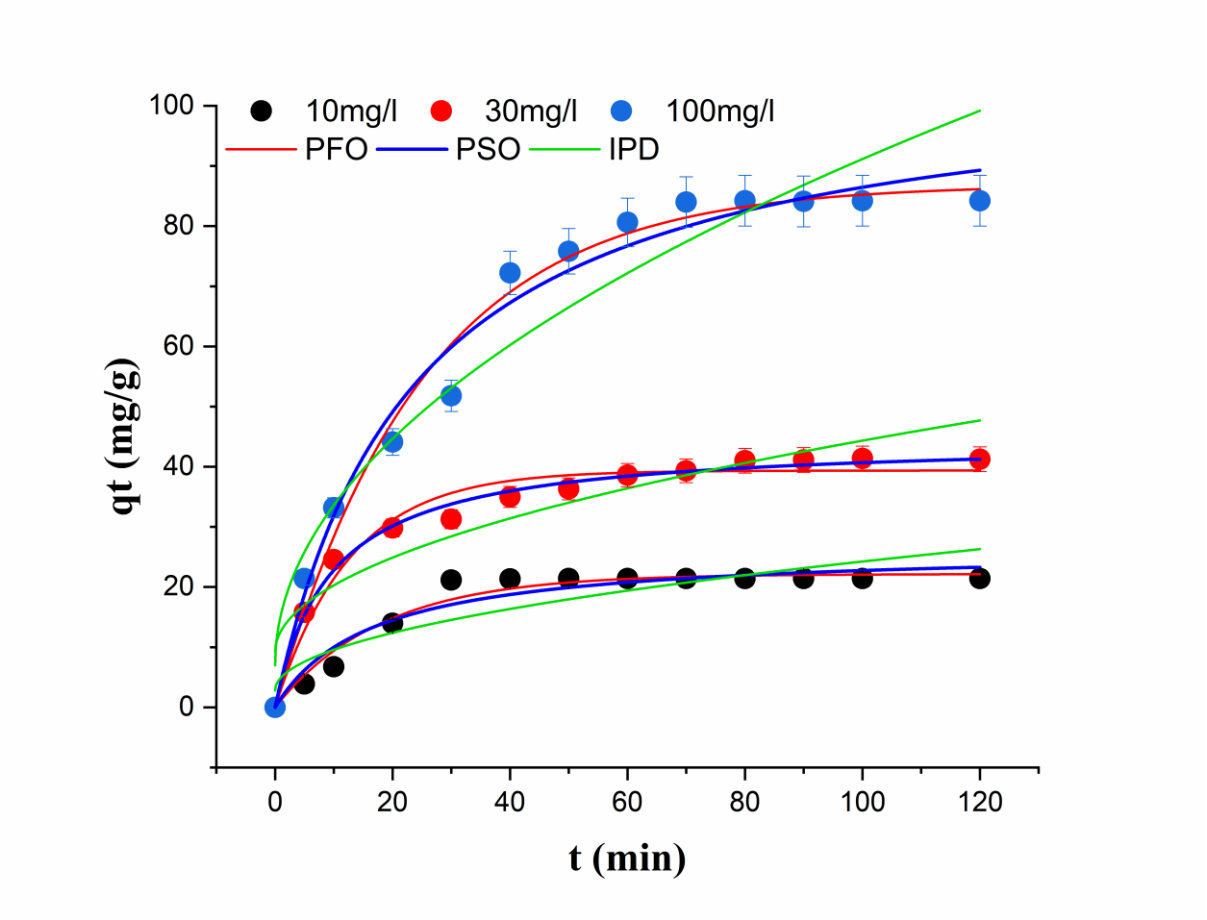


Figure III. 11: Nonlinear PFO, PSO and IPD kinetics models fits for MB adsorption on HNTs (C0=10, 30 and 100mg/l).

5.6.Isotherm study

The equilibrium adsorption isotherm study provides fundamental insights into the interaction mechanisms between MB and HNTs. To comprehensively evaluate the adsorption performance of raw Algerian HNTs for MB removal, four classical isotherm models were applied in their non-linear forms: (1) The Langmuir model, describing monolayer adsorption on homogeneous surfaces [41], (2) The Freundlich model, representing multilayer adsorption on heterogeneous surfaces [37], (3) The Sips model, combining features of both Langmuir and Freundlich isotherm [42], and (4) The Temkin model, accounting for adsorbate-adsorbate interaction [43]. These nonlinear models are given by equations (16 to 19) respectively [29].

$$q_e = \frac{q_m KCe}{1 + KCe} \quad \text{(III.16)}$$

$$q_e = kFC_e^{1/n} \quad \text{(III.17)}$$

$$q_t = \frac{q_e k_s C_e^{ns}}{1 + k_s C_e^{ns}} \quad \text{(III.18)}$$

$$q_e = \frac{RT}{b_{TM}} ln\, K_{TM}\, C_e \quad \text{(III.19)}$$

Where q_t is the amount of solute adsorbed (mg/g), q_e is the maximum adsorption capacity of the adsorbent (mg/g), Ce is the equilibrium concentration of the adsorbate (mg/L), k_s is the adsorption constant which is related to the energy of adsorption (L/mg) and n is an empirical constant that describe the shape of the adsorption isotherm, b_{TM} is the Temkin constant and K_{TM} (L/mg) is the equilibrium binding constant [41].

The adsorption isotherms of MB onto Algerian HNTs at a temperature of 25°C are depicted in **Fig. III. 12**. The experimental adsorption equilibrium data were analyzed using nonlinear regression analysis in Origin software, with the fitting parameters for the Langmuir, Freundlich, Sips, and Temkin isotherm models systematically summarized in **Table III.6.** Analysis of the fitting results indicates that Langmuir isotherm model shows superior agreement with the experimental MB adsorption data on the studied material, as evidenced by its higher determination coefficient ($R^2 = 0.963$) compared to other evaluated models. This optimal fitting indicates the homogenous adsorption process and provides insight into the spatial distribution of MB molecules on the HNTs surface. The maximum adsorbed amount obtained by the Langmuir model is 149.57 mg/g. To further understand the adsorption process R_L value was calculated and found that R_L value ($0.35 < R_L < 0.84$) indicates favorable adsorption of MB onto HNTs. The parameter n of the Freundlich model, known as the heterogeneity factor is used to determine the nature of adsorption, as $1/n < 1$ this indicates the chemisorption nature of process [40], and as Temkin constant $b_T > 0$ this indicates the endothermic nature of process [29].

5.7. Statistical physics

The Langmuir and Freundlich isotherms are commonly used to model adsorption, but they remain limited at the molecular level. As they do not take into account physicochemical parameters, they do not allow for precise estimation of the number of adsorbed molecules, interaction energy, or multilayer formation [44]. To better understand the adsorption of MB onto HNTs, a monolayer model inspired by Langmuir was used, incorporating the possibility of variable site interactions depending on temperature. The equations used to calculate the physicochemical parameters are given as follows [45]:

$$q = \frac{q_0}{1+\left(\frac{C_{1/2}}{C_e}\right)^n} = \frac{n.N_m}{1+\left(\frac{C_{1/2}}{C_e}\right)^n} \quad \text{(III.20)}$$

$$\Delta E = R * T * Ln\frac{Cs}{C1/2} \quad \text{(III.21)}$$

Where: q ($mg.g^{-1}$): adsorbed quantity. n: number of ions per site, N_m ($mg.g^{-1}$): sites receptor density, q_0 ($mg.g^{-1}$); adsorbed quantity at saturation, $C_{1/2}$($mg\ .L^{-1}$) : the concentration at half saturation, C_e ($mg.L^{-1}$) is the equilibrium dye concentration in the solution. Cs is the solubility of MB [46].

The effectiveness of the statistical physics model in fitting the experimental data is demonstrated in **Fig. III.12.** The corresponding parameter values are summarized and shown in **Table III.6**.

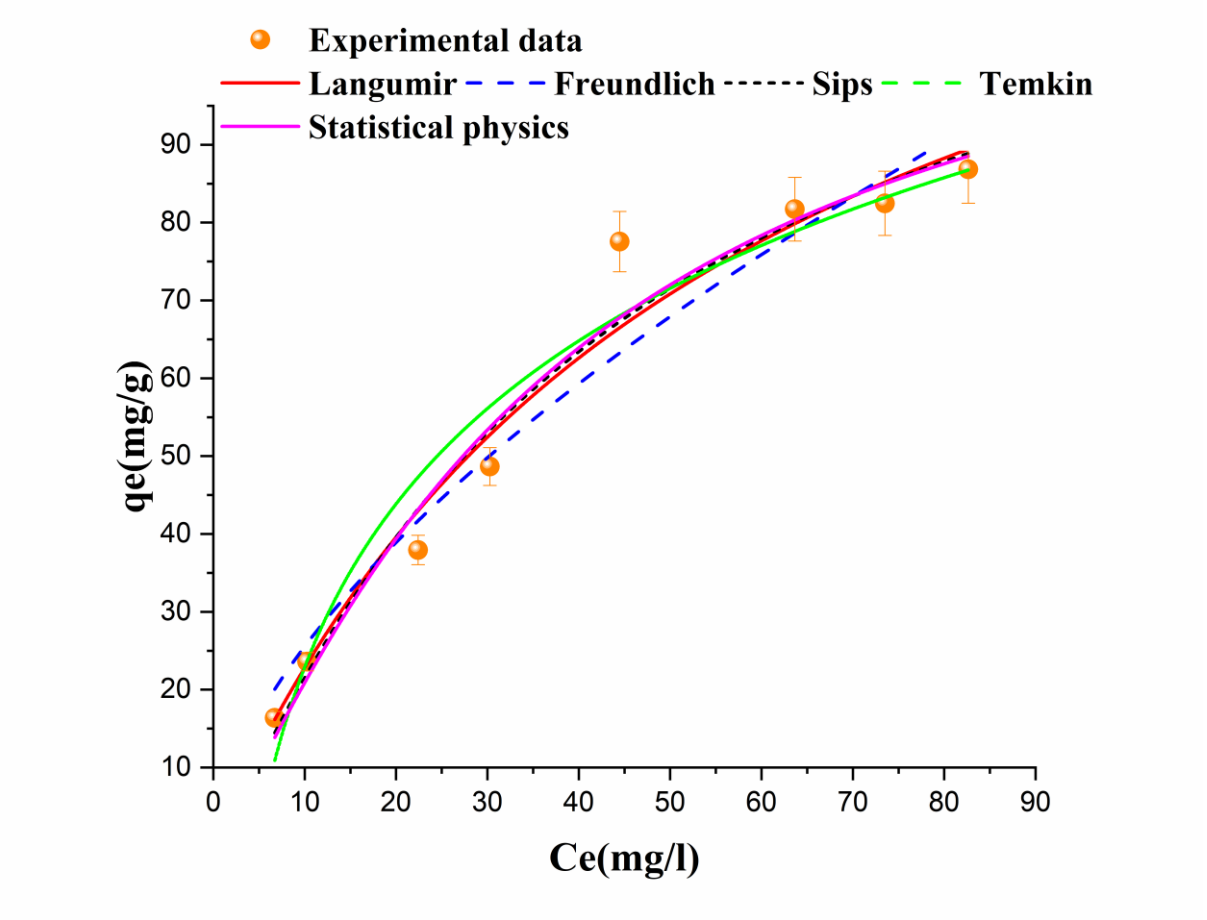


Figure III. 12: Langmuir, Freundlich, Sips, Temkin and Statistical physics non- linear fits to the experimental data of MB adsorption by HNTs at 298 K (pH=10, m=10mg, V=30ml).

Table III. 6: Parameters of the langumir, Freundlich, Sips, and Temkin isotherms and statistical physics models for MB adsorption on HNTs at 298K.

Adsorption isotherm	Parameter	Value ± SE
Langmuir	q_m (mg/g)	149.57±21.34
	K_L (l/mg)	0.0179±0.005
	R^2	0.963
Freundlich	Kf (mg/g (L/mg)	6.297±1.9
	1/n	0.608±0.2
	R^2	0.941
Sips	q_m (mg/g)	136.68±32.0
	K_S (L/mg)	0.029±0.03
	n	1.24±0.73
	R^2	0.957

Temkin	K_T (L/mg)	0.213±0.04
	b_T (J/mol)	80.58±2.76
	R^2	0.944
Statistical physics	n	1.2±0.34
	N_m (mg/g)	101.44±56.95
	$C_{1/2}$ (mg/l)	37.07±20.19
	R^2	0.959

The experimental data show a good fit with the model (R^2 = 0.958), with n = 1.2, indicating a non-parallel orientation of MB molecules and multiple adsorptions per site, in contrast to the classical Langmuir model.

The calculated maximum adsorption capacity is 121.73 mg/g, and the half-saturation concentration is 37.07 mg/L.

The obtained adsorption energy (ΔE = 1.981 kJ/mol) suggests an endothermic process, supporting the idea of specific interactions between MB and the surface of HNTs [47].

5.8. Quantum chemical calculations

Methylene Blue (MB) was used in this work as an adsorption target, for that deep quantum study was effectuated. **Fig. III.13(a)** depicts the optimized molecular structure of MB, showing an almost planar geometry containing carbon atoms in grey, nitrogen in blue, sulfur in yellow, and hydrogen in white, the molecule has an estimated surface area of about 130 $Å^2$ [48].

The **Fig. III.13(b)** shows the total electron density surfaces mapped with electrostatic potential characteristic of the MB molecule, the negative surfaces are related to high electron densities and depicted by red and yellow colours. These surfaces are mainly located around oxygen, nitrogen, and sulfur atoms, and are favourable targets for nucleophile interactions, giving a highest negative potential of $-5.31*10^{-2}$V. In return, the surfaces depicted by blue colour is

located around hydrogen atoms and methyl groups, these regions are related to a loss of the electron density and are favourable targets for electrophile interactions.

Furthermore, the **Fig. III.13(c and d)** illustrates the FMOs and the corresponding gap energy, it can be seen that the HOMO is almost extended on the entire of MB-molecular except the hydrogen atoms and methyl groups; the LUMO is also extended on a large zone of the molecule, except the sulfur, and central nitrogen and some hydrogen atoms. These covered regions may participates in electron exchange with the external medium, regarding the computed energies, E_{HOMO}=-5.218eV and E_{LUMO}=-2.221eV, the low absolute value of E_{LUMO} indicates that the MB is more acceptor than donor, these finding may predict the formation of chemisorption of MB molecules onto the HNTs surface.

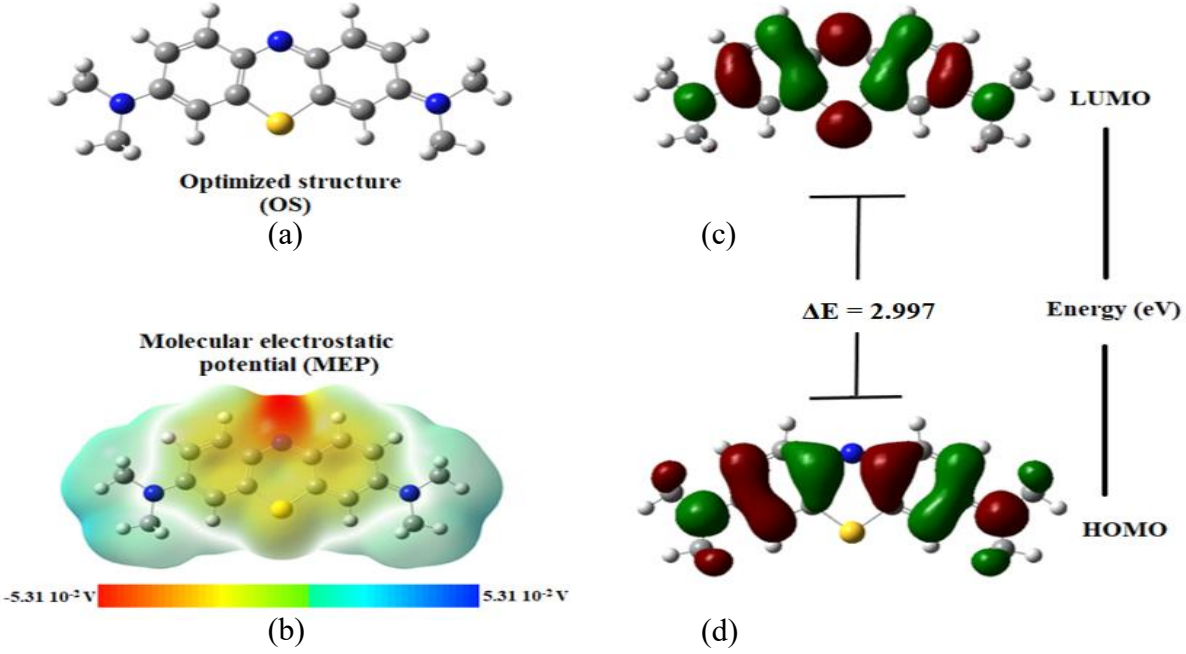


Figure III. 13: (a) optimized molecular structure, (b) total electron density surfaces mapped with electrostatic potential (MEP), (d) Lowest Unoccupied Molecular Orbital (LUMO), and (c) Highest Occupied Molecular Orbital (HOMO) of the molecule (MB), calculated conside.

Moreover, GQCDs are parameters derived from FMOs energies (**Table III.7**), providing insights into a molecule's electronic structure and properties, enabling the correlation of the

molecular structure with properties like reactivity, stability, and the prediction of adsorption performance.

The smaller ΔE_{Gap}=2.997eV of MB molecule suggests its reactivity, which may promotes the charge transfer with HNTs surface, this suggestion is more explained by the high negative value of the chemical potential μ=-3.720eV, high electronegativity χ=3.720eV and negative back-donation energy= -3.740eV [49], confirming that MB have tendency to accept electron from external medium as HNTs adsorbent [50]. In addition, the global hardness of a molecule reveals its resistance to deformation or polarization under perturbations in chemical process as adsorption, and inversely for the softness, the values of these parameters for MB-molecule are: η =1.498 and σ=0.667 respectively, that are moderately low and high respectively. Illustrating the low resistance to deformation and/or polarization when adsorbed on HNTs surface [51]. The electrophilicity index (ω=4.616eV) reflects the strong electrophilic character of MB, this make it ideal for adsorption on electrons rich, and polar surfaces as HNTs, reinforcing the electrostatic and π-π interactions [52]. On the other hand, the dipole moment is a measure of polarity of MB, its high value μ_0=3.719Debey suggest the implication of dipolar interactions in the adsorption mechanism, and reinforce the physi-sorption of MB on HNTs surface.

Table III. 7: Quantum Chemical Parameters of MB as Computed at the B3LYP/6-311+G(d,p) Level of Theory in Aqueous Solution.

		MB
Total energy	E_0	-32191.265
Energy of highest occupied molecular orbital (eV)	E_H	-5.218
Energy of lowest occupied molecular orbital (eV)	E_L	-2.221
Energy gap (eV)	ΔE	2.997
Dipole moments (debye)	μ	3.719
Global hardness (eV)	η	1.498
The back-donation energy	ΔE_{b-d}	-0.374
Absolute electronegativity (eV)	χ	3.719

Electrophilicity index (eV)	ω	4.616
Global softness (eV^{-1})	σ	0.667

5.9.MD simulations

We shed light in **Fig. III.14** on the structure of kaolinite, which is a 1:1 layered silicate structure generated by the connection of one silicon-oxygen tetrahedron and one aluminum-oxide polyhedron via a common vertex, O. Each layer consists of a six-atom sub-layer of H-O-Al-O-Si-O, with hydrogen bonds primarily linking the structural units [53], [54]. Due to these typical structure, a cleavage in (0 0 -1) direction of kaolinite gives aluminum-hydroxyl and silico-oxygen moieties in external planes [7].

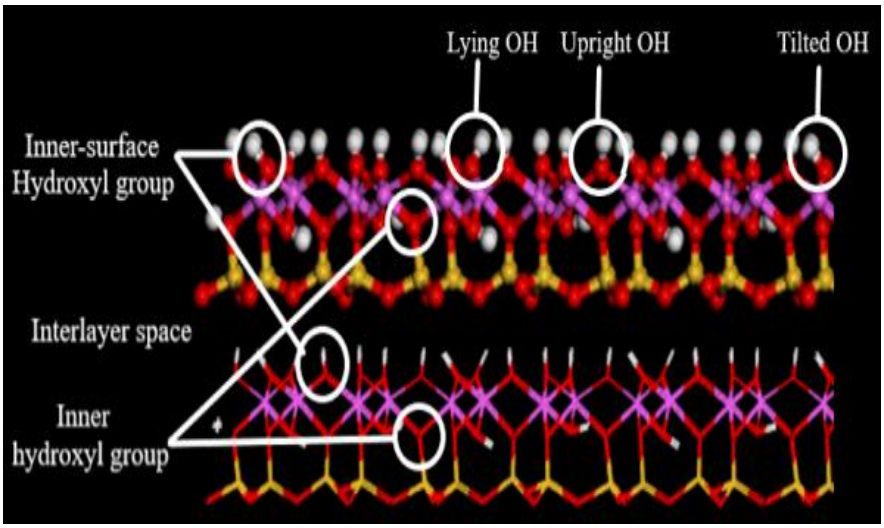


Figure III. 14: Side view of the atomic structure of kaolinite crystal. Hydrogen is white, oxygen is red, aluminum is purple, and silicon is yellow.

To investigate the complex interactions between MB and the HNTs surfaces, the MD simulations provide a detailed analysis of binding behaviour and dynamic molecular processes. This approach facilitates a deeper understanding of the adsorption mechanisms governing MB attachment to clay substrates. The adsorption energies listed in **Table III.8**are negative, signifying the spontaneity of the adsorption process. Additionally, the deformation energy suggests that MB adsorption induces conformational rearrangement, leading to decreased

stability of both MB molecule and the HNTs surface. While, the adsorption rigid is the free energy (-38,183 kcal/mol) when the not-relaxed MB molecule is adsorbed on the HNTs surface before geometry adjustment [55]. The output energy values reveal that the adsorption process is just composed by a rigid adsorption and deformation at the interfacial zone, verifying the following formula:

$$E_{adsorption} = E_{rigid\text{-}adsorption} + E_{deformation}$$

Table III. 8: Calculated energies for the adsorption of the BM molecule on the HNT surface.

Adsorption energy (kcal/mol)	Rigid adsorption energy (kcal/mol)	Deformation energy (kcal/mol)
-98,419	-38,183	-60,236

Fig. III.15 illustrates the most equilibrium configuration of MB molecules onto HNTs surface. Specifically, the MB molecule tends to adsorb in longitudinal manner on HNTs surface, the almost planar deposition facilitates the formation of van der Waals interactions with the kaolinite siloxane surface [56]. Moreover, chemical adsorption may occur due to electron interactions involving sulfur, nitrogen, and oxygen atoms. Additionally, the longitudinal deposit of the MB's aromatic rings suggest the presence of π-cation interaction with the siloxane surface, as revealed by GQCD.

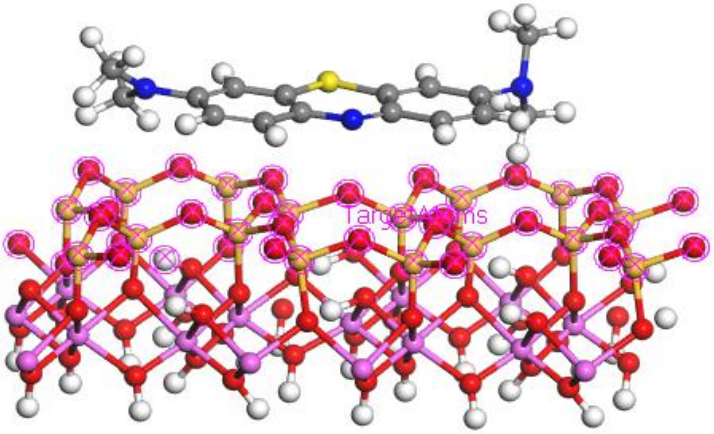


Figure III. 15: Side view of the most equilibrium configuration of MB adsorption onto HNTs surface.

5.10. Proposal of an adsorption mechanism

The adsorption mechanism of MB onto HNTs involves a synergy of physicochemical interactions, governed by the ionic nature of the dye and the surface chemistry of the material. In aqueous solution, MB, being cationic in nature, primarily interacts via electrostatic attraction with the outer surface of the HNTs, which is rich in siloxane groups (Si–O^-) that confer a negative charge [57]. This interaction is strongly influenced by the pH of the solution, with higher pH values promoting increased negative charge and, consequently, more effective adsorption [58]. Additionally, hydrogen bonds may form between the amine groups of MB (–NH_2) and surface hydroxyls (–OH), especially those present on the aluminous inner surface (Al–OH) or at the edges of the layers [59]. These interactions help stabilize the attachment of the dye to the tubular structure. Furthermore, the presence of aromatic rings in the structure of MB promotes π–π interactions, particularly with electron-rich regions on the HNT surface, such as defects or heterogeneous sites [60]. A diagram illustrating the interaction mechanism of MB on the surface of halloysite nanotubes is attached (**Fig. III.16**).

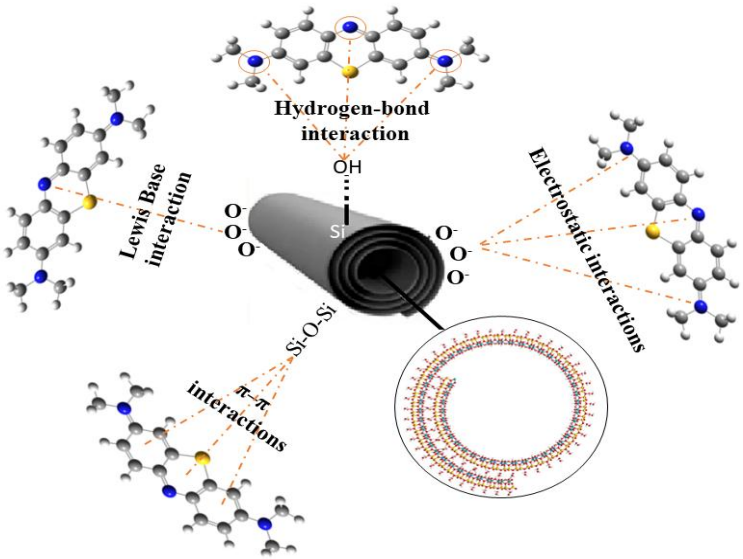


Figure III. 16: Illustration of the possible interaction between HNTs and MB dye.

5.11. Adsorbent efficiency

Table III.9 presents the adsorption capacities of halloysite-based adsorbents and Algerian halloysite. Indeed, raw Algerian HNTs shows a very good capacity to adsorb MB, comparable to or even higher than that of modified clays. This performance is achieved without any chemical or thermal treatment, thanks to its natural properties (large surface area, porous structure, silica and alumina composition). This makes it a promising, efficient, and cost-effective material for practical applications.

Table III. 9: Adsorption capacities for MB by different clay adsorbents

Clay Sample	Q_{max} (mg/g)	Reference
Algerian raw Halloysite	149.57	**This study**
Halloysite (Dunino cave)	47.46	
Raw Kaolin (Silonijan, India)	13.99	
Kaolin (Silonijan, India) treated with NaOH	16.34	[39]
C-HNTs	103.63	[4]
TMG	147.71	[61]
Bentonite	65,36	[40]

Reference of chapter III:

[1] E. Igberase et I. Mkhize, « Adsorptive Removal of Methylene Blue (MB) from Wastewater: A Comparative Modeling Study Utilizing RSM, ANN, and ANFIS Model », *Eng. Chem.*, vol. 9, p. 85-92, 2025.

[2] A. I. Boulahbal *et al.*, « Enhancing adsorptive performance of Cu-Al layered double hydroxides from aluminum saline slags: Insights from response surface methodology and molecular dynamic simulation », *Miner. Eng.*, vol. 219, p. 109067, 2024.

[3] M. J. Frisch *et al.*, « Gaussian 09 Revision A.1. Gaussian Inc », janv. 2009.

[4] A. D. Becke, « Density-functional thermochemistry. III. The role of exact exchange », *J. Chem. Phys.*, vol. 98, nº 7, p. 5648-5652, 1993.

[5] Á. Kuki, L. Nagy, M. Zsuga, et S. Kéki, « Fast identification of phthalic acid esters in poly(vinyl chloride) samples by Direct Analysis In Real Time (DART) tandem mass spectrometry », *Int. J. Mass Spectrom.*, vol. 303, nº 2, p. 225-228, juin 2011, doi: 10.1016/j.ijms.2011.02.011.

[6] Y.-C. Lan, S. Kamal, C.-C. Lin, Y.-H. Liu, et K.-L. Lu, *Ultra-Thin Zr-MOF/PVA/Melamine Composites with Remarkable Sound Attenuation Effects*. 2022. doi: 10.21203/rs.3.rs-2257532/v1.

[7] R. Šolc, M. H. Gerzabek, H. Lischka, et D. Tunega, « Wettability of kaolinite (001) surfaces — Molecular dynamic study », *Geoderma*, vol. 169, p. 47-54, déc. 2011, doi: 10.1016/j.geoderma.2011.02.004.

[8] « Molecular Dynamics Simulation of Nanocomposites using BIOVIA Materials Studio, Lammps and Gromacs - 2nd Edition | Elsevier Shop ». Consulté le: 24 décembre 2025. [En ligne]. Disponible sur: https://shop.elsevier.com/books/molecular-dynamics-simulation-of-nanocomposites-using-biovia-materials-studio-lammps-and-gromacs/sharma/978-0-443-26704-8

[9] B. H. Hameed et A. A. Ahmad, « Batch adsorption of methylene blue from aqueous solution by garlic peel, an agricultural waste biomass », *J. Hazard. Mater.*, vol. 164, nº 2-3, p. 870-875, mai 2009, doi: 10.1016/j.jhazmat.2008.08.084.

[10] C. Giovannoli, C. Passini, G. Volpi, F. Di Nardo, L. Anfossi, et C. Baggiani, « Peptide-based affinity media for solid-phase extraction of ochratoxin A from wine samples: Effect of the solid support on binding properties », *Talanta*, vol. 144, p. 496-501, 2015.

[11] M. Gackowski, K. Tarach, Ł. Kuterasiński, J. Podobiński, B. Sulikowski, et J. Datka, « Spectroscopic IR and NMR studies of hierarchical zeolites obtained by desilication of zeolite Y: Optimization of the desilication route », *Microporous Mesoporous Mater.*, vol. 281, p. 134-141, 2019.

[12] C. Ferlito *et al.*, « Influence of Halloysite Nanotubes from different deposits on the degradation of organic molecules », *Ceram. Int.*, 2025.

[13] A. Hayoune, H. Akkari, T. Mekhalif, et F. Martin, « Sono-assisted adsorption of methylene blue dye from aqueous medium using magnetic Algerian Halloysite clay (Fe3O4-HKDD3) », *Int. J. Environ. Anal. Chem.*, vol. 104, nº 2, p. 424-438, 2024.

[14] M. T. Aytekin et H. L. Hoşgün, « Characterization studies of heat-treated halloysite nanotubes », *Chem. Pap.*, vol. 74, nº 12, p. 4547-4557, 2020.

[15] X. Jiang *et al.*, « Structural characteristics, surface properties and methylene blue adsorption application of halloysite nanotubes regulated with controllable treatment processes », *Int. J. Miner. Metall. Mater.*, vol. 32, nº 6, p. 1331-1344, 2025.

[16] R. Liu, K. Fu, B. Zhang, D. Mei, H. Zhang, et J. Liu, « Removal of methyl orange by modified halloysite nanotubes », *J. Dispers. Sci. Technol.*, vol. 33, nº 5, p. 711-718, 2012.

[17] T. Altun et H. Ecevit, « Adsorption of malachite green and methyl violet 2B by halloysite nanotube: Batch adsorption experiments and Box-Behnken experimental design », *Mater. Chem. Phys.*, vol. 291, p. 126612, 2022.

[18] S. Mellouk *et al.*, « Intercalation of halloysite from Djebel Debagh (Algeria) and adsorption of copper ions », *Appl. Clay Sci.*, vol. 44, nº 3-4, p. 230-236, 2009.

[19] S. Sahnoun, M. Boutahala, H. Zaghouane-Boudiaf, et L. Zerroual, « Trichlorophenol removal from aqueous solutions by modified halloysite: kinetic and equilibrium studies », *Desalination Water Treat.*, vol. 57, nº 34, p. 15941-15951, 2016.

[20] A.-T. Mohammad, A. S. Abdulhameed, et A. H. Jawad, « Box-Behnken design to optimize the synthesis of new crosslinked chitosan-glyoxal/TiO2 nanocomposite: methyl orange adsorption and mechanism studies », *Int. J. Biol. Macromol.*, vol. 129, p. 98-109, 2019.

[21] C. Nayak, B. Babu, V. Manoj, C. V. Raghunath, M. L. D. Bhatlu, et P. Pandey, « Optimization of process parameters by RSM-BBD for the removal of titan yellow dye from aqueous solution by acid-treated Phyllanthus acidus leaves », *Biomass Convers. Biorefinery*, vol. 14, nº 18, p. 23125-23141, 2024.

[22] N. Fettah *et al.*, « Application of response surface methodology to optimise the Metronidazole antibiotic removal by a developing Bio-Electro-Fenton process », *Int. J. Environ. Anal. Chem.*, p. 1-22, 2025.

[23] S. S. Moghaddam, M. A. Moghaddam, et M. Arami, « Response surface optimization of acid red 119 dye from simulated wastewater using Al based waterworks sludge and polyaluminium chloride as coagulant », *J. Environ. Manage.*, vol. 92, nº 4, p. 1284-1291, 2011.

[24] F. B. Shahri et A. Niazi, « Synthesis of modified maghemite nanoparticles and its application for removal of acridine orange from aqueous solutions by using Box-Behnken design », *J. Magn. Magn. Mater.*, vol. 396, p. 318-326, 2015.

[25] D. Aurelio-Soria *et al.*, « Response surface methodology for capillary electrochromatography and sample stacking in the analysis of food additive residues in environmental water samples », *Int. J. Environ. Anal. Chem.*, p. 1-18, 2025.

[26] R. Subramaniam et S. K. Ponnusamy, « Novel adsorbent from agricultural waste (cashew NUT shell) for methylene blue dye removal: Optimization by response surface methodology », *Water Resour. Ind.*, vol. 11, p. 64-70, 2015.

[27] A. S. Abdulhameed, R. H. Al Omari, M. Abualhaija, et S. Algburi, « Chitosan/modified sidr (Ziziphus spina-christi) tree leaves biocomposite for removal of methylene blue dye: characterization, adsorption optimization, isotherms, and kinetics », *Biomass Convers. Biorefinery*, vol. 15, nº 10, p. 15747-15761, 2025.

[28] N. N. Abd Malek, A. H. Jawad, A. S. Abdulhameed, K. Ismail, et B. Hameed, « New magnetic Schiff's base-chitosan-glyoxal/fly ash/Fe3O4 biocomposite for the removal of anionic azo dye: an optimized process », *Int. J. Biol. Macromol.*, vol. 146, p. 530-539, 2020.

[29] H. Chaima *et al.*, « Adsorptive removal of cationic dye from aqueous solutions using activated carbon prepared from *Crataegus monogyna*/sodium alginate/polyaniline composite beads: Experimental study and molecular dynamic simulation », *J. Mol. Liq.*, vol. 408, p. 125372, août 2024, doi: 10.1016/j.molliq.2024.125372.

[30] F. Batana, M. Taouti, et A. Guibadj, « Cinétique de l'adsorption du bleu de méthylène sur bentonite brute et traitée », *Algerian J. Environ. Sci. Technol.*, vol. 5, nº 4, 2019.

[31] M. Zhao et P. Liu, « Adsorption behavior of methylene blue on halloysite nanotubes », *Microporous Mesoporous Mater.*, vol. 112, nº 1-3, p. 419-424, 2008.

[32] D. Ghosh et K. G. Bhattacharyya, « Adsorption of methylene blue on kaolinite », *Appl. Clay Sci.*, vol. 20, nº 6, p. 295-300, 2002.

[33] I. Anastopoulos et G. Z. Kyzas, « Agricultural peels for dye adsorption: A review of recent literature », *J. Mol. Liq.*, vol. 200, p. 381-389, déc. 2014, doi: 10.1016/j.molliq.2014.11.006.

[34] N. Boukhalfa, M. Boutahala, N. Djebri, et A. Idris, « Kinetics, thermodynamics, equilibrium isotherms, and reusability studies of cationic dye adsorption by magnetic alginate/oxidized multiwalled carbon nanotubes composites », *Int. J. Biol. Macromol.*, vol. 123, p. 539-548, 2019.

[35] M. Radjai *et al.*, « Adsorptive removal of cationic and anionic dyes on a novel mesoporous adsorbent prepared from diatomite and anionic cellulose nanofibrils: Experimental and theoretical investigations », *J. Mol. Liq.*, vol. 361, p. 119670, sept. 2022, doi: 10.1016/j.molliq.2022.119670.

[36] N. Slougui, M. Slama, Y. Boudaoud, et A. S. Bendrihem, « Optimization of GC-MS Method for Analysis of Basil Essential Oils from Algeria: Design of Experiments and Exploratory Pattern Recognition », *J. Chem.*, vol. 2022, nº 1, p. 5880539, 2022.

[37] J. Wang et X. Guo, « Adsorption kinetic models: Physical meanings, applications, and solving methods », *J. Hazard. Mater.*, vol. 390, p. 122156, 2020.

[38] J. Kikuvi, G. Mutua, R. O. Gembo, et F. Orata, « Kinetic, isothermal and thermodynamic study on the adsorptive removal of chloramphenicol from water by iron-impregnated Kenyan clinoptilolite zeolite », *React. Kinet. Mech. Catal.*, p. 1-23, 2025.

[39] M. Musah, Y. Azeh, J. Mathew, M. Umar, Z. Abdulhamid, et A. Muhammad, « Adsorption kinetics and isotherm models: a review », *Caliphate J. Sci. Technol.*, vol. 4, nº 1, p. 20-26, 2022.

[40] A. Benhouria, H. Zaghouane-Boudiaf, R. Bourzami, F. Djerboua, B. Hameed, et M. Boutahala, « Cross-linked chitosan-epichlorohydrin/bentonite composite for reactive orange 16 dye removal: Experimental study and molecular dynamic simulation », *Int. J. Biol. Macromol.*, vol. 242, p. 124786, 2023.

[41] M. A. Al-Ghouti et D. A. Da'ana, « Guidelines for the use and interpretation of adsorption isotherm models: A review », *J. Hazard. Mater.*, vol. 393, p. 122383, 2020.

[42] B. Faouzia *et al.*, « Sustainable biomass-derived activated biochar/polyaniline/alginate composite beads for enhanced methylene blue adsorption: Experimental and theoretical investigations », *Int. J. Biol. Macromol.*, vol. 305, p. 141338, 2025.

[43] N. Ayawei, A. N. Ebelegi, et D. Wankasi, « Modelling and interpretation of adsorption isotherms », *J. Chem.*, vol. 2017, nº 1, p. 3039817, 2017.

[44] O. Amrhar, L. El Gana, et M. Mobarak, « Calculation of adsorption isotherms by statistical physics models: a review », *Environ. Chem. Lett.*, vol. 19, nº 6, p. 4519-4547, déc. 2021, doi: 10.1007/s10311-021-01279-8.

[45] C. Djama, D. Chebli, A. Bouguettoucha, I. Doudou, et A. Amrane, « Statistical physics modelling of azo dyes biosorption onto modified powder of Acorus calamus in batch reactor », *Biomass Convers. Biorefinery*, vol. 13, nº 2, p. 1013-1028, janv. 2023, doi: 10.1007/s13399-020-01190-2.

[46] O. R. Benkouachi *et al.*, « Advanced green peel utilization for efficient methylene blue removal: Integrated analysis and predictive modeling », *J. Mol. Liq.*, p. 125951, 2024.

[47] M. El-Desouky, M. Khalil, M. El-Afify, A. El-Bindary, et M. El-Bindary, « Effective methods for removing different types of dyes–modelling analysis, statistical physics treatment and DFT calculations: a review », *Desalination Water Treat.*, vol. 280, p. 89-127, 2022.

[48] Y. Yukselen et A. Kaya, « Suitability of the methylene blue test for surface area, cation exchange capacity and swell potential determination of clayey soils », *Eng. Geol.*, vol. 102, nº 1-2, p. 38-45, 2008.

[49] X. Jaramillo-Fierro, L. F. Capa, F. Medina, et S. González, « DFT study of methylene blue adsorption on ZnTiO3 and TiO2 surfaces (101) », *Molecules*, vol. 26, nº 13, p. 3780, 2021.

[50] J. Wang, L. Fu, et H. Yang, « Structural modulation of kaolinite nanoclay via DFT and molecular dynamics simulations: A review », *Appl. Clay Sci.*, vol. 258, p. 107473, 2024.

[51] A. Kausar *et al.*, « Cellulose, clay and sodium alginate composites for the removal of methylene blue dye: Experimental and DFT studies », *Int. J. Biol. Macromol.*, vol. 209, p. 576-585, 2022.

[52] N. Chafai, S. Chafaa, K. Benbouguerra, D. Daoud, A. Hellal, et M. Mehri, « Synthesis, characterization and the inhibition activity of a new α-aminophosphonic derivative on the corrosion of XC48 carbon steel in 0.5 M H2SO4: Experimental and theoretical studies », *J. Taiwan Inst. Chem. Eng.*, vol. 70, p. 331-344, 2017.

[53] C. E. White, J. L. Provis, T. Proffen, D. P. Riley, et J. S. Van Deventer, « Density functional modeling of the local structure of kaolinite subjected to thermal dehydroxylation », *J. Phys. Chem. A*, vol. 114, nº 14, p. 4988-4996, 2010.

[54] E. Badogiannis, G. Kakali, et S. Tsivilis, « Metakaolin as supplementary cementitious material: optimization of kaolin to metakaolin conversion », *J. Therm. Anal. Calorim.*, vol. 81, nº 2, p. 457-462, 2005.

[55] V. V. Mehmeti et A. R. Berisha, « Corrosion study of mild steel in aqueous sulfuric acid solution using 4-methyl-4H-1, 2, 4-Triazole-3-Thiol and 2-mercaptonicotinic acid—an experimental and theoretical study », *Front. Chem.*, vol. 5, p. 61, 2017.

[56] A. Spepi *et al.*, « Experimental and DFT characterization of halloysite nanotubes loaded with salicylic acid », *J. Phys. Chem. C*, vol. 120, nº 47, p. 26759-26769, 2016.

[57] R. K. Ghosh, D. P. Ray, S. Debnath, A. Tewari, et I. Das, « Optimization of process parameters for methylene blue removal by jute stick using response surface methodology », *Environ. Prog. Sustain. Energy*, vol. 38, nº 5, p. 13146, 2019, doi: 10.1002/ep.13146.

[58] Z. Han, K. Wang, Y. Zhang, A. Xian, X. Wei, et Z. Wang, « Study on Methylene Blue Adsorption Properties of Biochar/Montmorillonite Composites », *Earth Sci.*, vol. 13, nº 4, p. 163-181, 2024.

[59] F. N. Türk, M. Ş. A. Eren, et H. Arslanoğlu, « Adsorption of Reactive Black 5 dye from aqueous solutions with a clay halloysite having a nanotubular structure: Interpretation of mechanism, kinetics, isotherm and thermodynamic parameters », *Inorg. Chem. Commun.*, vol. 171, p. 113600, 2025.

[60] R. Kecili et C. M. Hussain, « Mechanism of adsorption on nanomaterials », in *Nanomaterials in chromatography*, Elsevier, 2018, p. 89-115.

[61] M. El-Habacha *et al.*, « An efficient and adsorption of methylene blue dye on a natural clay surface: modeling and equilibrium studies », *Environ. Sci. Pollut. Res.*, vol. 31, nº 53, p. 62065-62079, 2024.

CHAPTER IV

Chapter IV: Insights into the adsorption mechanism of Methyl Orange using Halloysite/Polyaniline composite

1. Introduction

the present study focuses on the development of a cost-effective adsorbent for the removal of anionic dyes by modifying natural halloysite nanotubes sourced from the abundant Jbel Debagh deposit in Guelma (Algeria) with polyaniline. Given the strategic importance of this local resource, the adsorption performance of raw HNTs and pure PANI was first evaluated and then compared with that of the HNTs–PANI composite, in order to demonstrate the synergistic enhancement achieved through functionalization. The HNT-PANI composite was synthesized and characterized using a range of physicochemical techniques to confirm successful functionalization and structural modification. The adsorption process was further examined through equilibrium, kinetic, and thermodynamic modeling to provide deeper mechanistic understanding. These experiments help us understand how PANI-functionalized halloysite adsorbs dyes.

2. Choice of adsorbent

The adsorption of MO on HNT, PANI, and HNT-PANI materials is strongly influenced by the structural and chemical properties of each material. Raw HNT exhibited poor performance, with a low adsorption capacity q_e = 14.63 mg g^{-1}. In contrast, PANI showed a moderately higher adsorption capacity (q_e=62.29 mg/g), although equilibrium was not fully achieved within the studied contact time. While the immobilization of PANI to the HNT resulted in a more than 30% increase in adsorption capacity, achieving 83.91 mg/g equilibrium adsorbed quantities after 90 min.

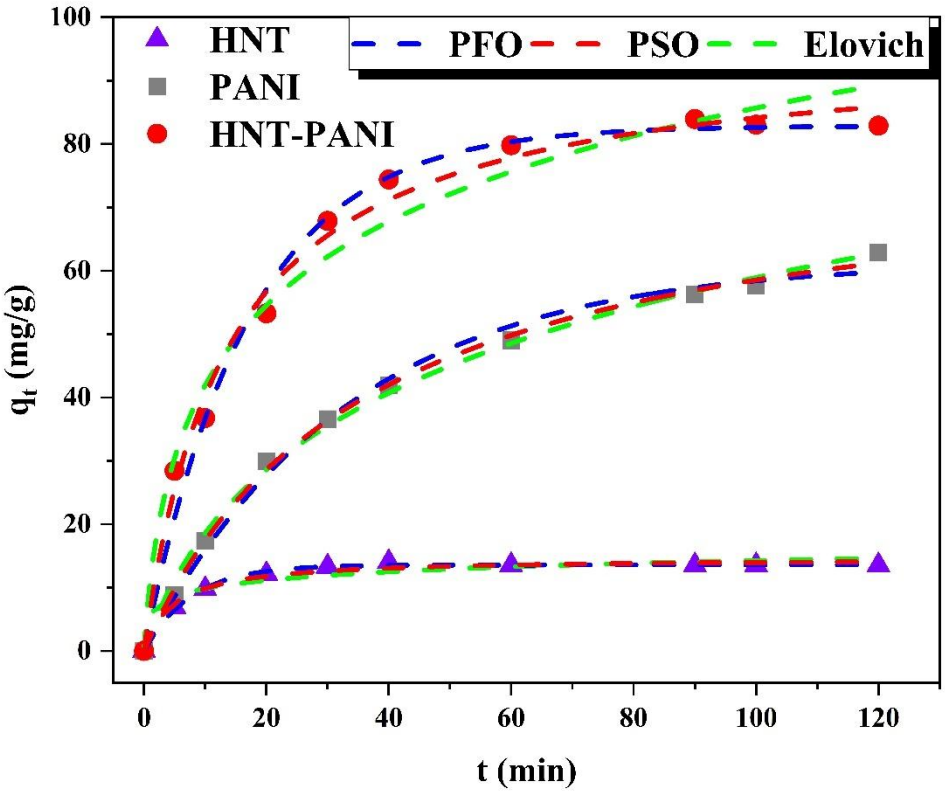


Figure IV.1. Effect of adsorbents on MO adsorption capacity
($T = 25 \pm 2$ °C, $V_{sol} = 100$ mL, $pH_{sol} = 6.3$, $C_i = 100$ mg/L, $m_{HNT-PANI} = 40$ mg).

Raw HNT exhibit a high specific surface area (S_{BET} = 185 m²/g) and a moderate average pore diameter of (11.5 nm), providing numerous accessible adsorption sites mainly located on the external surface. These sites are dominated by uniformly distributed hydroxyl groups ($Al-OH$ and $Si-OH$), which permit MO adsorption primarily through Vand Der Waals bonding. Additional uptake could arise from Lewis's acid/base interactions involving trace metal impurities (e.g., Fe^{3+}, Mn^{2+}), while electrostatic attraction plays a negligeable role under neutral conditions due to the surface neutrality. As adsorption occurs mainly at the surface, diffusion limitations are minimal; however, the lack of strong or specific functional groups restricts the overall adsorption capacity. This behavior is well described by the *PFO* kinetic model, with high $R^2 = 0.995$ and AIC =-17.06 low values confirming the predominance of physisorption-controlled uptake (**Table IV.1**).

Table IV.1. Kinetic model parameters for MO adsorption by different adsorbents.

Model	Parameter	HNT	PANI	HNT − PANI
PFO	q_e (mg/ g)	13.56	58.80	82.86
	k_1 (1/ min)	0.131	0.036	0.0583
	R^2	0.995	0.995	0.988
	AIC	-17.06	15.26	29.91
PSO	q_e (mg/g)	14.63	73.84	95.72
	k_2 (g/ (mg min))	0.014	0.00049	0.00075
	R^2	0.996	0.987	0.991
	AIC	-4.14	26.76	28.36
Elovich	A (mg/ (g min))	31.14	2.90	14.27
	B (g/ mg)	0.517	0.044	0.049
	R^2	0.939	0.996	0.973
	AIC	34.45	9.70	38.57

On the other hand, although *PANI* has a lower surface area (38 m2/g), it has a robust affinity for MO due to its larger pores (22.9 nm) and high density of $-\mathrm{NH}-$ and $-=\mathrm{N}-$ functional groups. By contrast, PANI has a lower surface area (38 m²/g). MO adsorption takes place through hydrogen bonding and acid-base exchange with sulfonic groups, complemented by $\pi-\pi$O stacking between the aromatic rings of the adsorbate molecules and the conjugated backbone of PANI. However, even though these interactions considerably enhance adsorption capacity, their heterogeneous distribution leads to site competition and intraparticle diffusion resistance at higher concentrations. The *Elovich* model best fits the kinetic data $R^2 = 0.996$ and AIC =9.7, reflecting surface heterogeneity and variable adsorption energies, while the PSO behavior indicates that limited site-specific interactions govern MO transport on PANI.

The HNT – PANI composite combines the structural accessibility and adjustable textural properties of HNT with the rich functional chemistry of PANI, resulting in enhanced adsorption performance. The presence of surface hydroxyl and nitrogen-containing groups on HNT andPANI , respectively, enables multiple interaction forces to act simultaneously.

Furthermore, HNT serves as a structural template that limits PANI domain growth, improves functional group dispersion, and enhances interfacial contact that reduces diffusion limitations. MO adsorption proceeds predominantly via surface-controlled processes across numerous sites, consistent with the excellent fitting of the PSO model (high $R^2 = 0.991$ and low $AIC = 28.36$).

3. Results and discussion

3.1.Materials characterizations

XRD analysis provides detailed insights into the phase composition and structural evolution of halloysite nanotubes HNT upon functionalization with PANI. The raw HNT and its PANI-functionalized derivative are slightly crystalline, whereas pristine PANI appears largely amorphous (**Fig. IV.2**).

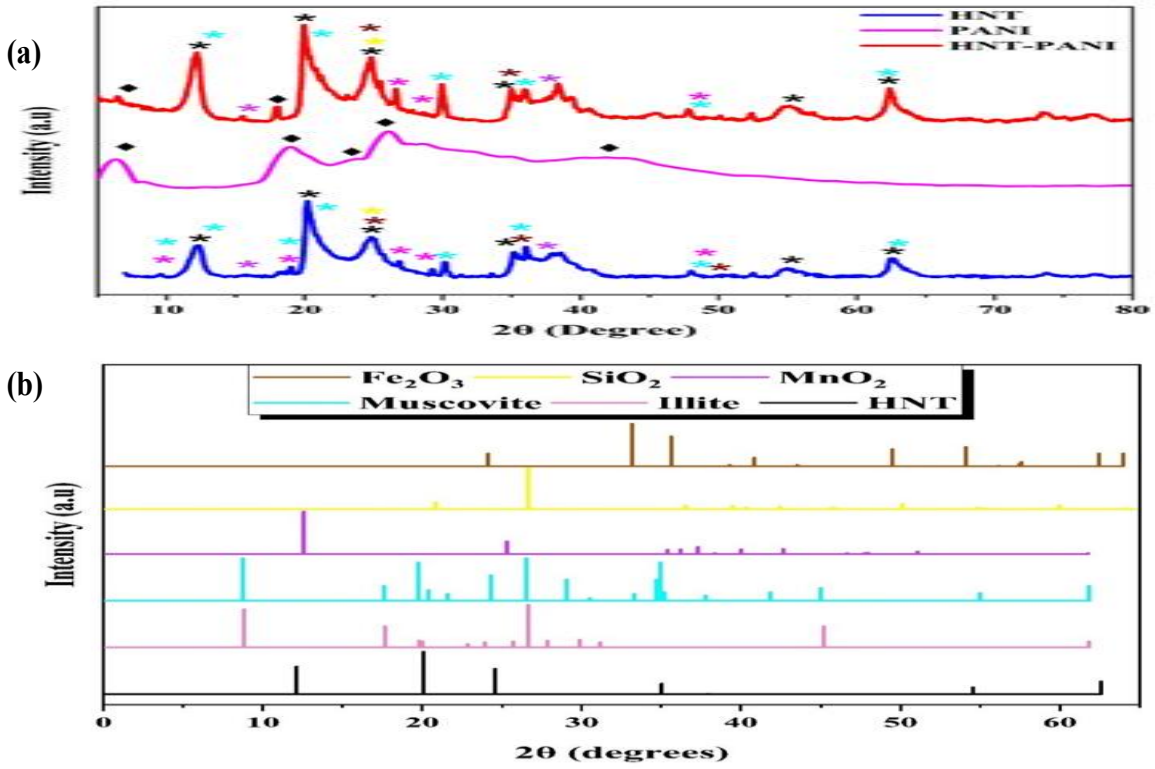


Figure IV. 2: *a) XRD patterns of the studied samples, b) JPCDS files for the detected phases of the studies materials.*

The phase proportions for each sample quantified by Rietveld refinement are given in **Table IV.2**. The dominant halloysite phase (64.5 wt%) was accompanied by minor contributions from illite (21.9 wt%), muscovite (3.8 wt%), birnessite MnO_2 (4.9 wt%), quartz SiO_2 (0.9 wt%), and hematite Fe_2O_3 (2.7%), as were identified via JCPDS reference patterns and were quantified through Rietveld refinement (**Table IV.2**)[1]. Detrital micas-like muscovite, oxides, and carbonates coexist with the primary halloysite phase, reflecting the natural heterogeneity of the clay. According to **Ferlito et al**[2], Algerian halloysite from Guelma HNT typically contains high silicon and aluminum contents, along with metallic impurities such as Mn, K, Ca, Mg, and others. The HNT elemental composition supports the identification of secondary minor oxide phases in the present Rietveld-refined pattern[3].

Table IV.2 Calculated parameters from XRD and N_2 physisorption analysis.

Parameter			HNT	PANI	HNT – PANI
XRD parameters	Phase composition percentage (%)	*Halloysite*	70.1	–	72.5
		PANI	–	100	7.2
		Illite	1.6	–	5
		Muscovite	0.6	–	9.6
		Birnessite MnO_2	9	–	4.8
		Quartz SiO_2	3	–	0.2
		Hematite $Fe_2\ O_3$	0.3	–	0.
		Calcite $CaCO_3$	15.3		0.7
	Crystallite size (nm)	*HNT*	7.8	-	10.1
		PANI		-	25
N_2 physisorption Parameters		Surface area S_{BET} (m^2/g)	185	38	34.47
		Mean pore diameter (nm)	11.5	22.91	21.32
		Total pore volume (cm^3/g)	0.21	0.236	0.184

Upon PANI immobilization, the HNT phase fraction increased to 72.5 wt%, accompanied by the incorporation of 7.2 wt% PANI. Muscovite and illite contents were also elevated to 9.6 wt% and 5 wt%, respectively. In contrast, calcite and birnessite decreased to 0.7 wt% and 4.8 wt%, respectively, and the hematite phase disappeared completely. The changes in mineral phase composition are attributed to the acidic conditions of oxidative polymerization. Less crystalline or chemically unstable phases were selectively destabilized, undergoing partial dissolution or transformation, whereas the more stable clay fractions were preserved, increasing the apparent proportion of stable phyllosilicates.

The lattice parameters obtained from the XRD diagrams for each sample are analyzed. For the raw HNT material, the 001 basal reflection appeared at $2\theta = 12.30°$, consistent with dehydrated halloysite ($d = 7.2$ Å). Considering the basal spacing, the number of coherent layers contributing to diffraction was calculated to be about 11. The full width at half maximum ($FWHM = 1.05°$) of this reflection was used for crystallite size estimation by the Scherrer equation. The corresponding crystallite size along the stacking direction was approximately 7.8

nm. This sets a baseline for the structural order of raw HNT prior to polymer modification. In fact, the additional weak peak at $2\theta = 9.70°$, ($d = 9.2$ Å) can be ascribed to a minor hydrated halloysite component. However, its contribution was negligible according to Rietveld refinement. Following functionalization with PANI, the 001 reflection in the HNT − PANI pattern was shifted slightly to $2\theta = 12.20°$, and the FWHM was decreased to $0.81°$. The crystallite size increased to approximately 10.1 nm, corresponding to an estimated 14 coherent silicate layers along the stacking direction. This observation is consistent with the Rietveld refinement, which showed an increased HNT fraction. The improved ordering within the nanotube layers likely resulted from the stabilizing effect of the polymer coating. PANI not only functionalized the surface of the nanotubes but also promotes important structural coherence within the halloysite framework[4].

In addition to the HNT phase reflections, the HNT − PANI composite exhibited distinct peaks attributable to PANI at $2\theta = 6.45°, 18.55°$ and $26.3°$. The low-angle peak at $6.45°$($d = 13.7$ Å) was related to the long-period backbone repeat or lamellar spacing of the polymer chains. The second reflection at $18.55°$ ($d = 4.8$ Å), corresponding to the 110 or 020 plane. It is associated with inter-chain lateral packing and denotes the spacing between polymer chains. The corresponding crystallite size along the inter-chain packing direction was approximately 25 nm. A roughly 50 repeating aniline units could be present. The high-angle peak at $26.3°$ ($d = 3.4$ Å) was associated with $\pi - \pi$ stacking between conjugated polymer backbones. Although PANI is largely semi-crystalline and partially amorphous, it forms locally ordered domains when bound to the HNT surface. The lamellar and inter-chain reflections corroborate that the polymer chains adopt regular packing patterns, while the $\pi - \pi$ stacking reflects alignment of the conjugated backbones. PANI not only coats the HNT surface but also contributes to the stabilization and enhanced ordering of the nanotube framework. HNT act as

a template, guiding polymer organization and preserving a significant fraction of mesoporosity, while limiting large, loosely packed polymer aggregates.

SEM images complemented the XRD findings by highlighting the morphological changes induced by PANI functionalization. The microstructure of HNT was investigated by SEM and TEM analysis in the previous chapter. Observations revealed that the nanotubes ranged in length from 40 to 1300 nm, with external diameters of 35 – 43 nm and internal lumen diameters of 8 – 16 nm. HNT possesses a nanoscale hollow tubular framework combined with an elongated morphology [2]. HNT offers strong potential for hosting guest molecules and for surface functionalization.

PANI morphology indicated its semi-crystalline nature and reflected the tendency of the polymer chains to self-assemble into dense clusters. When immobilized on HNT, the polymer coating caused the nanotube surfaces to become roughened and luminous, as revealed in **Fig. IV.3**. The coating covered the nanotubes effectively, altering the surface morphology and increasing surface irregularities. Numerous surface cavities were observed, suggesting that interstitial spaces developed between the nanotubes[5].

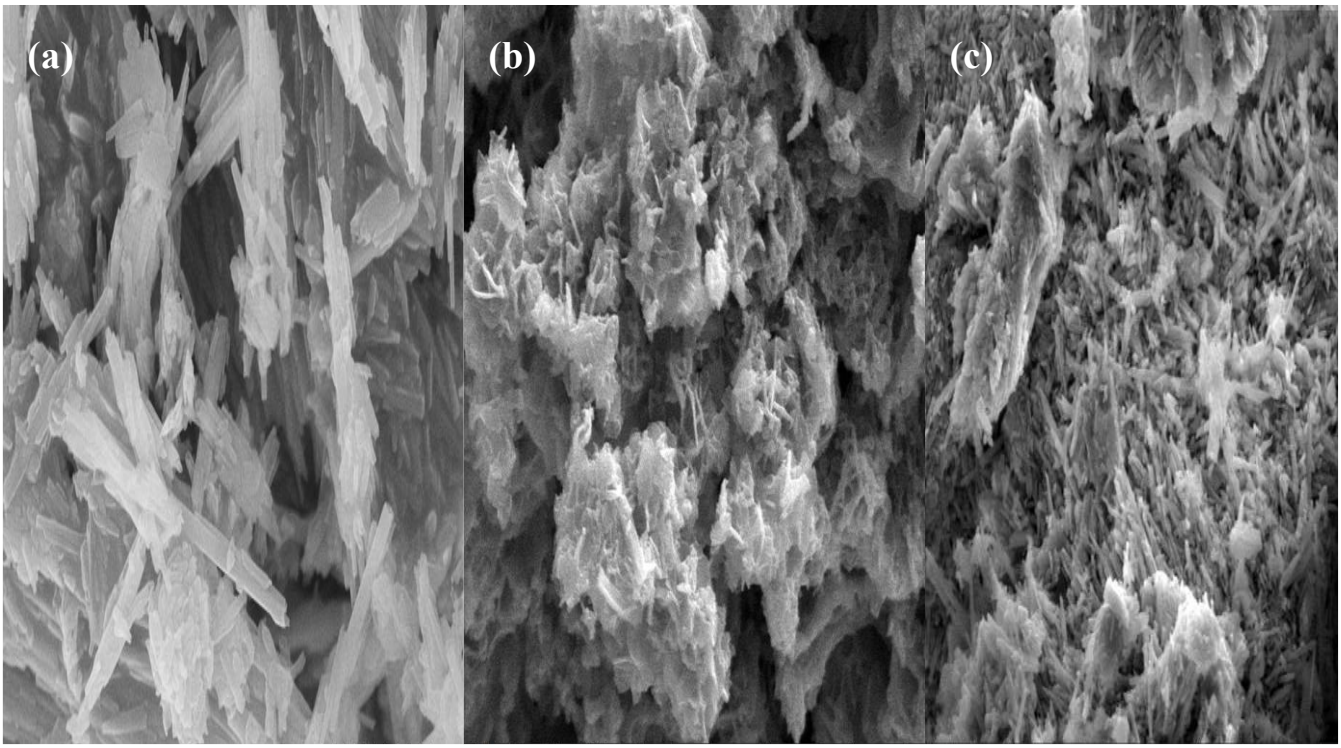


Figure IV. 3: *SEM images for a) HNT, b) PANI and c) HNT-PANI.*

Nitrogen N_2 adsorption-desorption measurements were performed to evaluate the surface properties and porosity of HNT and the effects of PANI functionalization (**Figure IV. 1**). The physisorption isotherms of the studied materials were Type IV, indicating the presence of mesopores[6]. Raw HNT exhibited an H4 hysteresis loop, characteristic of narrow slit-like pores formed by the tubular lumen and interstitial spaces between stacked nanotubes. In contrast, both pure PANI and HNT – PANI displayed H3 hysteresis loops, indicative of irregular slit-shaped mesopores arising from polymer aggregation and partial filling of the nanotube lumens[7]. The calculated textural parameters calculated from BET and BJH analyses are summarized in **Table IV.2**. PANI immobilization to the HNT surface decreased the surface area and total pore volume of HNT while increasing the average pore diameter. The PANI immobilization covered the external surfaces and partially occupied the nanotube lumens.

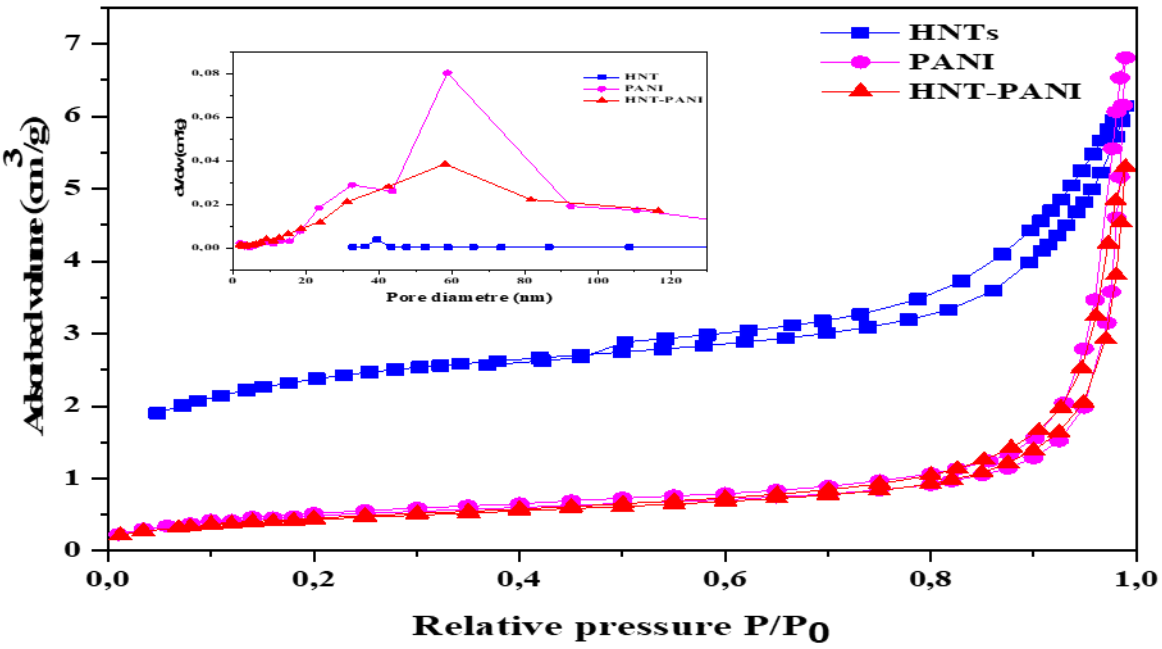


Figure IV. 2: *BET and BJH plots for HNTs, PANI, HNT-PANI.*

Pore size distributions provide further insight into the microstructural changes (**Figure IV. 3**). HNT pores were concentrated at 3.6 nm, whereas both PANI and HNT – PANI displayed populations around 6.5 nm, consistent with interfacial voids or bridging between polymer chains and nanotube surfaces. Both materials also showed larger macropore populations concentrated around 60 nm. Notably, the maximum pore size was decreased from 140 nm in pure PANI to 110 nm in HNT – PANI, consistent with confinement of the polymer along the nanotube surfaces and suppression of excessive aggregation. This results in a denser and more uniform microstructure.

FTIR analysis of the studied materials reveals the effects of HNT functionalization by PANI (**Figure IV.5**). The HNT spectra displayed the presence of functional groups characteristic of aluminosilicate clays. Two sharp O – H stretching (ν) bands were observed in the 3600-3700 cm^{-1} region, corresponding to hydroxyl groups on the inner and outer surfaces

of the nanotubes. The higher-frequency band at approximately 3690 cm^{-1} arose from $Al-OH$ groups in the inner octahedral sheets, which are relatively isolated and less involved in hydrogen bonding[8]. The lower-frequency band around 3627 cm^{-1} is attributed to outer-surface hydroxyls that participate in stronger hydrogen bonding interactions. A broad absorption near 3459 cm^{-1} is assigned to $O-H$ stretching of interlayer water molecules, consistent with $H-O-H$ bending (δ) vibrations observed around 1600-1700 cm^{-1}[9]. HNT retains moisture both on the outer surface and within the lumen. The band at approximately 1636 cm^{-1} can also be attributed to CO_3^{2-} bending vibrations from dolomite, supported by the calcite phase presence (**Table IV.2**). Moving to the low-wavenumber region, weaker absorption bands were observed between 1400 and 1500 cm^{-1}. They correspond to deformation (δ) vibrations of $Al-OH$ and $Si-OH$ hydroxyl groups, perturbed by hydrogen bonding with water molecules[10]. Broad absorptions were noticed in the 1000-1200 cm^{-1} range, attributed to $Si-O$ stretching (ν) vibrations of the tetrahedral framework. Absorbance features near 1030-1045 cm^{-1} originated from asymmetric $Si-O-Si$ stretching, while bands around 1100-1120 cm^{-1} are assigned to $Si-O-Al$ stretching, reflecting the linkage between tetrahedral and octahedral sheets. A distinct band at approximately 920 cm^{-1} was observed and assigned to $Al-OH$ bending (δ) vibrations of the octahedral sheet. This band indicates the structural integrity of hydroxyl groups within the lattice. At lower wavenumbers 500-800 cm^{-1}, bending δ vibrations of $Si-O-Si$ and $Si-O-Al$ predominates. They indicate deformations of the framework and interactions between tetrahedral and octahedral layers of the clay mineral[11].

The FTIR spectrum of PANI revealed characteristic absorptions that reflect its chemical structure, protonation state, and conjugation. In the high-wavenumber region 3200-3500 cm^{-1}, broad bands appeared for $N-H$ stretching vibrations of secondary amine groups in the polymer backbone. These bands were often broadened due to hydrogen bonding influenced by

the polymer's environment or interactions with a substrate. Weak contributions from $O-H$ stretching may also occur if moisture is present, but in pure PANI, the signal is predominantly due to $N-H$. In the 2800-3200 cm^{-1} range, aromatic $C-H$ stretching vibrations 3000-3100 cm^{-1} were detected, with weaker aliphatic $C-H$ stretches 2850-2950 cm^{-1} present if dopants or substituents are incorporated. In the 1400-1650 cm^{-1} region, three prominent absorptions were recorded: the band at 1580-1620 cm^{-1} was assigned to $C=C$ stretching of quinoid rings Q, the band at 1480-1515 cm^{-1} corresponded to $C=C$ stretching of benzenoid rings B, and a weaker band near 1300-1350 cm^{-1} was attributed to $C-N$ stretching of aromatic amines. The bands are useful for assessing the Q/B ratio, which serves as a measure of PANI's oxidation state, with $Q/B < 1$ indicating benzenoid units dominate. In the 1200-1350 cm^{-1} region, bands were identified for $C-N$ stretching of aromatic amine groups and $C-N^{+}$ stretching in protonated emeraldine salt. They are sensitive to polymer doping and indicate the degree of charge delocalization along the conjugated backbone. Minor bands between 1100-1200 cm^{-1} manifested in the spectra, corresponding to in-plane $C-H$ and $N-H$ bending vibrations. Characteristic features of the aromatic polymer framework could be discerned in this region.

The FTIR spectrum of the $HNT-PANI$ composite demonstrated successful polymer immobilization and strong interfacial interactions between PANI and the HNT. In the high-wavenumber region > 3500 cm^{-1}, the hydroxyl stretching bands of HNT, originally at 3690 cm^{-1} (inner $Al-OH$) and 3627 cm^{-1} (outer surface $O-H$), shifted to 3695 and 3632 cm^{-1}, respectively. A hydrogen bond formation between PANI amine groups and HNT surface hydroxyls was occurred and $O-H$ vibration intensity was reduced, perturbing the electronic environment. In the 3200-3400 cm^{-1} region, the $N-H$ stretching vibration of PANI, initially centered at 3350 cm^{-1}, narrowed and shifted to 3380 cm^{-1}, confirming hydrogen-bonding

interactions and anchoring of the polymer onto the nanotube surface. The 2800-3100 cm^{-1} region showed aromatic C – H stretching vibrations of PANI rings. Weaker aliphatic C – H stretches were also noticed, revealing the integrity of the polymer backbone and minor dopant or substituent contributions. In the 1400-1650 cm^{-1} region, HNT – PANI exhibited a single prominent peak at 1512 cm^{-1}, corresponding to combined C = C stretching of benzenoid and quinoid rings[12]. The merging into a single peak is discerned and could be due to partial reduction of PANI and strong interactions with the HNT surface. Hydrogen bonding and Van Der Waals interactions with the nanotubes alter vibrational energies. Polymer immobilization on HNT surfaces promote local ordering of the polymer chains. Despite partially blocking the pores, the presence of PANI introduces a new chemical functionality.

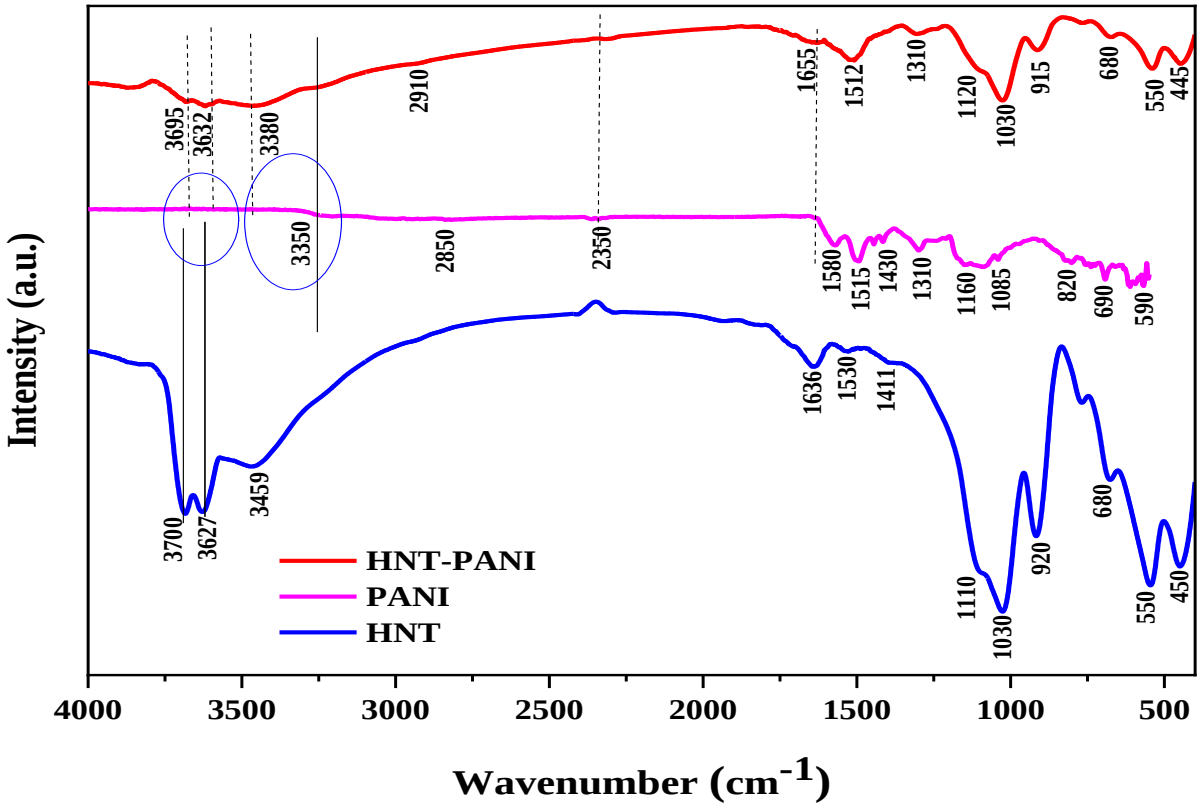


Figure IV. 5: *FTIR spectrums of the studied materials.*

the TGA – DTG profiles of raw HNT free PANI, and HNT-immobilized PANI provided detailed insight into their thermal stability and structural interactions (**Figure IV.5**). Raw HNT

exhibited five characteristic weight-loss regions; 30 °C (7.5%) due to physically adsorbed water on surfaces and within the lumen; 104 °C for coordinated water in the Al – OH layers; 240 °C reflecting dehydration from interlayer defects or partial hydroxyl condensation; 480 °C (12.5%) corresponding to dihydroxylation of inner Al – OH layers forming metakaolinite; and 755 °C (1.56%) associated with high-temperature transformation into mullite and cristobalite[13]. The early weight-loss steps below 150 °C indicated the presence of adsorbed and interlayer water in HNT. This is consistent with the XRD and FTIR observations, where the hydrated and dehydrated HNT phases coexist.

Free PANI showed an endothermic peak at 145 °C, attributed to the release of physically adsorbed water and residual dopants, followed by the 200-400 °C region (10%) corresponding to partial polymer backbone degradation and desorption of low-molecular-weight PANI oligomers[14]. The 400-800 °C region (34%) reflects extensive carbonization of the conjugated polymer chains, while lower-temperature exothermic events (72-316 °C) result from minor oxidative reactions, chain cyclization, or crosslinking.

In the HNT-immobilized PANI, the endothermic peak shifted to 165 °C, indicating stabilization of the PANI chains via interactions with the HNT surface, such as hydrogen bonding and π – π stacking. The material exhibited three major weight loss; 83 °C (4%) for water removal, 275 °C (5%) for initial PANI decomposition, and 525 °C (19%) representing combined dihydroxylation of HNT Al – OH layers and PANI backbone carbonization. The shift to higher temperature and the reduced weight loss compared to pure PANI indicate that HNT enhances the thermal stability of the polymer. Based on the 400-800 °C weight-loss data and the respective contributions of HNT (14%) and PANI (34%), the PANI – OH content in the material is estimated at 15 wt%, consistent with surface coating rather than intercalation[15]. HNT-immobilized PANI retains the nanotubular framework of HNT, incorporates surface-

bound semi-crystalline PANI domains, and exhibits enhanced thermal stability compared to the free polymer.

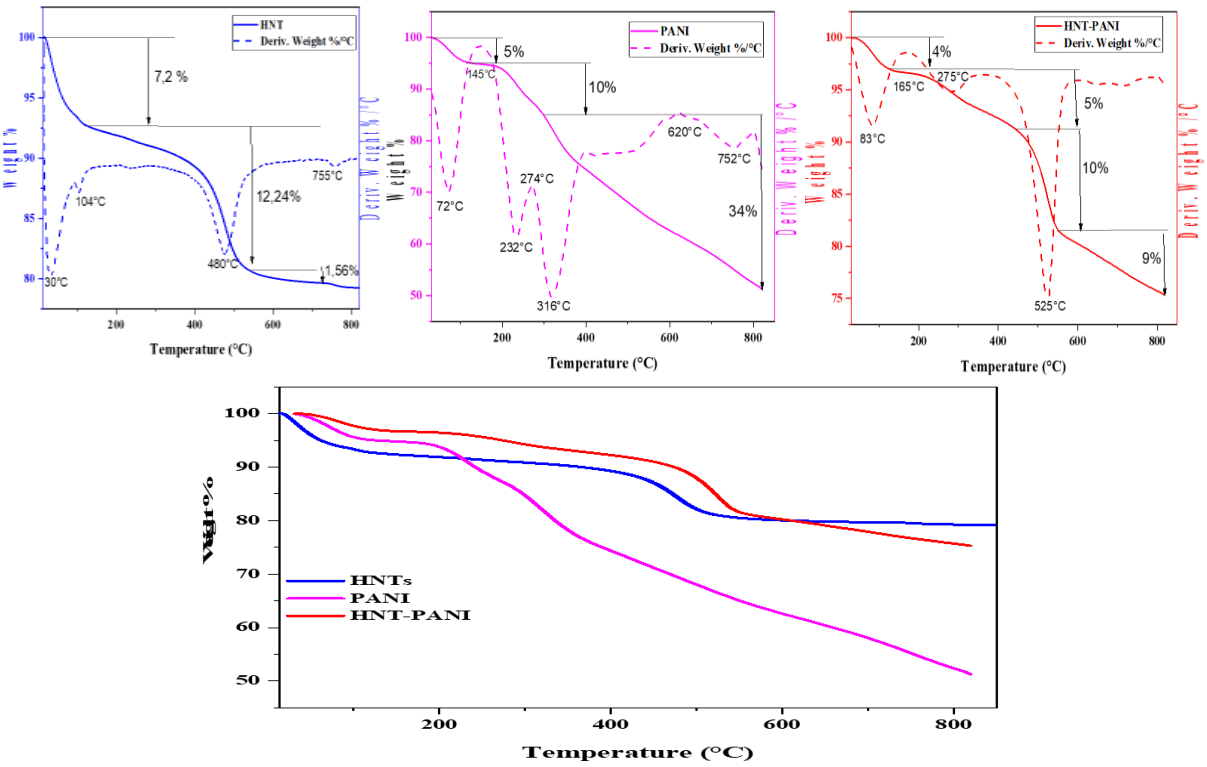


Figure IV. 6: *ATG/DTA plots for HNTs, PANI and HNTs/PANI.*

The zero charge point pH_{zpc} of the samples was determined using the pH drift method (**Figure IV.6**), giving values of 6.9 for HNT, 4.2 for PANI, and 4.6 for HNT − PANI. At pH values below pH_{zpc}, the sample surface has a net positive charge; at pH values above pH_{zpc}, however, it becomes negative. The near-neutral pH_{zpc} of HNT reflects its weak amphoteric character, arising from surface hydroxyl groups (Al − OH in the inner layer and Si − OH in the outer layer can exchange protons) that can undergo proton exchange. In contrast, PANI exhibits an acidic $pH_{p}zc$ because its amine and imine nitrogen sites are readily protonated, as supported by FTIR evidence. The nitrogen functionalities therefore behave as basic proton-accepting sites rather than intrinsically negative centers. For the HNT − PANI composite, the relatively low

PANI loading combined with the amphoteric hydroxyl groups of HNT was sufficient to produces a balanced surface chemistry, resulting in an intermediate pH_{zpc}. The shift toward a more acidic value (4.6) confirms the contribution of protonatable nitrogen sites while indicating that the clay surface chemistry still influences the overall charge behavior.

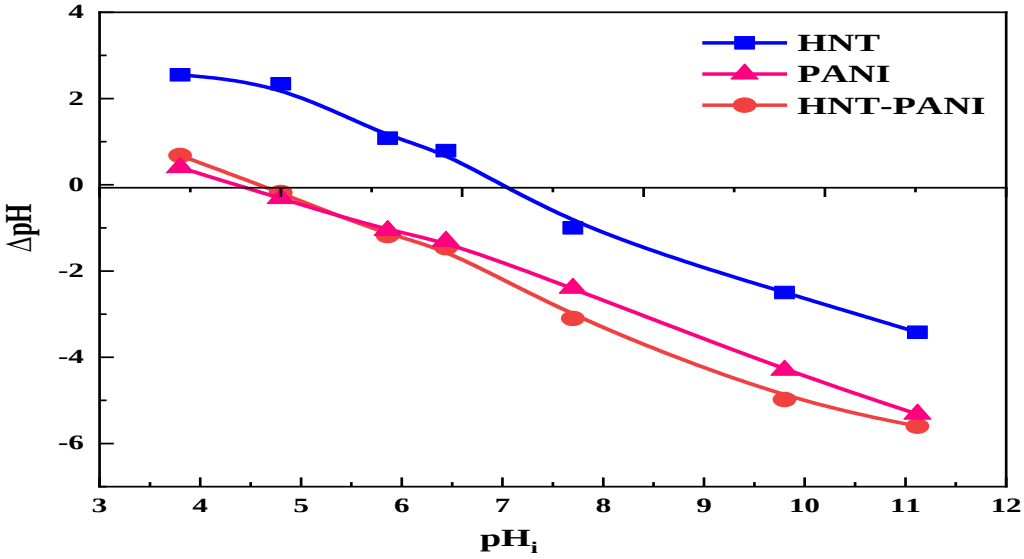


Figure IV. 7: *pH_{pzc} for HNT, PANI and HNT-PANI.*

3.2.Macroscopic analysis of MO adsorption behavior on HNT – PANI

The mechanism of MO adsorption by HNT – PANI was first investigated by kinetic and equilibrium conventional isotherms modelling. The effects of contact time at different initial adsorbate concentration on the adsorption of MO onto HNT – PANI at room temperature are illustrated in **Figure IV.8**. The kinetic profiles followed the expected adsorption behavior (**Figure IV.8.a**). The adsorption capacity of HNT – PANI increased progressively over the first minutes. The abundance of available active sites enabled rapid MO uptake. However, the adsorption rate gradually decreased as the number of unoccupied sites declined. Saturation occurred through continuous occupation of adsorption sites and equilibrium was established

after approximately 90 min. Meanwhile, as MO concentration increased, there was a noticeable improvement in adsorption capacity. The q_e value increased from 47.5 mg/g at 50 mg/L to 229.6 mg/g at 600 mg/L, with a similar required equilibrium time. Higher MO concentrations provided a greater driving force for mass transfer, leading to increased uptake of MO molecules [16]. Similarly, the kinetic models described in the previous section were used to analyze the experiment results.

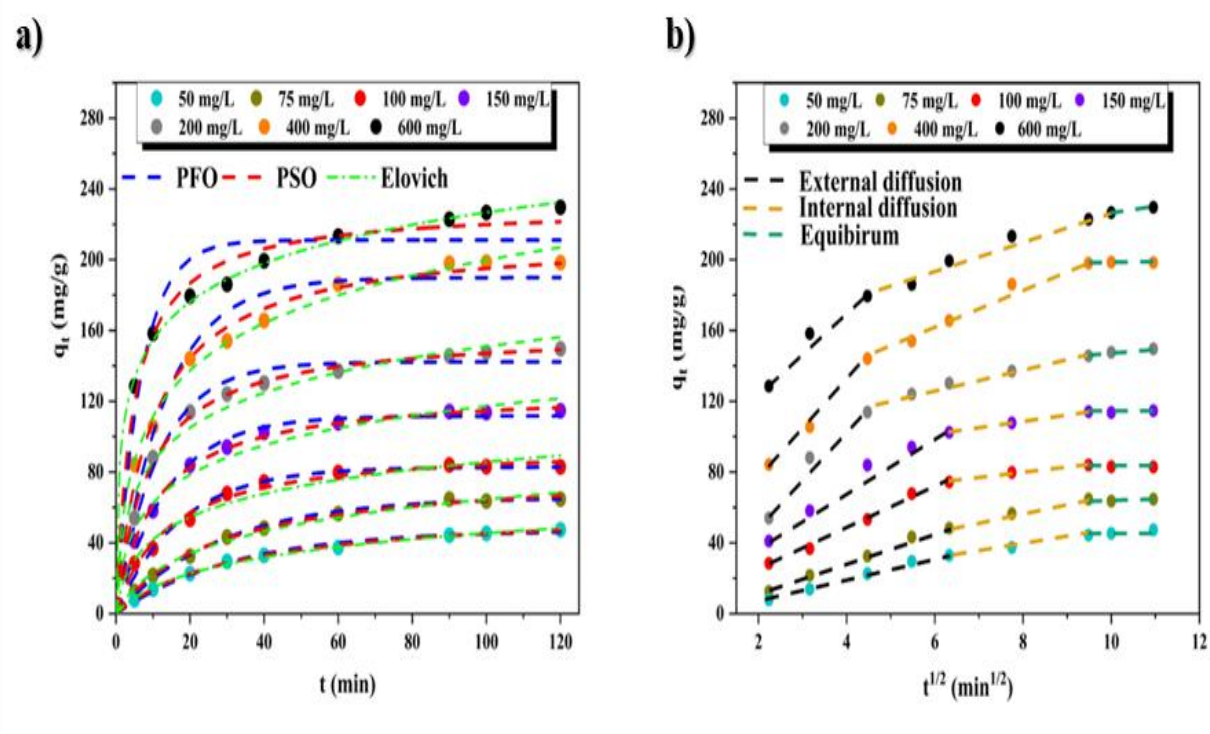


Figure IV.8. Effect of contact time on MO quantity adsorbed at various initial concentrations.

a) *PFO*, *PSO*, and *Elovich* nonlinear kinetic fits; b) *IPD* plots showing adsorption steps.(T $= 25 \pm 2$ °C, $V_{sol} = 100$ mL, $pH_{sol} = 6.3$, $m_{HNT-PANI} = 40$ mg).

The PSO model provides the best fit for all initial MO concentrations (**Table IV.3**). MO/HNT − PANI surface interactions predominate the adsorption process. However, a non-monotonic trend for PSO rate constant suggests that secondary rate-controlling mechanisms operate depending on the initial dye loading. It is suggested that at lower concentrations,

surface interactions control the adsorption kinetics. However, at higher concentrations, diffusion limitations and site competition increasingly affect the adsorption rate.

Linear intraparticle diffusion IPD analysis was employed to elucidate the rate-controlling mass-transfer steps (**Figure IV.8.b and Table IV.3**). The IPD curves revealed a total of three distinct stages, corresponding to external diffusion of the film $IPD-1$, diffusion into the pores $IPD-1$, and equilibrium $IPD-2$. At low initial concentrations (50-150 mg/L), two regions were more clearly expressed. The first region corresponds to boundary-layer diffusion and the rapid attainment of equilibrium step. The significant contribution of external film diffusion is demonstrated through the extended duration of this region and the progressive increase of the IPD rate constant k_{IPD1} with MO concentration. Mass transfer from the bulk solution to the adsorbent surface was limited by a weak concentration gradient at low MO loading. IPD contributed minimally under these conditions. Thus, MO adsorption at low loading was primarily governed by external diffusion, followed by rapid saturation of readily accessible sites.

Table IV.3. Kinetic model parameters for MO adsorption by HNT – PANI at different initial concentrations

Model	Parameter							
	C_i (mg/L)	**50**	**75**	**100**	**150**	**200**	**400**	**600**
PFO	q_e (mg/g)	47.07	65.63	82.86	111.68	142.26	189.88	211.07
	k_1 (1/min)	0.031	0.0355	0.058	0.071	0.086	0.076	0.149
	R^2	0.994	0.996	0.988	0.990	0.984	0.959	0.944
PSO	q_e (mg/g)	60.13	81.99	95.72	126.81	159.92	213.76	230.05
	k_2 (g /(mg min))	0.0005	0.0004	0.00075	0.00073	0.00071	0.00048	0.0009
	R^2	**0.998**	**0.997**	**0.990**	**0.998**	**0.997**	**0.991**	**0.987**
Elovich	A (mg/ (g min))	2.425	4.138	14.271	29.153	53.609	62.954	427.17
	B (g/mg)	0.060	0.046	0.0499	0.040	0.034	0.0254	0.0318

	R^2	0.996	0.990	0.974	0.979	0.978	0.993	0.998
IPD-1	K_{IPD1} (mg (g $min^{1/2}$))	6.294	8.146	11.77	15.24	28.295	26.95	22.30
	C_1	−5.932	−4.117	1.102	9.854	−1.157	22.61	82.02
	R^2	0.993	0.984	0.991	0.970	0.935	0.991	0.924
IPD -2	K_{IPD2} (mg/(g $min^{1/2}$))	3.622	3.510	2.994	3.685	6.087	11.24	9.101
	C_2	9.739	29.751	55.891	79.14	89.388	94.20	139.20
	R^2	0.989	0.770	0.963	0.999	0.961	0.976	0.963
IPD -3	K_{IPD3} ((mg/ g $min^{1/2}$)	2.083	2.593	−0.649	2.20	2.631	0.132	4.419
	C_3	24.52	37.60	89.89	91.47	120.93	196.96	181.52
	R^2	0.998	0.697	0.421	0.780	0.943	−0.727	0.882

At higher initial concentrations the duration of the external diffusion region decreased. The intraparticle diffusion rate increased as the concentration gradient became larger, enhancing mass transfer to both the external and internal surfaces of HNT – PANI. Both diffusion mechanisms contributed to MO uptake for moderate initial adsorbate concentrations. Nevertheless, at concentrations between 400 and 600 mg/L the diffusion rate constants decreased and equilibrium was not fully achieved. MO adsorption was limited by site competition and restricted pores volume, although the concentration gradient continued to drive adsorption until equilibrium was approached. MO adsorption onto HNT – PANI is controlled by multiple rate-limiting steps, with the contribution of each step depending on the initial dye concentration. The presence of surface is suggested by the good agreement with the PSO model, while MO molecules transport through the macropore population and the tortuous architecture of HNT – PANI justifies the noted changes in IPD diffusion pathways within the composite[17].

Figure.IV.9 illustrates the equilibrium adsorption isotherms of MO by HNT – PANI together with the fitted curves obtained from the classical (*Langmuir* and *Freundlich*) as well generalized (*Temkin*, *Sips*, *Liu* and *Toth*) isotherms models at different temperatures.

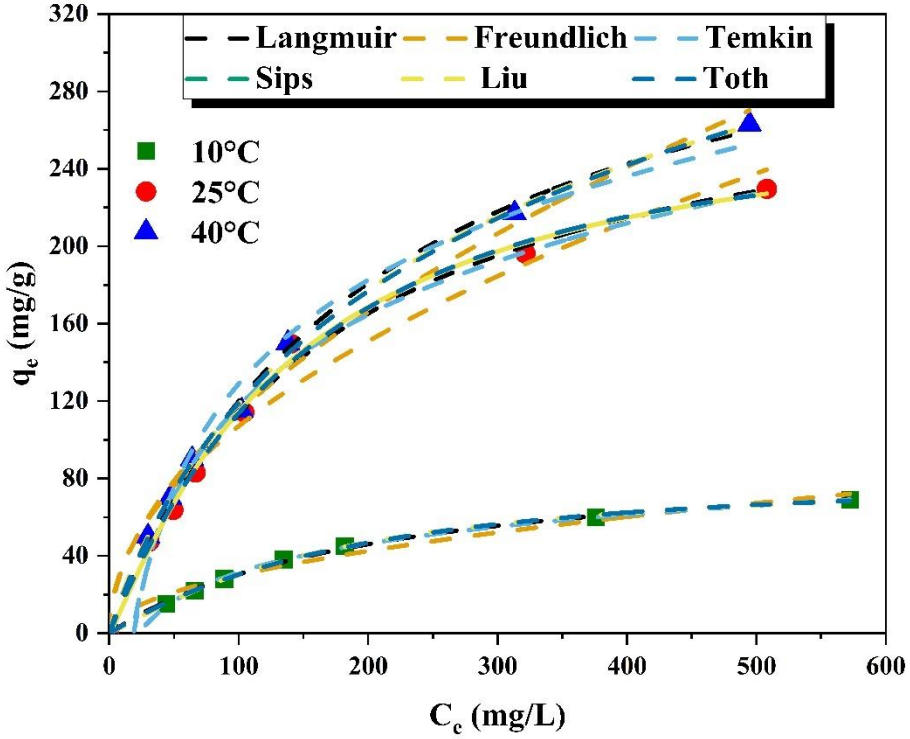


Figure IV.9. Equilibrium isotherms modelling of MO adsorption by HNT − PANI at different temperature (V_{sol} = 100 mL, pH_{sol} = 6.3, $m_{HNT-PANI}$ = 40 mg, t_{cont} = 24h).

The adsorbed amount increased progressively with increasing equilibrium concentration until the available adsorption sites start to be saturated evidenced by decreased the adsorption capacity rate. In addition, the adsorption capacity increased with temperature, indicating the endothermic nature of the adsorption process[18]. At elevated temperatures the mobility and solvation of MO molecules are enhanced.

Among all tested models, the *Langmuir* isotherm (q_{max}=306.4mg/g at 25°C) showed the best overall agreement with the experimental data at all temperatures, as confirmed by its higher R^2 = 0.995 and lower AIC = 37.3 values (**Table IV.4**). It is suggested that MO adsorption occurs predominantly on a homogeneous energetically equivalent active sites and proceeds via minimum layers coverage. In particular, the *Langmuir* separation factor R_L values were found to lie between 0 and 1 for all investigated temperatures and initial MO concentrations,

confirming the favorable nature of the process[19]. Regarding the obtained data from general isotherm models. At low temperature (10 °C and 25 °C), the $Temkin$ model was provided to present the excellent fit to the experimental data. The model provides that adsorbate/ adsorbate interactions influence the adsorption mechanism, with a linear decrease in adsorption energy as surface coverage increases. This means that more MO molecules occupy the surface was experienced slightly less favorable adsorption energy due to steric or electrostatic repulsion. In this context, the B parameter, which quantifies the variation of adsorption energy with surface coverage, provides insight into the adsorption mechanism. At 10 °C, the lower B value (21.447 mg/g) indicates stronger interactions at the initial stages of adsorption, leading to a progressive stabilization of the adsorbed quantity as high-energy sites are occupied. At 25 °C, the increase in B suggests that adsorbate/adsorbate interactions are less restrictive, allowing a higher adsorption capacity. Conversely, at 40 °C set temperature the adsorption equilibrium is better described by the $Toth$ model, indicating that surface energetic heterogeneity starts to becomes more pronounced. However, the $Toth$ heterogeneity parameter remains close to unity, indicating that deviations from uniform adsorption energies are slight and that lower-energy sites become accessible at elevated temperatures.

The MO adsorption mechanism evolves with temperature, from interaction-driven adsorption at low temperatures to site-multiplicity-driven adsorption at higher temperatures. Temperature increments enhance adsorption capacity by improving solute diffusion and increasing the accessibility of adsorption sites.

Table IV.4. Conventional isotherm parameters for MO adsorption by HNT − PANI.

Model	Isotherm parameters			
	Temperature	10	25	40
Langmuir isotherm	$q_m\ (mg/g)$	94.3	306.4	368.4
	$K_L(L/g)$	0.0047	0.0058	0.005
	R^2	0.998	0.995	0.997
	AIC	8.39	37.30	33.12
Freundlich isotherm	$K_f\ (L/mg)$	3.003	10.939	9.645
	n	1.998	2.019	1.861
	R^2	0.978	0.972	0.991
	AIC	29.50	50.64	43.62
Temkin isotherm	B (mg/g)	21.447	68.093	77.353
	A (L/mg)	0.0436	0.0562	0.0529
	R^2	0.999	0.992	0.987
	AIC	4.12	40.99	46.43
Sips isotherm	q_{max}(mg/g)	84.9	278.8	432.7
	Ks $(L/mg)^{1/n}$	0.0060	0.0072	0.0033
	N	1.143	1.133	0.877
	R^2	0.999	0.995	0.998
	AIC	9.68	45.07	38.82
Liu isotherm	q_{max}(mg/g)	84.9	278.7	432.7
	k_g(L/g)	0.006	0.007	0.003
	n_L	1.143	1.332	0.877
	R^2	0.999	0.995	0.998
	AIC	9.68	45.07	38.82
Toth isotherm	q_{max}(mg/g)	117.8	385.6	239.2
	k_T(mg/g)	0.004	0.005	0.008
	T	1.114	1.115	0.841
	R^2	0.998	0.994	0.998
	AIC	14.23	45.62	38.59

Thermodynamic analysis at macroscopic scale was performed by using the linear Van't Hoff equation to elucidate the temperature dependence of MO adsorption on the $HNT -$

$PANI$ composite at the macroscopic scale. Standard Gibbs free energy $\Delta G°$, enthalpy ($\Delta H°$), and entropy $\Delta S°$ changes were obtained by plotting the equation II.18 (**Figure IV.10**)[20]. The corresponding thermodynamic parameters are compiled in **Table IV.5**. The negative values of $\Delta G°$ over the investigated temperature range demonstrate that the adsorption process proceeds spontaneously. The progressive decrease in $\Delta G°$ from -26.72 kJ mol^{-1} at 10°C to -30.18kJmol^{-1}at 40°C indicates that increasing temperature enhances the thermodynamic favorability of MO uptake. The positive enthalpy change confirms the endothermic nature of the process. In addition, the positive entropy change reflects an increase in randomness at the $solid/liquid$ interface, which can be attributed to the displacement of structured water molecules by MO during adsorption, resulting in important configurational freedom within the interfacial region. The enthalpy magnitude indicates mainly physical adsorption. Overall, MO adsorption onto $HNT-PANI$ is spontaneous, endothermic, and driven by increased interfacial disorder[21].

Table IV. 5. Thermodynamic parameters for the adsorption of MO on HNT-PANI.

$T(K)$	$Ln\ K_c$	$\Delta G^0(kJ.mol^{-1}K^{-1})$	$\Delta H^0(kJ.mol^{-1})$	$\Delta S^0\ (J.K^{-1}mol^{-1})$
283	11,355	-26.716		
298	11,565	-28.653	6.062	116.063
313	11,599	-30.184		

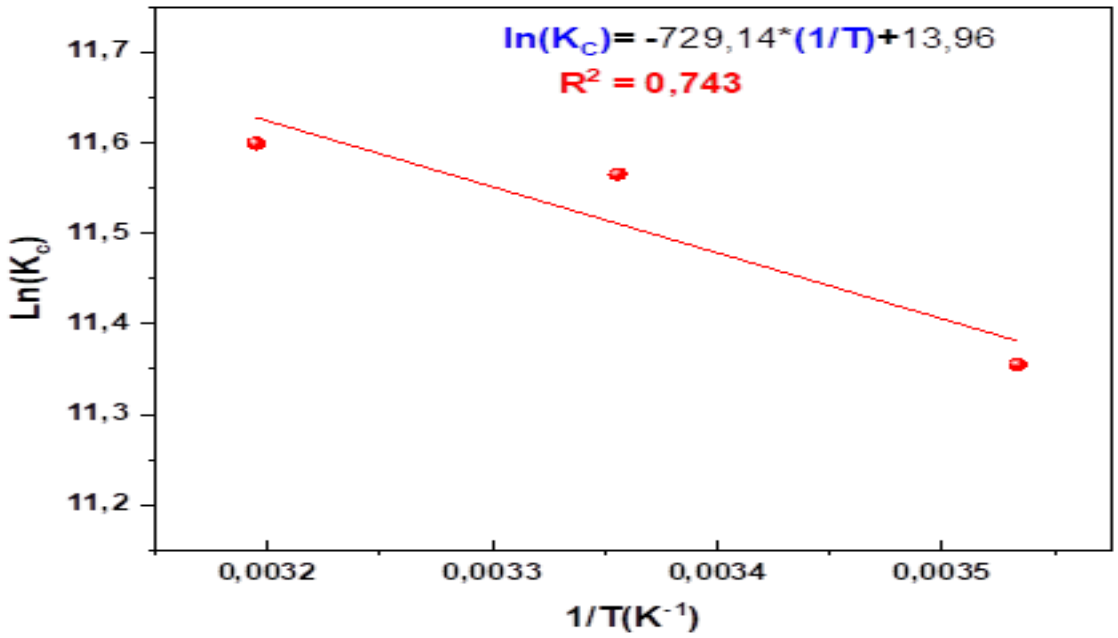


Figure IV.10. *plot of Ln(k) = f(1/T).*

3.3.Theorical studies of MO adsorption by HNT − PANI

To further elucidate the adsorption interactions between MO and the constituents of the HNT − PANI composite, a differential charge density maps and theoretical approach using DFT simulations to visualize the MO/HNT − PANI interactions were carried out.

Electrostatic potential and color-coded approach were mapped to the electron density to create the molecular electrostatic potential **MEP** graph. In the **Figure IV.11**, areas of nucleophilic attack with negative potential are indicated by regions ranging from red to green, while sections ranging from green to blue with positive potential indicate electrophilic reactivity. The MEP analysis revealed a region of maximal electron density (red color) corresponding to the nucleophilic character of the MO molecule[22]. The nucleophilic character of the MO molecule electron-rich zone, localized at the molecular center, arises from the synergistic contributions of delocalized π −electrons within the aromatic benzene rings, lone pair electrons from the azo (−N = N −) functional group, and conjugated π −electron

density distributed across the sulfonate ($-SO_3^- -$) group. In addition, MEP analysis revealed moderate negative potential regions (yellow color) surrounding the nitrogen atoms in the azo groups. This electronic distribution suggests the presence of significant electron-donating capacity through the nucleophilic centers of sufonic and azo groups[23].

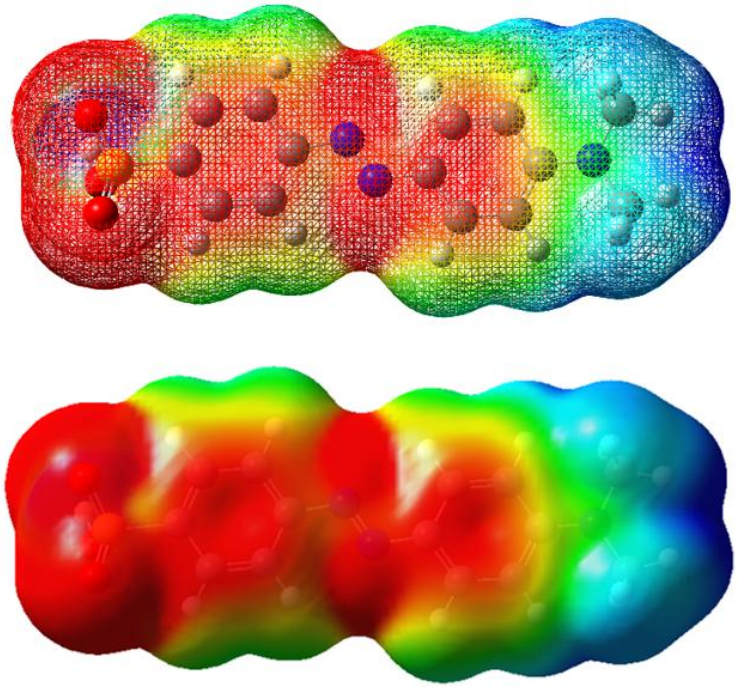


Figure IV.11. Electron density distributions in optimized molecular geometries of MO.

The interaction of MO with $HNT - PANI$ was explored through a computational study employing both DFT and molecular dynamics techniques. Analysis of interatomic distances (**Figure IV.12**) together with DFT-derived adsorption energies provides a detailed understanding of the MO/adsorbent interactions [23]. Interaction distances of 3.1–4.8 Å between raw HNT hydroxyl groups and the MO sulfonic anions, alongside an E_{int} of −21 kcal/mol, indicate that the adsorption is governed by weak van der Waals forces characteristic of physisorption. The negligible deformation energy at the given distances indicates that the interaction strength is insufficient to induce noteworthy structural rearrangements of the adsorbed molecule. By contrast, adsorption by PANI results in a considerable increase in

affinity ($E_{ads} = -34.8$ kcal/mol), accompanied by a decrease in interaction distance (**Figure IV.12.b**). The maximum distance between the electrophilic part of MO and the functional groups of the polymer is approximately $2.6 - 3.1$ Å. Weak hydrogen bonds and $\pi - \pi$ stacking interactions occur between the aromatic rings of the organic molecule and the polyaniline chain during adsorption. A pronounced qualitative change is evident in the HNT − PANI (**Figure IV.12.c**) with E_{int} of −82.6 kcal/mol and the maximum distance of $2.55 - 2.75$ Å. The nitrogen sites of the composite establish highly directional hydrogen bonds with the dye's functional groups. Concurrently, π–π stacking between aromatic rings contributes significantly to the stability of the MO/HNT − PANI system, preserving interplanar distances similar to those in MO/PANI.

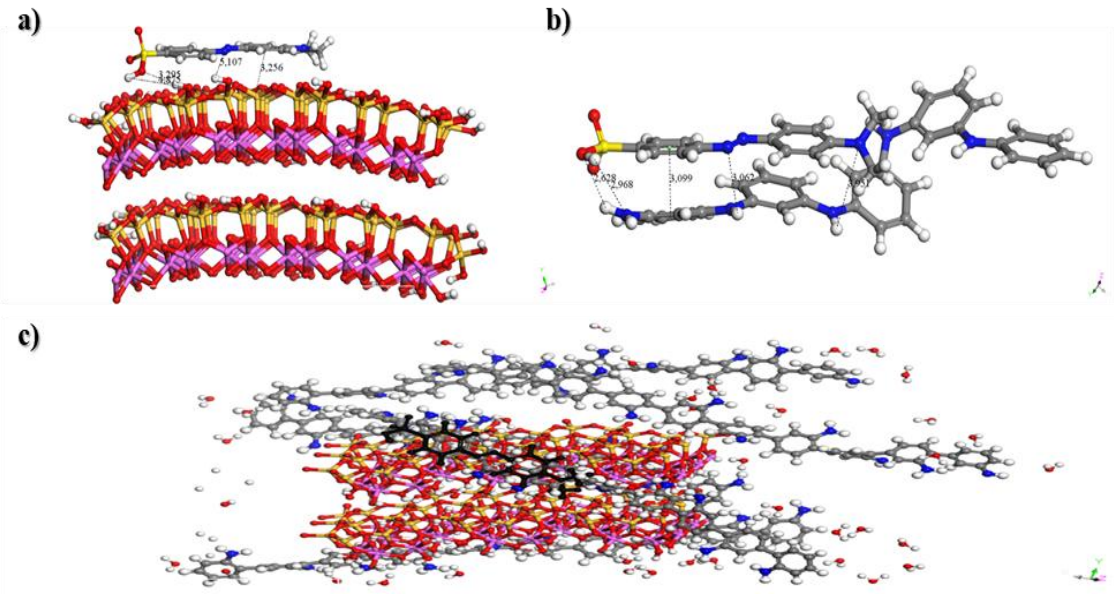


Figure 12. Optimized equilibrium configurations of MO on the investigated surfaces from DFT calculations. **a)** MO/HNT, **b**) MO/PANI, **c**) MO/HNT-PANI

The increase in deformation energy reflects a significant rearrangement to the structure of the MO molecules caused by the strong attraction between the adsorbate/adsorbent. This energy loss is largely offset by the increase in interaction energy, resulting in a total adsorption

energy E_{ads} of −48.6 kcal/mol. Accordingly, the MO adsorption by HNT − PANI lies at the boundary between strong physisorption and nascent chemisorption.

Furthermore, in aqueous conditions, adsorption remains favorable with only a slight decrease in the interaction and adsorption energies compared to the water molecules-free conditions (E_{ads} = −46.3 kcal/mol; E_{int}= −79.4 kcal/mol). The interaction is preserved despite competition from water molecules, with the latter participating in secondary hydrogen-bond networks that further stabilize the adsorption complex.

The combined geometric and energetic analyses confirm that cooperative interactions in HNT − PANI create a robust adsorption interface, maximizing MO binding and stability, consistent with experimental observations.

Table IV.6. Obtained adsorption energies and MO/surface distances from DFT calculations.

System	E_{ads} (kcal/mol)	E_{rigid} (kcal/mol)	E_{def} (kcal/mol)	E_{int} Kcal/mol)	$MO/surface$ distance (Å)
MO/HNT	**-12.4**	-8.6	**+3.8**	−21.0	3.2- 5.1
MO/PANI	**-34.8**	-22.7	**+12.1**	−56.9	2.60- 3.1
MO/HNT − PANI	**-48.6**	-35.2	**+13.4**	−82.6	2.55- 2.8
$MO/50H_2O$/HNT − PANI	-46.3	-33.1	+13.2	−79.4	-

3.4.Adsorption conditions optimization

The effect of HNT − PANI dosage and solution pH on the adsorption efficiency of MO was evaluated at an initial dye concentration of 100 mg/L **(Figure IV.13)**. The MO removal efficiency and adsorption capacity exhibited opposite trends as a function of HNT − PANI dosage (**Figure IV.13.a**). At low adsorbent loading, a limited number of available active sites resulted in relatively low MO removal percentage (26.6 %), while the adsorbed quantity of MO remained high due to the effective use of the adsorbent surface area. As the MO dose increased, the adsorption capacity gradually decreased and reached a minimum value of approximately 83mg/g, indicating that the available MO molecules were distributed over a larger mass of adsorbent. Beyond this dosage, the adsorbed quantity remained nearly constant, reflecting

saturation of accessible surface sites. In contrast, the removal efficiency continued to increase with increasing adsorbent mass due to the availability of numerous adsorption sites, allowing more uptake of MO from solution. An optimal adsorbent dosage of 40 mg was therefore identified for the MO/HNT − PANI system, providing high removal efficiency without compromising surface accessibility or material utilization.

Figure IV.13.b illustrates the impact of pH_{sol} on the adsorption of MO by the HNT − PANI composite.

The initial pH of the aqueous solution scarcely impacted the MO adsorbed quantity with a maximum variation in removal efficiency of ±10%. This suggests that electrostatic interactions are not a significant factor in the MO adsorption process under the conditions of our experiment. This is clearly evident at higher pH values, where both HNT − PANI and MO are negatively charged. However, the repulsive force does not impact the adsorption efficiency. Under acidic conditions, MO removal showed a slight increase, as the HNT–PANI adsorbent carries mostly positive surface charges, promoting favorable adsorption of the anionic dye. MO uptake on the mostly positively charged HNT − PANI adsorbent is easy. Nevertheless, at lower pH values, the stability of immobilized PANI may be reduced as a result of over-protonation and increased affinity for the aqueous phase. Accordingly, a neutral pH was chosen as the optimal condition, allowing for effective MO removal while maintaining the structural stability of the HNT − PANI composite without risk of polymer leaching. This condition ensures both high performance and practical relevance for potential applications in wastewater treatment. In this context, **Table IV.7** presents a comparative study of various modified clay-based adsorbents reported in the literature, in which HNT − PANI appears as a good candidate for dye adsorption.

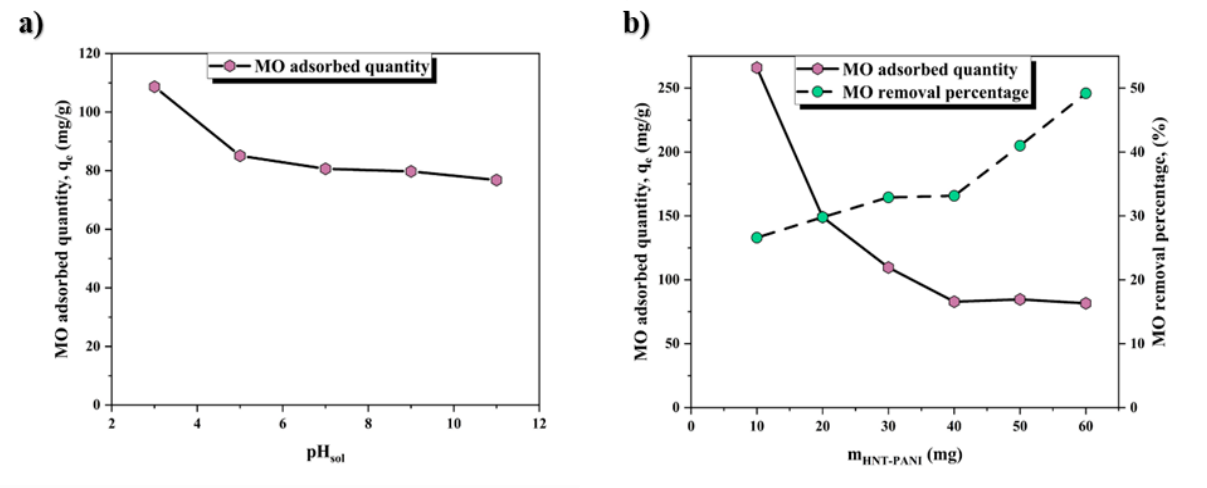


Figure IV.13. Influence of the operator conditions parameters on the adsorption of MO by HNT − PANI. **a**) effect of HNT − PANI dosage on the MO adsorbed quantity and removal efficiency, **b**) Effect of pH_{sol} on the MO adsorbed quantity ($V_{sol} = 100$ mL, $C_i = 100$ mg/L, $t_{cont} = 120$min).

Table IV.7. Comparative overview of modified clay-based adsorbents reported in the literature for MO removal.

Adsorbent	q_{max} (mg/g)	Ref.
HNT/PPy nanocomposite	214.6	[24]
Biopolymer-based composite adsorbent (BCA)	98.04	[25]
Sulfonated nanocellulose–PANI composite (SNC–PANI)	194.1	[26]
CTAB-modified raw clay (CTAB–Clay)	15.6	[27]
Organic-matter-modified clay (OM–Clay)	41.7	[28]
Chitosan-functionalized bentonite (CS–Bent)	20.1	[29]
Polypyrrole-decorated magnetic bentonite (PPy–MBent)	98.0	[30]
Chitosan/tannin/MMT film (CS/Tan/MMT)	57.4	[31]
HDTMA-modified halloysite nanotubes (HDTMA–HNT)	91.7	[32]
Chitosan–clay/Fe_3O_4 nanoparticles	130	[33]
HNT − PANI	**306.4**	**This work**

3.5.Adsorption mechanism

For the HNTs-PANI composite, as revealed in **Fig. IV.14** the adsorption mechanism becomes more complex due to the synergistic effect of both halloysite and PANI. In this system, the X-SO_3^- group primarily interacts with the NH_3^+ groups of the polyaniline backbone[34], while halloysite offers additional sites for adsorption through its external and internal surfaces. The mechanism involves a combination of electrostatic interactions, π-π interactions between the aromatic rings of PANI and the dye, Lewis acid-base interactions, and hydrogen bonding between the oxygen atom of the sulfonate (S=O) group in methyl orange and the hydrogen atom of the amine groups in PANI[35].

Overall, MO adsorption behavior reflects the interplay between surface area, pore structure, and chemical functionality. HNT enables rapid adsorption on relatively uniform sites but exhibits moderate total uptake[36]. PANI achieves higher capacity due to strong site-specific interactions despite slower adsorption rates. HNT-PANI successfully combines both advantages to deliver the highest q_e and adsorption efficiency, confirming the superiority of the composite in both capacity and kinetics.

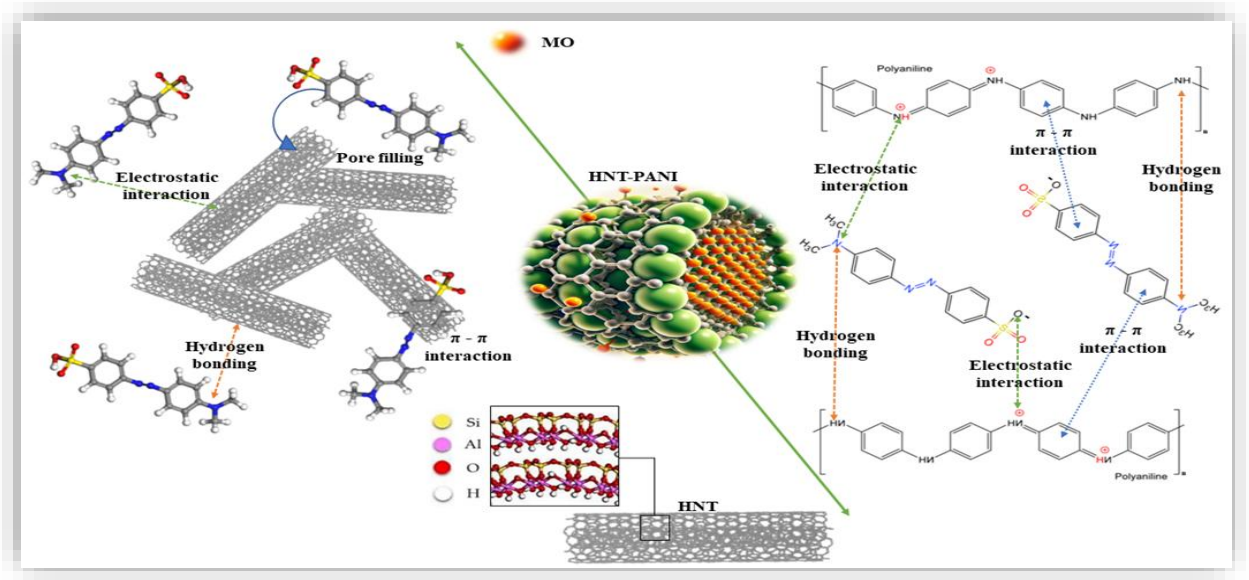


Figure IV. 14: Illustration of the possible interaction between HNTs/PANI composite and MO.

References of chapter IV

[1] P. Yuan *et al.*, "Changes in structure, morphology, porosity, and surface activity of mesoporous halloysite nanotubes under heating," *Respir. Care*, vol. 58, no. 3, pp. 561–573, 2013, doi: 10.1346/CCMN.2012.0600602.

[2] L. L. Chiara Ferlito, Carla Rizzo, Roufaida Merir, Giuseppe Cavallaro and G. L. Antonio Palumbo Piccionello, "Influence of Halloysite Nanotubes from different deposits on the degradation of organic molecules," *Journal of Building Engineering*, vol. c, p. 108404, 2024, doi: 10.1016/j.ceramint.2025.02.403.

[3] D. Sid *et al.*, "Improved biological performance of ketoprofen using novel modified halloysite clay nanotubes," *Appl. Clay Sci.*, vol. 216, no. October 2021, p. 106341, 2022, doi: 10.1016/j.clay.2021.106341.

[4] E. Gianni *et al.*, "New detail insight into Halloysite structure: Mechanism behind nanotubular morphology described by density functional theory and molecular dynamics supported by experiments," *J. Mol. Struct.*, vol. 1287, no. April, 2023, doi: 10.1016/j.molstruc.2023.135639.

[5] H. Huang *et al.*, "Facile preparation of halloysite/polyaniline nanocomposites via in situ polymerization and layer-by-layer assembly with good supercapacitor performance," *J. Mater. Sci.*, vol. 51, no. 8, pp. 4047–4054, 2016, doi: 10.1007/s10853-016-9724-y.

[6] A. K. T. Mohammad, A. S. Abdulhameed, and A. H. Jawad, "Box-Behnken design to optimize the synthesis of new crosslinked chitosan-glyoxal/TiO2 nanocomposite: Methyl orange adsorption and mechanism studies," *Int. J. Biol. Macromol.*, vol. 129, pp. 98–109, 2019, doi: 10.1016/j.ijbiomac.2019.02.025.

[7] S. Mihai, A. Bondarev, C. Călin, and E. E. Sîrbu, “Adsorbent Biomaterials Based on Natural Clays and Orange Peel Waste for the Removal of Anionic Dyes from Water,” *Processes*, vol. 12, no. 5, 2024, doi: 10.3390/pr12051032.

[8] I. Anastopoulos *et al.*, “A review on halloysite-based adsorbents to remove pollutants in water and wastewater,” *J. Mol. Liq.*, vol. 269, pp. 855–868, 2018, doi: 10.1016/j.molliq.2018.08.104.

[9] C. S. C. Chiew *et al.*, “Halloysite/alginate nanocomposite beads: Kinetics, equilibrium and mechanism for lead adsorption,” *Appl. Clay Sci.*, vol. 119, pp. 301–310, Jan. 2016, doi: 10.1016/j.clay.2015.10.032.

[10] D. Lacin and A. Z. Aroguz, “Kinetic studies on adsorption behavior of methyl orange using modified halloysite, as an eco-friendly adsorbent,” *SN Appl. Sci.*, vol. 2, no. 12, 2020, doi: 10.1007/s42452-020-03799-4.

[11] Y. Zhao, E. Abdullayev, A. Vasiliev, and Y. Lvov, “Halloysite nanotubule clay for efficient water purification,” *J. Colloid Interface Sci.*, vol. 406, pp. 121–129, 2013, doi: 10.1016/j.jcis.2013.05.072.

[12] Yu. V. Noskov, V. N. Bliznyuk, and A. A. Pud, “Polyaniline, Halloysite Nanotubes and Their Nanocomposite As Adsorbents for Organic Dyes,” *Polym. J.*, vol. 45, no. 3, pp. 221–231, 2023, doi: 10.15407/polymerj.45.03.221.

[13] A. Raghdi, M. Heraiz, M. Rasheed, and A. Keziz, “Investigation of halloysite thermal decomposition through differential thermal analysis (DTA): Mechanism and kinetics assessment,” *Journal of the Indian Chemical Society*, vol. 101, no. 11, p. 101413, Nov. 2024, doi: 10.1016/j.jics.2024.101413.

[14] L. Zhang, T. Wang, and P. Liu, “Polyaniline-coated halloysite nanotubes via in-situ chemical polymerization,” *Appl. Surf. Sci.*, vol. 255, no. 5 PART 1, pp. 2091–2097, 2008, doi: 10.1016/j.apsusc.2008.06.187.

[15] W. L. Zhang and H. J. Choi, “Fabrication of semiconducting polyaniline-wrapped halloysite nanotube composite and its electrorheology,” *Colloid Polym. Sci.*, vol. 290, no. 17, pp. 1743–1748, Nov. 2012, doi: 10.1007/s00396-012-2719-6.

[16] A. M. Zayed, M. S. M. Abdel Wahed, E. A. Mohamed, and M. Sillanpää, “Insights on the role of organic matters of some Egyptian clays in methyl orange adsorption: Isotherm and kinetic studies,” *Appl. Clay Sci.*, vol. 166, pp. 49–60, Dec. 2018, doi: 10.1016/J.CLAY.2018.09.013.

[17] F.-C. Wu, R.-L. Tseng, and R.-S. Juang, “Initial behavior of intraparticle diffusion model used in the description of adsorption kinetics,” *Chemical engineering journal*, vol. 153, no. 1–3, pp. 1–8, 2009.

[18] K. Imene *et al.*, “Thermal treatment of Cu-doped hydrotalcite-like adsorbents for improved removal of methyl orange from water,” *Sep. Purif. Technol.*, vol. 365, no. February, p. 132656, 2025, doi: 10.1016/j.seppur.2025.132656.

[19] N. Ayawei, A. N. Ebelegi, and D. Wankasi, “Modelling and Interpretation of Adsorption Isotherms,” *J. Chem.*, vol. 2017, 2017, doi: 10.1155/2017/3039817.

[20] A. Harrou, E. Gharibi, H. Nasri, and M. El Ouahabi, “Thermodynamics and kinetics of the removal of methylene blue from aqueous solution by raw kaolin,” *SN Appl. Sci.*, vol. 2, no. 2, 2020, doi: 10.1007/s42452-020-2067-y.

[21] S. El Bourachdi *et al.*, “Enhancing Graphene Oxide Production and Its Efficacy in Adsorbing Crystal Violet: An In-Depth Study of Thermodynamics, Kinetics, and DFT Analysis,” *International Journal of Chemical Engineering*, vol. 2024, 2024, doi: 10.1155/2024/8222314.

[22] S. Mutahir *et al.*, “Synthesis and Micromechanistic Studies of Sensitized Bentonite for Methyl Orange and Rhodamine-B Adsorption from Wastewater: Experimental and DFT-Based Analysis,” *Molecules*, vol. 27, no. 17, Sep. 2022, doi: 10.3390/molecules27175567.

[23] Q. Liang *et al.*, “Recent Design Principles and Construction Strategies of Polyaniline-Based Composites: Toward Electrochemical and Non-Electrochemical Adsorption Applications,” *Polymers (Basel).*, vol. 17, no. 23, Dec. 2025, doi: 10.3390/polym17233151.

[24] M. Zhang, L. Chang, and Z. Yu, “Fabrication of halloysite nanotubes/polypyrrole nanocomposites for efficient removal of methyl orange,” *Desalination Water Treat.*, vol. 110, no. 6, pp. 209–218, Apr. 2018, doi: 10.5004/dwt.2018.22220.

[25] P. Jamwal, S. Chauhan, K. Kumar, and G. S. Chauhan, “Fabricating pine needles derived spherical nanocellulose with polyaniline and montmorillonite clay for simultaneous removal of cationic and anionic dyes from binary mixtures,” *Int. J. Biol. Macromol.*, vol. 301, p. 140340, Apr. 2025, doi: 10.1016/j.ijbiomac.2025.140340.

[26] L. Zhang, P. Hu, J. Wang, Q. Liu, and R. Huang, “Adsorption of methyl orange (MO) by Zr (IV)-immobilized cross-linked chitosan/bentonite composite,” *Int. J. Biol. Macromol.*, vol. 81, pp. 818–827, Nov. 2015, doi: 10.1016/j.ijbiomac.2015.09.017.

[27] B. Abbou *et al.*, “Improved removal of methyl orange dye by adsorption using modified clay: Combined experimental study using surface response methodology,” *Inorg. Chem. Commun.*, vol. 155, p. 111127, Sep. 2023, doi: 10.1016/j.inoche.2023.111127.

[28] A. M. Zayed, M. S. M. Abdel Wahed, E. A. Mohamed, and M. Sillanpää, “Insights on the role of organic matters of some Egyptian clays in methyl orange adsorption: Isotherm and kinetic studies,” *Appl. Clay Sci.*, vol. 166, pp. 49–60, Dec. 2018, doi: 10.1016/j.clay.2018.09.013.

[29] Z. Ahamad and A. Nasar, “Polypyrrole-decorated bentonite magnetic nanocomposite: A green approach for adsorption of anionic methyl orange and cationic crystal violet dyes from contaminated water,” *Environ. Res.*, vol. 247, p. 118193, Apr. 2024, doi: 10.1016/j.envres.2024.118193.

[30] R. Liu, K. Fu, B. Zhang, D. Mei, H. Zhang, and J. Liu, “Removal of Methyl Orange by Modified Halloysite Nanotubes,” *J. Dispers. Sci. Technol.*, vol. 33, no. 5, pp. 711–718, 2012, doi: 10.1080/01932691.2011.579855.

[31] A. M. El Shafey *et al.*, “Removal of methyl orange from wastewater using sustainable and facilely synthesized weathered basalt/chitosan/polyaniline composites,” *Int. J. Biol. Macromol.*, vol. 335, p. 149151, Jan. 2026, doi: 10.1016/j.ijbiomac.2025.149151.

[32] A. Bassam, R. Bassam, M. El Alouani, Y. Rachdi, H. Saufi, and S. Belaaouad, “Synthesis of geopolymer powder and beads based on red clay waste for the adsorption of methyl orange dye from aqueous solutions: Characterization, application of response surface methodology, and cost analysis,” *Sustain. Chem. Pharm.*, vol. 39, p. 101575, Jun. 2024, doi: 10.1016/j.scp.2024.101575.

[33] Y. Dehmani *et al.*, “Synthesis and characterization of novel chitosan–clay coated iron oxide nanoparticles for optimized adsorption and mechanistic study of methyl orange in industrial wastewater,” *Int. J. Biol. Macromol.*, vol. 347, p. 150568, Feb. 2026, doi: 10.1016/j.ijbiomac.2026.150568.

[34] M. Duhan and R. Kaur, “Adsorptive removal of methyl orange with polyaniline nanofibers: an unconventional adsorbent for water treatment,” *Environmental Technology (United Kingdom)*, vol. 41, no. 23, pp. 2977–2990, 2020, doi: 10.1080/09593330.2019.1593511.

[35] W. L. Danbature, A. Kwaji, and I. A. Sarkinfawa, “Synthesis , Characterization And Methyl Orange Adsorption Kinetics By Thermally Activated Bentonite Clay,” no. February, 2025, doi: 10.53882/IJEASR.2024.1101005.

[36] M. A. U. R. AL-Kazragi, D. T. A. AL-Heetimi, and L. D. Wilson, “Adsorption of methyl orange on low-cost adsorbent natural materials and modified natural materials: a review,” *Int. J. Phytoremediation*, vol. 0, no. 0, pp. 1–30, 2023, doi: 10.1080/15226514.2023.2259989.



CHAPTER V



Chapter V: The removal of anionic and cationic dyes using novel adsorbent

1. Introduction

This chapter provides the conclusion of chapters III and IV about the use and modifications of raw halloysite nanotube to enhance the removal of anionic and cationic dyes (MB and MO), in addition this chapter provide a detailed description about the new synthesized materials (HNTs/PANI/SA) and was applied to remove both MO and MB from water sources, To the best of our knowledge, no studies have explored the application of combining the three mentioned materials into a single system. and to further grasp the physical characteristics of the novel composite several characterization techniques were employed: SEM, FTIR, DRX, ATG/DTA and BET techniques, a different approach was used to enhance the operation conditions (pH, adsorbent dosage, initial solution concentration and temperature) by applying both the Response of surface methodology (RSM-BBD) and artificial neural network (ANN) combined with hybrid optimization algorithms (grey wolf (GWO) and genetic (GA) algorithms), different models of kinetics and isotherms were applied and the interaction mechanisms was investigated.

2. Design of experiments

The adsorption process was optimized using a Box-Behnken Design (BBD) within the Response Surface Methodology (RSM) framework. This three-level factorial design (-1, 0, +1) was implemented to maximize the methylene blue removal efficiency MB% of the HNTs/PANI/SA composite as the target response. Four critical process parameters were selected as independent variables: (1) initial pH (A), (2) adsorbent dosage (b), (3) temperature (C), and (4) initial MB concentration (D).

The experimental ranges for each factor (**Table V.1**) were established through preliminary screening studies to ensure operational relevance. A total of 29 randomized runs were generated

based on eq (V.1) to account for experimental variability while maintaining statistical power. The quadratic model was expressed in eq (V.2)[1].

$N = 2k (k - 1) + C_0$ ……..…….……(V.1)

Where k is the factor number, and C_0 is the replicate number of the central points.

$Y= \beta_0 + \sum \beta i Xi + \sum \beta ii\ Xi^2 + \sum \beta ij\ Xi\ Xj$ ……(V.2)

In this equation, Y represents the predicted response corresponding to each level of the factors, β_0 denotes the constant coefficient, β_i refers to the linear coefficients, β_{ii} indicates the quadratic coefficients, and βij represents the interaction coefficients. Xi and Xj are the coded values of the independent variables[2].

Table V. 1: *Experimental range and levels of independent process variables.*

	Range and level		
Independent variable	-1	0	+1
PH	5	8	11
W (mg)	10	20	30
Temperature (°C)	20	30	40
C0 (mg/l)	100	200	300

The design consisted of 29 runs was carried out to optimize the levels of the selected independent factors, where A: pH (5-11), B: adsorbent dosage (10-30mg), C: Temperature (20-40°C) and D: initial solution concentration (100-300mg/l). all experiments were done in an 100ml Erlenmeyer flasks containing 50 ml of dye solution, the flasks were kept in an 25^0C and agitated at a fixed shaking speed of 250rpm at fixed shaking time of 3h, after 3h the adsorbent

was separated using centrifuges and MB concentration was measured using a UV-VIS Spectrophotometer (Shimadzu UV-1700 Pharma Spec) at maximum wave length of 664 nm.

The response MB% was determined using eq (V.3).

$$MB\ \% = \frac{C0-Ce}{C0} \times 100 \quad \text{.....(V.3)}$$

The adsorption capacity q (mg/g) of the composite was calculated by eq (V.4).

$$q = \frac{C0-Ce}{W} V \quad \text{..... (V.4)}$$

Where C_0 and $C_{t,e}$ are the concentrations of MB at time 0 and at time t respectively (mg/L), W is the adsorbent dosage (mg) and V represents the volume of solution (L)

The full BBD matrix and results of the experimental design are mentioned in **Table V.2**, the factors values are showed in uncoded unit.

Table V. 2: *BBD design matrix with experimental values.*

pH	Adsorbent dosage (mg)	Temperature (°C)	Concentration (mg/L)	Removal efficiency MB%
8	20	30	200	72.6394
8	20	30	200	76.2911
11	20	40	200	88.7581
8	20	40	100	83.0891
11	20	30	300	92.7296
8	20	30	200	74.9966
5	20	30	300	62.3586
8	20	30	200	76.3435
8	10	40	200	79.7382
11	20	30	100	89.2385
5	20	30	100	70.5981
8	10	20	200	78.3329

5	20	40	200	79.6541
8	10	30	100	85.1549
8	20	30	200	76.6123
8	20	20	100	89.5028
5	10	30	200	41.3164
5	30	30	200	68.8686
8	20	40	300	91.1922
8	20	20	300	89.751
11	10	30	200	80.4468
8	10	30	300	71.1746
8	30	30	300	93.9066
11	20	20	200	91.6286
8	30	20	200	92.9258
5	20	20	200	81.7559
8	30	40	200	94.1268
11	30	30	200	84.6265
8	30	30	100	90.3675

3. ANN-GWO & ANN-GA hybrid algorithms

Artificial neural networks (ANNs) represent a robust computational modeling approach inspired by the information processing mechanisms of the human brain[3]. Due to their ability to capture complex nonlinear relationships, ANNs are particularly effective in predicting the behavior of nonlinear systems. The efficiency of an artificial neural network (ANN) architecture is highly dependent on the optimal selection of weights and biases. However, manually determining these parameters through trial-and-error methods is not only computationally inefficient but may also yield suboptimal model performance. To mitigate these limitations, integrating a hybrid neural network architecture can significantly enhance both the predictive accuracy and computational efficiency of the system[4]. In contemporary computational intelligence research, nature-inspired metaheuristics have emerged as powerful tools for

optimization challenges. Among these, the Grey Wolf Optimization (GWO) algorithm has demonstrated remarkable efficacy in solving diverse optimization problems across various domains. This bio-inspired approach mimics the hierarchical hunting behavior of grey wolf packs, offering robust performance in complex solution spaces[5]. The GWO algorithm incorporates a four-tiered social hierarchy modeled after grey wolf packs, comprising alpha, beta, delta, and omega members. This hierarchical structure facilitates efficient optimization through three biologically-inspired hunting phases: (1) prey identification and search, (2) strategic encirclement, and (3) final exploitation through targeted attacks. These mechanisms collectively enable effective exploration and exploitation of the solution space[5]. A number of studies confirmed the efficacity of the GWO in solving optimization problems[6].

Likewise, Genetic algorithm (GA) is used in order to solve optimization problems, GA represents a population-based metaheuristic optimization technique inspired by principles of natural selection and Mendelian genetics. This evolutionary computation method operates through an iterative process that maintains a population of candidate solutions, each encoded as chromosomal strings using a defined alphabet. The algorithm employs biologically-inspired operators including mutation (random modification of individual solutions) and crossover (recombination of parental solutions) to successively generate improved solution variants. by systematically exploring the solution space through these mechanisms, GA effectively identifies optimal or near-optimal solutions to complex optimization problems[7]. Several researches employed the GA to optimize dye adsorption efficiency such as **Nader et al**[8], reported the exploitation of RSM-BBD, GA and ANN to describe the adsorption of MB on the surface of sodium alginate-kaolin composite, where results showed that ANN is best fit with a correlation coefficient of 0.97.

The two hybrid algorithms ANN-GA and ANN-GWO were employed in this study to describe and optimize the removal efficiency of MB by HNTs/PANI/SA.

In order to model and optimize the dye adsorption from aqueous solutions, a hybrid artificial neural network-grey wolf optimization algorithm (ANN-GWO) and artificial neural network-genetic algorithm (ANN-GA) approaches were implemented. The neural architecture employs a four-layer feedforward topology (4-H-1), where H represents the optimized number of hidden neurons, as illustrated in **Fig. V.1**. This configuration enables comprehensive analysis of the adsorption data through supervised learning while benefiting from GA's and GWO's enhanced optimization capabilities[9].

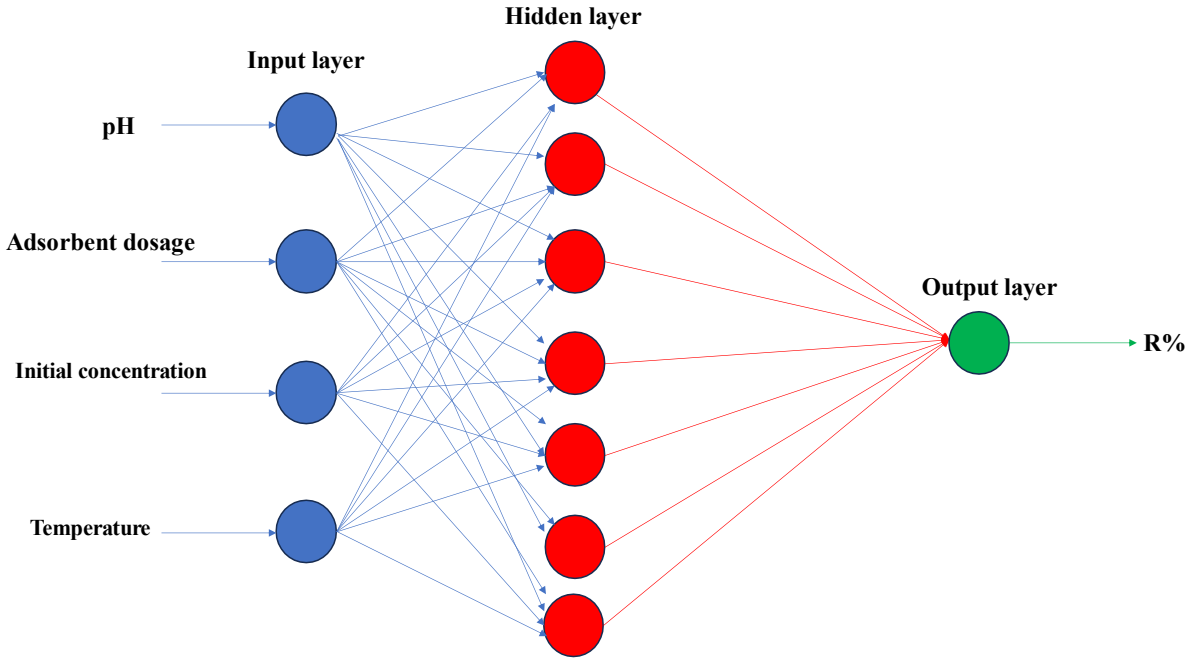


Figure V. 1: *Schematic diagram of the ANN model.*

The neural network architecture incorporated four input neurons representing key adsorption parameters: solution pH (A), adsorbent dosage (B), temperature (C), and initial concentration (D). A single output neuron quantified methylene blue removal efficiency (R%). The hidden layer neuron count (H) was identified as a critical hyperparameter significantly influencing model performance. An optimal H-value was determined through systematic trial-and-error optimization to maximize prediction accuracy[10].

The network employed distinct transfer functions for different layers: a tangent sigmoid (tansig) activation function in the hidden layer demonstrated superior nonlinear mapping capabilities, while a linear (purelin) function at the output layer maintained appropriate scaling. For enhanced optimization, genetic algorithm (GA) and grey wolf optimizer (GWO) techniques were implemented, with all computational procedures executed using MATLAB 2024 software.

4. Results and discussion

4.1.Choice of adsorbent

To validate the synergistic effects arising from the incorporation of individual adsorbents (HNTs, PANI, and SA) within the HNTs/PANI/SA composite, as well as its efficiency in adsorbing both cationic and anionic contaminants, systematic adsorption experiments were conducted. The study comparatively assessed the performance of HNTs, PANI, HNTs/PANI, HNTs/SA, and the composite HNTs/PANI/SA in removing the cationic model (Methylene Blue, MB) and anionic model (Methyl Orange, MO) dyes from aqueous solutions (**Fig. V2**).

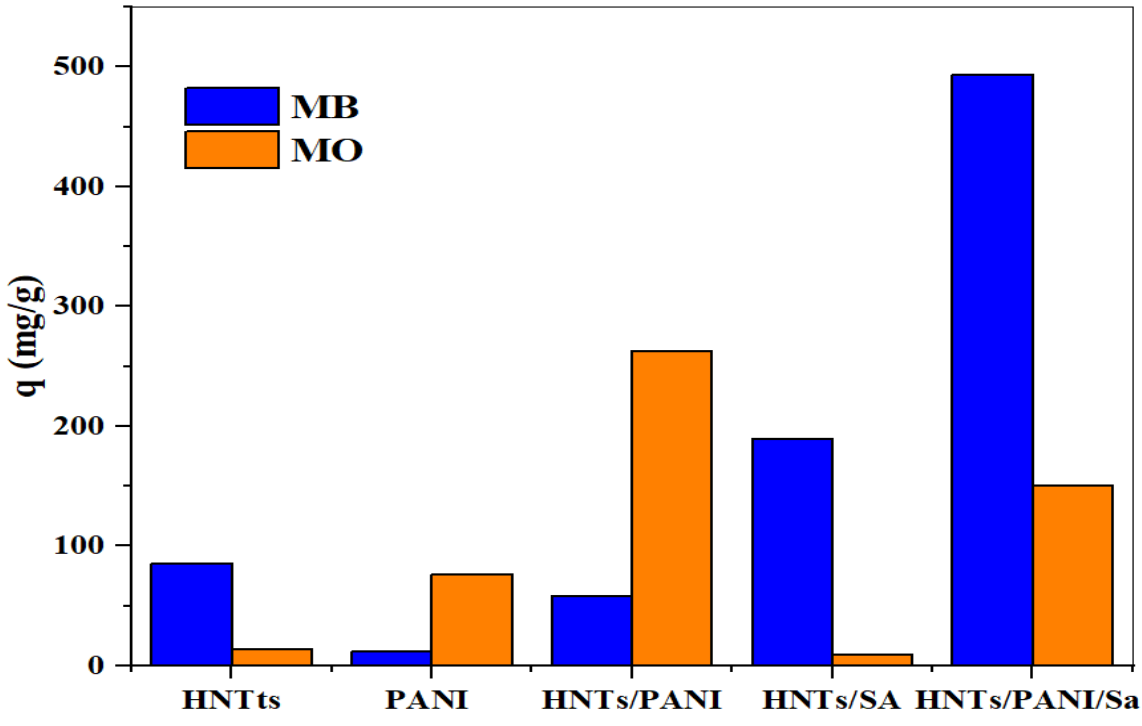


Figure V. 2: *Different materials adsorption capacities for MB and MO.*

The adsorption studies revealed significant differences in performance among the tested materials. For MB, the HNTs/PANI/SA composite demonstrated the highest adsorption capacity (493.87 mg/g), substantially outperforming HNTs/SA beads (189.5 mg/g) and raw HNTs (85.7 mg/g). In contrast, for MO, PANI alone showed moderate adsorption (76.69 mg/g), while HNTs/PANI exhibited improved uptake (263 mg/g). The HNTs/PANI/SA composite, though slightly lower in MO adsorption (150.55 mg/g) compared to HNTs/PANI, still displayed enhanced performance over PANI alone, confirming the beneficial role of PANI incorporation.

These results highlight the synergistic enhancement of the combination of HNTs, PANI, and SA significantly boosted MB adsorption, suggesting strong electrostatic and structural interactions, in addition the competitive site occupation noted in the slight reduction in MO adsorption for HNTs/PANI/SA compared to HNTs/PANI may be due to PANI partially blocking accessible sites in the composite. Nevertheless, the overall improvement over PANI alone underscores PANI's contribution to adsorption efficiency.

Given its superior MB adsorption performance, the HNTs/PANI/SA composite was selected for further detailed investigation in this study. The following sections focus exclusively on MB adsorption mechanisms, kinetics, and optimization using this novel adsorbent.

4.2.Characterization

SEM analysis was conducted to characterize the surface morphology of PANI, HNTs/PANI, HNTs/SA, and HNTs/PANI/SA composites. As shown in **Fig. V.3**, the HNTs/PANI composite exhibited a rough, porous surface with a modified nanotubular structure, where the original distinct tubular morphology of HNTs was no longer observable. This morphological transformation confirms successful surface functionalization with PANI[11].

Fig. V.3 presents SEM micrographs of HNTs/PANI/SA composite beads, comparing their surface characteristics before and after methylene blue (MB) adsorption, we can observe in the Pre-adsorption **(Fig. V.3e)**: The beads displayed a highly rough and porous surface texture, optimal for dye adsorption due to its large surface area and accessible active sites. However, in Post-adsorption **(Fig. V.3f)**: The surface morphology appeared significantly smoother, suggesting pore occupation and surface coverage by adsorbed MB molecules. This morphological change provides direct evidence of successful dye uptake and interaction with the composite's active sites[12].

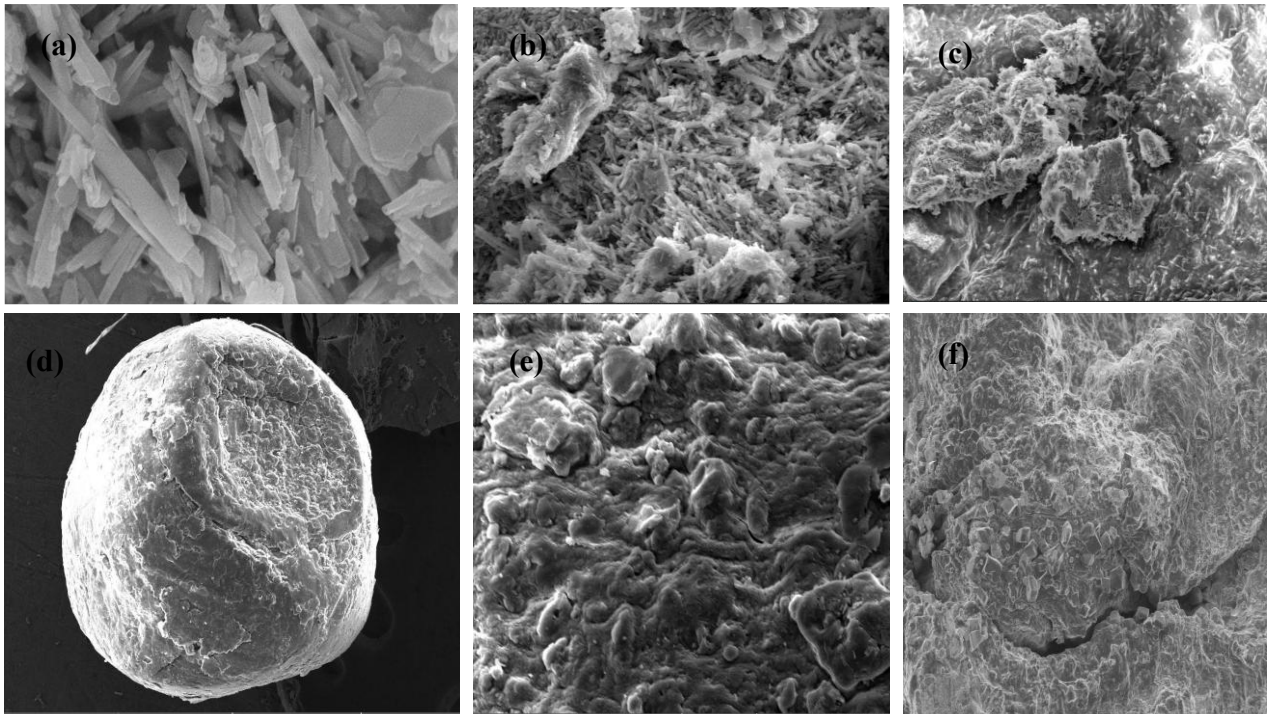


Figure V. 3: *SEM images of a). HNT, b). HNT-PANI, c). HNT-SA, d) HNT-PANI-SA beads, e) HNT-PANI-SA surface before adsorption and f) HNT-PANI-SA surface after adsorption*

Fig. V.4 displays the FT-IR spectra of HNTs, PANI, SA, HNTs/PANI and HNTs/SAg composite, and HNTs/PANI/SA. The HNTs spectrum exhibits two prominent absorption bands at 3690 cm^{-1} and 3627 cm^{-1}, assigned to the hydroxyl groups on the inner aluminol surfaces[13]. A broad absorption band at 3459 cm^{-1} arises from O–H stretching vibrations, suggesting the presence of interlayer water molecules, while deformation vibrations of H–O–H bonds appear

in the 1500–1700 cm^{-1} region. Additional bands at 1020 cm^{-1} (Si–O–Si asymmetric stretching) and 920 cm^{-1} (Al–O–H bending) further confirm the HNTs structure[14].

In the HNTs/PANI composite, new characteristic peaks emerge at 1639 cm^{-1}, 1516 cm^{-1}, and 1308 cm^{-1}, corresponding to PANI vibrational modes. The band at 1212 cm^{-1} is attributed to N=Q=N stretching (where Q denotes the quinoid ring), a distinctive feature of PANI's emeraldine base form[15]. Additionally, N–H stretching vibrations appear in the 3600–3700 cm^{-1} range, while absorptions at 1589 cm^{-1} (C=C aromatic, benzenoid) and 1516 cm^{-1} (C=N, quinoid) further confirm PANI's presence[16].

The HNTs/PANI/SA spectrum retains the 1020 cm^{-1} band (Si–O–Si), confirming HNTs' structural integrity. Peaks at 1600 cm^{-1} and 1300 cm^{-1} correspond to PANI vibrations, while the characteristic large bond of SA observed at 3505 was shifted to 3300 cm-1 for HNT-SA, then almost disappeared at 3360 cm^{-1} for HNT-PANI-SA spectrum[17]

The small pic at 2926 in the SA spectrum has disappeared in the HNT-SA and HNT-PANI-SA spectra. The other characteristics pics of SA were shifted in the spectrum of HNT-SA.

The characteristic pics of HNT at 3700 and 3627 were observed in HNT-SA and disappeared in HNT-PANI SA, as for the characterisric bonds for HNT at 1030 it still shown in HNT-SA and HNT-PANI-SA with a small shift.broad band at 3360 cm^{-1} signifies O–H stretching from SAg.

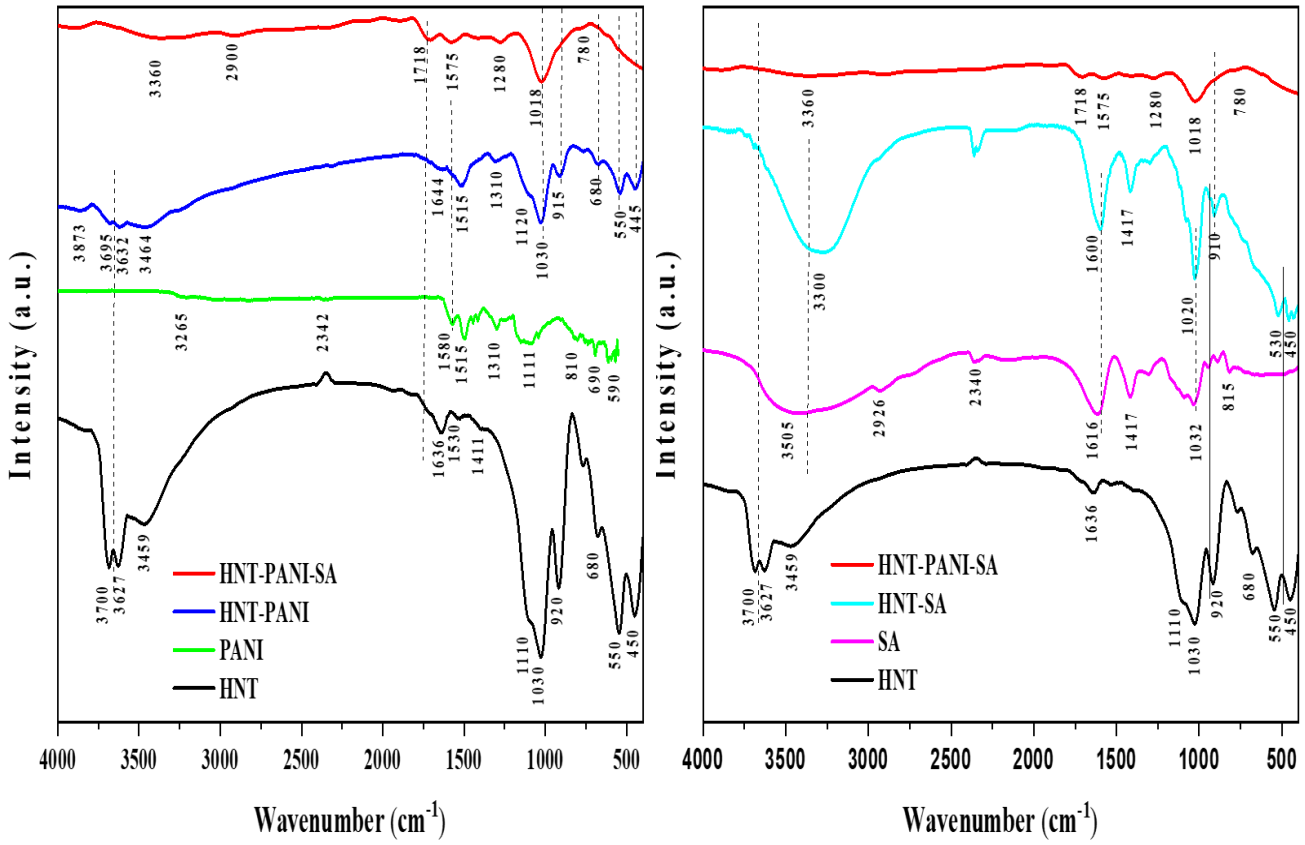


Figure V. 4: *FTIR spectrum for HNT-PANI-SA, SA, HNT-PANI, HNT-SA, PANI and HNT.*

Fig. V.5 presents the XRD patterns of HNTs, PANI, and the HNTs/PANI composite. The HNTs spectrum exhibits a prominent peak at 12.27° (2θ), characteristic of dehydrated halloysite, corresponding to a basal spacing of 7.12 Å (d = 0.712 nm)[18]. Distinct halloysite reflections are observed at 2θ = 13.0°, 20.5°, and 29.0°[19], whereas the HNTs/PANI composite displays reduced peak intensities and slight shifts to 12.0°, 20.0°, and 27.0°. This displacement suggests the intercalation of PANI chains into the interlamellar spaces of HNTs, consistent with the effects of in situ polymerization. The close alignment of these diffraction profiles with literature data confirms the successful functionalization of HNTs with PANI[20].

SA a semicrystalline polymer, does not exhibit discernible diffraction peaks in the analyzed range. The HNTs/PANI/SA spectrum retains characteristic HNTs and PANI reflections, alongside multiple peaks attributable to kaolinite impurities. A minor peak at 40.0° (2θ) may arise from structural defects associated with carbonaceous residues.

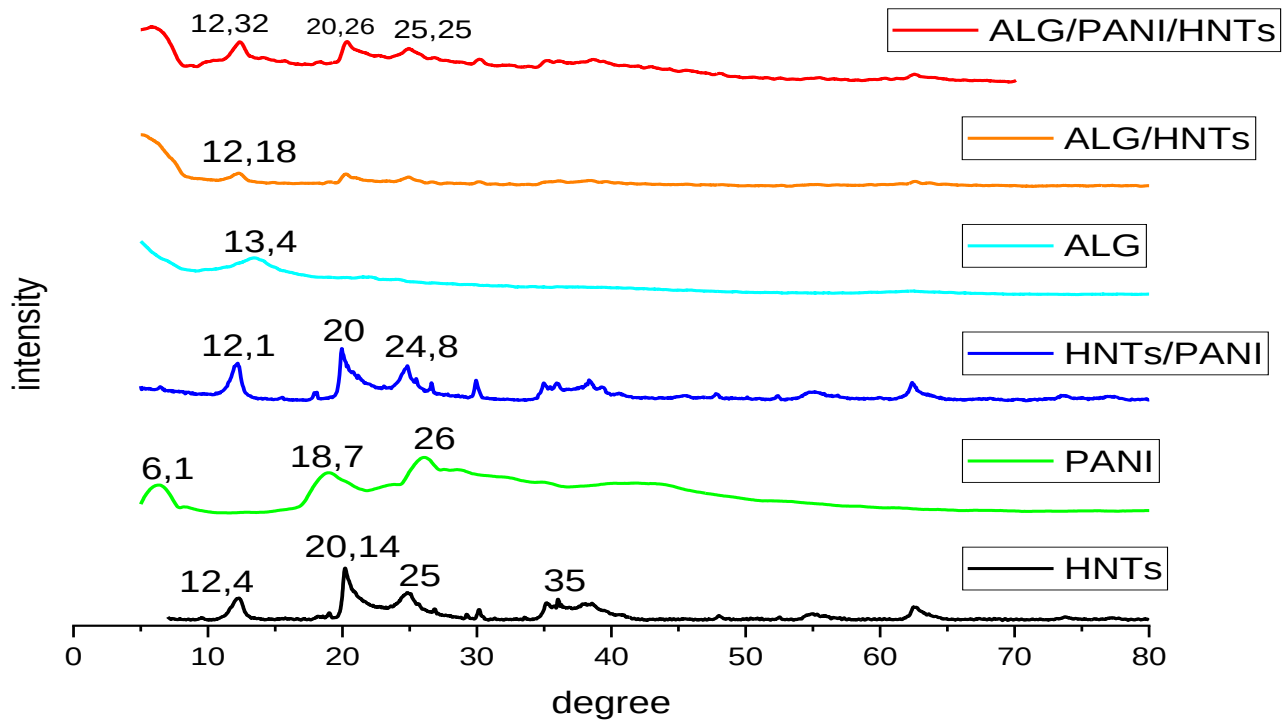


Figure V. 5: *XRD patterns for HNTs/PANI/SA, HNTs/SA, SA, HNTs/PANI, PANI and HNTs.*

As illustrated in **Fig. V.6**, TGA was employed to evaluate the weight composition and thermal stability of HNTs, PANI, and the HNTs/PANI composite. The HNTs/PANI composite exhibited a weight-loss profile similar to pure halloysite[21], with two additional degradation stages,

- **400–550 °C**: Corresponding to polymer backbone decomposition.
- **>600 °C**: Attributable to oligomer degradation.

Initial mass loss (<120 °C) reflected the evaporation of adsorbed and interlayer water, while complete HNTs decomposition occurred by 550 °C.

Thermal Behavior TGA/DTA analysis of the HNTs/PANI/SA composite (**Fig. V.6**) revealed a two-stage degradation process:

- **Stage 1 (50–310 °C)**: 38% mass loss, driven by moisture and volatile component evaporation.
- **Stage 2 (>310 °C)**: Sharp decline due to material decomposition[22].

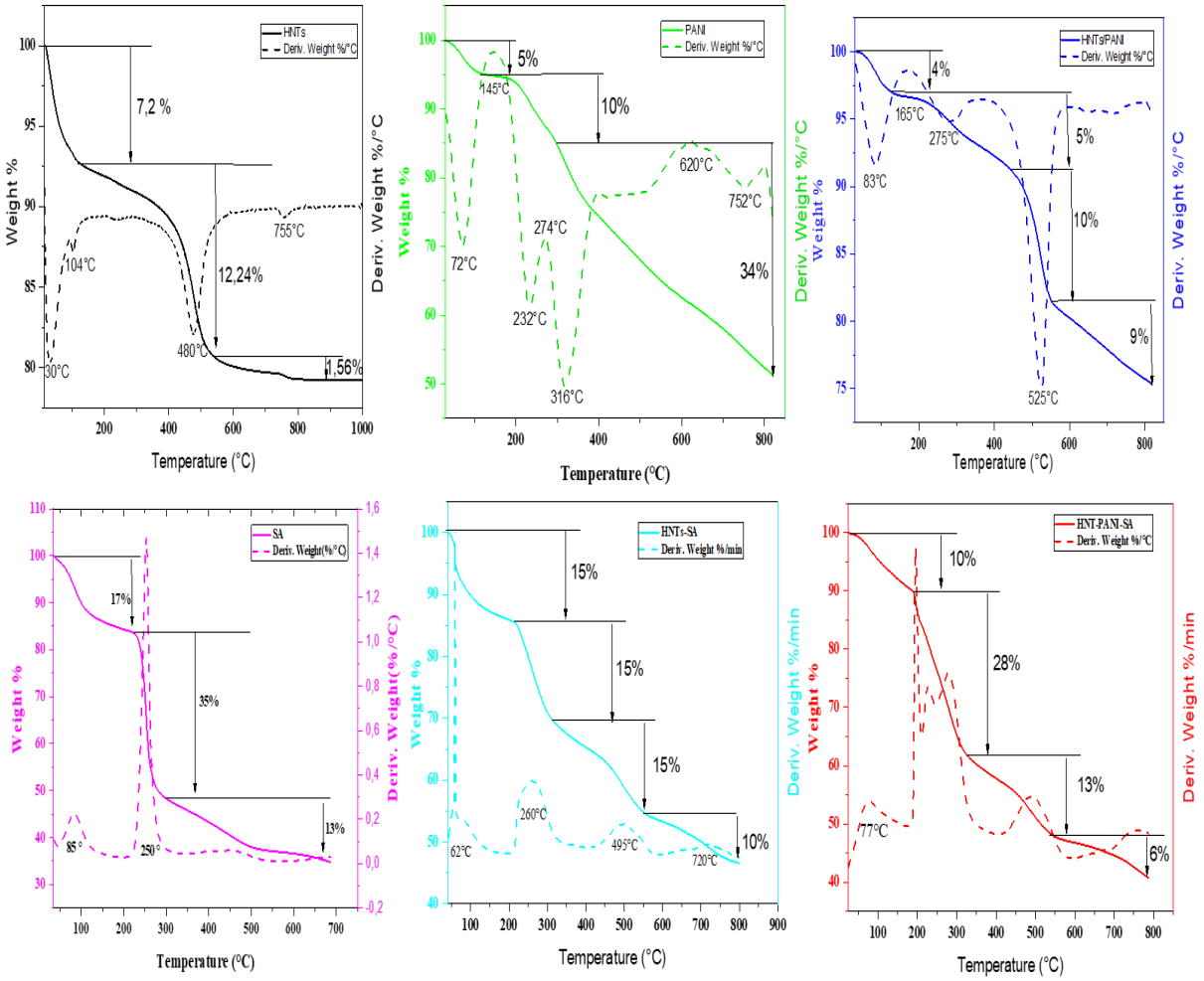
The DTA curve exhibited three endothermic peaks:

i) **77 °C**: Dehydration (moisture/volatile removal).

ii) **250 °C**: PANI chain dissociation**.**

iii) **490 °C**: Alginate matrix degradation[23].

These findings demonstrate the composite's thermal resilience, with degradation requiring elevated temperatures, underscoring its stability under thermal stress



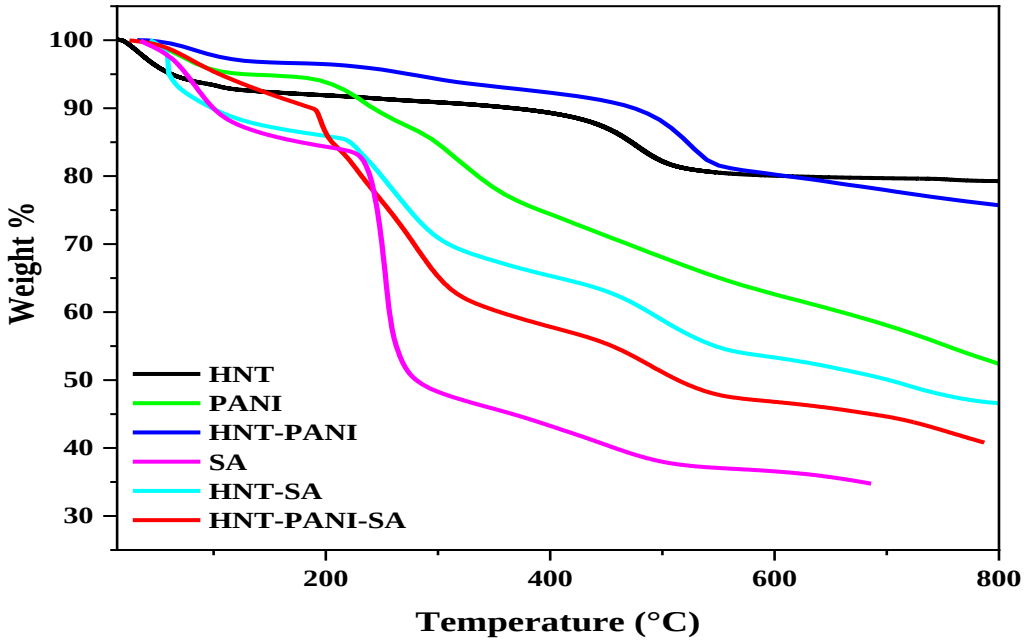


Figure V. 6: *TGA /DTA curves of a) HNTs, b) PANI, c) HNTs/PANI, d) HNTs/SA and e) HNTs/PANI/SA.*

Fig. V.7 presents the N_2 adsorption-desorption isotherms of HNTs, PANI, HNTs/PANI, and HNTs/PANI/SA composites. All materials exhibit Type IV isotherms (IUPAC classification) [7], confirming their mesoporous nature (2-50 nm pore size). BET analysis revealed significant differences in textural properties among the samples (**Table V.3**). While pristine HNTs demonstrated a high surface area (185 m^2/g), small pore diameter (11.5 nm), and substantial pore volume (0.21 cm^3/g) - consistent with literature reports[24]The HNTs/PANI composite exhibited a reduced surface area (34.47 m^2/g), increased pore diameter (21.32 nm), and a lower pore volume (0.184 cm^3/g). This reduction suggests successful PANI incorporation, where polymer chains occupy HNTs' active sites, resulting in comparable surface areas between HNTs/PANI and pure PANI.

Further modification with SA produced HNTs/PANI/SA beads with dramatically decreased surface area (2.175 m^2/g) and pore volume (0.0174 cm^3/g), though maintaining a large pore diameter (32.04 nm). This textural reduction likely stems from increased cross-linking density within the composite matrix. Notably, despite these changes, the HNTs/PANI/SA system retains

sufficient surface area for effective molecular adsorption, particularly for methylene blue (MB) dye molecules.

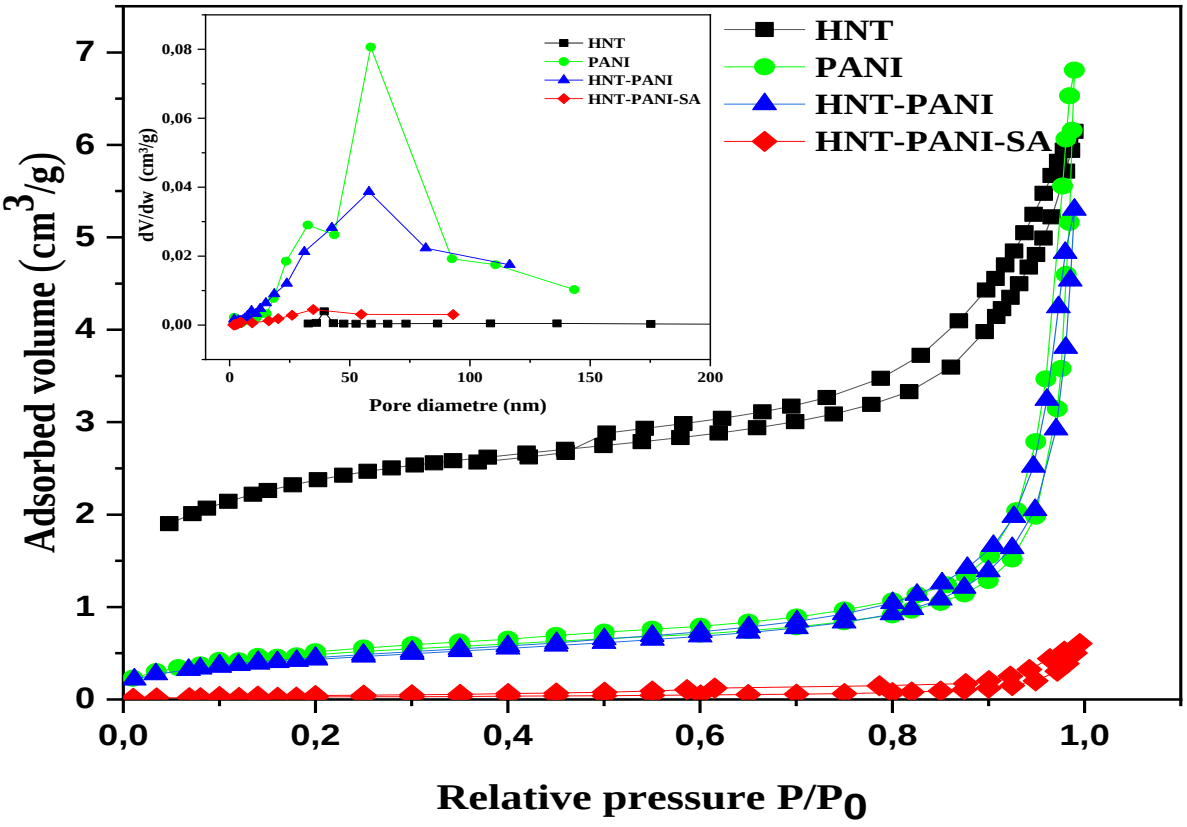


Figure V. 7: *N_2 adsorption-desorption isotherms for HNTs, PANI, HNTs/PANI and HNTs/PANI/SA.*

Table V. 3: *The elemental analysis, and textural properties of HNTs, PANI, HNTs/PANI and HNTs/PANI/SA.*

Surface properties	HNTs	PANI	HNTs/PANI	HNTs/PANI/SA
Total pore volume (cm^3/g)	0.21	0.24	0.184	0.0174
BET surface area (m^2/g)	185.4	37.9	34.47	2.175
Mean pore diameter (nm)	11.5	24.9	21.32	32.0466

4.3. Box Behnken design

The effects of key operational parameters including initial pH, adsorbent dosage, temperature, and initial MB concentration on methylene blue removal efficiency were systematically investigated using a Box-Behnken Design (BBD) approach. The model's statistical significance was rigorously evaluated through analysis of variance (ANOVA), with detailed results presented in **Table V.4**. The BBD model demonstrated strong predictive capability, as evidenced by an F-value of 13.91 and a highly significant p-value (0.0001), confirming the model's reliability for describing the adsorption process[25].

The model's goodness-of-fit was further supported by a coefficient of determination (R^2) of 0.8682, indicating an acceptable agreement between experimental observations and model predictions. The adjusted R^2 value (0.8058) showed good consistency with the predicted R^2 (0.6093), validating the model's robustness. Moreover, the adequate precision value of 15.159 substantially higher than the threshold of 4 confirmed the model's strong signal-to-noise ratio and its suitability for effective design space exploration[26].

The validity of the Box-Behnken Design (BBD) model was further substantiated through graphical diagnostic methods, including residual distribution analysis and experimental-predicted value correlation. As shown in **Fig. V.8(a)**, the normal probability plot of residuals exhibited a linear trend along the theoretical distribution line, confirming the normality and independence of residuals. **Fig. V.8(b)** demonstrates the model's predictive accuracy through the close alignment of data points along the 45° reference line, indicating strong agreement between experimental MB removal efficiencies and model predictions. These complementary graphical analyses collectively validate the BBD model's statistical adequacy and its capability to accurately simulate the adsorption process, confirming proper error structure, absence of systematic bias, and robust predictive performance within the investigated experimental domain[27].

Table V. 4: *ANOVA results for MB removal efficiency.*

Source	Sum of squares	df	Mean square	F-value	p-value	
Model	3203.44	9	355.94	13.91	< 0.0001	significant
A-pH	1258.22	1	1258.22	49.17	< 0.0001	
B-m	655.02	1	655.02	25.60	< 0.0001	
C-T	4.49	1	4.49	0.1754	0.6801	
D-C	3.90	1	3.90	0.1523	0.7007	
AB	136.57	1	136.57	5.34	0.0323	
BD	76.73	1	76.73	3.00	0.0995	
A^2	76.97	1	76.97	3.01	0.0990	
C^2	696.73	1	696.73	27.23	< 0.0001	
D^2	263.02	1	263.02	10.28	0.0047	
Residual	486.20	19	25.59			

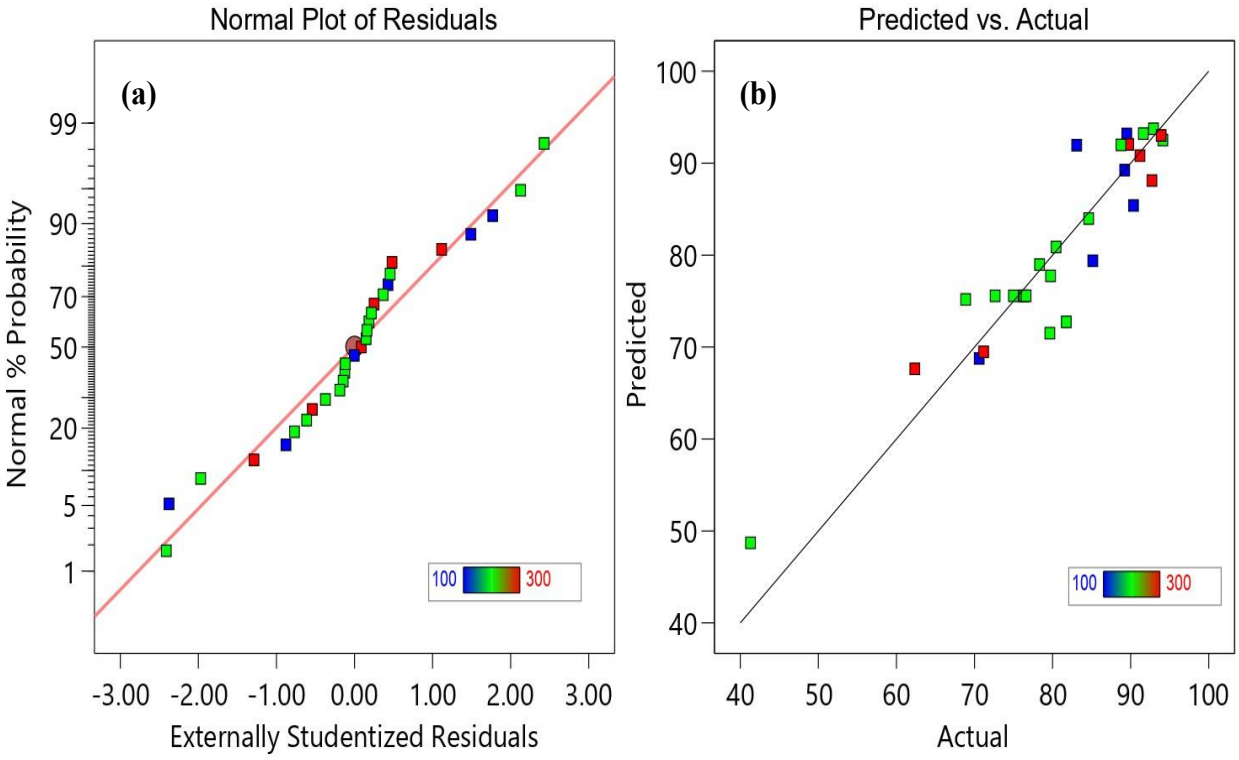


Figure V. 8: *(a) Normal probability plot of residuals for MB% (b) plot of the relationship between the predicted and actual values of MB%.*

4.4. System Performance as a Function of Process Variables

4.4.1. Effect of Solution pH on Adsorption Mechanism

This study investigates the pH_pzc and the influence of solution pH on the adsorption performance of the cationic dye MB onto HNTs/PANI/SA beads. The relevant results are illustrated in Fig. V.9. The pH_pzc of the composite adsorbent was found to be 5.2, indicating that the surface acquires a net negative charge at pH values higher than this threshold. Moreover, under alkaline conditions, the adsorption process is further enhanced by the deprotonation of amine functional groups (–NH) present on the adsorbent surface, which arises from the incorporation of PANI. This deprotonation increases electrostatic attraction toward the positively charged MB molecules [23].

This study examines the pH dependent adsorption behavior of MB on HNTs/PANI/SA beads, focusing on the point of zero charge (pHpzc = 5.2) and its implications. When the solution pH exceeds MB's pKa (4-4.5), deprotonation of amine groups increases the adsorbent's negative surface charge, enhancing electrostatic attraction with cationic MB and improving adsorption capacity. Conversely, at pH values below the pHpzc, the surface becomes positively charged, creating repulsive forces with MB that reduce adsorption efficiency. These charge-dependent interactions are clearly demonstrated in **Fig. V.10**, which shows increasing MB removal efficiency with rising pH, highlighting the critical role of pH in controlling the adsorption process through modulation of surface charge characteristics. Notably, the maximum removal efficiency is achieved at a pH of 8.22, However, at elevated pH levels, the beads experience degradation, resulting in desorption of the adsorbate[4], [23].

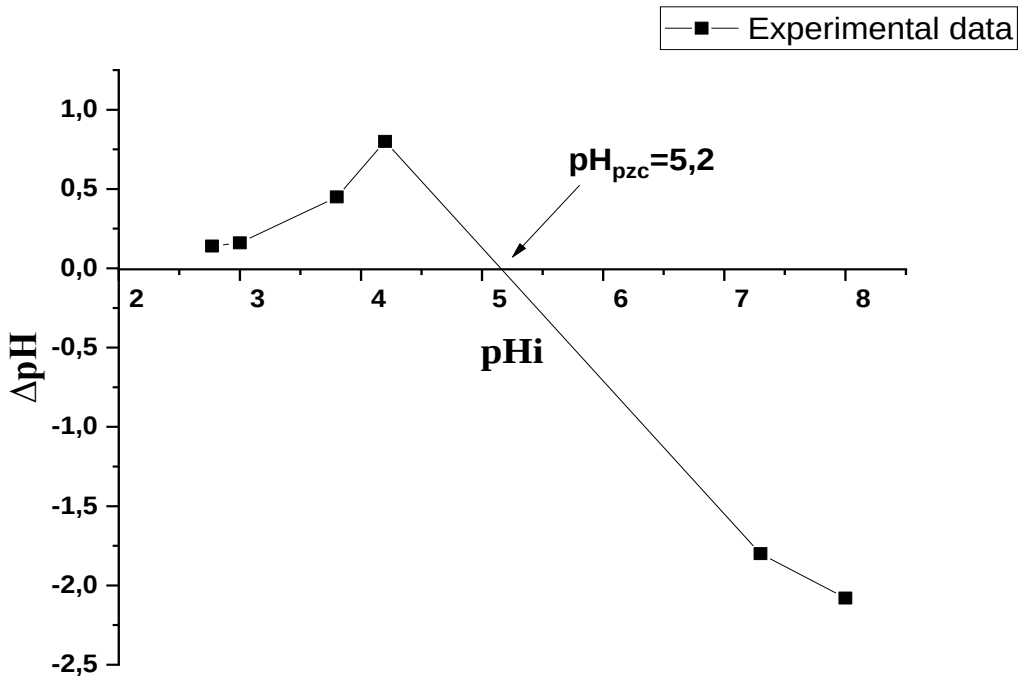


Figure V. 9: *pHpzc of HNTs/PANI/SA composite.*

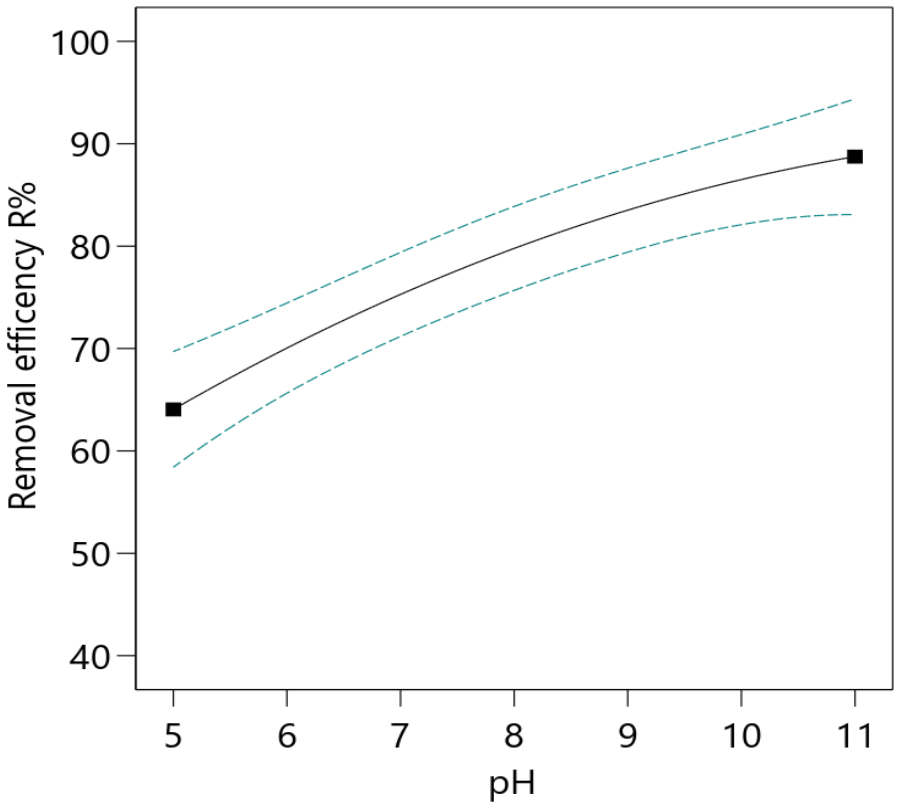


Figure V. 10: *pH effect on the removal of MB.*

4.4.2. Effect of adsorbent dosage

The study systematically evaluated the impact of adsorbent dosage on MB removal efficiency using HNTs/PANI/SA beads. Experimental results demonstrated that increasing the adsorbent quantity from 10 to 30 mg enhanced the MB removal percentage from 62% to 80%, attributable to greater surface area availability and increased active site density. However, this dosage elevation concurrently caused a significant decrease in adsorption capacity (q_e), This inverse relationship stems from reduced concentration gradient driving force at higher dosages, where near equilibrium conditions between solution and adsorbent surfaces were established within the 24-hour contact period, thereby diminishing the thermodynamic potential for further MB uptake[28].

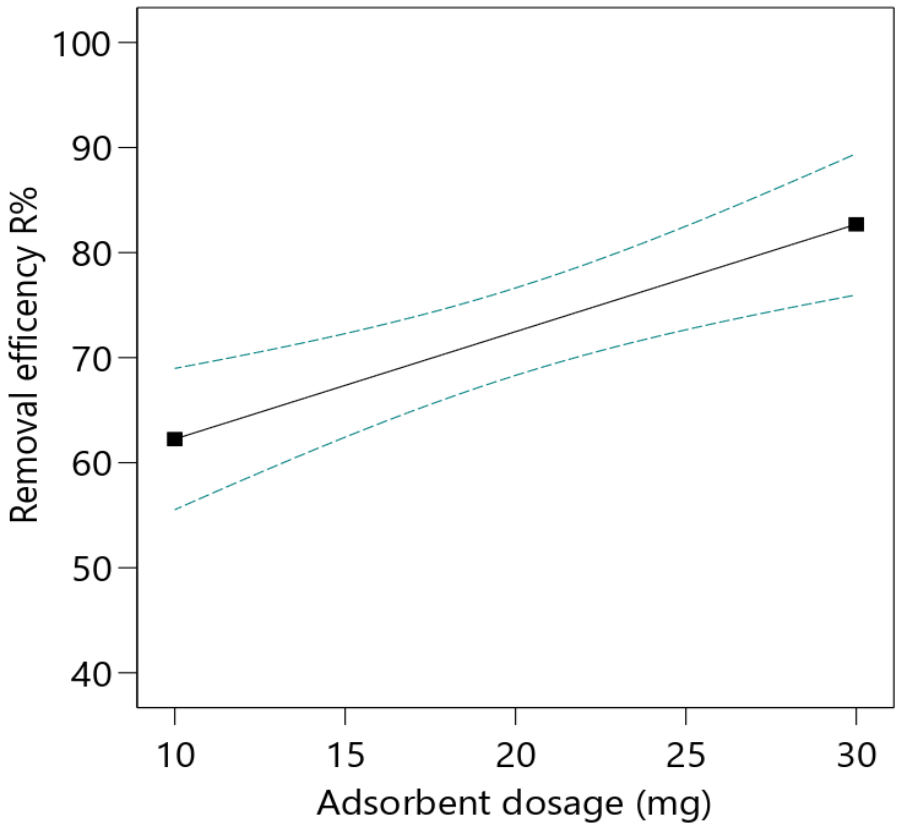


Figure V. 11: *pH effect on the removal of MB.*

4.4.3. Effect of initial concentration

The adsorption performance of HNTs/PANI/SA composite was evaluated across varying initial MB concentrations (100, 200, and 300 mg/L) over a 120-minute contact period. Kinetic profiles revealed distinct adsorption trends at each concentration, with the composite demonstrating exceptional removal capacities throughout the tested range. These results confirm strong adsorbate-adsorbent interactions facilitating efficient MB sequestration. The observed concentration dependence aligns with established mass transfer principles, where higher initial concentrations (300 mg/L) enhance the driving force for adsorption, as evidenced by increased uptake rates compared to lower concentrations (100 mg/L). This phenomenon is attributed to [29]:

- Greater collision frequency between MB molecules and active sites.
- Improved concentration gradient across the liquid-solid interface.
- Enhanced diffusion kinetics at elevated concentrations.

4.5. Interaction effects on response and process optimization

The response surface methodology (RSM) analysis presented in **Fig. V.12** highlights significant interactive effects between solution pH and adsorbent dosage, as well as between temperature and adsorbent dosage. The three-dimensional surface plots indicate that optimal adsorption efficiency is attained under conditions of alkaline pH (8–11) and moderate adsorbent dosage, which facilitate the protonation of active surface functional groups, thereby enhancing electrostatic attraction between the cationic methylene blue (MB) and the adsorbent. Similarly, elevated temperatures coupled with appropriate adsorbent dosages contribute to improved adsorption performance, likely due to increased molecular diffusion rates and enhanced interaction kinetics between MB molecules and the active sites on the adsorbent surface.

The nonlinear curvature of response surfaces and significant contour distortions ($p < 0.05$) quantitatively validate the existence of local maxima in the design space and the statistical significance of quadratic terms in the regression model[2].

the quadratic interaction terms (AC, AD, BC, and CD) demonstrated statistically insignificant effects on adsorption capacity, as evidenced by P-values above the critical threshold ($P > 0.05$).

The regression model generated by the design software provides a quantitative representation of the adsorption process, where the sign and magnitude of each coefficient reflect its influence on the response variable. Positive coefficients indicate favorable effects on adsorption capacity, while negative values denote inhibitory impacts, with the absolute value representing the relative strength of each factor. These coefficients demonstrate excellent agreement with the trends observed in the 3D response surface plots, confirming the model's validity.

$$Y = +75.57 + 10.24\,A + 7.39\,B - 0.6115\,C - 0.5699\,D - 5.84\,AB + 4.38\,BD - 3.38\,A^2 + 10.18\,C^2 + 6.25\,D^2 \quad \text{.....(V.7)}$$

The model's structure reveals that first-order terms generally dominate the adsorption behavior, while quadratic and interaction terms show comparatively weaker effects. This mathematical formulation not only corroborates the graphical analysis but also provides precise quantification of each parameter's contribution, enabling accurate prediction of system performance under various conditions. The consistency between coefficient values and experimental observations underscores the model's reliability for process optimization.

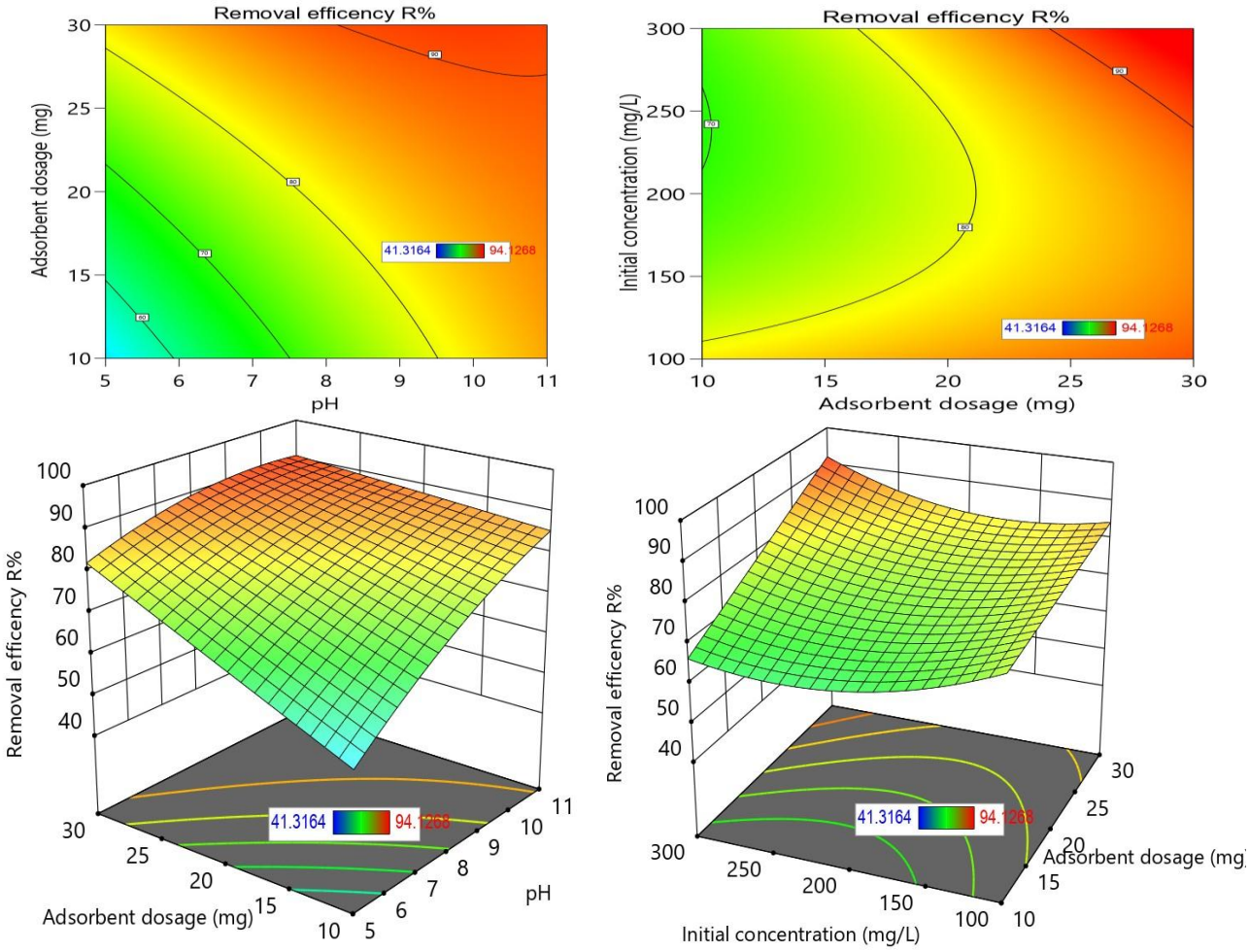


Figure V. 12: *Contour and 3D surface plots for the interactive effects of (a, c), initial pH and adsorbent dosage (b, d), initial dye concentration and adsorbent dosage on the MB%.*

4.6.ANN Model

The ANN model was trained using 29 input datasets, comprising initial pH, initial MB concentration, adsorbent mass, and temperature, with removal efficiency (MB%) as the output variable. From the total experiments conducted, 23 datasets were assigned for model training, while 3 were reserved for testing, and the remaining datasets were used for validation. This methodology was implemented to assess the model's predictive accuracy for unseen data and evaluate its generalization capacity when applied to novel inputs.

Model performance was quantified using correlation coefficients to determine the predictive accuracy of degradation efficiency based on the specified input parameters. Correlation coefficients were computed for the training, validation, testing, and combined datasets, with the optimal ANN architecture selected based on the highest correlation coefficients obtained[30].

In this investigation, multiple training algorithms were evaluated to identify the optimal neuron configuration for predicting degradation efficiency, based on the comparative analysis, the algorithm employing ten neurons in the hidden layer demonstrated superior predictive performance, yielding the highest R^2 values. Specifically, this configuration achieved an overall R^2 value of 0.97182, R^2 = 0.99525, and R^2=0.98352 for both training and validation phases, and an acceptable value (R^2 = 0.90737) for the testing dataset.

The analysis revealed that the optimal neural network architecture for predicting removal efficiency consisted of a 4–7–1 configuration **(Fig. V.13)**. To assess model performance, regression analyses were conducted by plotting predicted values against experimental measurements. These regression plots were generated for the training, validation, testing, and combined datasets **(Fig. V.13)**. The resulting R^2 indicated a high degree of agreements between predicted and observed values, confirming the model's capability to accurately represent the underlying relationships. Collectively, these results demonstrate that the developed neural network is a robust predictive tool for estimating degradation efficiency.

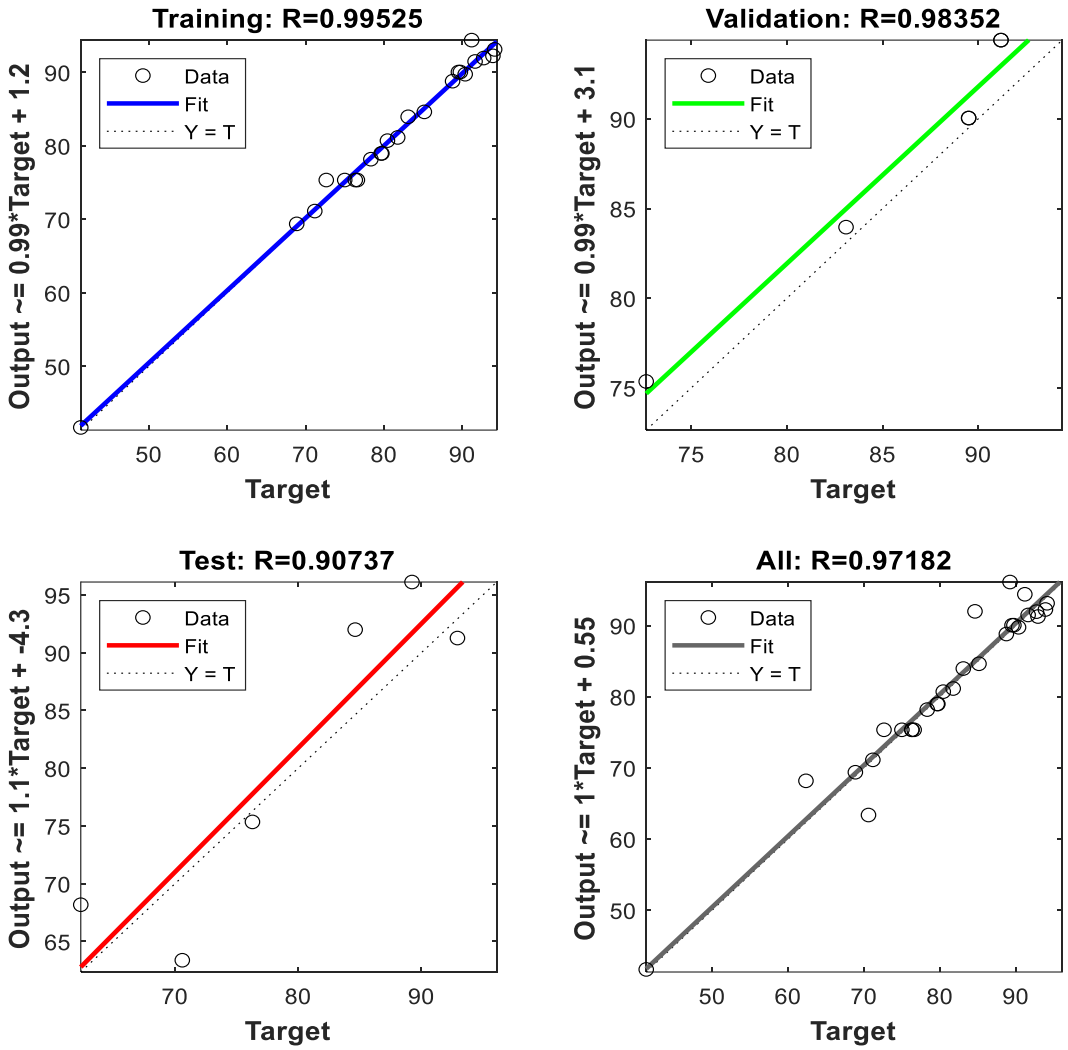


Figure V. 13: *The correlation values of the datasets in the ANN model.*

4.7. Optimization

This study employed multiple optimization strategies to enhance process parameters. The RSM model was optimized using Derringer's desirability function, where a desirability value of 1 signifies an optimal response meeting the predefined criteria[31]. Concurrently, the ANN model was refined using Grey Wolf Optimizer (GWO) and Genetic Algorithm (GA) techniques to maximize adsorption efficiency. As illustrated in **Fig. 13**, numerical optimization achieved a MB removal efficiency of 94.81% with a desirability value of 1 under the following conditions:

pH 8.22, adsorbent dosage 23.15 mg, temperature 39.91°C, and initial MB concentration 298.89 mg/L.

To validate these predictions, confirmatory experiments were performed in duplicate using the optimized parameters. The experimental results exhibited strong concordance with the numerically optimized data, affirming the efficiency of the BBD coupled with desirability functions in optimizing MB adsorption conditions for the HNTs/PANI/SA composite.

Additionally, conventional optimization via ANN-GWO and ANN-GA yielded an MB removal efficiency of 97.88% under the following conditions: pH 9.62, adsorbent dosage 30 mg, temperature 40°C, and initial MB concentration 300 mg/L. These results demonstrate the predictive accuracy of the ANN-GWO and ANN-GA models. The primary goal of these methodologies was to maximize MB removal efficiency, with the optimal process conditions detailed in Table SM1.

Table V. 5: *Optimal process conditions following RSM-BBD, ANN-GWO and ANN-GA.*

Method	**pH**	**Adsorbent dosage (mg)**	**Temperature (°C)**	**MB concentration (mg/L)**	**Removal efficiency R%**
RSM-BBD	8.22	23.15	39.91	298.89	94.81
ANN-GWO	9.62	30	40	300	97.88
ANN-GA	9.62	30	40	300	97.88

4.8.**Kinetic study**

To investigate the adsorption kinetics and identify the rate-limiting mechanisms in the removal of MB using HNTs/PANI/SA composite, three nonlinear kinetic models were systematically

examined: PFO, PSO, and IPD. This comparative analysis of kinetic models provides critical insights into the adsorption dynamics and the predominant mechanisms governing the MB removal process.

Table V. 6: *PFO, PSO and IPD nonlinear fits parameters for MB adsorption on HNTs/PANI/SA at different concentrations (100, 200 and 300mg/l).*

Concentration		**PFO**			**PSO**			**IPD**		
n	q_{exp}	q_{cal}	K_1	R^2	q_{cal}	K_2	R^2	K_{IPD}	C	R^2
mg/L	mg/g	mg/g	1/h		mg/g	g/mgh				
100	163.8	169.51	0.044	0.989	220.99	0.0018	0.985	19.76	6.03	0.951
200	219.8	235.38	0.049	0.979	307.6	0.0014	0.961	29.15	0.46	0.894
300	290	290.64	0.057	0.994	353.39	0.0017	0.981	31.41	28.28	0.879

The kinetic evaluation demonstrated that the pseudo-first-order (PFO) model most accurately described the MB adsorption behavior on HNTs/PANI/SA composite across all tested concentrations. This conclusion was supported by a consistently high correlation coefficient ($R^2 > 0.98$) and the close correspondence between calculated ($q_{e,cal}$) and experimentally determined ($q_{e,exp}$) equilibrium adsorption capacities.

The predominant fit of the PFO model, coupled with the observed agreement in equilibrium capacities, provides compelling evidence for a physisorption-dominated mechanism. This process appears to be principally governed by electrostatic interactions between the positively charged MB molecules and negatively charged functional groups present on the composite surface.

The IPD analysis yielded further mechanistic insights, non-linear plots with non-zero intercepts ($C > 0$), failure of regression lines to pass through the origin and multi-linear curve progression across time domains[32]. These characteristics indicate that while pore diffusion contributes to the adsorption process, the rate-limiting step is governed by alternative mechanisms, potentially including: Liquid-film boundary layer resistance, surface adsorption kinetics and External mass transfer limitations[33].

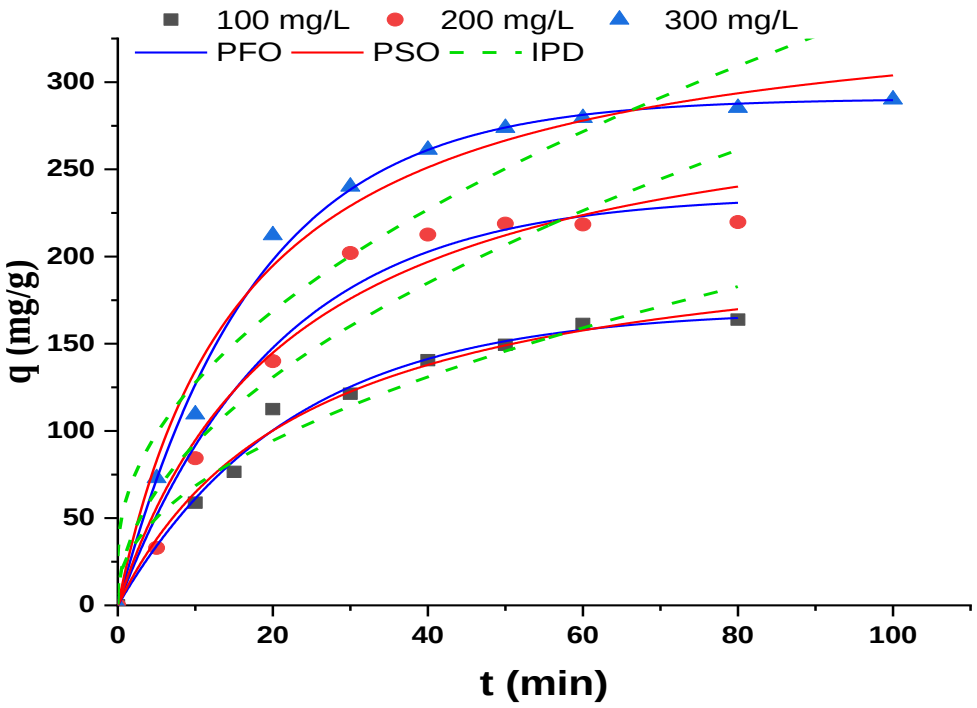


Figure V. 14: *Nonlinear PFO, PSO and IPD kinetics models fits for MB adsorption on HNTs/PANI/SA composite (C0=100, 200 and 300mg/l).*

4.9.**Isotherm modeling**

The equilibrium adsorption behavior of MB on the composite material was systematically investigated across temperature variations (283, 293, 303 and 313°K) through comprehensive isotherm analysis **(Fig. V.15)**. The observed L-type isotherm (Giles classification) revealed a high Affinity Characteristics that shows a significant uptake efficiency at low equilibrium

concentrations (C_e) and demonstrates a strong adsorbate-adsorbent interaction. In this study we applied different isotherm models such as Langmuir, Frendlich, and Dubinin-Radushkevich (D-R).

The adsorption isotherm data were analyzed using nonlinear regression in Origin Pro 2018 software (**Fig. V.15**) and fitted to various adsorption models. As summarized in Table 6, the Langmuir model provided the best fit for the MB adsorption isotherm on the composite, exhibiting a higher determination coefficient ($R^2 = 0.98$) compared to the Freundlich ($R^2 = 0.92$) and Dubinin-Radushkevich ($R^2 = 0.95$) models. This suggests monolayer adsorption on a homogeneous surface. The Langmuir model predicted a maximum adsorption capacity of approximately 530 mg/g.

The favorability of MB adsorption was further evaluated using the Langmuir separation factor. An R_L value between 0 and 1 indicates a favorable process, whereas $R_L > 1$ suggests unfavorable adsorption, and $R_L = 1$ denotes linear adsorption. In this study, R_L values ranged from 0.1 to 0.8, confirming favorable adsorption[32].

Additionally, the Freundlich constant (1/n) was used to assess the nature of adsorption: $1/n > 1$ implies physical adsorption, while $1/n < 1$ suggests chemisorption. The obtained value of $1/n < 1$ indicates that there could be chemical interactions present in the sorption process[34].

Moreover, the mean free energy (E) derived from the D-R isotherm model was found to be within the range of 0–0.2 kJ/mol, further supporting the conclusion that MB adsorption onto the composite is primarily governed by physical interactions[23].

Table V. 7: *Parameters of the Langumir, Freundlich and D-R isotherms models for MB adsorption on HNTs/PANI/SA at different temperature.*

Model	Parameters	Obtained values			
	Temperature(°C)	10	20	30	40
Langumir	qm (mg/g)	168.38	231.22	470.17	530.06
	K_L (L/mg)	0.102	0.087	0.04	0.023
	R^2	0.981	0.990	0.925	0.941
Freundlich	K_f (L/mg)	66.49	53.90	89.63	76.68
	1/n	0.16	0.27	0.28	0.29
	R^2	0.932	0.887	0.822	0.817
D-R	qm (mg/g)	148.12	202.13	402.55	443.91
	E (kJ/mol)	0.109	0.124	0.053	0.032
	R^2	0.911	0.867	0.952	0.968

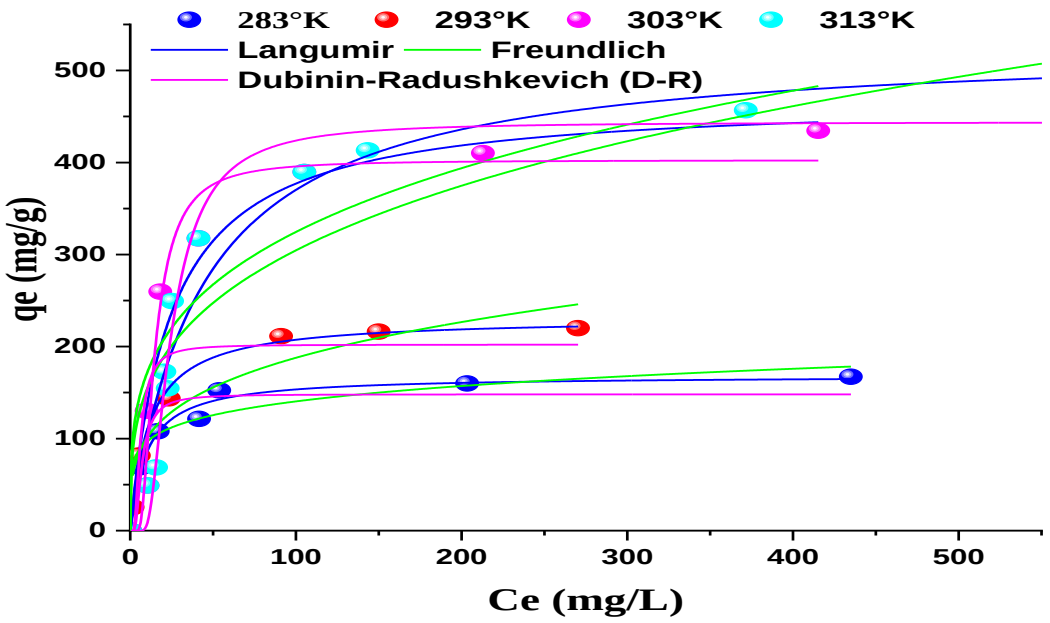


Figure V. 15: *Langmuir, Freundlich, and D-R non- linear fits to the experimental data of MB adsorption by HNTs/PANI/SA composite at different temperatures (pH=9, m=30mg, V=30ml).*

4.10. Thermodynamic study

A comprehensive thermodynamic investigation was conducted to elucidate the adsorption characteristics of MB onto the HNTs/PANI/SA composite at varying temperatures (283, 293, 303 and 313°K). The fundamental thermodynamic parameters, including Gibbs free energy change (ΔG°), enthalpy change (ΔH°), and entropy change (ΔS°), were quantitatively evaluated using the following relationships[35]:

$\Delta G° = -R\ T\ Ln\ K$ ……(V.8)

$$Log\left(\frac{1000*qe}{Ce}\right) = 1 + \frac{-\Delta H°}{2.303*RT} + \frac{\Delta S°}{2.303*R} \quad \text{……...…(V.9)}$$

Where R (8.314 J/mol K) is the universal gas constant, T is the absolute temperature (K), and K_L is the equilibrium constant (l/mg).

Table V.8 presents the values of the thermodynamics parameters. The adsorption of MB on the HNTs/PANI/SA surface was spontaneous due to the negative values of ΔG°[36], in addition the positive value of ΔH° (38.37KJ/mol) indicates the endothermic nature of adsorption[37]. Moreover, the increasing in adsorption capacity of HNTs/PANI/SA at high temperature can be attributed to the effect of this later on the internal structure of the composite, thus facilitating faster diffusion of MB molecules into the HNTs/PANI/SA interspaces structure. Furthermore, ΔH° inferior to 85 KJ.mol-1, confirmed the physical adsorption nature, ΔS° was positive, indicates the affinity between MB and HNTs/PANI/SA with an increase in randomness degree during adsorption[38].

Table V. 8: *Thermodynamic properties of MB adsorption on HNTs/PANI/SA.*

T(°K)	ΔH°(KJ/mol)	ΔS° (J/mol. K)	ΔG°(KJ/mol)
283	**35.04**	**222.06**	**-27.62**
293			**-30.37**
303			**-32.04**
313			**-31.88**

4.11. Adsorption Mechanism

The hierarchical construction of HNT-PANI/SA composite beads is driven by the interfacial compatibility between inorganic nanotubes, the conducting polymer, and the biopolymer matrix, beginning with the *in situ* oxidative polymerization of aniline onto halloysite nanotubes (HNTs) [1]. This process is governed by electrostatic anchoring, where anilinium cations ($C_6H_5NH_3^+$) are attracted to negatively charged external silanol (Si-OH) groups on the HNTs in acidic media, ensuring the formation of a core-shell tubular morphology that is further stabilized by hydrogen bonding between the PANI backbone and clay surface hydroxyls Upon integration into sodium alginate (SA), the mixture undergoes ionotropic gelation via the (egg-box) model, where Ca^{2+} ions physically entrap the HNT-PANI hybrids within a porous 3D scaffolding [2]. This architecture is chemically reinforced by electrostatic coupling between the protonated amine sites of the PANI emeraldine salt and the anionic carboxylate groups of the alginate, ensuring mechanical integrity and preventing the leaching of the mineral phase [3].

The sequestration of Methylene Blue (MB) within this network involves a multi-step diffusion and complexation process, where the high aspect ratio of embedded HNTs facilitates dye access to internal active sites through a mesoporous network [4]. The dominant chemical interactions driving MB removal include primary electrostatic attraction between the cationic dye and deprotonated carboxylate groups at neutral or basic pH, as well as strong π – π stacking between the aromatic rings of MB and the PANI chains [3]. Furthermore, hydrogen bonding between nitrogen atoms in the MB structure and the adsorbent's hydroxyl and amine groups, alongside the cation exchange of Ca^{2+} ions for MB^+ cations, effectively locks the dye within the bead structure [5].

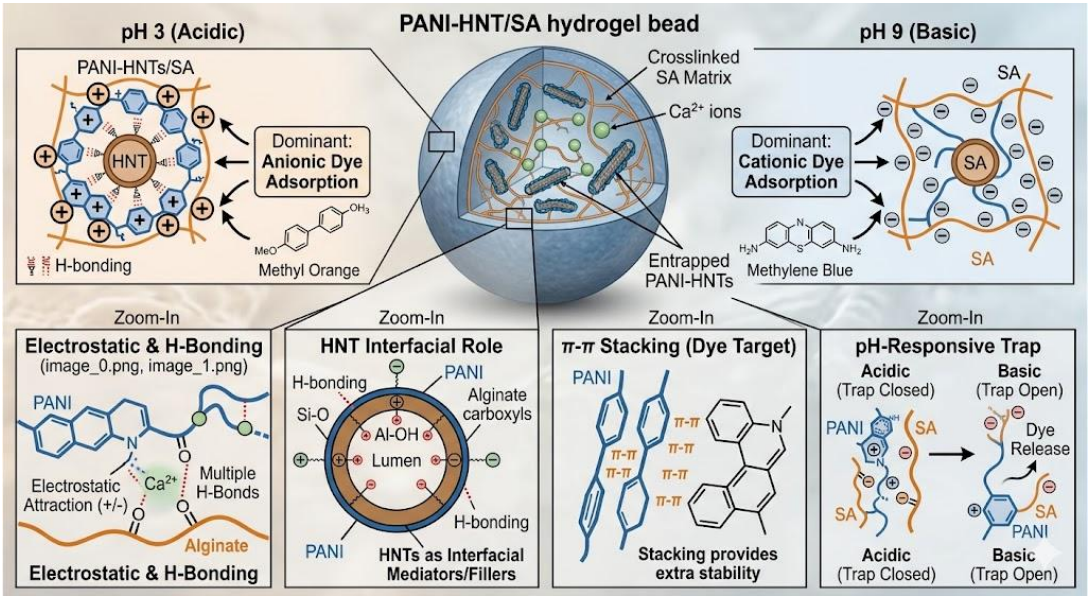


Figure V. 16: *Proposed mechanism for the adsorption of MB on the surface of HNTs-PANI/SA.*

References of Chapter V

[1] M. K. Younes, S. Algburi, R. H. Al Omari, and A. S. Abdulhameed, "Application of chitosan/acid-treated biomass composite for dye wastewater treatment: Adsorption modeling using Box-Behnken Design," *Desalination Water Treat*, vol. 320, Oct. 2024, doi: 10.1016/j.dwt.2024.100795.

[2] A. S. Bendrihem *et al.*, "Experimental and theoretical studies of the interaction of cationic dye in halloysite nanotubes," *Reaction Kinetics, Mechanisms and Catalysis*, Aug. 2025, doi: 10.1007/s11144-025-02933-w.

[3] H. Çiftçi, İ. S. Atli, F. E. Aysal, İ. Çelik, and M. Gürsoy, "Artificial Neural Network Modeling for Basic Dye Adsorption onto Montmorillonite," *Journal of Macromolecular Science, Part B: Physics*, vol. 62, no. 7, pp. 350–365, 2023, doi: 10.1080/00222348.2023.2213912.

[4] S. Soleimani, A. Heydari, M. Fattahi, and A. Motamedisade, "Calcium alginate hydrogels reinforced with cellulose nanocrystals for methylene blue adsorption: Synthesis, characterization, and modelling," *Ind Crops Prod*, vol. 192, no. March 2022, p. 115999, 2023, doi: 10.1016/j.indcrop.2022.115999.

[5] S. Mirjalili, S. M. Mirjalili, and A. Lewis, "Grey Wolf Optimizer," *Advances in Engineering Software*, vol. 69, pp. 46–61, 2014, doi: 10.1016/j.advengsoft.2013.12.007.

[6] N. Bouchelkia *et al.*, "Optimizing adsorption efficiency: A novel application of SVM_Boosting_IGWO for methylene blue dye removal using low-cost fruit peels adsorbents," *Chemometrics and Intelligent Laboratory Systems*, vol. 261, Jun. 2025, doi: 10.1016/j.chemolab.2025.105377.

[7] G. Alam, I. Ihsanullah, M. Naushad, and M. Sillanpää, "Applications of artificial intelligence in water treatment for optimization and automation of adsorption processes: Recent advances

and prospects," *Chemical Engineering Journal*, vol. 427, p. 130011, 2022, doi: 10.1016/j.cej.2021.130011.

[8] N. Marzban *et al.*, "Intelligent modeling and experimental study on methylene blue adsorption by sodium alginate-kaolin beads," *Int J Biol Macromol*, vol. 186, no. March, pp. 79–91, 2021, doi: 10.1016/j.ijbiomac.2021.07.006.

[9] T. O. Ozcelik, E. Altintig, M. Cetinkaya, D. B. Ak, B. Sarici, and A. Ates, "Methylene Blue Removal Using Activated Carbon from Olive Pits: Response Surface Approach and Artificial Neural Network," *Processes*, vol. 13, no. 2, 2025, doi: 10.3390/pr13020347.

[10] M. Tanzifi *et al.*, "Artificial neural network optimization for methyl orange adsorption onto polyaniline nano-adsorbent: Kinetic, isotherm and thermodynamic studies," *J Mol Liq*, vol. 244, pp. 189–200, 2017, doi: 10.1016/j.molliq.2017.08.122.

[11] L. Zhang, T. Wang, and P. Liu, "Polyaniline-coated halloysite nanotubes via in-situ chemical polymerization," *Appl Surf Sci*, vol. 255, no. 5 PART 1, pp. 2091–2097, 2008, doi: 10.1016/j.apsusc.2008.06.187.

[12] L. Liu, Y. Wan, Y. Xie, R. Zhai, B. Zhang, and J. Liu, "The removal of dye from aqueous solution using alginate-halloysite nanotube beads," *Chemical Engineering Journal*, vol. 187, pp. 210–216, 2012, doi: 10.1016/j.cej.2012.01.136.

[13] Y. Noskov, N. Ogurtsov, V. Bliznyuk, Y. Lvov, I. Myronyuk, and A. Pud, "Synthesis and properties of core–shell halloysite–polyaniline nanocomposites," *Applied Nanoscience (Switzerland)*, vol. 12, no. 4, pp. 1285–1294, 2022, doi: 10.1007/s13204-021-01812-9.

[14] C. S. C. Chiew *et al.*, "Halloysite/alginate nanocomposite beads: Kinetics, equilibrium and mechanism for lead adsorption," *Appl Clay Sci*, vol. 119, pp. 301–310, 2016, doi: 10.1016/j.clay.2015.10.032.

[15] T. Zhou, C. Li, H. Jin, Y. Lian, and W. Han, "Effective Adsorption/Reduction of Cr(VI) Oxyanion by Halloysite@Polyaniline Hybrid Nanotubes," *ACS Appl Mater Interfaces*, vol. 9, no. 7, pp. 6030–6043, 2017, doi: 10.1021/acsami.6b14079.

[16] F. Hu *et al.*, "Core/shell structured halloysite/polyaniline nanotubes with enhanced electrochromic properties," *J Mater Chem C Mater*, vol. 6, no. 21, pp. 5707–5715, 2018, doi: 10.1039/c8tc01163j.

[17] G. Cavallaro, A. Gianguzza, G. Lazzara, S. Milioto, and D. Piazzese, "Alginate gel beads filled with halloysite nanotubes," *Appl Clay Sci*, vol. 72, pp. 132–137, 2013, doi: 10.1016/j.clay.2012.12.001.

[18] Y. Zhao, E. Abdullayev, A. Vasiliev, and Y. Lvov, "Halloysite nanotubule clay for efficient water purification," *J Colloid Interface Sci*, vol. 406, pp. 121–129, 2013, doi: 10.1016/j.jcis.2013.05.072.

[19] M. Zhao and P. Liu, "Adsorption behavior of methylene blue on halloysite nanotubes," *Microporous and Mesoporous Materials*, vol. 112, no. 1–3, pp. 419–424, 2008, doi: 10.1016/j.micromeso.2007.10.018.

[20] R. Liu, K. Fu, B. Zhang, D. Mei, H. Zhang, and J. Liu, "Removal of Methyl Orange by Modified Halloysite Nanotubes," *J Dispers Sci Technol*, vol. 33, no. 5, pp. 711–718, 2012, doi: 10.1080/01932691.2011.579855.

[21] S. Mellouk *et al.*, "Intercalation of halloysite from Djebel Debagh (Algeria) and adsorption of copper ions," *Appl Clay Sci*, vol. 44, no. 3–4, pp. 230–236, 2009, doi: 10.1016/j.clay.2009.02.008.

[22] B. Faouzia *et al.*, "Sustainable biomass-derived activated biochar/polyaniline/alginate composite beads for enhanced methylene blue adsorption: Experimental and theoretical

investigations," *Int J Biol Macromol*, vol. 305, p. 141338, May 2025, doi: 10.1016/J.IJBIOMAC.2025.141338.

[23] H. Chaima *et al.*, "Adsorptive removal of cationic dye from aqueous solutions using activated carbon prepared from Crataegus monogyna / sodium alginate / polyaniline composite beads : Experimental study and molecular dynamic simulation," *J Mol Liq*, vol. 408, no. June, p. 125372, 2024, doi: 10.1016/j.molliq.2024.125372.

[24] A. Hayoune, H. Akkari, T. Mekhalif, and F. Martin, "Sono-assisted adsorption of methylene blue dye from aqueous medium using magnetic Algerian Halloysite clay (Fe3O4-HKDD3)," *Int J Environ Anal Chem*, vol. 104, no. 2, pp. 424–438, Jan. 2024, doi: 10.1080/03067319.2021.2020770.

[25] N. Slougui, M. Slama, Y. Boudaoud, and A. S. Bendrihem, "Optimization of GC-MS Method for Analysis of Basil Essential Oils from Algeria: Design of Experiments and Exploratory Pattern Recognition," *J Chem*, vol. 2022, p. 5880539, 2022, doi: 10.1155/2022/5880539.

[26] A. I. Boulahbal *et al.*, "Enhancing adsorptive performance of Cu-Al layered double hydroxides from aluminum saline slags : Insights from response surface methodology and molecular dynamic simulation," *Miner Eng*, vol. 219, no. June, p. 109067, 2024, doi: 10.1016/j.mineng.2024.109067.

[27] K. Imene *et al.*, "Thermal treatment of Cu-doped hydrotalcite-like adsorbents for improved removal of methyl orange from water," *Sep Purif Technol*, vol. 365, no. February, p. 132656, 2025, doi: 10.1016/j.seppur.2025.132656.

[28] S. Sahnoun and M. Boutahala, "Adsorption removal of tartrazine by chitosan/polyaniline composite: Kinetics and equilibrium studies," *Int J Biol Macromol*, vol. 114, no. 2017, pp. 1345–1353, 2018, doi: 10.1016/j.ijbiomac.2018.02.146.

[29] N. Boukhalfa, M. Boutahala, N. Djebri, and A. Idris, “Kinetics, thermodynamics, equilibrium isotherms, and reusability studies of cationic dye adsorption by magnetic alginate/oxidized multiwalled carbon nanotubes composites,” *Int J Biol Macromol*, vol. 123, pp. 539–548, 2019, doi: 10.1016/j.ijbiomac.2018.11.102.

[30] S. Kumari *et al.*, “An exploration of RSM, ANN, and ANFIS models for methylene blue dye adsorption using Oryza sativa straw biomass: a comparative approach,” *Sci Rep*, vol. 15, no. 1, p. 2979, Dec. 2025, doi: 10.1038/s41598-025-87274-3.

[31] C. Nayak, B. Babu, V. Manoj, C. V. Raghunath, M. L. D. Bhatlu, and P. Pandey, “Optimization of process parameters by RSM-BBD for the removal of titan yellow dye from aqueous solution by acid-treated Phyllanthus acidus leaves,” *Biomass Convers Biorefin*, vol. 14, no. 18, pp. 23125–23141, 2024, doi: 10.1007/s13399-023-04474-5.

[32] M. Musah, Y. Azeh, J. Mathew, M. Umar, Z. Abdulhamid, and A. Muhammad, “Adsorption Kinetics and Isotherm Models: A Review,” *Caliphate Journal of Science and Technology*, vol. 4, no. 1, pp. 20–26, 2022, doi: 10.4314/cajost.v4i1.3.

[33] J. Wang and X. Guo, “Adsorption kinetic models: Physical meanings, applications, and solving methods,” *J Hazard Mater*, vol. 390, no. January, p. 122156, 2020, doi: 10.1016/j.jhazmat.2020.122156.

[34] A. Abollé, K. Y. Urbain, K. Ollo, K. Y. Tchonrontcha, and K. A. Rodrigue, “Adsorption of Methyl Orange on Corncob Activated Carbon: Kinetic, Equilibrium, and Thermodynamic Studies,” *Earthline Journal of Chemical Sciences*, no. August, pp. 205–224, 2022, doi: 10.34198/ejcs.8222.205224.

[35] A. Harrou, E. Gharibi, H. Nasri, and M. El Ouahabi, “Thermodynamics and kinetics of the removal of methylene blue from aqueous solution by raw kaolin,” *SN Appl Sci*, vol. 2, no. 2, 2020, doi: 10.1007/s42452-020-2067-y.

[36] S. B. A. Z. Salem Atia, Salah Neghmouche Nacer, and D. G. , Noureddine Elboughdiri, "Activating Illite kaolinite clay with CTAB for adsorbing Methylene blue: Isotherms, Kinetics, and thermodynamics studies," *Tuijin Jishu/Journal of Propulsion Technology*, vol. 44, no. 5, pp. 812–829, Dec. 2023, doi: 10.52783/tjjpt.v44.i5.2678.

[37] K. Benamar *et al.*, "Adsorption of cationic dye by Celtis australis leaves biomass: characterization, kinetic, thermodynamic, and response surface methodology study," *Chemistry and Ecology*, 2025, doi: 10.1080/02757540.2025.2508995.

[38] M. J. Baari, L. Rudi, and L. Harimu, "Adsorption isotherms, thermodynamics, and kinetics of activated carbon as adsorbent to water pollutants: a review," 2025, *Ural Federal University*. doi: 10.15826/chimtech.2025.12.2.14.

[39] D. Xu *et al.*, « Micro-Nanostructured Polyaniline Assembled in Cellulose Matrix via Interfacial Polymerization for Applications in Nerve Regeneration », *ACS Appl. Mater. Interfaces*, vol. 8, nº 27, p. 17090-17097, juill. 2016, doi: 10.1021/acsami.6b03555.

[39] P. Gadziński *et al.*, « Ionotropic Gelation and Chemical Crosslinking as Methods for Fabrication of Modified-Release Gellan Gum-Based Drug Delivery Systems », *Pharmaceutics*, vol. 15, nº 1, p. 108, janv. 2023, doi: 10.3390/pharmaceutics15010108.

[40] E. N. Heybet, V. Ugraskan, B. Isik, et O. Yazici, « Adsorption of methylene blue dye on sodium alginate/polypyrrole nanotube composites », *International Journal of Biological Macromolecules*, vol. 193, p. 88-99, déc. 2021, doi: 10.1016/j.ijbiomac.2021.10.084.

[41] S. Radoor, J. Karayil, J. Parameswaranpillai, et S. Siengchin, « Adsorption of methylene blue dye from aqueous solution by a novel PVA/CMC/halloysite nanoclay bio composite: Characterization, kinetics, isotherm and antibacterial properties », *J Environ Health Sci Engineer*, vol. 18, nº 2, p. 1311-1327, déc. 2020, doi: 10.1007/s40201-020-00549-x.

[42] A. Nasar et F. Mashkoor, « Application of polyaniline-based adsorbents for dye removal from water and wastewater—a review », *Environ Sci Pollut Res*, vol. 26, nº 6, p. 5333-5356, févr. 2019, doi: 10.1007/s11356-018-3990-y.

CHAPTER VI

1. Introduction

This chapter is based on the use of different biomass to synthesize different biochar materials at various temperatures to enhance the removal efficiency of MB, the best biochar was further enhanced by the use of sodium alginate, and then applying RSM to ensure the best experimental conditions for the study.

2. Adsorbent choice

To determine the appropriate calcination temperature for the biochar, the histogram (**Fig. VI.1**) illustrates the evolution of the adsorbed amount as a function of the pyrolysis temperature.

The test was conducted under identical conditions: m = 30 mg, C_0 = 100 mg/L, V = 100 mL, pH = 6.7. The results show that the pyrolysis temperature influences the adsorption capacity. This effect may be attributed to the formation of new active sites responsible for binding the positively charged BM^+ ions. The adsorbed amounts were 14.4, 55.2, and 45.62 mg/g for the biochar materials initially calcined at 300, 500, and 700 °C, respectively. All subsequent studies were therefore carried out using BC500 (biochar calcinated at 500°C).

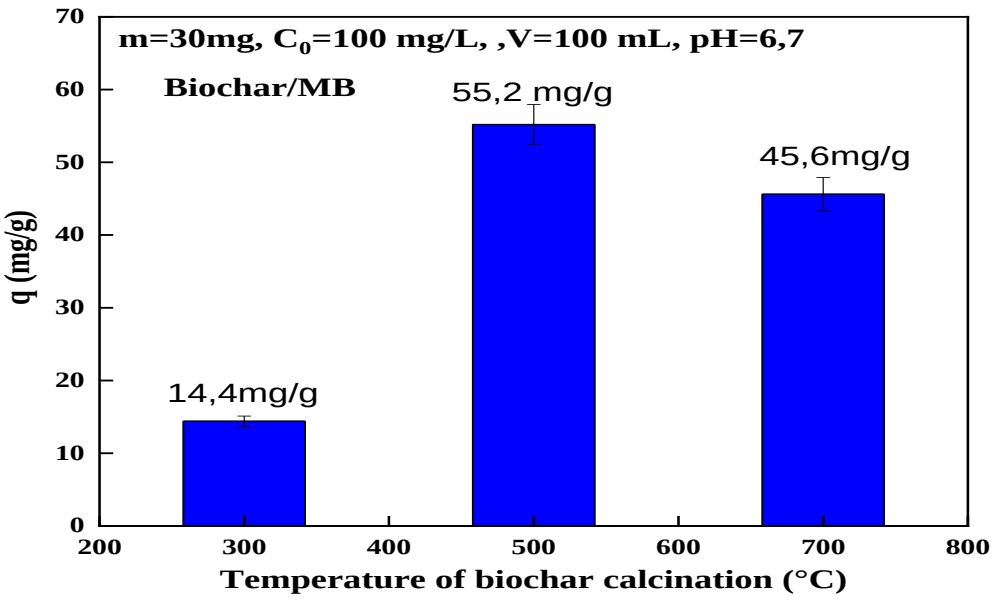


Figure VI. 1: Adsorption capacities of different biochars at different pyrolysis temperatures.

3. Characterization

3.1.Scanning electron microscopy (SEM)

SEM was employed to investigate the surface morphology and structural evolution of the raw biomass, the produced biochar, and the alginate–biochar composite, as presented in **Fig. 2**.

Fig. 2a illustrates the morphology of the raw biomass, which exhibits an irregular and heterogeneous surface characterized by compact lamellar and fibrous structures. The particles appear aggregated and display a multiform arrangement. This relatively dense morphology is mainly attributed to the presence of lignocellulosic components, including cellulose, hemicellulose, and lignin, which form the structural framework of the biomass [1].

Fig. 2b shows the SEM image of the produced biochar. Compared with the raw biomass, the biochar exhibits a rougher surface and a significantly greater number of pores, indicating a more porous structure. This transformation is associated with the thermal degradation of lignocellulosic components during pyrolysis. The decomposition of hemicellulose and cellulose, accompanied by the release of volatile compounds, generates voids and channels within the carbon matrix. Consequently, this process promotes pore formation and structural rearrangement, increasing surface area and the number of accessible active sites, which are beneficial for adsorption applications [2].

Fig. 2c presents the morphology of the alginate–biochar composite. The micrograph reveals a heterogeneous porous structure in which biochar particles appear as irregular fragments embedded within a continuous alginate matrix. The polymer forms a network surrounding the biochar particles, confirming their successful encapsulation while maintaining the porous characteristics of the carbon material. Such structural features contribute to the stability of the composite and support its potential for adsorption processes [3].

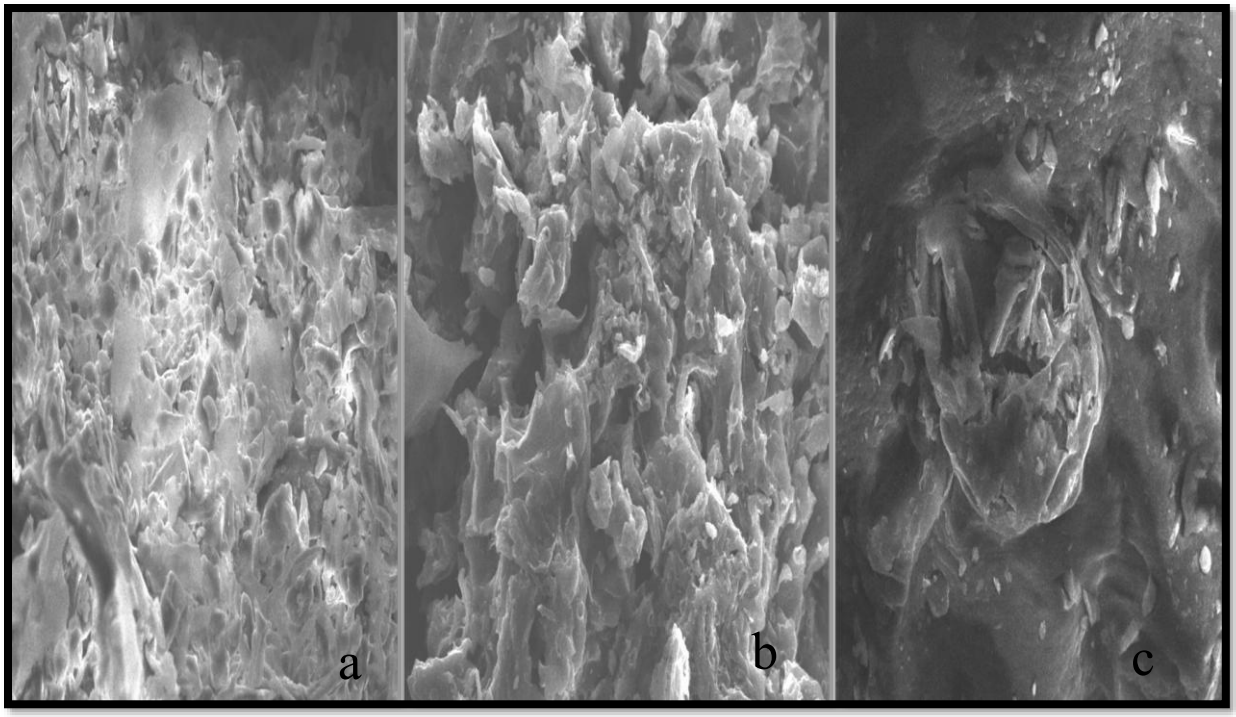


Figure VI. 2: *SEM micrographs of (a) raw biomass, (b) biochar, and (c) alginate–biochar composite.*

3.2.FTIR analysis

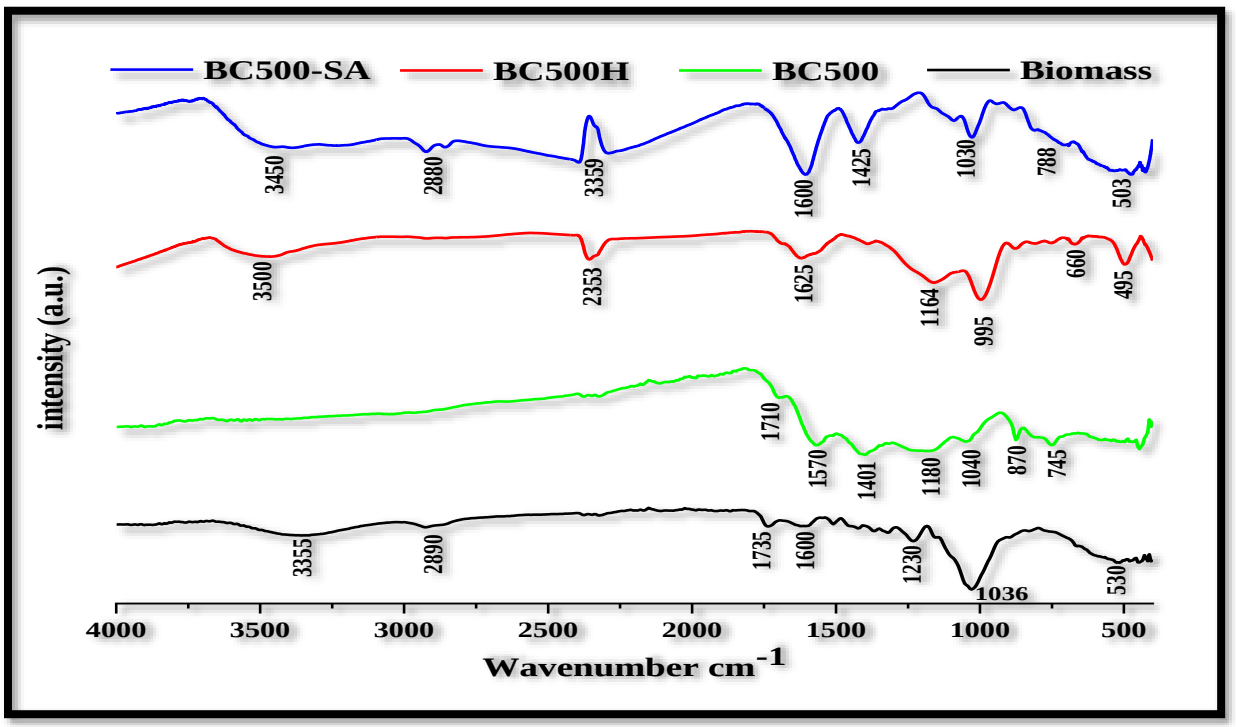


Figure VI. 3*: FTIR spectrum of Biomass, BC500, BC500H and BC500-SA.*

3.2.1. Biomass spectra:

Broad band at 3355 cm^{-1}, indicates O-H stretching vibrations, commonly from hydroxyl groups present in cellulose, hemicellulose, or water content [4]. Small peak at 2890 cm^{-1} corresponds to C-H stretching vibrations from aliphatic groups such as methyl and methylene groups found in lignin and polysaccharides [5]. Intense small peak at 1735 cm^{-1} assigned to C=O stretching vibrations of carbonyl groups, such as ester groups or carboxylic acids commonly found in hemicellulose and lignin. another small peak at 1600 cm^{-1} generally corresponds to aromatic C=C stretching vibrations in lignin or conjugated C=O in carbonyl groups [6]. Several intense small peaks around 1230 cm^{-1}: related to C-O stretching in acetyl groups or ethers, typical of hemicellulose and lignin [6]. Large intense peak at 1036 cm^{-1}: mainly due to C-O, C-C stretching vibrations and C-O-H bending vibrations, characteristic of cellulose and polysaccharides, and a small band at 530 cm^{-1}, often attributed to out-of-plane bending vibrations or skeletal vibrations, related to inorganic components or mineral matter [7].

3.2.2. BC500 and BC500Hspectra:

After calcination of the biomass at 500°C, the FTIR spectral changes indicate substantial chemical transformations [8], [9], [10]:

FTIR spectra in **Fig.VI.3** clearly demonstrate the progressive structural evolution of the biomass after thermal treatment and H_3PO_4 modification. Thermal treatment leads to the disappearance of the broad O–H band at ~3355 cm^{-1}, indicating dehydration and degradation of cellulose and hemicellulose hydroxyl groups. The shifts of bands to ~1710 and ~1570 cm^{-1} suggest the formation of carbonyl groups and the modification or condensation of lignin-derived aromatic structures. The strong decrease and shift of bands in the 1400–1000 cm^{-1} region, particularly the attenuation of the intense C–O band near 1036 cm^{-1}, confirm the

breakdown of polysaccharide structures, while bands at 870 and 745 cm^{-1} are attributed to aromatic C–H out-of-plane vibrations and/or mineral residues formed during pyrolysis.

After H_3PO_4 activation of BC500, new spectral features confirm successful phosphorus functionalization. The appearance of an intense band at ~2353 cm^{-1} is associated with P=O vibrations [11], while the shift of the aromatic band from ~1570 to ~1625 cm^{-1} reflects further chemical modification of the carbon matrix [12], [13]. The disappearance of the 1401 cm^{-1} band and the shifts from 1180 to 1164 cm^{-1} and from 1040 to ~995 cm^{-1} indicate the formation of C–O–P and P–O–C linkages. Additionally, new bands at ~660 and 495 cm^{-1}, assigned to P–O and P–O–P vibrations, provide strong evidence for the incorporation of phosphate groups on the BC500 surface [14].

3.2.3. BC500-SAg beads

Since the calcined sample exhibited a higher adsorption capacity than the phosphoric-acid-treated material, it was selected for encapsulation in alginate to form biochar–alginate beads. The FTIR spectrum in **Fig.VI.3** of the encapsulated material displays contributions from both biochar and alginate. The broad band at ~3450 cm^{-1} is assigned to O–H stretching vibrations from alginate hydroxyl and carboxyl groups as well as residual moisture [10]. Weak bands at ~2880 cm^{-1} correspond to C–H stretching of the alginate polysaccharide backbone [15]. The intense peaks at ~1600 and ~1425 cm^{-1} are attributed to the asymmetric and symmetric stretching of carboxylate (COO^-) groups of alginates, showing shifts relative to the biochar bands (~1570 and 1401 cm^{-1}), which indicates interaction between alginate and biochar [3]. The band at ~1030 cm^{-1} arises from C–O–C and C–O stretching vibrations, while the low-frequency bands around ~780 and ~503 cm^{-1} are associated with skeletal or bending modes [15]. Overall, these features confirm successful encapsulation and the presence of abundant oxygen-containing functional groups favorable for adsorption.

3.3.ATG/DTA analysis

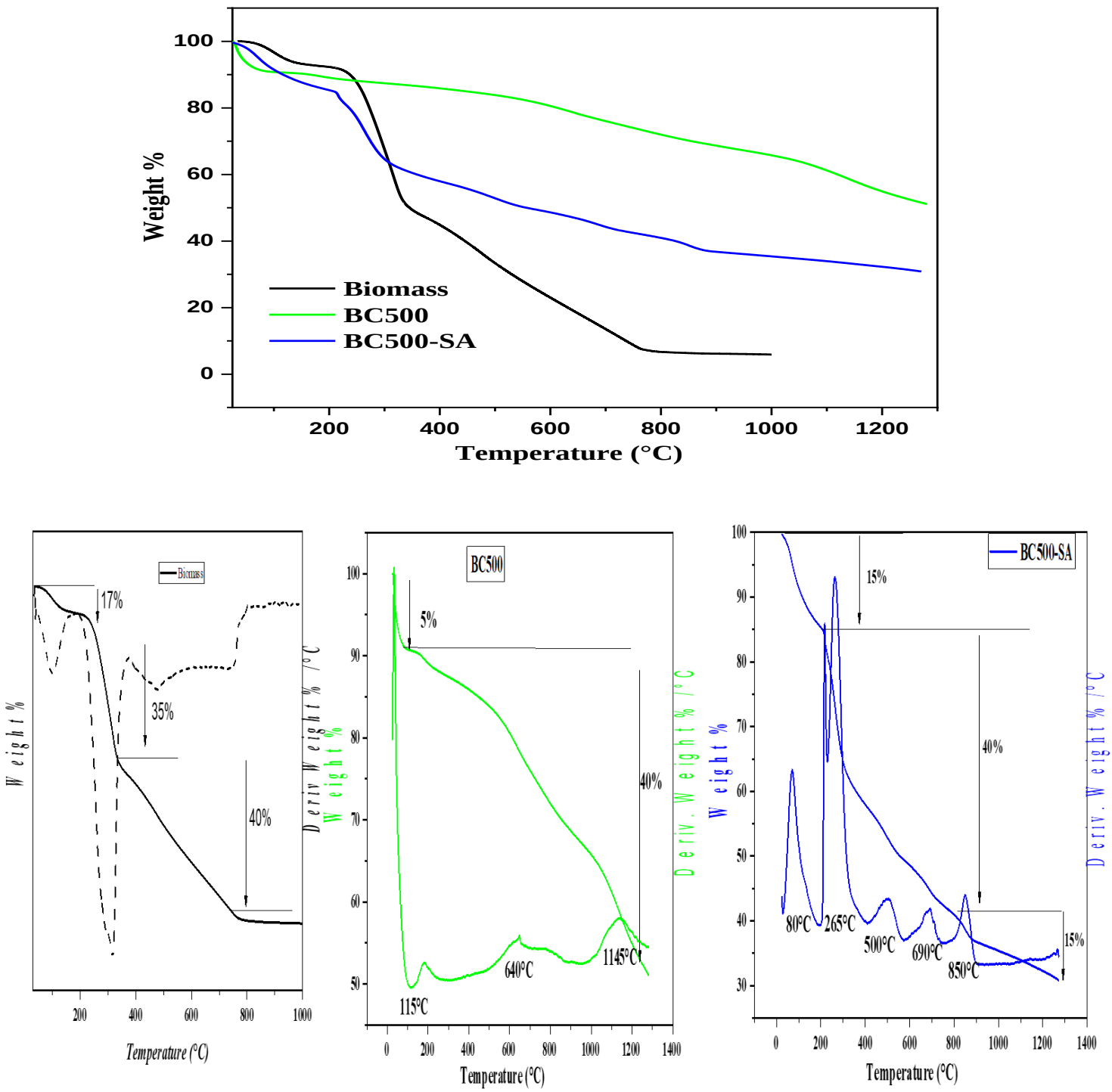


***Figure VI. 4**: ATG/DTA plots of Biomass, BC500, and BC500-SA.*

The TGA/DTA analysis in **Fig.VI.4** of raw biomass shows a first mass loss is visible between 100°C and 200°C (17%), accompanied by a slight endothermic peak on the DTA curve, corresponding to the evaporation of moisture and some volatile compounds [16]. Then, between 200°C and 700°C, a significant drop in mass is observed on the TGA curve (35%), associated with a marked endothermic peak on the DTA curve, indicating the decomposition of the main organic components such as cellulose and hemicellulose. Above 700°C, the TGA curve stabilizes, indicating the presence of non-decomposable inorganic residues, while the DTA curve remains stable, suggesting no new thermal reactions [17]. This figure shows the thermal degradation stages of a material, typical of a biomass, with a stable final phase due to inorganic residues.

The TGA/DTA analysis of the calcined biomass at 500°C indicates the following thermal behavior:

Stage 1 (25–90 °C) with 5% mass loss corresponds to moisture evaporation and removal of physically adsorbed water, which is supported by the small endothermic peak at 115 °C in the DTA curve, Stage 2 (90–1280 °C) with 40% mass loss represents the thermal degradation of the more stable organic components of the biomass or structural decomposition. The two exothermic peaks at 640 °C and 1145 °C in the DTA curve indicate oxidative reactions such as char combustion or structure rearrangements releasing heat at these elevated temperatures [18], [19].

Overall, the thermal analysis reveals that the calcined biomass retains some residual organics that decompose at higher temperatures and exhibits typical moisture loss at low temperatures [20]. The exothermic peaks signal active thermal degradation and oxidation stages of the biochar material formed after calcination, which is common for biomass-derived chars suggesting their potential thermal stability and combustion characteristics [18].

The thermal behavior of the biochar/sodium alginate composite, as revealed by TGA/DTA, can be interpreted as follows:

Stage 1 (20–200 °C) with 15% mass loss corresponds largely to moisture loss and dehydration of physically adsorbed water from the alginate and biomass; this is supported by the DTA exothermic peak at around 80 °C, which may reflect some structural rearrangements or water desorption.

Stage 2 (200–800 °C) showing 40% mass loss represents the major thermal degradation phase, likely involving decomposition of sodium alginate polymer chains and residual organic components from the calcined biomass [21]. The multiple exothermic peaks at 265, 500, and 690 °C indicate successive oxidative decomposition steps such as fragmentation, rupture of glycosidic bonds in alginate, and combustion of char.

Stage 3 (800–1260 °C), with an exothermic peak at 850 °C, likely reflects the final decomposition and stabilization of residual carbonaceous material along with mineral transformations or crystallization in the biochar-alginate composite [22].

3.4.DRX spectrum analysis

Fig. VI.5 illustrates the diffraction pattern of raw biomass, manifesting a distinct prominent peak at 2θ = 22° attributed to the (0 0 2) crystallographic plane, alongside a minor peak at 2θ = 15° corresponding to the (1 0 1) plane [23]. The XRD spectrum shows that for the 2-theta analysis range above 40°, there are no distinct diffraction peaks of crystalline cellulose. Instead, there are mainly amorphous peaks. This implies that the predominant components of the native pulp are non-cellulosic substances, such as hemicellulose and lignin [4]. These observations collectively signify the characteristic structural features associated with cellulose I [24].

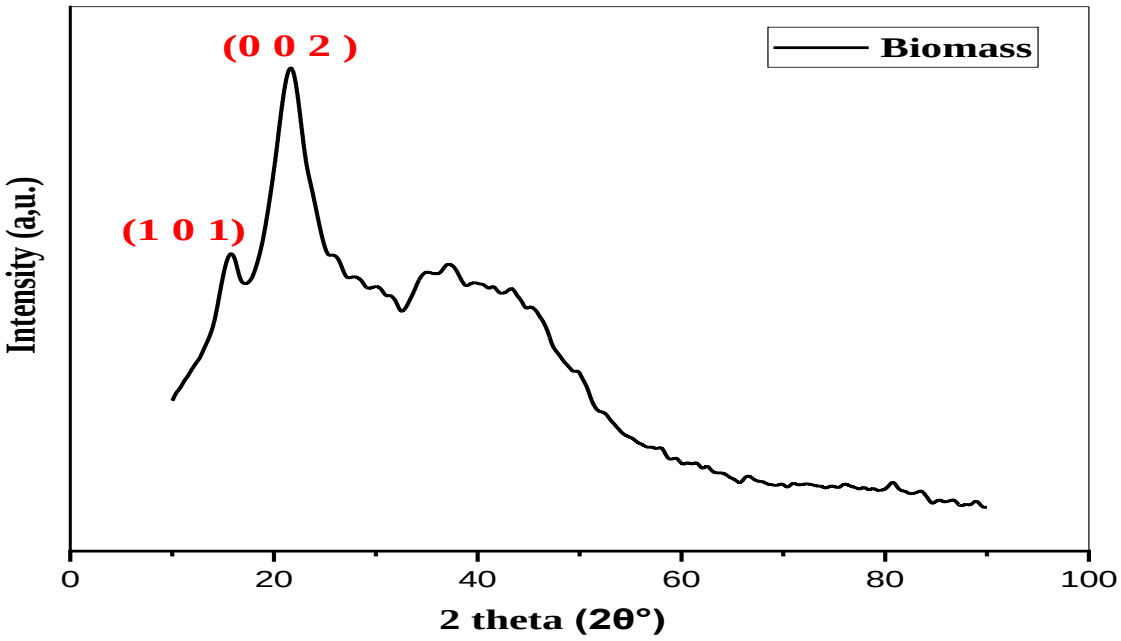


Figure VI. 5: *XRD patterns of raw biomass.*

4. Effects of process parameters

4.1.pH effect:

In this study, the pHpzc value and the influence of pH on the adsorption of the positively charged BM adsorbate by BC500@Alg, BC500H, and BC500 were examined. The results are presented in **Fig. III.6**. The pHpzc values of the obtained materials were 6.2, 6.5, and 8.4 for BC500@Alg, BC500H, and BC500, respectively. These values indicate that the surface of the adsorbents becomes negatively charged when the solution pH exceeds the pHpzc. This deprotonation is attributed to the fact that the pKa of MB (3.8) is lower than the solution pH, which increases the negative charge on the adsorbent [25]. This enhances the electrostatic interactions between the adsorbent and the positively charged MB, leading to a higher adsorption capacity [26].

Conversely, when pH < pH_{pzc}, the materials become positively charged, resulting in repulsive forces between the adsorbent and the adsorbate due to their similar charges. **Fig. VI.6** illustrates the diffraction pattern of raw biomass, manifesting a distinct prominent peak at 2θ = 22° attributed to the (0 0 2) crystallographic plane, alongside a minor peak at 2θ = 15° corresponding to the (1 0 1) plane [23]. The XRD spectrum shows that for the 2-theta analysis range above 40°, there are no distinct diffraction peaks of crystalline cellulose. Instead, there are mainly amorphous peaks. This implies that the predominant components of the native pulp are non-cellulosic substances, such as hemicellulose and lignin [4]. These observations collectively signify the characteristic structural features associated with cellulose I [24], shows that the amount adsorbed increases with increasing pH, reaching a maximum value of 260 $mg \cdot g^{-1}$ at pH = 12 for BC500@Alg, 138 $mg \cdot g^{-1}$ at pH = 12 for BC500H, and 130 $mg \cdot g^{-1}$ at pH = 12 for BC500.

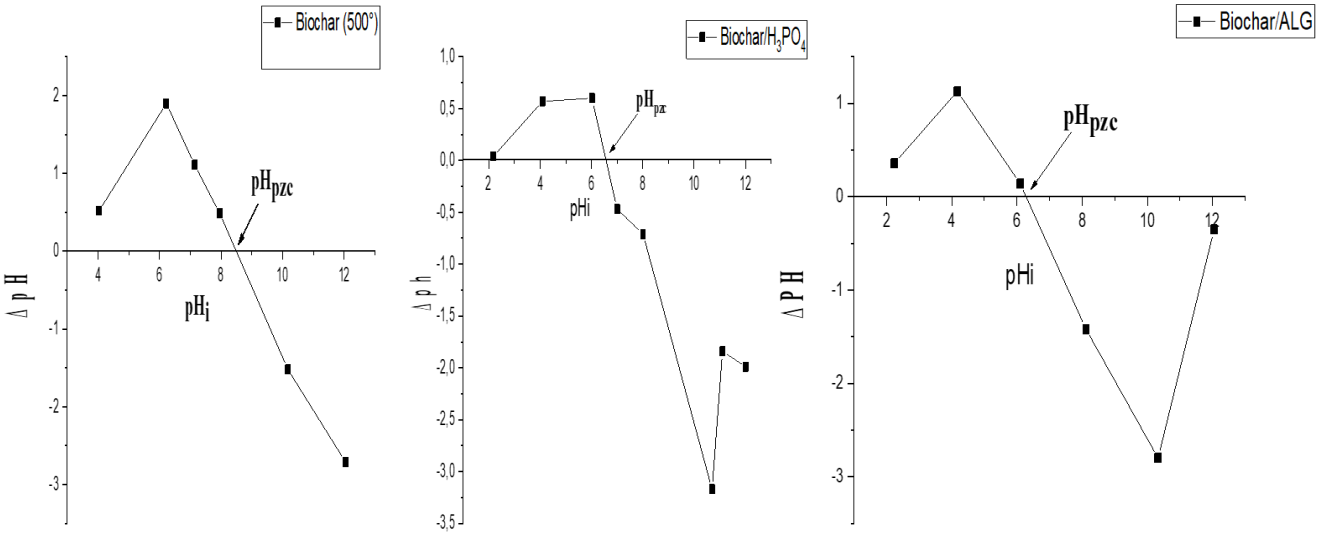


Figure VI. 6: *Effect of pH.*

4.2.The mass effect

Fig. III.7 presents the equilibrium adsorption capacity of MB as a function of the adsorbent mass. The **figure VI.7** shows that, in all cases, the percentage of dye removal increases with increasing adsorbent mass. This phenomenon is easily explained: a higher adsorbent mass provides a larger specific surface area, and therefore a greater number of active sites available for adsorption, which leads to an increase in the amount of dye retained [27].

However, although the adsorption percentage increases with adsorbent mass, it tends to level off beyond a certain point [28]. This stabilization can be attributed to the progressive saturation of adsorption sites and the reduction of the concentration gradient between the solution and the adsorbent, which limits the transfer of dye molecules to the remaining available sites [29].

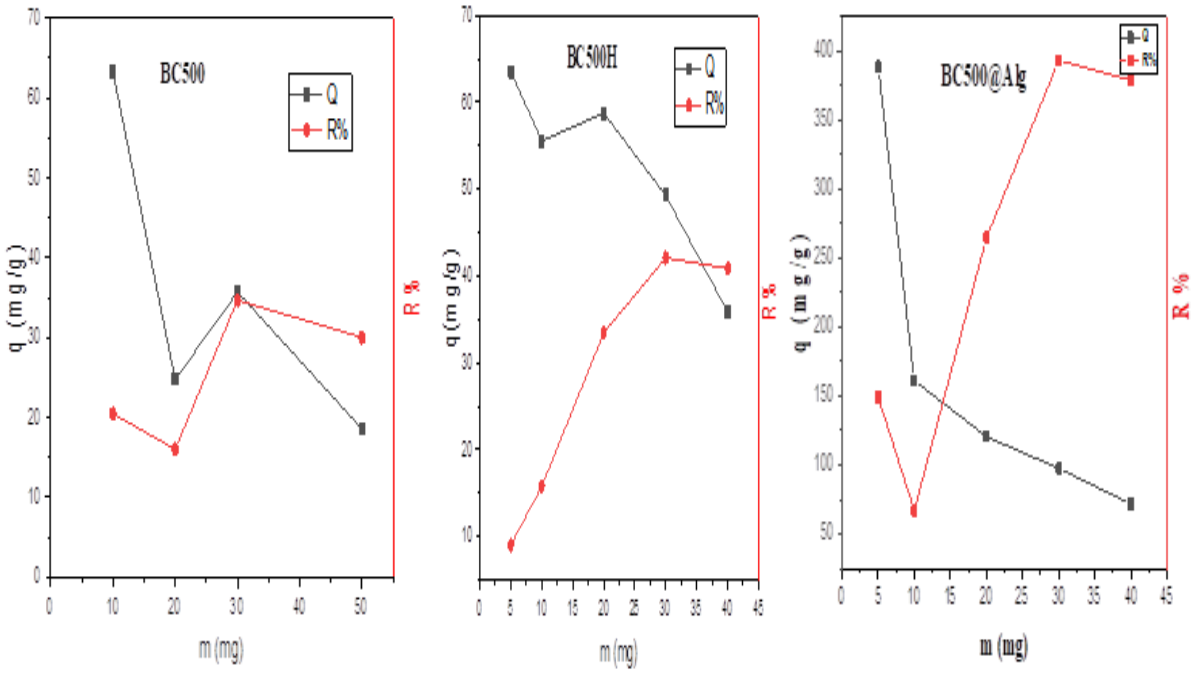


Figure VI. 7: *the masse effect on the adsorption of MB on BC500, BC500H and BC500-SA.*

5. Design of Experiments:

A Box–Behnken design consisting of 17 experiments was employed to evaluate the effects of the independent factors (A: pH, B: adsorbent dose, and C: initial concentration) and their interactions, with the adsorption capacity q (mg/g) as the response variable. The relationship between these variables was modeled using a second-order polynomial, whose performance was validated through the coefficient of determination (R^2) and an ANOVA (Table III.2). Only the significant terms (Prob < 0.05): A, B, C, BC, B^2, and C^2 were retained, while the remaining variables were excluded to optimize the model [30]. The final equation in coded factors is presented below:

$$q = +172.93-5.82*A-75.19*B+78.49*C-13.52*BC+25.07*B^2+19.05*C^2 \quad \text{.....(VI.1)}$$

A positive sign in Eq. (VI. 1) indicates a synergistic effect between the variables, whereas a negative sign reflects an antagonistic influence of the factors. The regression model exhibits a p-value of 0.001 ($p < 0.05$), confirming that the second-order polynomial model accurately fits the experimental data. The high R^2 value (0.989) ensures the model's suitability to the dataset, thereby validating its accuracy [31]. The complementary values of the adjusted R^2 (0.982) and the predictive R^2 (0.95) further demonstrate strong consistency. The adequate precision analysis revealed a signal-to-noise ratio of 45.453, well above the minimum threshold of 4 required for model reliability. Graphical methods (**Fig. VI.8**) confirmed the positive correlation between the predicted and experimental adsorption values of MB, supporting the validity of the BBD model [32].

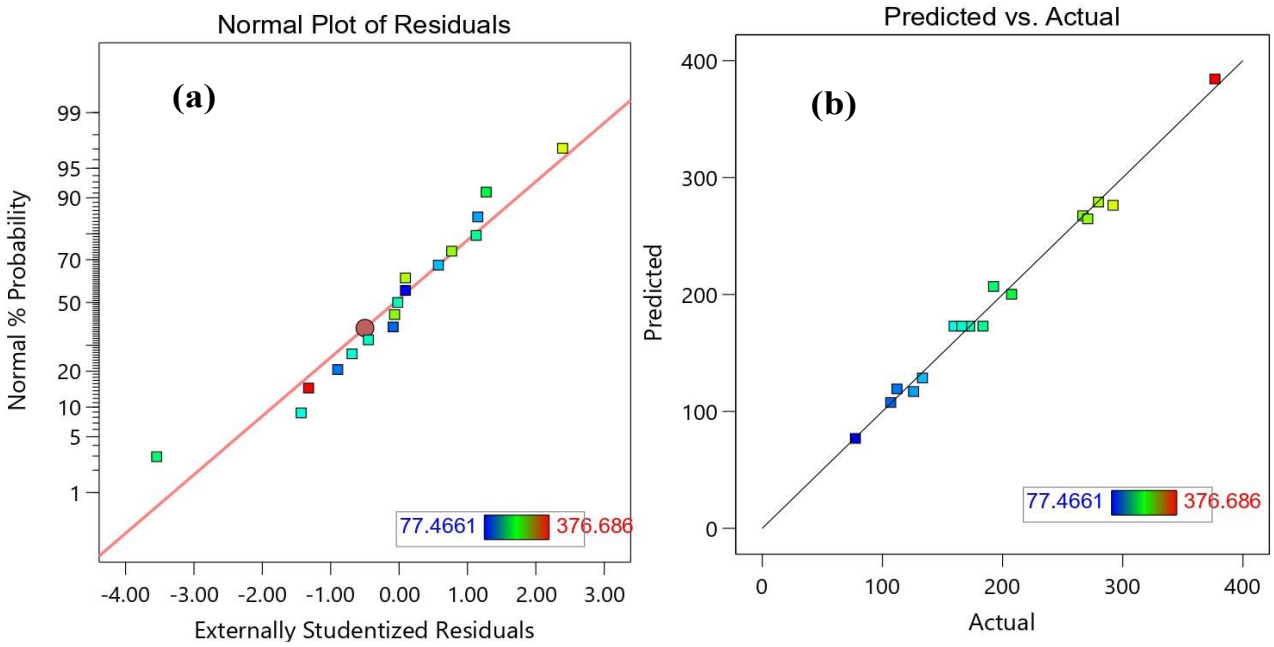


Figure VI. 8: *(a) Normal probability plot of residuals for BC500-SA adsorption capacity, (b) plot of the relationship between the predicted and actual values of BC500-SA adsorption capacity.*

Table VI. 1: *ANOVA results for the adsorption capacity of MB.*

Source	Sum of squares	Df	Mean square	F-value	p-value
Model	99937.51	6	16656.25	149.99	< 0.0001
A-Ph	271.32	1	271.32	2.44	0.1491
B-M	45222.49	1	45222.49	407.24	< 0.0001
C-C	49290.58	1	49290.58	443.87	< 0.0001
BC	731.16	1	731.16	6.58	0.0281
B^2	2652.82	1	2652.82	23.89	0.0006
C^2	1531.54	1	1531.54	13.79	0.0040
Residual	1110.46	10	111.05		

5.1.Interactions effect

The analysis of interaction effects revealed a significant influence between the adsorbent dose and the initial concentration (BC) ($p = 0.0281$), as illustrated by the 3D surface plots and 2D contour diagrams in Figure 3. The adsorption capacity increased with decreasing adsorbent dose and increasing initial concentration [29]. In contrast, the interactions between pH and initial concentration AC ($p = 0.506$) and between pH and adsorbent dose AB ($p = 0.8127$) were found to be non-significant ($p > 0.05$) and were therefore excluded from the final model.

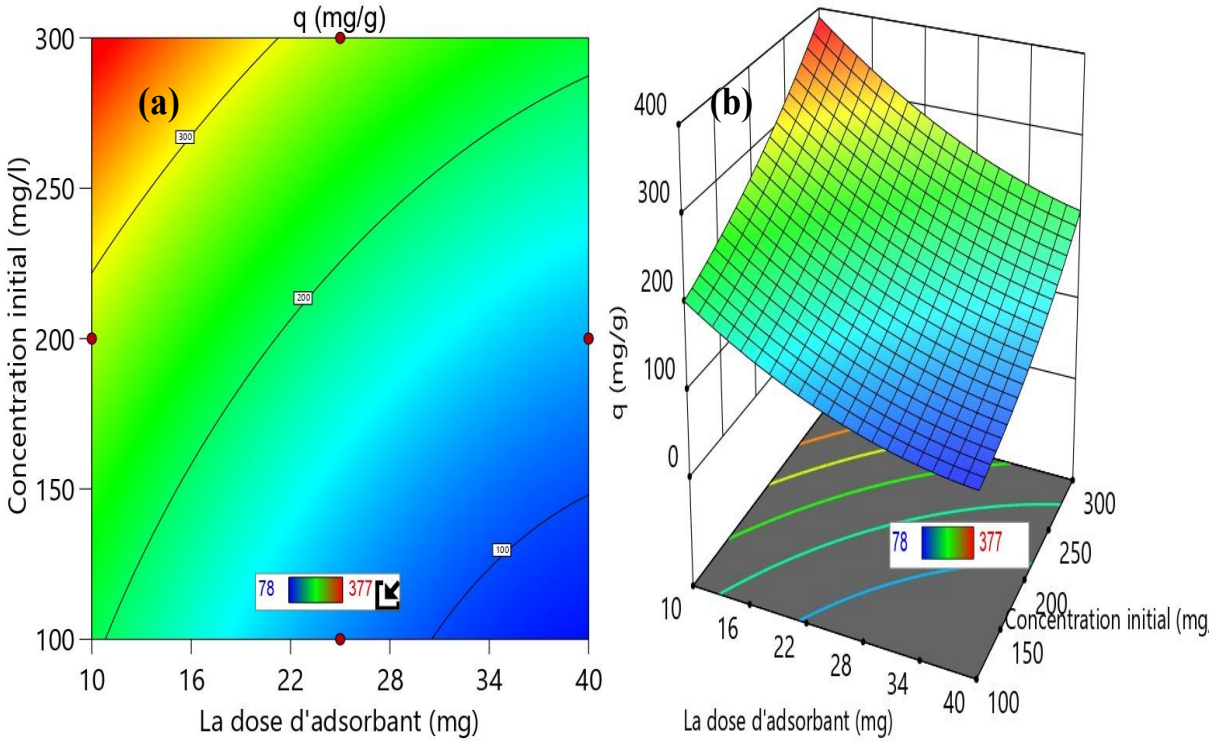


Figure VI. 9: *(a), Contour and (b) 3D surface plots for the interactive effects of adsorbent dosage and initial dye concentration BC500-SA adsorption capacity.*

5.2.Optimization study

To determine the optimal conditions for maximizing the adsorption percentage of MB, the Design-Expert software employed a numerical optimization method. The optimization process consisted of setting the adsorption variables to “within range” and the response i.e., the MB adsorption percentage to “maximize” [33]. The program generated several possible solutions,

and the one with the highest desirability function was selected as the optimal set of conditions that would yield the maximum response. The optimal values determined by the software were: an initial concentration of 300 mg/L, an initial pH of 8, and an adsorbent dose of 10 mg (Fig. 10). Under these conditions, a maximum MB adsorption capacity of 384.24 mg/g was achieved.

Verification tests were conducted using the optimized conditions to confirm the relevance and accuracy of the model [34]. The results showed that the predicted value was very close to the experimental value, resulting in a desirability rate of 100%. Therefore, the Response Surface Methodology (RSM) can be successfully applied to simulate MB adsorption onto the biochar/Sodium alginate composite [35].

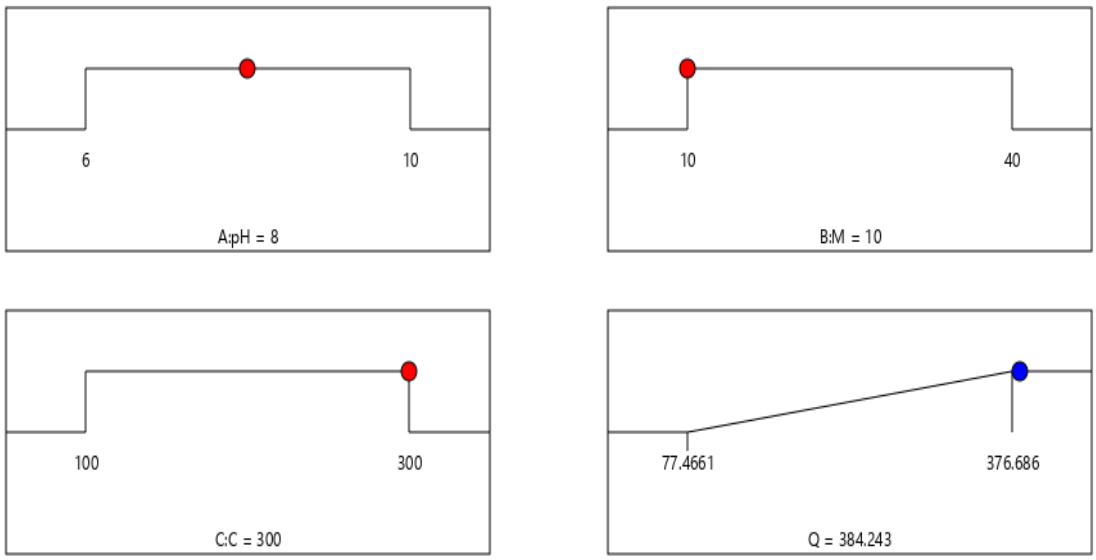


Figure VI. 10: *Optimized values for the process parameters.*

6. Kinetic study:

In order to evaluate the adsorption rate of the MB on the surface of BC500-SA composite, two kinetic models were applied: Pseudo first order (PFO), Pseudo second ordre (PSO). To predict the diffusion mechanism of MB onto the surface of biochar-alginate composite, the adsorption behavior was further tested applying the intra-particle diffusion model (IPD).

The most suitable model for studying the adsorption kinetics is selected based on the correlation coefficient. The higher this coefficient, the more appropriate the model is for describing the adsorption process [36].

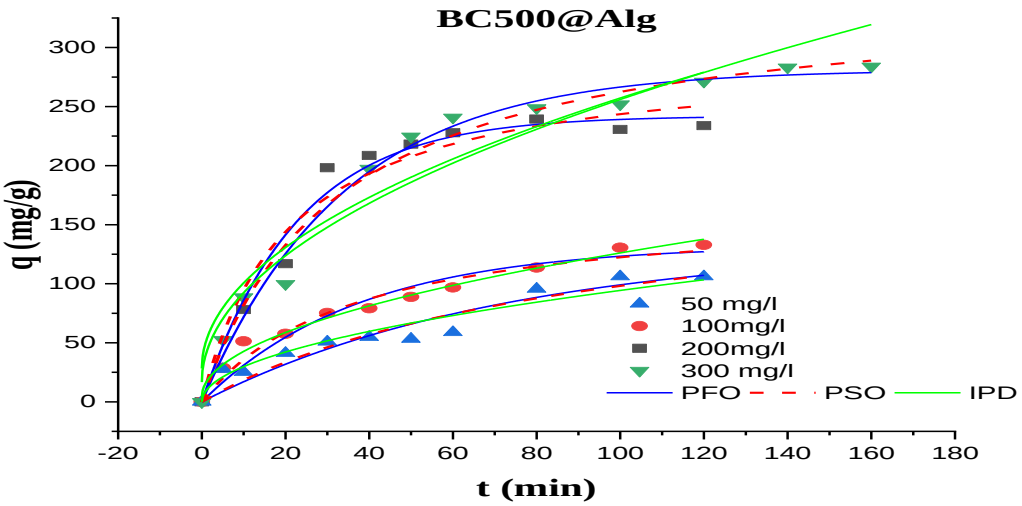


***Figure VI. 11**: Nonlinear PFO, PSO and IPD kinetics models fits for MB adsorption on BC500-SA (C0=50, 100, 200 and 300mg/L).*

***Table VI. 2:** PFO, PSO and IPD models parameters for MB adsorption on BC500-SA at different concentrations (50, 100, 200 and 300mg/L)*

Concentration	q_{exp}	**PFO**			**PSO**			**IPD**		
mg/L	**mg/g**	q_{ecal} **mg/g**	k_1 **1/h**	R^2	q_{ecal} **mg/g**	k_2 **g/mgh**	R^2	**Ki**	**C**	R^2
50 mg/l	106.02	132.72	0.013	0.900	189.23	5.69	0.906	9.4	0	0.929
100 mg/l	132.9	132.57	0.026	0.942	167.42	1.623	0.962	12.19	4.15	0.989
200mg/l	233.82	242.1	0.043	0.975	294.68	1.617	0.952	22.89	28.3	0.835
300mg/l	284.08	281.23	0.029	0.984	347.41	8.88	0.982	23.93	16.7	0.929

The PFO model fits the experimental data better than the PSO model, as indicated by the comparison of the correlation coefficients (R^2). Both models overestimate the adsorption capacity. The variation of the rate constants with concentration reflects a change in the adsorption mechanism or an improved accessibility of active sites at higher concentrations. The PFO model indicates that the process is predominantly governed by physisorption [37].

The intra-particle diffusion (IPD) model also shows good correlations (R^2 values ranging from 0.835 to 0.989). However, the presence of a non-zero constant C, except at the concentration of 50 mg/L, indicates that intra-particle diffusion is not the sole rate-limiting mechanism in the adsorption process. This suggests the involvement of additional steps, such as film diffusion or surface adsorption [38].

7. Adsorption isotherms

The equilibrium adsorption behavior of MB on the different biochar-based materials was investigated at 293, 303, and 313 K using the Langmuir and Freundlich isotherm models. Nonlinear fitting of the experimental data using OriginPro 2018 demonstrated that the Langmuir model better described the adsorption process, with higher correlation coefficients (R^2 = 0.917–0.972) than those obtained for the Freundlich model (R^2 = 0.670–0.911). This indicates that MB adsorption predominantly occurs as a monolayer on a relatively homogeneous surface with energetically equivalent active sites. The Langmuir model predicted maximum adsorption capacities of 141.53 mg/g for BC500H, 302.89 mg/g for BC500, and 524.72 mg/g for BC500SA, highlighting the enhanced adsorption performance of the modified materials.

An R_L value between 0 and 1 indicates a favorable process, whereas RL > 1 suggests unfavorable adsorption, and R_L = 1 denotes linear adsorption. In this study, R_L values ranged

from 0.1 to 0.8, confirming favorable adsorption [25]. Additionally, the Freundlich constant (1/n) was used to assess the nature of adsorption: 1/n > 1 implies physical adsorption, while 1/n < 1 suggests chemisorption [39]. He calculated Langmuir separation factor R_L values between 0.1 and 0.8, further confirming the favorable nature of the adsorption process. In addition, Freundlich constants (1/n < 1) suggest that the adsorption is favorable and likely governed by chemical interactions between MB molecules and surface functional groups of the biochars.

Table VI. 3: *Parameters of the Langumir and Freundlich models for MB adsorption on BC500-SA at 298K.*

Material	**BC500**	**BC500H**	**BC500-SA**
Langumir	qm= 302.89mg/g	qm= 141.53mg/g	qm= 524.72mg/g
	K_L= 0.01	K_L= 0.0087	K_L = 0.019
	R^2= 0.817	R^2= 0.972	R^2= 0.848
Freundlich	n= 2.61	n= 2.43	n= 3.21
	K_f= 23.27	K_f= 8.289	K_f= 70.89
	R^2= 0.67	R^2= 0.911	R^2= 0.743

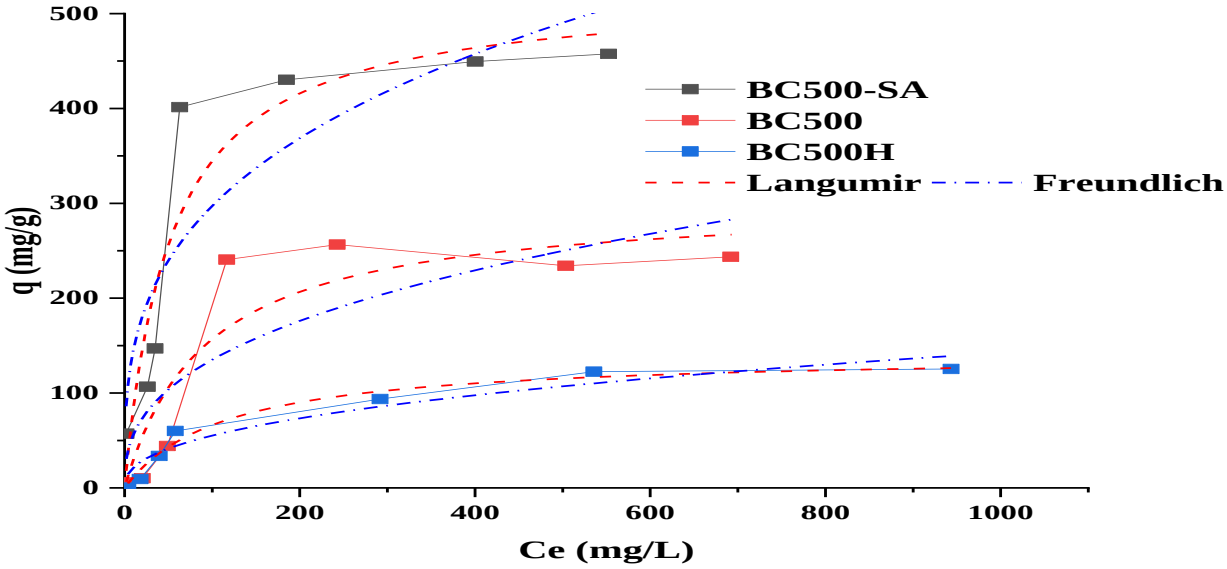


Figure VI. 12: *Langmuir and Freundlich non- linear fits to the experimental data of MB adsorption by BC500-SA at 298 K.*

8. Thermodynamic study

A comprehensive thermodynamic investigation was conducted to elucidate the adsorption characteristics of MB onto the BC500-SA composite at varying temperatures (283, 293 and 303 °K). The fundamental thermodynamic parameters, including Gibbs free energy change (ΔG°), enthalpy change (ΔH°), and entropy change (ΔS°), were quantitatively evaluated using the following relationships [4], [40]:

$$\Delta G° = -R\ T\ Ln\ K$$

$$\text{Log}\left(\frac{1000*qe}{Ce}\right) = 1 + \frac{-\Delta H°}{2.303*RT} + \frac{\Delta S°}{2.303*R}$$

Where R (8.314 J/mol K) is the universal gas constant, T is the absolute temperature (K), and K_L is the equilibrium constant (L/mg).

Table VI.5 presents the values of the thermodynamics parameters. The adsorption of MB on the BC500-SA surface was spontaneous due to the negative values of ΔG°, in addition the positive value of ΔH° (55.32KJ/mol) indicates the endothermic nature of adsorption [41]. Moreover, the increasing in adsorption capacity of BC500-SA at high temperature can be attributed to the effect of this later on the internal structure of the composite, thus facilitating faster diffusion of MB molecules into the BC500-SA interspaces structure. Furthermore, ΔH° inferior to 85 KJ.mol-1, confirmed the physical adsorption nature, ΔS° was positive, indicates the affinity between MB and BC500-SA with an increase in randomness degree during adsorption [42].

Table VI. 4: *Langmuir parameters at different temperature.*

Température (°C)	**20°C**	**30°C**	**40°C**
Langumir	$\mathbf{q_m}$**= 321.99**mg/g	$\mathbf{q_m}$**= 427** mg/g	$\mathbf{q_m}$= 524.72mg/g
	$\mathbf{K_L}$= 0.0168	$\mathbf{K_L}$= 0.0114	$\mathbf{K_L}$= 0.019
	$\mathbf{R^2}$= 0.921	$\mathbf{R^2}$= 0.872	$\mathbf{R^2}$= 0.848

Table VI. 5: *thermodynamic properties of MB adsorption on BC500-SA.*

T(°K)	ΔH°(KJ/mol)	ΔS° (J/mol. K)	ΔG°(KJ/mol)
293	**55.32**	**298.72**	**-31.87**
303			**-35.88**
313			**-37.80**

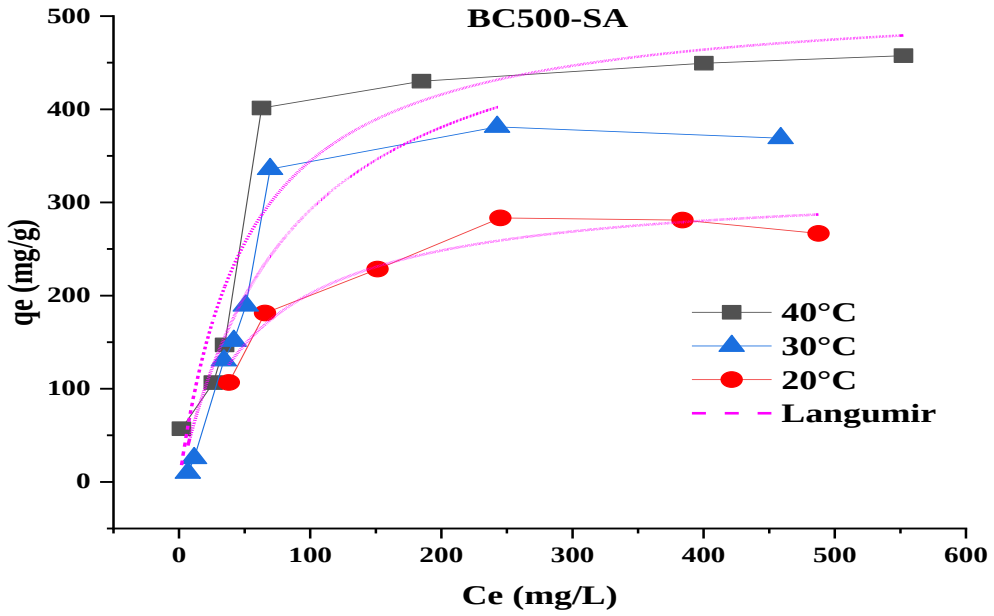


Figure VI. 13: *Langmuir non- linear fits to the experimental data of MB adsorption by BC500-SA at different temperatures.*

9. Desorption and regeneration studies

The regeneration, reuse, and recycling potential of an adsorbent in wastewater treatment represents a critical parameter from both economic and environmental perspectives [40]. In this study, the regeneration procedure was conducted as follows: a 1 M ethanol solution was employed as the desorbing agent, into which the dried composite beads saturated with MB were introduced and subjected to stirring for 1 hour. The resulting mixture was subsequently centrifuged to separate the solid phase, which was then washed and dried in preparation for the next adsorption cycle. This process was repeated for five consecutive cycles, and the

corresponding results are illustrated in **Fig. VI.14** with each cycle the adsorption capacity q (mg/g) is decreasing from 115.3 to 55.47 mg/g.

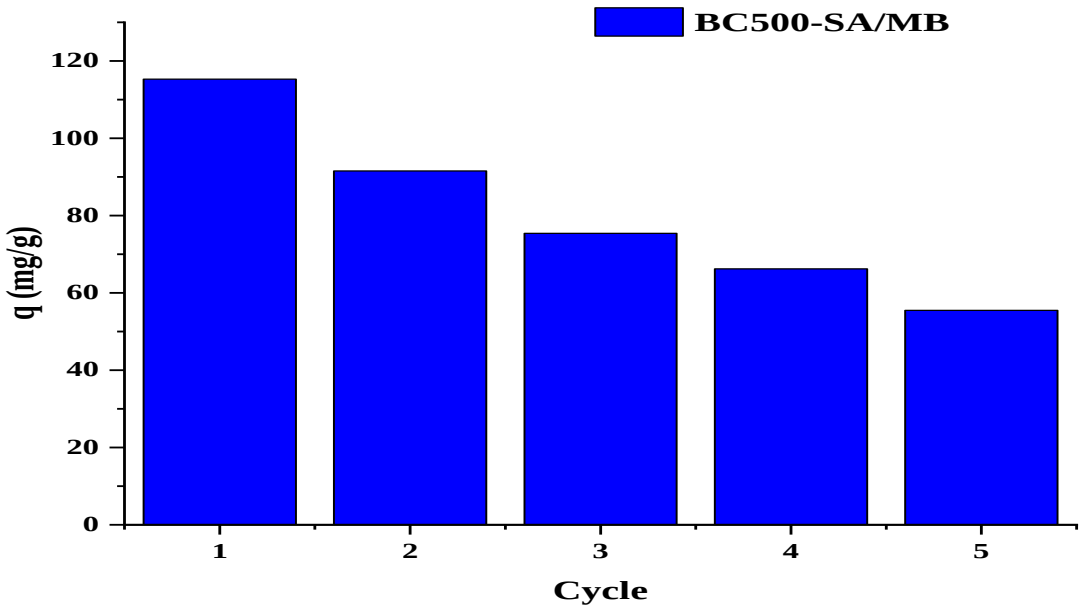


Figure VI. 14: *Regeneration cycles of MB adsorption by BC500-SA beads.*

10. Adsorption mechanism

The adsorption mechanism of MB onto BC500-SA beads is based on a combination of physical processes. The biochar, which is rich in aromatic carbon structures and oxygenated functional groups, exhibits a high specific surface area and significant porosity, promoting the physical adsorption of the dye through π–π interactions between the aromatic rings of the biochar and the benzene nuclei of methylene blue. These hydrophobic interactions are further strengthened by van der Waals forces between the BM^+ cations and the negatively charged surface of BC500-SA under basic conditions [43].

In parallel, alginate a natural polysaccharide containing carboxylate groups ($–COO^–$) plays a complementary role. When crosslinked with calcium ions (Ca^{2+}), it forms a stable gel in which the biochar is dispersed. The $–COO^–$ groups of alginates can interact electrostatically with the positive charges of the cationic methylene blue, thereby promoting adsorption through

electrostatic and van der Waals interactions [44]. Moreover, the hydrogel matrix facilitates easy access of MB molecules to the active sites of the biochar while simultaneously stabilizing the structure of the adsorbent material [45].

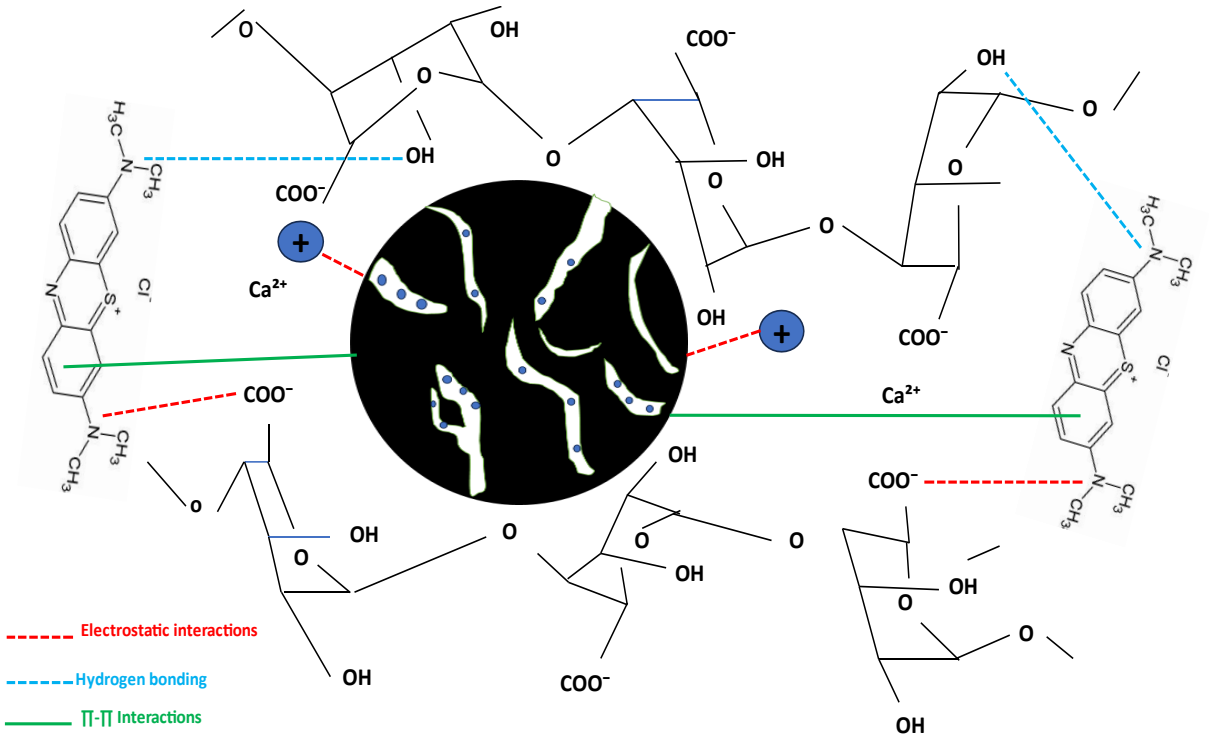


Figure VI. 15: *Proposed mechanism of adsorption of MB by BC500-SA beads.*

Reference of chapter VI

[1] S. A. Echeverría, R. Froidevaux, S. Gaborieau, A. Zaparucha, et E. Heuson, « Hybrid catalysis: an efficient tool for biomass valorization and for the production of new building blocks in chemistry », *Comptes Rendus. Chimie*, vol. 28, nº G1, p. 481-505, mai 2025, doi: 10.5802/crchim.398.

[2] A. I. Abd-Elhamid, A. G. Mostafa, A. A. Nayl, et M. A. Akl, « Novel sulfonic groups grafted sugarcane bagasse biosorbent for efficient removal of cationic dyes from wastewater », *Sci Rep*, vol. 14, nº 1, p. 19129, août 2024, doi: 10.1038/s41598-024-60193-5.

[3] L. Chen, D. Wang, L. Zhang, S. shun Sun, et H. Feng, « Magnetic biochar enhanced sodium alginate microspheres: Fabrication, multifunctional performance and mechanisms for nitrogen-rich wastewater treatment », *Journal of Environmental Chemical Engineering*, p. 120035, 2025.

[4] O. R. Benkouachi *et al.*, « Advanced green peel utilization for efficient methylene blue removal: Integrated analysis and predictive modeling », *Journal of Molecular Liquids*, p. 125951, 2024.

[5] C. Djama, D. Chebli, A. Bouguettoucha, I. Doudou, et A. Amrane, « Statistical physics modelling of azo dyes biosorption onto modified powder of Acorus calamus in batch reactor », *Biomass Conv. Bioref.*, vol. 13, nº 2, p. 1013-1028, janv. 2023, doi: 10.1007/s13399-020-01190-2.

[6] T. M. Eldeeb *et al.*, « Adsorption of methylene blue (MB) dye on ozone, purified and sonicated sawdust biochars », *Biomass Conv. Bioref.*, vol. 14, nº 8, p. 9361-9383, avr. 2024, doi: 10.1007/s13399-022-03015-w.

[7] W. Chen *et al.*, « Insight into KOH activation mechanism during biomass pyrolysis: Chemical reactions between O-containing groups and KOH », *Applied Energy*, vol. 278, p. 115730, nov. 2020, doi: 10.1016/j.apenergy.2020.115730.

[8] R. T. Kapoor, M. Rafatullah, M. R. Siddiqui, et M. Alam, « Adsorptive potential of coconut fruit shell biochar as low-cost adsorbent for sequestration of rhodamine B dye: kinetics, thermodynamics and phytotoxicity studies », *Biomass Conversion and Biorefinery*, vol. 15, nº 17, p. 24609-24628, 2025.

[9] P. Borpujari, S. Khan, J. Dutta, et D. Borah, « Biochar-metal nanocomposites for azo dye removal: advancements, mechanisms, and future prospects », *Discover Applied Sciences*, vol. 7, nº 9, p. 1023, 2025.

[10] E. C. Emenike *et al.*, « Application of rice husks-based biochar for removal of pollutants from water and wastewater », *Separation & Purification Reviews*, p. 1-22, 2025.

[11] K.-Q. Du, J.-F. Li, M. A. Farid, W.-H. Wang, et G. Yang, « Preparation of high-efficient phosphoric acid modified biochar toward ciprofloxacin removal from wastewater », *Industrial Crops and Products*, vol. 226, p. 120649, 2025.

[12] Y. Li *et al.*, « Review of modified biochar for removing humic acid from water: analysis of structure-activity relationship », *Biochar*, vol. 7, nº 1, p. 1, 2025.

[13] S. Shakerizadeh, I. Mobasherpour, E. Salahi, M. Razavi, M. M. Sabzehmeidani, et M. Takalo, « Platanus orientalis L. leaves residue-derived biochar: investigating the effects of synthesis temperature », *Biomass Conversion and Biorefinery*, vol. 15, nº 10, p. 15305-15310, 2025.

[14] C. Qi *et al.*, « Acid-modified biochar-based bacterial fertilizer and increase soil available phosphorus », *Journal of Soils and Sediments*, vol. 25, nº 1, p. 59-66, 2025.

[15] X. Cui, X. Dai, K. Y. Khan, T. Li, X. Yang, et Z. He, « Removal of phosphate from aqueous solution using magnesium-alginate/chitosan modified biochar microspheres derived from Thalia dealbata », *Bioresource technology*, vol. 218, p. 1123-1132, 2016.

[16] M. M. R. Rabby *et al.*, « Production of CNC from agro-waste biomass (maize shells) as a potential reinforcement in bio-nanocomposites: Extraction, modification, and characterization study », *Carbohydrate Polymer Technologies and Applications*, vol. 9, p. 100671, 2025.

[17] C. Jlassi, M. Jabli, H. Agougui, et S. B. Abdessalem, « Preparation of activated carbon from Zilla spinosa biomass by means of microwave for efficient bio-sorption of hazardous methylene blue colorant from water », *Biomass Conversion and Biorefinery*, vol. 15, n° 7, p. 11279-11291, 2025.

[18] M. K. Rafiq, R. T. Bachmann, M. T. Rafiq, Z. Shang, S. Joseph, et R. Long, « Influence of pyrolysis temperature on physico-chemical properties of corn stover (Zea mays L.) biochar and feasibility for carbon capture and energy balance », *PloS one*, vol. 11, n° 6, p. e0156894, 2016.

[19] A. S. Yusuff, L. T. Popoola, et A. I. Igbafe, « Response surface modeling and optimization of hexavalent chromium adsorption onto eucalyptus tree bark-derived pristine and chemically-modified biochar », *Chemical Engineering Research and Design*, vol. 182, p. 592-603, 2022.

[20] E. El-Sayed, E. Abd El-Aziz, H. Othman, et A. G. Hassabo, « Azo dyes: Synthesis, classification and utilisation in textile industry », *Egyptian Journal of Chemistry*, vol. 67, n° 13, p. 87-97, 2024.

[21] D. He, Z. Zhang, W. Zhang, H. Zhang, et J. Liu, « Municipal sludge biochar skeletal sodium alginate beads for phosphate removal », *International Journal of Biological Macromolecules*, vol. 261, p. 129732, 2024.

[22] R. Li *et al.*, « Study of the Factors Influencing the Adsorption of Heavy Metal Pollutants in Water by Activated Carbon Gel Particles », *Journal of Environmental Engineering*, vol. 150, nº 7, p. 04024024, 2024.

[23] C. Djama, D. Chebli, A. Bouguettoucha, I. Doudou, et A. Amrane, « Statistical physics modelling of azo dyes biosorption onto modified powder of Acorus calamus in batch reactor », *Biomass Conv. Bioref.*, vol. 13, nº 2, p. 1013-1028, janv. 2023, doi: 10.1007/s13399-020-01190-2.

[24] F. P. da Silva, L. C. Felippe, C. P. Borges, A. Casellato, et F. V. da Fonseca, « Enhanced Removal of Organic Compounds Assisted by Activated Carbon/Copper (II) Complex Composite », *Processes*, vol. 13, nº 2, p. 447, 2025.

[25] S. T. Al-Asadi, F. F. Al-Qaim, H. F. S. Al-Saedi, I. F. Deyab, H. Kamyab, et S. Chelliapan, « Adsorption of methylene blue dye from aqueous solution using low-cost adsorbent: kinetic, isotherm adsorption, and thermodynamic studies », *Environ Monit Assess*, vol. 195, nº 6, p. 676, juin 2023, doi: 10.1007/s10661-023-11334-2.

[26] F. Batana, M. Taouti, et A. Guibadj, « Cinétique de l'adsorption du bleu de méthylène sur bentonite brute et traitée », *Algerian Journal of Environmental Science and Technology*, vol. 5, nº 4, 2019.

[27] S. Dardouri et J. Sghaier, « Adsorptive removal of methylene blue from aqueous solution using different agricultural wastes as adsorbents », *Korean J. Chem. Eng.*, vol. 34, nº 4, p. 1037-1043, avr. 2017, doi: 10.1007/s11814-017-0008-2.

[28] O. R. Benkouachi *et al.*, « Innovative Valorization of Agricultural Waste for Enhanced Adsorption Efficiency of Organic Pollutants: Leveraging Density Functional Theory, Molecular Dynamics Simulations, and Advanced Artificial Intelligence Techniques (Ann_Fdb-Lfd, Svm_Fdb-Lfd, Gpr_Fdb-Lfd, and Knn_Fdb-Lfd) », *Molecular Dynamics Simulations, and Advanced Artificial Intelligence Techniques (Ann_Fdb-Lfd, Svm_Fdb-*

Lfd, Gpr_Fdb-Lfd, and Knn_Fdb-Lfd), Consulté le: 15 octobre 2024. [En ligne]. Disponible sur: https://papers.ssrn.com/sol3/papers.cfm?abstract_id=4869666

[29] H. Chaima *et al.*, « Adsorptive removal of cationic dye from aqueous solutions using activated carbon prepared from *Crataegus monogyna*/sodium alginate/polyaniline composite beads: Experimental study and molecular dynamic simulation », *Journal of Molecular Liquids*, vol. 408, p. 125372, août 2024, doi: 10.1016/j.molliq.2024.125372.

[30] A. S. Bendrihem *et al.*, « Experimental and theoretical studies of the interaction of cationic dye in halloysite nanotubes », *Reac Kinet Mech Cat*, août 2025, doi: 10.1007/s11144-025-02933-w.

[31] G. A. Al-Hazmi *et al.*, « Elimination of Ni (II) from wastewater using metal-organic frameworks and activated algae encapsulated in chitosan/carboxymethyl cellulose hydrogel beads: Adsorption isotherm, kinetic, and optimizing via Box-Behnken design optimization », *International Journal of Biological Macromolecules*, vol. 299, p. 140019, 2025.

[32] Y. Hu *et al.*, « Facile preparation of cucurbituril-modified magnetic chitosan microspheres for efficient removal of Cr (VI) and MB from wastewater: Adsorption experiments, statistical optimization, and mechanistic insights », *International Journal of Biological Macromolecules*, p. 144207, 2025.

[33] K. Imene *et al.*, « Thermal treatment of Cu-doped hydrotalcite-like adsorbents for improved removal of methyl orange from water », *Separation and Purification Technology*, vol. 365, p. 132656, sept. 2025, doi: 10.1016/j.seppur.2025.132656.

[34] N. Slougui, M. Slama, Y. Boudaoud, et A. S. Bendrihem, « Optimization of GC-MS Method for Analysis of Basil Essential Oils from Algeria: Design of Experiments and Exploratory Pattern Recognition », *Journal of Chemistry*, vol. 2022, n° 1, p. 5880539, 2022.

[35] N. Fettah *et al.*, « Application of response surface methodology to optimise the Metronidazole antibiotic removal by a developing Bio-Electro-Fenton process », *International Journal of Environmental Analytical Chemistry*, p. 1-22, 2025.

[36] A. E. Kuyucu, A. Selçuk, Y. Önal, İ. Alacabey, et K. Erol, « Effective removal of dyes from aqueous systems by waste-derived carbon adsorbent: physicochemical characterization and adsorption studies », *Scientific Reports*, vol. 15, nº 1, p. 28835, 2025.

[37] B. B. Kargule *et al.*, « Sustainable removal of dyes from wastewater using eggshell-derived calcium carbonate nanoparticles: adsorption isotherms, kinetics, and thermodynamic analysis supporting Sustainable Development Goals (SDGs) », *ASEAN Journal of Science and Engineering*, vol. 5, nº 2, p. 369-394, 2025.

[38] O. Abdelwahab, A. El Nemr, A. El-Sikaily, et A. Khaled, *Use of rice husk for adsorption of direct dyes from aqueous solution: A case study of direct F. Scarlet*, vol. 31. 2005.

[39] H. R. Ahmed, K. F. Kayani, A. M. Ealias, et K. H. H. Aziz, « A Comprehensive Review of Forty Adsorption Isotherm Models: An In-depth Analysis of Ten Statistical Error Measures », *Water, Air, & Soil Pollution*, vol. 236, nº 6, p. 346, 2025.

[40] A. Guediri, A. Bouguettoucha, D. Chebli, et A. Amrane, « The use of encapsulation as a proposed solution to avoid problems encountered with conventional materials in powder form: Application in methylene blue removal from aqueous solutions », *Journal of Molecular Liquids*, vol. 316, p. 113841, oct. 2020, doi: 10.1016/j.molliq.2020.113841.

[41] S. S. Imam et M. F. Hamza, « Adsorptive removal of neutral red dye from aquatic environments: a review of adsorbent materials, kinetics, isotherms, thermodynamics and future prospects », *Environmental Technology Reviews*, vol. 14, nº 1, p. 69-93, 2025.

[42] E. Misran, W. Pratama, K. I. K. Napitupulu, M. D. Supardan, D. A. Iryani, et V. Pramananda, « Ultrasonic-assisted adsorption of methylene blue using shrimp shells as a low-cost adsorbent: evaluation on the adsorption isotherm, kinetics, and

thermodynamics », *South African Journal of Chemical Engineering*, vol. 52, p. 111-126, 2025.

[43] W. Fan et X. Zhang, « Magnetic coconut shell biochar/sodium alginate composite aerogel beads for efficient removal of methylene blue from wastewater: Synthesis, characterization, and mechanism », *International Journal of Biological Macromolecules*, vol. 284, p. 137945, 2025.

[44] S. Bose, P. Senthil Kumar, B. Chitra, et G. Rangasamy, « Remediation of chlorpyrifos and methylene blue dye using biochar-modified Bacillus cell-immobilized alginate beads », *Biomass Conversion and Biorefinery*, vol. 15, nº 8, p. 11959-11971, 2025.

[45] A. G. Shoaib, M. Yılmaz, A. El Sikaily, M. A. Hassaan, M. A. El-Nemr, et A. El Nemr, « Isotherm, kinetics and ANN analysis of methylene blue adsorption onto nitrogen doped Ulva lactuca Biochar », *Scientific Reports*, vol. 15, nº 1, p. 10642, 2025.



CHAPTER VII



1. Introduction

In this study, CTAB was used to achieve organic modification of commercial Montmorillonite (MTM-K10) to enhance the removal of MO from water sources. The physicochemical properties were investigated by applying different approaches, such as FTIR, DRX, ATG, and the isoelectric point. The kinetics and isotherm models were applied for a better understanding of the adsorption mechanism.

2. Characterization

2.1.FTIR analysis

The FT-IR analysis of the MTM-K10 and MTM-K10-CTAB materials **(Fig.VII.1)** reveals significant structural differences between the two samples. For both materials, a characteristic absorption band at 3630 cm^{-1} is observed, which is assigned to the stretching vibrations of hydroxyl groups (Al–OH and Si–OH) associated with the montmorillonite structure [1]. In addition, an absorption band at 3440 cm^{-1} is detected, corresponding to the stretching vibrations of water molecules adsorbed on the surface or located within the interlayer spaces [2]. The low-frequency region exhibits a broad band centered at 1045 and 1085 cm^{-1}, characteristic of Si–O stretching vibrations, along with an additional band at 801 cm^{-1}, indicating the presence of quartz impurities [3]. The modification with CTAB is clearly evidenced by the emergence of two new absorption bands at 2925 cm^{-1} and 2848 cm^{-1} in the spectrum of MTM-K10-CTAB [4]. These bands are respectively attributed to the asymmetric and symmetric stretching vibrations of methylene ($–CH_2–$) and methyl ($–CH_3$) groups associated with the alkyl chain of CTAB [5]. These spectroscopic findings confirm the successful grafting of the cationic surfactant onto the montmorillonite surface, leading to the formation of an organo-montmorillonite [6]. The presence of characteristic vibrational signatures associated with organic functional groups demonstrates the effectiveness of the

modification process and substantiates the hybrid organo-mineral nature of the CTAB-MTM-K10 material.

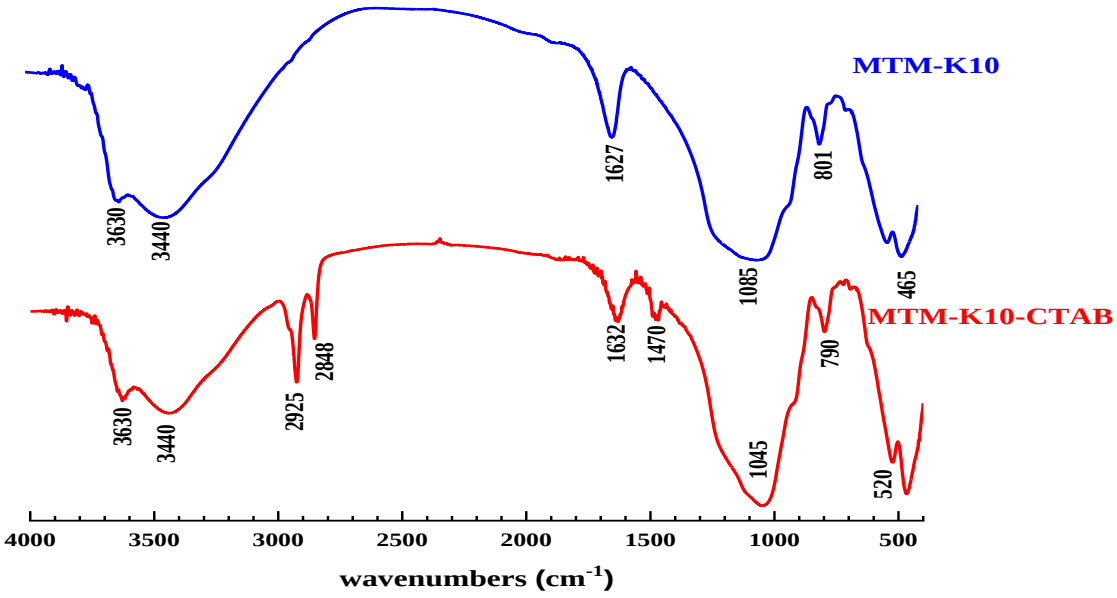


Figure VII. 1: *FTIR spectrum of MTM-K10 and MTM-K10-CTAB.*

2.2.X-ray diffraction analysis

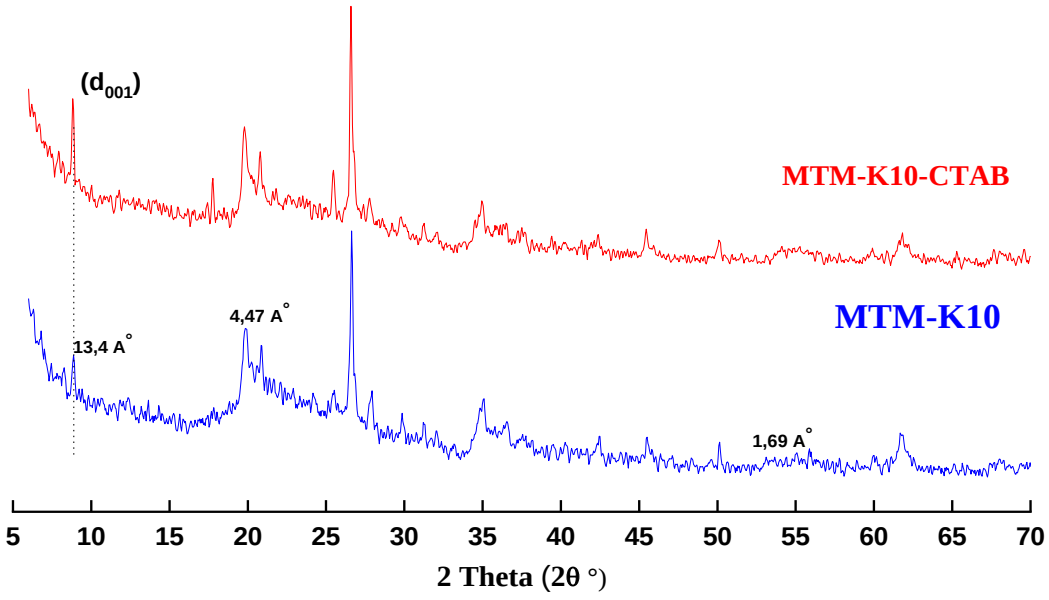


Figure VII. 2: *X-ray diffraction patterns of MTM-K10 and MTM-K10-CTAB.*

The X-ray diffraction (XRD) pattern of pristine MTM-K10 **(Fig.VII.2)** reveals the presence of clay minerals along with well-defined crystalline phases characteristic of bentonitic materials. The main diffraction peaks, with interplanar spacings of d_{020} = 4.47 Å and d_{150} = 1.69 Å, are respectively associated with 2:1 type clay minerals [7] and confirm the presence of dioctahedral smectite phases [8]**.** In addition, impurity phases are detected, notably quartz (**SiO_2**) with reflections at 2θ = 26.6°, 27.9°, and 50.18°, as well as feldspar (**albite, $NaAlSi_3O_8$**) evidenced by a diffraction peak at 2θ = 23.6°. Additional reflections of low intensity are also observed and can be attributed to carbonate phases, specifically calcite, with a diffraction peak located at 2θ = 20.93° [2], [8].

The first reflection appearing at 2θ = 8.85° is characteristic of clay mineral groups and corresponds to the basal (001) reflection, which defines the interlayer spacing $\mathbf{d_{001}}$. The basal spacing obtained for the studied bentonite is d_{001} = 13.4 Å. This value falls within the typical range of 12–16 Å, which is characteristic of T–O–T (tetrahedral–octahedral–tetrahedral) type clay minerals [9].

It was observed that, following modification of MTM-K10 with CTAB, the reflection corresponding to the (001) plane shifted a little, while the remaining reflections remained essentially unchanged [10]. The indexed diffraction peaks indicated that the mineralogical composition of both MTM-K10 and MTM-K10-CTAB was predominantly composed of montmorillonite and quartz. These observations are consistent with findings reported in the literature [3].

2.3.ATG analysis

The comparative thermogravimetric analysis of MTM-K10 and its CTAB modified counterpart, CTAB–MTM-K10 (**Fig.VII.3**), reveals markedly different thermal behaviors. For the pristine material, the thermal profile displays three distinct decomposition stages:

First, an initial mass loss occurring between 35 and 200 °C, attributed to the removal of physically adsorbed surface water, interlayer dehydration in the temperature range of 250–480 °C, at last a structural degradation above 500 °C, associated with the release of constitutionally bound water from the crystalline lattice.

CTAB modification results in a more pronounced mass loss compared with that of the pristine montmorillonite, particularly within the 160–800 °C temperature range, where the decomposition of intercalated alkylammonium groups occurs. This distinct thermal behavior confirms the successful intercalation of CTAB organic cations into the interlayer spaces of the clay [11], similarly replacing the originally present exchangeable inorganic cations and interlayer water molecules [12]. The increased thermal instability of CTAB–MTM-K10 relative to the pristine material further attests to the hybrid organo mineral nature of the resulting composite, in which the surfactant alkyl chains significantly diminish the overall thermal stability of the system [4].

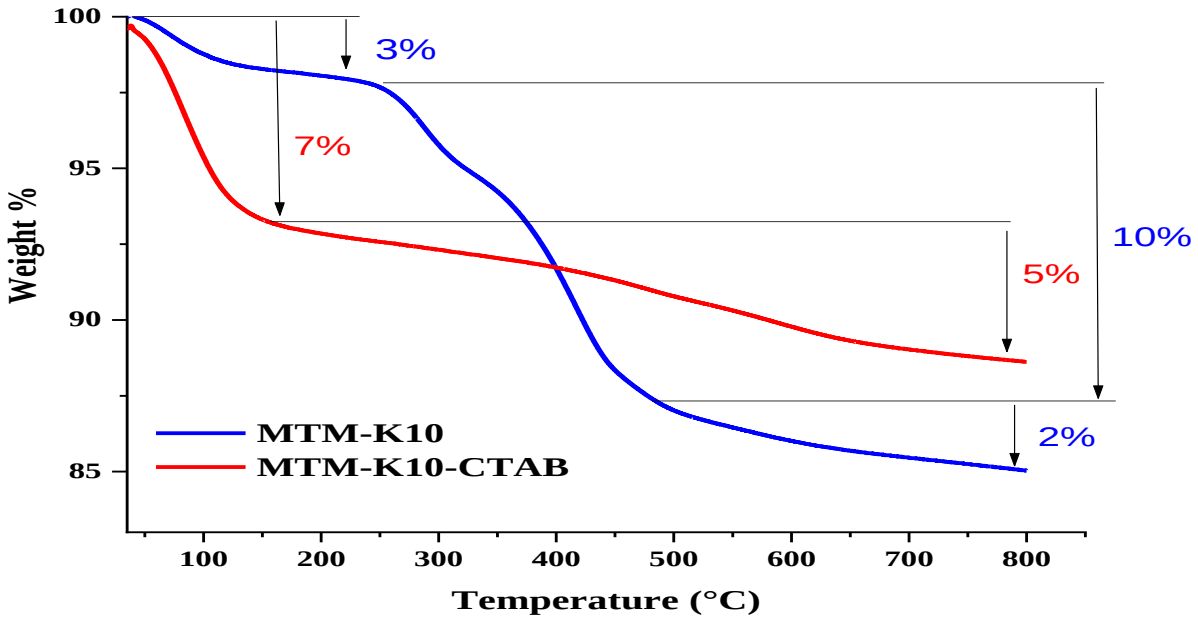


Figure VII. 3: *ATG curve plots for MTM-K10 and MTM-K10-CTAB.*

2.4.Iso-electric point (pHpzc)

Fig.VII.4 illustrates the evolution of the pH at the point of zero charge (pH_{pzc}) of the investigated materials. Analysis of the point of zero charge reveals a significant alteration of surface properties induced by CTAB functionalization. Natural montmorillonite (MTM) exhibits a pH_{pzc} of approximately 4.5, which is characteristic of a negatively charged surface arising from isomorphic substitutions within its tetrahedral and octahedral framework [13].

This negative surface charge progressively increases with rising pH values (> 4.8) due to the preferential adsorption of hydroxyl ions. In contrast, the CTAB-modified form, CTAB–MTM-K30, exhibits a pronounced shift of the pH_{pzc} toward approximately 7.2, resulting from the anchoring of positively charged quaternary ammonium groups [14]. This surface modification imparts remarkable amphoteric properties to the material: under acidic conditions (pH < 6.5), the $–N^{+}(CH_3)_3$ groups predominate, generating an overall positively charged surface favorable for anion adsorption, whereas under alkaline conditions, the native silanol (Si–OH) sites of the clay become dominant, preserving a certain affinity toward cations [2], [14].

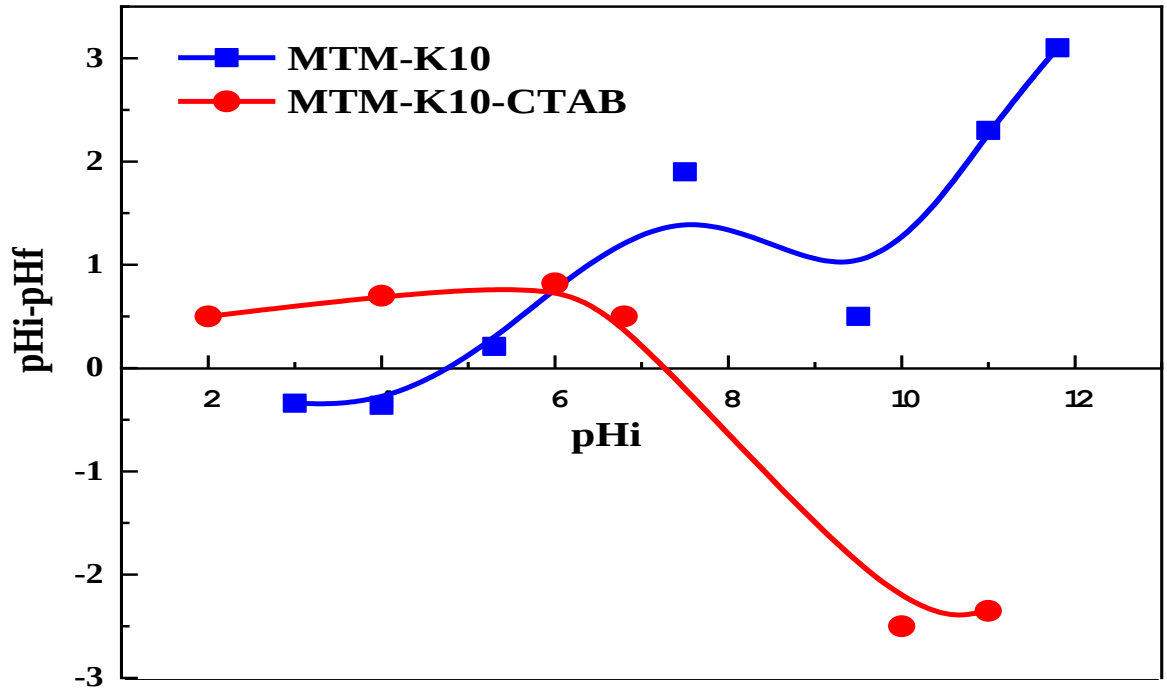


Figure VII. 4: *pHpzc points for MTM-K10 and MTM-K10-CTAB.*

3. Kinetic study

The variation in the amount of MO adsorbed by MTM-K10-CTAB as a function of contact time is presented in **Fig. VII.5**. The results show a rapid increase in MO adsorption during the initial 20 min, followed by a gradual decline in the adsorption rate with prolonged contact time. This behavior can be attributed to the high availability of active adsorption sites on the surface of the organophilic bentonite and the relatively low mass transfer resistance at the early stage of the process. Adsorption equilibrium was reached within 30 min, with adsorption capacities of 11.67 mg g^{-1} and 32.11 mg g^{-1} at initial MO concentrations of 50 and 100 mg L^{-1}, respectively, indicating a strong affinity of the dye for the MTM-K10-CTAB surface. The pronounced initial uptake is associated with the abundance of vacant surface sites, whereas the subsequent slower adsorption rate may be related to anion exchange interactions between MO molecules and the negatively charged bentonite surface [6], [15]. The kinetic parameters derived from the experimental data are summarized in **Table VII.1**. The pseudo-first-order model exhibited a low correlation coefficient, suggesting its inadequacy in describing the adsorption behavior. In contrast, the pseudo-second-order model provided a high coefficient of determination (R^2), and the calculated adsorption capacity closely matched the experimental value. These findings indicate that MO adsorption onto MTM-K10-CTAB is better described by a pseudo-second-order kinetic model, implying that the process is governed primarily by chemisorption [16].

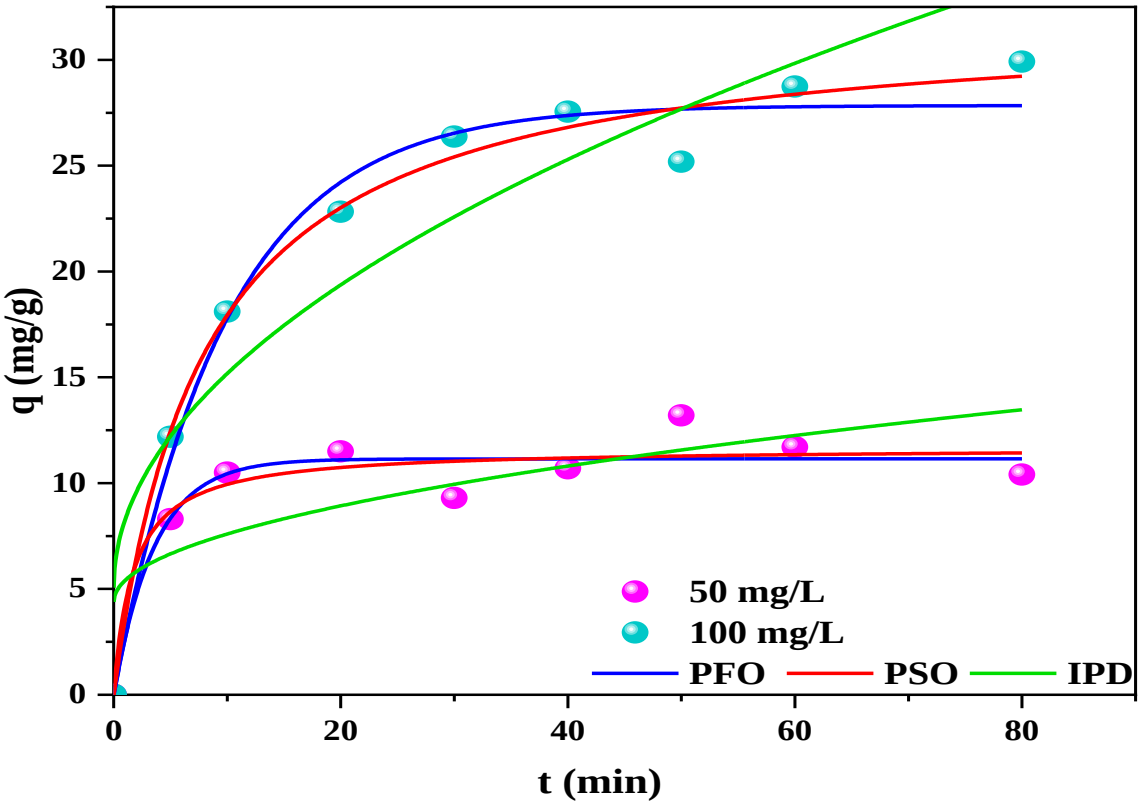


Figure VII. 5: *Nonlinear PFO, PSO and IPD kinetics models fits for MO adsorption on MTM-K10-CTAB (C0=50 and 100mg/L).*

Table VII. 1: *PFO, PSO and IPD models parameters for MO adsorption on MTM-K10-CTAB at different concentrations (50 and 100 mg/L).*

Concentration	q_{exp}	PFO (AIC=15.18)			PSO(AIC=10.43)			IPD (AIC=31.23)		
mg/L	mg/g	q_{cal} mg/g	K_1 1/h	R^2	q_{cal} mg/g	K_2 g/mgh	R^2	K_{IPD}	C	R^2
50	11.7	11.14	0.27	0.914	11.67	0.049	0.911	31.01	4.38	0.515
100	29.91	27.84	0.10	0.977	32.11	0.0039	0.986	3.198	5.06	0.868

4. Isotherm study

Adsorption isotherm analysis was employed to determine the maximum uptake capacities of MB and MO on MTM-K10 and MTM-K10-CTAB surfaces, respectively, under constant temperature conditions. As illustrated in Fig. VII.6, the equilibrium adsorption capacity of both dyes increased with rising equilibrium dye concentrations in solution. The experimental equilibrium data were fitted to the Langmuir and the Freundlich isotherm models. As shown in Fig. VII.6, the adsorption behavior for both systems was more accurately described by the Langmuir model compared to the Freundlich model. The corresponding isotherm parameters summarized in Table VII.2 indicate that the Langmuir model yielded higher correlation coefficients than the Freundlich model for both adsorption systems, with R^2 values of 0.994 versus 0.945 for the MTM-K10-CTAB/MO system and 0.876 versus 0.616 for the MTM-K10/MB system. These results suggest that the adsorption of both dyes predominantly follows a monolayer adsorption mechanism [15], [17]. Furthermore, the relatively low Langmuir affinity constants (KL) indicate moderate to low interactions between the dye molecules and the active sites of MTM-K10-based adsorbents.

Table VII. 2: *Langmuir and Freundlich parameters values for different adsorption systems.*

Isotherm	**Parameters**	**Adsorption system**	
		MTM-K10-CTAB/MO	**MTM-K10/MB**
Langmuir	**q_m (mg/g)**	84.56	106.008
	K_L	0.034	0.668
	R^2	0.994	0.876
Freundlich	**1/n**	0.264	0.106
	K_F	17.375	59.58
	R^2	0.945	0.616

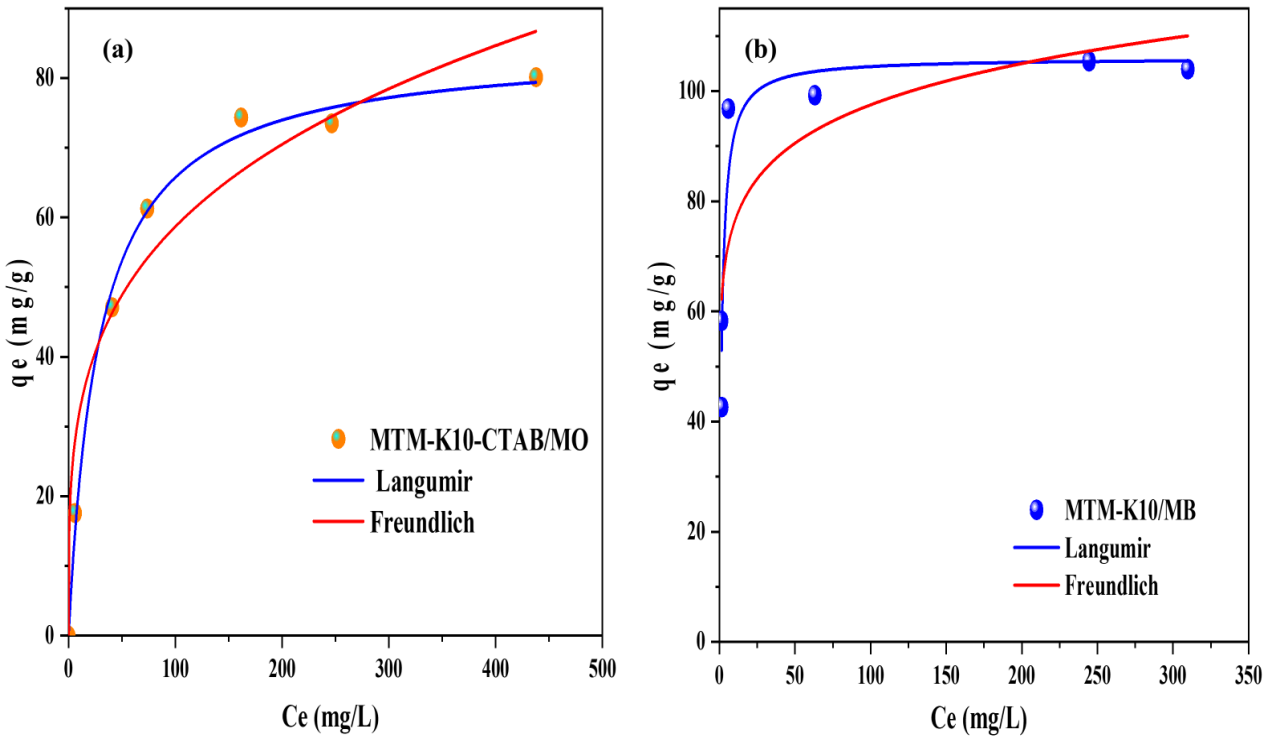


Figure VII. 6: *Langmuir and Freundlich non linear fits for a). MTM-K10-CTAB/MO and b). MTM-K10/MB at pH=6, v=30ml, m=30mg and T=25°C.*

5. Adsorption mechanism

Methyl orange, an anionic dye, interacts efficiently with K10 montmorillonite rendered organophilic through modification with the cationic surfactant cetyltrimethylammonium bromide (CTAB). This functionalization imparts both hydrophobic character and a net positive surface charge to the clay, thereby promoting multiple interaction mechanisms [18]. The predominant interaction arises from electrostatic attraction between the quaternary ammonium groups ($–NR_4^+$) of the surfactant anchored onto the montmorillonite surface and the negatively charged sulfonate groups of MO [19]. In addition, hydrophobic interactions between the alkyl chains of the surfactant (CTAB) and the aromatic, hydrophobic moieties of the dye further enhance adsorption [20], [21]. These effects are complemented by Van der Waals forces and potentially, π–π interactions between the aromatic rings of MO and those associated with the

modified clay structure [22]. The synergy of these interactions accounts for the strong affinity of organophilic montmorillonite toward MO, highlighting its effectiveness as an adsorbent for the treatment of dye-contaminated wastewater [19].

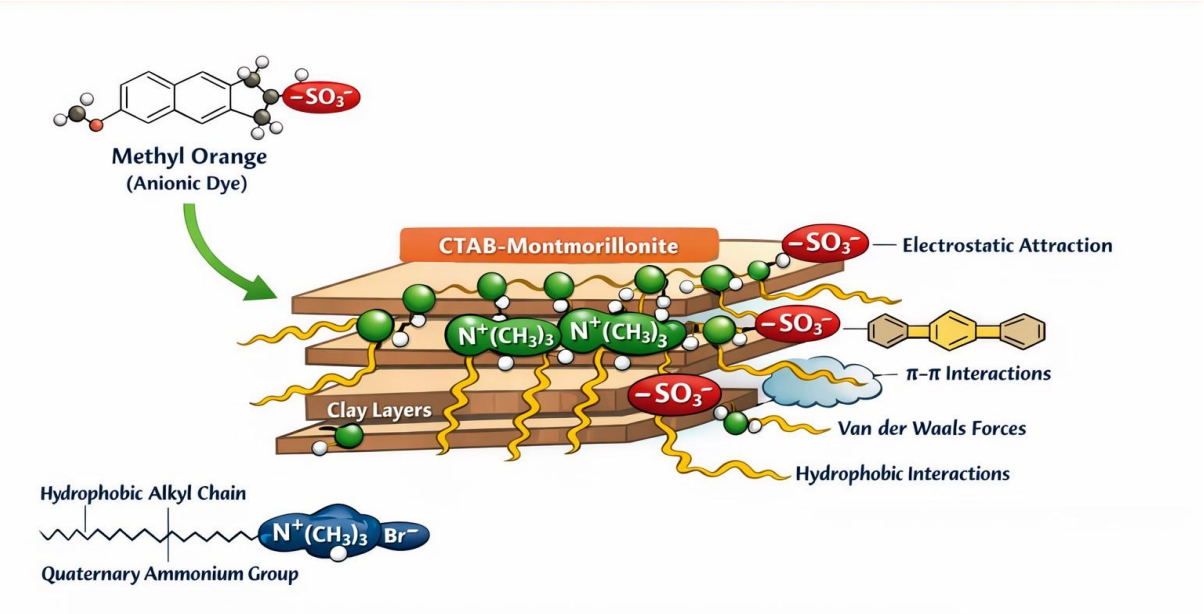


Figure VII. 7: *Proposed mechanism for the adsorption of MO on the surface of MTM-K10-CTAB.*

Reference of chapter VII

[1] K. Essifi *et al.*, « Enhanced removal of cationic and anionic dyes using Alg@NaMMT hybrid microcapsules: a sustainable encapsulation strategy outperforming adsorption », *Inorganic Chemistry Communications*, vol. 180, p. 114933, oct. 2025, doi: 10.1016/j.inoche.2025.114933.

[2] A. Mansouri, A. A. Aghazzaf, et K. Draoui, « Characterization of Moroccan Raw and Modified Clay and Its Application in Removal of Methyl Orange Dye », *International Journal of Chemical Kinetics*, vol. 57, nº 5, p. 297-314, 2025, doi: 10.1002/kin.21777.

[3] M. S. Sando, A. M. Farhan, et A. H. Jawad, « Chitosan-triphosphate/food grade algae/montmorillonite clay for adsorptive removal of methyl violet 2B dye removal: Behnken design optimization », *Biomass Conv. Bioref.*, vol. 15, nº 7, p. 11243-11258, avr. 2025, doi: 10.1007/s13399-024-05912-8.

[4] N. Mahjoubi, M. Araissi, et E. Elaloui, « Comparative adsorption study of cationic yellow 28 and anionic congo red dyes using Tunisian natural chert », *Euro-Mediterr J Environ Integr*, vol. 10, nº 1, p. 63-77, févr. 2025, doi: 10.1007/s41207-024-00635-8.

[5] T. Gasti, S. Dixit, R. B. Chougale, et S. P. Masti, « Poly (vinyl alcohol)/montmorillonite clay/poly (1-vinylpyrrolidone-co-vinyl acetate) composite films for the effective removal of methylene blue », *Iran J Sci*, vol. 49, nº 2, p. 519-529, avr. 2025, doi: 10.1007/s40995-024-01718-5.

[6] B. Mekidiche, K. Khaldi, A. Dali, S. El Korso, A. Choukchou-Braham, et I. Rekkab-Hammoumraoui, « Congo red dye removal from aqueous solution using Algerian clay: adsorption isotherms, thermodynamics, and kinetics », *J IRAN CHEM SOC*, vol. 22, nº 1, p. 191-205, janv. 2025, doi: 10.1007/s13738-024-03141-4.

[7] S. Venu Sreekala, A. Sreeja Pramod, A. Parola, J. Kazhuthuttil Kochu, et R. Thoppil Ramakrishnan, « Modified bentonite loaded with nonmetal doped titanium dioxide for the

removal of heavy metal ions and dyes from wastewater », *J Sol-Gel Sci Technol*, vol. 114, nº 2, p. 349-364, mai 2025, doi: 10.1007/s10971-025-06683-y.

[8] I. Kouda *et al.*, « Enhanced cationic dyes adsorption: Experimental and theoretical insights into Moroccan clays vs. commercial montmorillonite », *Surfaces and Interfaces*, vol. 59, p. 105946, févr. 2025, doi: 10.1016/j.surfin.2025.105946.

[9] A. Iqajtaoune, H. Saufi, B. Aouan, M. Ben Tourtit, et M. Taibi, « Enhanced Removal of Rhodamine B Dye by Adsorption and Photodegradation Processes Using Bentonite-Semiconductor-Based Nanocomposites: Synthesis, Characterization, Kinetic Study, and Cost Analysis », *Chemistry Africa*, vol. 8, nº 4, p. 1627-1645, mai 2025, doi: 10.1007/s42250-025-01219-x.

[10] H. Rezala, A. Romero, et N. Tidjani, « Investigating the comparative adsorption of methyl orange and methyl green on commercial bentonite », *Bulletin of the Chemical Society of Ethiopia*, vol. 39, nº 4, p. 643-657, janv. 2025, doi: 10.4314/bcse.v39i4.4.

[11] N. Badni *et al.*, « Kinetics of methylene blue adsorption on low cost Algerian pozzolan », *Reac Kinet Mech Cat*, vol. 138, nº 4, p. 2517-2534, août 2025, doi: 10.1007/s11144-025-02834-y.

[12] N. Mennas, « Développement de nouveaux adsorbants : polymère conducteur renforcé par des supports inorganiques pour application dans l'élimination des polluants organiques », Thesis, 2025. Consulté le: 9 janvier 2026. [En ligne]. Disponible sur: http://dspace.univ-mascara.dz:8080/jspui/handle/123456789/1235

[13] A. D. Meretoudi, I. Kalampogias, I. Koumentakou, I. K. Kalavrouziotis, A. K. Tolkou, et G. Z. Kyzas, « Chitosan/Montmorillonite/Graphene Oxide Composites for the Adsorption of Dyes from Single-Component Solutions, Binary Mixtures, and Real Textile Wastewaters: On Understanding the Adsorption Interactions », *Langmuir*, vol. 41, nº 34, p. 23198-23213, sept. 2025, doi: 10.1021/acs.langmuir.5c03148.

[14] M. Çetin et Y. Ozudogru, « Removal of malachite green dye by adsorption onto chitosan-montmorillonite nanocomposite: Kinetic, thermodynamic and equilibrium studies », *Journal of the Chinese Chemical Society*, vol. 72, nº 2, p. 196-210, 2025, doi: 10.1002/jccs.202400331.

[15] S. El Abbadi *et al.*, « Effective elimination of Congo red dye from tannery wastewater using Fe-pillared bentonite: Synthesis, adsorption isotherm, kinetics, and optimization via Box-Behnken design », *Microporous and Mesoporous Materials*, vol. 392, p. 113641, juin 2025, doi: 10.1016/j.micromeso.2025.113641.

[16] F. Z. Soufal, M. M. AL-Rajabi, S. S. Mahmod, A. Zehhaf, et I. S. Abdelkader Sid Larbi, « Sustainable Adsorption of Methyl Violet 2B from Wastewater Using Treated Algerian Clay: Isotherm and Kinetic Studies », *ChemistrySelect*, vol. 10, nº 41, p. e03544, 2025, doi: 10.1002/slct.202503544.

[17] S. Sumardiono, F. K. Setiawan, B. Jos, et H. Cahyono, « Photocatalytic adsorption-driven removal of rhodamine B by silver Tetratungstate-modified bentonite: Kinetic, isotherm, and thermodynamic analysis », *Inorganic Chemistry Communications*, vol. 182, p. 115616, déc. 2025, doi: 10.1016/j.inoche.2025.115616.

[18] P. Sharma, D. J. Borah, P. Das, et M. R. Das, « Cationic and anionic dye removal from aqueous solution using montmorillonite clay: evaluation of adsorption parameters and mechanism », *Desalination and Water Treatment*, vol. 57, nº 18, p. 8372-8388, juill. 2016, doi: 10.1080/19443994.2015.1021844.

[19] D. Samah et S. Ikram, « Etude de l'adsorption du Bleu de méthylène et de l'Orange méthyle en milieu aqueux par un biocomposite Chitosane / Argile », Faculté des sciences et de la technologie, 2025. Consulté le: 9 janvier 2026. [En ligne]. Disponible sur: https://dspace.univ-bba.dz/handle/123456789/527

[20] A. S. Elsherbiny, « Adsorption kinetics and mechanism of acid dye onto montmorillonite from aqueous solutions: Stopped-flow measurements », *Applied Clay Science*, vol. 83-84, p. 56-62, oct. 2013, doi: 10.1016/j.clay.2013.07.014.

[21] N. Mennas *et al.*, « Adsorption of Methylene Blue Dye by Cetyltrimethylammonium Bromide Intercalated Polyaniline-Functionalized Montmorillonite Clay Nanocomposite: Kinetics, Isotherms, and Mechanism Study », *Polymers*, vol. 15, nº 17, août 2023, doi: 10.3390/polym15173518.

[22] H. Essebaai, J. Bensalah, Z. Safi, N. Wazzan, A. Essamri, et E. H. Rifi, « Analysis of the kinetics and isotherm of the adsorption of the dyes on the Montmorillonite clay, as well as a modeling research using techniques from density-functional theory (DFT) », *Euro-Mediterr J Environ Integr*, vol. 10, nº 6, p. 4927-4947, déc. 2025, doi: 10.1007/s41207-025-00910-2.



CHAPTER VIII



Chapter VIII: Application of layered double hydroxides (LDHs) for the removal of anionic dyes

1. Introduction

Following the exploring of natural based adsorbents such as cationic natural clays, K10, halloysite nanotubes HNT, and biomass-derived biochars in the previous chapters. It is found that these materials show promising adsorption performance. Nevertheless, the primary constraint imposed by these materials is largely due to their predominantly negative charge or their inability to exchange anions. The intrinsic physico-chemical characteristics of previously studied materials generally indicated low efficiency for the removal of anionic pollutants such as MO specially when are not modified. The materials demonstrated mediocre adsorption capacity, notably in scenarios where robust electrostatic attraction and adaptable surface chemistry are essential. The hydrotalcite [$Mg_6Al_2CO_3(OH)_{16}\cdot 4(H_2O)$]-like layered double hydroxides (LDHs) emerge as an alternative class of materials that overcome many of the aforementioned constraints [1].

In contradistinction to natural aluminosilicate clays, HDL exhibit positively charged brucite-like layers, which are compensated by anions in the interlaminar space. The exchange and adaptation of constituent material elements can be facilitated by compositional control [2]. The occurrence of minerals belonging to the hydrotalcite group is rare from a mineralogical standpoint. The cationic clays have only been identified as secondary phases in metamorphosed serpentinised ultramafic rocks, which hinders their potential for direct application. Nevertheless, the natural occurrences have provided significant insights into the mechanisms of LDH formation and synthesis [3].

The majority of LDH materials employed in environmental applications are synthetic allowing precise control over metal composition and interlayer space contents. Substitution of the Mg^{2+} and Al^{3+} ions found in hydrotalcite crystallites, which are responsible for the octahedral sites, can occur during synthesis either through complete replacement or stoichiometric adjustment. The number of the hydroxyl anions occupy the corners, anionic

species and water content in the interlamellar space are generally affected by this, which compensate for the charge deficit according to the general formula [4]:

$$[M^{2+}_{1-x}\ M^{3+}_{x}\ (OH)_2]^{x+}(\ A^{n-})_{x/n}\ .mH_2O]$$

The adsorption capacity and selectivity of LDHs is strongly influenced by the type attraction induced by the overall composition, exchange capacity, and interlayer diffusion processes. In addition to the composition of metals present in adjustment and control, the LDH can be modified by a variety of strategies [5]. The main approaches involve controlling the size of the crystallites, undergoing heat treatment or adjusting the type of interlayer anion. The exchange capacity and active surface area can be enhanced through such modifications. The acidity type and density, structural stability, and adsorption kinetics can also be tuned for affinity towards specific pollutants [6].

The main objective of this chapter is to provide a preliminary investigation into the influence of interlayer anions on the adsorption behavior of layered double hydroxides (LDHs) toward Methyl Orange in aqueous solutions. In this regard, three LDH systems with Mg/Al 2/1 molar ratio containing different interlayer anions (CO_3^{2-}, SO_4^{2-}, and PO_4^{3-}) are comparatively evaluated in order to highlight the role of anion type on adsorption performance. The study is primarily focused on equilibrium analysis through adsorption isotherms, allowing for the assessment of adsorption capacity and interaction mechanisms.

This chapter provide a basis for the future design and optimization of modified LDH-based systems for environmental remediation applications.

2. Adsorbents screening

Mg_2Al_1LDH-based adsorbents with different interlayer anions are screened at 20 °C adsorption conditions under batch equilibrium, and the performance results expressed as maximum adsorption capacity are presented in **Figure VIII.1**

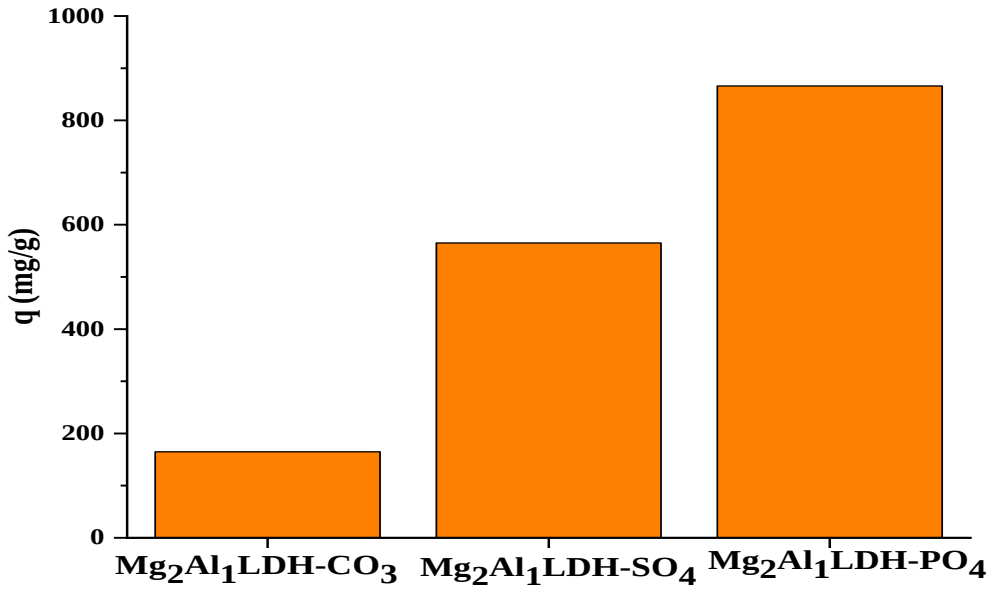


***Figure VIII. 1**: Adsorption capacity of Mg2Al1LDH-based adsorbents.*

The comparison between LDH materials containing different interlayer anions clearly demonstrates that the adsorption performance is strongly dependent on the nature of the intercalated species. The $Mg_2Al_1LDH\text{-}CO_3$ system exhibits the lowest adsorption capacity (q_{max} ≈ 165 $mg \cdot g^{-1}$), whereas $Mg_2Al_1LDH\text{-}SO_4$ reaches 565 $mg \cdot g^{-1}$ and $Mg_2Al_1LDH\text{-}PO_4$ shows the highest value (q_{max} ≈ 866 $mg \cdot g^{-1}$). The intrinsic properties of interlayer anions, such as their molecular size, geometry, charge distribution, and interaction strength with the host layers, can be analyzed to rationalize this trend.

$Mg_2Al_1LDH\text{-}CO_3$ exhibits the lowest exchange capacity due to the stability of carbonate within the interlayer space. The carbonate ions possess a planar geometry with a highly localized charge distribution, which leads to strong electrostatic interactions with the positively charged LDH layers. In addition, carbonate forms strong interactions with the existed water molecules, further stabilizing its position within the interlamellar space. As a result, CO_3^{2-} anions is poorly exchanged. The accessibility to the interlayer sites and therefore MO adsorption is restricted.

In contrast, $Mg_2Al_1LDH\text{-}SO_4^{2}$ exhibits improved ion-exchange behavior. The sulfate ion possesses a larger tetrahedral structure with a more delocalized charge distribution regarding carbonates. The affinity of sulfate toward the LDH layers is weaker. The reduced binding strength enhances the sulfonate mobility within the interlayer space and the resulting partial exchange with MO leads to a significant increase in adsorption capacity.

$Mg_2Al_1LDH\text{-}PO_4$ exhibits the highest adsorption performance. Under alkaline synthesis conditions (pH = 10), phosphate exists in the form of PO_4^{3-}/HPO_4^{2-}. This species is relatively large, highly basic, and has multiple oxygen donor sites. The configurations enable stronger interactions not only with the LDH layers but also with the target dye molecules. The interaction with the LDH layers remains sufficiently moderate to allow accessibility of interlayer sites. The highest capacity is achieved through a balance of structural stability and exchange flexibility combined with cooperative adsorption effects. However, this remains a theoretical concept requiring further characterization.

The experimental adsorption isotherms were analyzed using several non-linear regression models, including Langmuir, Freundlich, Temkin, Liu, and Sips, for all three Mg_2Al_1LDH samples. The corresponding fits are presented in the **Figure VIII.2**. Among the tested models, the Sips isotherm exhibited the best agreement with the experimental data for MO adsorption across all samples, as indicated by the highest adjusted coefficient of determination (R^2 = 0.973, 0.922 and 0.988) and the lowest AIC values (99.26, 122.04 and 54.58) (**Table VIII.1**). Furthermore, the difference between the theoretical and experimental adsorption capacities (q_e) was minimal, confirming the reliability of the Sips model in describing the adsorption behavior.

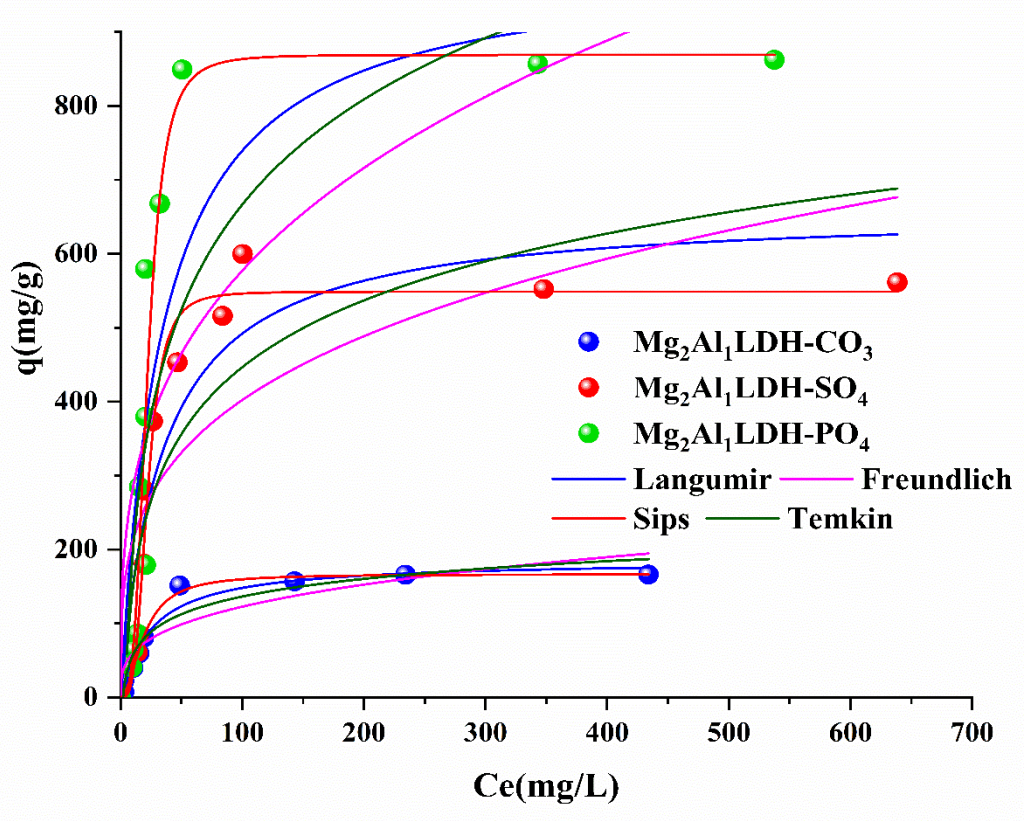


Figure VIII. 2: *Langumir, Freundlich, Temkin and Sips non-linear fits to the experimental data of MO adsorption by Mg2Al1LDH-based adsorbents.*

The Sips model is a multiparameter model isotherm that combines the features of both Langmuir and Freundlich models, making it particularly suitable for describing adsorption on heterogeneous surfaces with a finite number of active sites. The model assumes a continuous distribution of adsorption energies at low coverage, gradually approaching monolayer saturation at higher concentrations. The MO adsorption onto the studied series occurs at different active sites or may involve cooperative adsorption behavior with the formation of a few layers.

The obtained model parameters give more insight about the adsorption mechanism. The Sips affinity constant K_s (0.045–0.051 $L \cdot mg^{-1}$) remains nearly constant across all LDH systems, indicating a similar intrinsic interaction. It is suggested that the adsorption performance is primarily controlled by interlayer structural factors, rather than affinity differences. The N

factor, which provides information about surface heterogeneity and adsorption cooperativity, reveals these differences, particularly for $Mg_2Al_1LDH\text{-}CO_3$.

Table VIII. 1: *Parameters of the Langumir, Freundlich, Temkin and Sips isotherms models for MO adsorption on $Mg_2Al_1LDH\text{-}CO_3$, $Mg_2Al_1LDH\text{-}SO4$ and $Mg_2Al_1LDH\text{-}PO4$ at 20°C.*

Model	**Isotherm parameters**			
	MgAl-LDH	SO4	PO4	CO3
Langmuir isotherm	q_{max}**(mg/g)**	659.60	993.64	185.50
	KL (L/mg)	0.029	0.029	0.039
	R^2	**0.877**	**0.774**	**0.967**
	AIC	**113.02**	130.14	59.37
Freundlich isotherm	K_f***(L/mg)***	110.43	137.63	28.81
	n	3.56	3.21	3.18
	R^2	**0.699**	**0.636**	**0.857**
	AIC	**123.77**	**135.87**	74.08
***Temkin* isotherm**	***B*** **(mg/g)**	130.45	205.25	34.53
	A **(L/mg)**	0.30	0.25	0.51
	R^2	**0.812**	**0.734**	**0.937**
	AIC	118.13	132.10	65.87
Sips isotherm	q_{max}**(mg/g)**	548.77	869.18	166.60
	Ks (L/mg)$^{1/n}$	0.045	0.045	0.051
	N	3.55	3.31	1.90
	R^2	**0.973**	**0.922**	**0.988**
	AIC	**99.26**	**122.04**	54.58283

The lower N value for the LDH containing carbonate system reflects weaker cooperativity and closer behavior to a conventional Langmuir-type process. The low carbonate exchange capacity in LDH structures is consistent with this behavior. In contrast, the obtained values (N = 3.55 and 3.31 for LDH–SO_4 and LDH–PO_4, respectively) are so far higher than unity, indicating the presence of cooperative adsorption mechanisms. The adsorption of initial dye molecules facilitates subsequent adsorption, likely through intermolecular interactions or structural rearrangement within the LDH interlayer.

The maximum adsorption capacities (q_{max}) obtained from the Sips model clearly follow the order LDH–PO_4 (869.18 $mg \cdot g^{-1}$) > LDH–SO_4 (548.77 $mg \cdot g^{-1}$) > LDH–CO_3 (166.60 $mg \cdot g^{-1}$), confirming that the nature of the interlayer anion plays a dominant role in controlling adsorption performance. In contrast, the Sips affinity constant (K_s) shows relatively similar values for all samples (≈0.045–0.051 $L \cdot mg^{-1}$), suggesting that the intrinsic interaction strength between Methyl Orange molecules and the adsorption sites is comparable across the different LDH systems. Therefore, the differences in adsorption capacity are not primarily governed by adsorption affinity, but rather by the accessibility of active sites and the structural characteristics of the interlayer region. The lower n value for the CO_3^{2-} system reflects weaker cooperativity and a behavior closer to a conventional Langmuir-type process. The obtained values (n ≈ 3.55 for LDH–SO_4, 3.31 for LDH–PO_4, and 1.90 for LDH–CO_3) are all greater than unity, indicating deviation from ideal Langmuir behavior and suggesting the presence of cooperative adsorption mechanisms. The significantly higher n values for the SO_4^{2-} and PO_4-based systems indicate strong cooperative effects, where the adsorption of initial dye molecules facilitates subsequent adsorption, likely through intermolecular interactions or structural rearrangement within the LDH interlayer. These results further support that LDH systems can achieve high anionic adsorption capacities. However, the adsorption mechanism cannot be described solely by

classical models, and more experimental, modeling, and data-driven approaches relating adsorption behavior to intrinsic structural and textural properties are required.

References of Chapter VIII

[1] C. V. Flores *et al.*, « Layered double hydroxides (LDH) materials for effective phosphate adsorption from aqueous solution », *RSC Sustainability*, vol. 4, nº 1, p. 61-78, 2026, doi: 10.1039/D5SU00818B.

[2] G. Fetter et F. D. Velázquez-Herrera, « Intrinsic antimicrobial properties of LDH clays: a brief review », *emergent mater.*, vol. 8, nº 8, p. 7007-7022, déc. 2025, doi: 10.1007/s42247-025-01270-x.

[3] R. S. Umdor, I. T. Longchar, S. Sharma, K. Umdor, et D. Sinha, « LDH composite as an efficient material for the photocatalytic degradation of pharmaceutical pollutants using advanced oxidation process: A review », *Journal of Alloys and Compounds*, vol. 1022, p. 179798, avr. 2025, doi: 10.1016/j.jallcom.2025.179798.

[4] M. Shavandi, F. Abutalebian, M. Salimi, et S. S. Shafiei, « A Brief Review on Layered Double Hydroxides (LDH): Innovative Non-Viral Carriers for Nucleic Acid Delivery », *ChemistrySelect*, vol. 10, nº 16, p. e202500766, 2025, doi: 10.1002/slct.202500766.

[5] D. Brahma, M. P. Barman, D. Basak, et H. Saikia, « Prospects of layered double hydroxide (LDH)-based adsorbents for the remediation of environmental inorganic pollutants from wastewater: a critical review », *Environ. Sci.: Water Res. Technol.*, vol. 11, nº 4, p. 830-875, mars 2025, doi: 10.1039/D4EW01039F.

[6] A. A. Altalhi, E. A. Mohamed, et N. A. Negm, « Recent advances in layered double hydroxide (LDH)-based materials: fabrication, modification strategies, characterization, promising environmental catalytic applications, and prospective aspects », *Energy Advances*, vol. 3, nº 9, p. 2136-2151, 2024, doi: 10.1039/D4YA00272E.

GENERAL CONCLUSION

General conclusion

Water consumption is extensive in the industrial sector. Effluents containing organic compounds and synthetic dyes, which are highly toxic and poorly biodegradable, cause significant disturbances to aquatic ecosystems upon discharge. The treatment of dye-contaminated effluents is therefore essential for environmental protection. Furthermore, the identification of low-cost, locally available, and efficient materials that can be used as alternatives to commercial activated carbon for the removal of dyes from aqueous solutions is of significant interest, therefore the development of new adsorbents that are effective, environmentally friendly, renewable, and economically viable for water treatment represents a major scientific challenge.

The primary objective of this study was to synthesize and modify materials using simple and cost-effective approaches and to demonstrate their applicability in the treatment of dye contaminated wastewater. Methylene blue and methyl orange were selected as representative models of cationic and anionic dyes, respectively. To evaluate the performance of the developed materials, comprehensive investigations were conducted, including adsorption kinetics, equilibrium studies, analysis of operational parameters, and physicochemical characterization. For this purpose, four main classes of materials: halloysite nanotubes (HNTs), biochars, montmorillonite K10 (MTM-K10) and layered double hydroxides (LDHs) were prepared and employed as adsorbents for dye removal from aqueous solutions.

The different materials were characterized using FTIR, XRD, XRF, TEM, TGA/DTA, and BET techniques for a better understanding of the physical and chemical properties of the materials.

Raw HNTs from Algeria, was used to eliminate methylene bleu from aqueous medium, the study employed the Box-behnken design to optimize the adsorption conditions. Optimal

removal efficiency was obtained at pH 10 using an adsorbent dosage of 10 mg and an initial methylene blue concentration of 80 mg/L. Kinetic studies indicated that the adsorption process follows a pseudo-second-order model, suggesting that chemisorption is the dominant mechanism. The equilibrium data were best described by the Langmuir isotherm, yielding a maximum adsorption capacity of 149.6 mg/g. Furthermore, a statistical physics-based modeling approach, coupled with density functional theory (DFT) and molecular dynamics (MD) simulations, provided insight into the interaction mechanisms between methylene blue and halloysite nanotubes. The results revealed a preferential longitudinal alignment of methylene blue molecules along the nanotube surface, with adsorption governed by electrostatic, dipolar, and π–cation interactions.

A novel composite material was synthesized through the encapsulation of the HNTs/PANI composite within alginate beads. The resulting hybrid adsorbent exhibited high removal efficiencies for both methyl orange (MO) and methylene blue (MB), with adsorption capacities of 150.55 mg/g and 493.87 mg/g, respectively. Subsequent investigations focused primarily on methylene blue adsorption. Process parameter optimization was carried out using multiple approaches, including response surface methodology based on a Box–Behnken design (RSM-BBD), artificial neural networks coupled with a genetic algorithm (ANN-GA), and artificial neural networks integrated with the grey wolf optimizer (ANN-GWO). The optimization results obtained from these methodologies were highly consistent, identifying optimal conditions at pH 9, an adsorbent dosage of 30 mg, a temperature of 30 °C, and an initial methylene blue concentration of 300 mg/L. Kinetic and equilibrium analyses revealed that the adsorption process is well described by the pseudo-first-order (PFO) kinetic model and the Langmuir isotherm, respectively, indicating a predominantly physical adsorption mechanism occurring on a homogeneous surface. Thermodynamic parameters further demonstrated that the adsorption process is spontaneous, endothermic, and thermodynamically favorable.

The biomass-based component of this study focused on the synthesis of three distinct biochars derived from mandarin, pomegranate, and walnut peels mixture, with the objective of removing methylene blue (MB) from wastewater. The developed materials, denoted as BC500, BC500H, and BC500-SA, were initially carbonized at 500 °C, subsequently chemically activated using phosphoric acid, and finally encapsulated within alginate matrices. Adsorption experiments were conducted by systematically varying key operational parameters, including solution pH, initial dye concentration, and adsorbent dosage, in order to assess the adsorption performance of the prepared materials. Optimal conditions for methylene blue removal were identified through a design of experiments approach, yielding a pH of 6, an initial dye concentration of 300 mg/L, and an adsorbent dosage of 10 mg for BC500-SA. Thermodynamic analysis indicated that the adsorption process is spontaneous and endothermic. Kinetic data were best described by the pseudo-first-order (PFO) model, while equilibrium behavior followed the Langmuir isotherm, suggesting a physical monolayer adsorption mechanism. Notably, the maximum adsorption capacity of BC500-SA derived from the Langmuir model reached 525 mg/g, highlighting the excellent performance of this composite for methylene blue removal.

Negatively charged montmorillonite K10 exhibited a satisfactory adsorption capacity toward methylene blue, reaching 106 mg/g. To enhance its affinity for anionic dyes, the clay surface was modified using the cationic surfactant cetyltrimethylammonium bromide (CTAB), resulting in the organophilic composite MTM-K10-CTAB. This surface modification significantly improved the adsorption performance for methyl orange, with a maximum adsorption capacity of 84.56 mg/g. The enhanced removal efficiency is primarily attributed to electrostatic attraction between the anionic dye molecules and the positively charged CTAB-modified surface. Additionally, hydrophobic interactions between the alkyl chains of CTAB and the aromatic, hydrophobic moieties of the dye further contribute to adsorption. These

interactions are complemented by van der Waals forces and potential π–π interactions between the aromatic rings of methyl orange and those associated with the modified clay structure.

The adsorption performance of layered double hydroxides (LDHs) toward Methyl Orange is strongly governed by the nature of the interlayer anions. The significant variation in maximum adsorption capacities, following the order $PO_4^{3-} > SO_4^{2-} > CO_3^{2-}$, demonstrates that structural factors particularly interlayer accessibility and arrangement play a more decisive role than the intrinsic affinity between the adsorbent and adsorbate, which remains relatively constant across the systems.

Furthermore, the Sips model analysis reveals that adsorption proceeds through cooperative mechanisms rather than ideal monolayer behavior, especially for PO_4^{3-} and SO_4^{2-} intercalated LDHs. The elevated heterogeneity parameters ($n > 1$) indicate that initial dye adsorption enhances subsequent uptake, likely through intermolecular interactions and structural reorganization within the interlayer space. In contrast, the CO_3^{2-} system exhibits weaker cooperativity and a behavior closer to conventional Langmuir adsorption, consistent with its lower capacity.

These findings highlight that optimizing LDH adsorption efficiency requires careful control of interlayer chemistry to maximize accessible active sites and promote cooperative effects. At the same time, the complexity of the observed behavior suggests that classical adsorption models alone are insufficient to fully describe the system. A more integrated approach, combining experimental investigation with advanced modeling and structure property relationships, is necessary to better understand and predict adsorption performance in LDHs based materials.

International publications

1. ***Aymene Salah Bendrihem****, Chafia Tiar, Roufaida Merir, Imene Kecir, Messaoud Guellal, Riadh Bourzami & Mokhtar Boutahala.*, "Experimental and theoretical studies of the interaction of cationic dye in halloysite nanotubes," *Reaction Kinetics, Mechanisms and Catalysis*, Aug. 2025, doi: 10.1007/s11144-025-02933-w.
2. Imene K, Charf B, **Aymen Salah Bendrihem**, Mokhtar B. Thermal treatment of Cu-doped hydrotalcite-like adsorbents for improved removal of methyl orange from water. Sep Purif Technol 365:132656. https://doi.org/10.1016/j.seppur.2025.132656
3. A.I. Boulahbal , L. Santamaría, R. Bourzami, **A.S. Bendrihem**, M. Boutahala, S.A. Koril, A. Gil. Enhancing adsorptive performance of Cu-Al layered double hydroxides from aluminum saline slags : Insights from response surface methodology and molecular dynamic simulation. Miner Eng 219:109067.https://doi.org/10.1016/j.mineng.2024.10906
4. Hechaichi Chaima , BounouktaCharf Eddine , Benamraoui Faouzia , Houchet Rana , **Bendrihem AymeneSalah** , BoulahbalAziza Imene , Djerboua Ferhat, Bourzami Riadh, Boutahala Mokhtar "Adsorptive removal of cationic dye from aqueous solutions using activated carbon prepared from Crataegus monogyna / sodium alginate / polyaniline composite beads : Experimental study and molecular dynamic simulation," *J Mol Liq*, vol. 408, no. June, p. 125372, 2024, doi: 10.1016/j.molliq.2024.125372.
5. Slougui N, Slama M, Boudaoud Y, **Bendrihem AS** (2022) Optimization of GC-MS Method for Analysis of Basil Essential Oils from Algeria: Design of Experiments and Exploratory Pattern Recognition. J Chem 2022:5880539. https://doi.org/10.1155/2022/5880539

International Communications

BENDRIHEM A.S. Tiar C, Boutahala M. Removal of anionic cationic dyes from water sources by adsorption (ICCE"24 OGI) Setif 26th -27th November 2024.

BENDRIHEM A.S. Tiar C, Boutahala M , Merir R. Optimization and mechanistic study of cationic dye onto biomass derived biochar, (IWEE 25), October 7th – 8th , **2025.**

National Communications

BENDRIHEM A.S. Tiar C, Boutahala M. Removal of anionic cationic dyes from water sources by adsorption (ICCE"24 OGI) Setif 26th -27th November 2024.

BENDRIHEM A.S. Tiar C, Boutahala M , Merir R. Optimization and mechanistic study of cationic dye onto biomass derived biochar, (IWEE 25), October 7th – 8th , 2025.

Abstract: In this study, a series of 15 adsorbent materials based on halloysite, polyaniline, alginate, biochar, montmorillonite and layered double hydroxides materials were synthesized and systematically investigated. The prepared adsorbents were characterized by BET, FTIR, ATG/DTA, SEM, TEM, and XRD analyses to elucidate their structural and physicochemical properties. Their adsorption performance toward methylene blue (MB) and methyl orange (MO) was evaluated under different operating conditions (pH, temperature, initial concentration, and adsorbent dosage), which were further optimized using design of experiments and artificial intelligence approaches. The results showed that composite and encapsulated materials exhibited higher MB adsorption efficiency than their powdered counterparts, while organophilic montmorillonite significantly improved MO removal. While the different LDHs materials showed the best uptake for MO removal. Molecular dynamics simulations confirmed that adsorption is spontaneous and mainly governed by weak physical interactions, including van der Waals forces, hydrogen bonding, and π–π interactions.

Keywords: adsorbent, biochar, halloysite, LDHs, adsorption, methylene blue. Design of experiments

Résumé : Dans cette étude, une série de quinze matériaux adsorbants à base d'halloysite, de polyaniline, d'alginate, de biochar, de montmorillonite et de matériaux de type hydroxydes doubles lamellaires (LDHs) a été synthétisée et étudiée de manière systématique. Les adsorbants préparés ont été caractérisés par des analyses BET, FTIR, ATG/DTA, MEB, MET et DRX afin d'élucider leurs propriétés structurales et physicochimiques. Leurs performances d'adsorption vis-à-vis du bleu de méthylène (BM) et de méthyle orange (MO) ont été évaluées sous différentes conditions opératoires (pH, température, concentration initiale et dosage d'adsorbant), puis optimisées à l'aide de plans d'expériences et d'approches d'intelligence artificielle. Les résultats ont montré que les matériaux composites et encapsulés présentent une efficacité d'adsorption du BM supérieure à celle de leurs homologues sous forme pulvérulente, tandis que la montmorillonite organophile améliore significativement l'élimination du MO. Par ailleurs, les différents matériaux LDHs ont démontré les meilleures capacités d'adsorption pour l'élimination du MO. Les simulations de dynamique moléculaire ont confirmé que le processus d'adsorption est spontané et principalement régi par des interactions physiques faibles, incluant les forces de Van der Waals, les liaisons hydrogène et les interactions π–π.

Mots-clés : adsorbant, biochar, halloysite, HDLs, adsorption, bleu de méthylène, plans d'expérience.

ملخص

. في هذه الدراسة، تم تحضير سلسلة مكوّنة من خمسة عشر مادة ممتزة قائمة على الهالويزيت، والبوليانيلين، والألجينات، والبيوشار، والمونتموريلونيت، ومواد الهيدروكسيدات المزدوجة الطبقية، ودُرست بشكل منهجي. وقد تم تحليل هذه المواد باستخدام تقنيات تحليل مساحة السطح النوعية وتوزيع المسام بطريقة ادمصاص النيتروجين، والتحليل الطيفي بالأشعة تحت الحمراء، والتحليل الحراري الوزني ، والمجهر الإلكتروني الماسح، ، وحيود الأشعة السينية، وذلك بهدف تحديد خصائصها البنيوية والفيزيائية-الكيميائية. كما تم تقييم أدائها في ادمصاص كلٍّ من أزرق الميثيلين والبرتقالي الميثيلي تحت ظروف تشغيل مختلفة، وأظهرت النتائج أن المواد المركبة والمغلفة تتمتع بكفاءة أعلى في ادمصاص أزرق الميثيلين مقارنةً بنظيراتها المسحوقة، في حين ساهمت المونتموريلونيت المعدّلة لتصبح محبةً للمواد العضوية في تحسين إزالة البرتقالي الميثيلي بشكل ملحوظ. كما بيّنت مواد الهيدروكسيدات المزدوجة الطبقية أفضل سعة ادمصاص لإزالة هذا الصباغ.وأكدت محاكاة الديناميكيات الجزيئية أن عملية الادمصاص تلقائية، وتخضع أساسًا لتأثرات فيزيائية ضعيفة، تشمل قوى فان دير فالس، والروابط الهيدروجينية.

الكلمات المفتاحية :مادة ماصّة، بيوشار، هالويزيت، ألجينات، ادمصاص، أزرق الميثيلين.